High-Temperature Dielectrics Based on Tungsten Bronze Structured Niobate Ceramics

Thomas Anthony Brown

Submitted in accordance with the requirements for the degree of

Doctor of Philosophy

The University of Leeds

Functional Materials, Products and Devices

School of Chemical and Process Engineering

Primary Supervisors: Professor Steven J Milne and Professor Andy P Brown

November 2022

The candidate confirms that the work submitted is his/her own and that appropriate credit has been given where reference has been made to the work of others.

Part of the work in Chapter 4 of this thesis has appeared in publication as follows:

Brown, T., Brown, A., Hall, D., Hooper, T., Li, Y., Micklethwaite, S., Aslam, Z. and Milne, S. (2020). New high temperature dielectrics: Bi-free tungsten bronze ceramics with stable permittivity over a very wide temperature range, *Journal of the European Ceramic Society*, 41 (6), pp. 3416-3424. (See Appendix B)

I was responsible for generating data and figures, and writing of manuscript. The contribution of other authors was supervision and advice, and providing feedback and edits of manuscript except for:

Full Rietveld refinement – Dr Yizhe Li, University of Manchester

Transmission electron microscopy – Dr Zabeada Aslam, University of Leeds

Polarisation-electric field analysis – Dr David Hall, University of Manchester

Focused Ion Beam section – Mr John Harrington

Acknowledgements

First of all I would like to thank my supervisors Professor Steven Milne and Professor Andy Brown for all their help, encouragement and patience. Their insistence on high standards was always appreciated, even if this wasn't always stated.

Special thanks to Rob Simpson, Dr Faye Esat, and Dr Thomas Hooper for their continuous help and support throughout the duration of producing this thesis.

Also thanks to, Mo Javid, Dr Teresa Roncal-Herreo, Stuart Micklethwaite, Dr Anton Goetzee-Barral, Professor Andrew Bell, Dr Chloe Fisher, Dr Danielle Woodruff, Dr Yang Li, Dr Zabeada Aslam, Dr Yizhe Li, Dr David Hall and John Harrington for help at various points over the last four years.

Biggest thanks to Laura who always supported and believed in me throughout the whole process. Also the kids, Stan, Fred, and Joe, who were loud and annoying a lot of the time but much loved.

Abstract

A novel high temperature dielectric ceramic has been demonstrated based on strontium sodium niobate, $Sr_2NaNb_5O_{15}$ (SNN1.0), which has the tungsten bronze crystal structure and shows relaxor-like weak frequency dispersion. Initial experiments involved co-doping with low levels of, Ca^{2+}, Y^{3+} and Zr^{4+} to introduce chemical inhomogeneity to broaden the twin dielectric peaks (Curie peak at 305 ^oC, and a low temperature peak at -15 ^oC in SNN1.0). The resulting materials were observed to exhibit high and stable relative permittivity across the technologically important -55 to 300 ^oC temperature range, with the aim of restricting the variation in permittivity to within the Electronics Industries Alliance R-type ±15 % value. Unlike previously reported materials with similar dielectric properties, the new dielectrics do not contain Bi or Pb. In principle this makes them compatible with base metal electrode multilayer ceramic manufacturing processing.

For tri-doped compositions, $Sr_{2-x-y}Ca_xY_xNaNb_{5-y}Zr_yO_{15}$ (SCNN-YZ) dielectric peaks became very diffuse. At x = y = 0.05, median ε_r values were 1310 +/-10 % from -65 to 300 °C, with dielectric loss tangents, tan δ, ≤ 0.035 from -34 to 378 °C. Microstructural analyses excluded core-shell mechanisms being responsible for the flattening of the ε_r –T response. A further series of experiments with individual dopants were performed to examine the reasons for peak suppression and attainment of R-type stability in relative permittivity. It was also realised that SNN was a solid solution $Sr_{2+x}Na_{1-2x}Nb_5O_{15}$ (SNN). On cooling from sintering temperatures the SNN1.0 composition, x = 0, lies outside the single phase solid solution region at room temperature and exists as a two phase mixture of the limiting solid solution composition, (x ~ 0.9), and a Sr modified $NaNbO_3$ phase. Sodium deficient variants of SNN ($Sr_{2.1}Na_{0.8}Nb_5O_{15}$, SNN0.8) were therefore investigated to produce a single phase composition. Nevertheless, because the early tri-doped results were based on x = 0 ($Sr_2NaNb_5O_{15}$) it was decided to continue to use this as a starting point from which to examine the effects of single-dopants. The single doping experiments indicated that A-site vacancies bring about a severe suppression of the Curie peak. However the presence of all three dopants is required to produce the near flat response which was observed for SCNN-YZ (x = y = 0.05).

Although the dielectric properties of the SCNN-YZ ceramics appear favourable in terms of developing new high temperature capacitor materials, the presence of Na vacancies in the SNN solid compositions is a drawback. A greater problem was discovered in the latter months of the project. It had been reported in the literature that SNN was metastable below ~1200 °C. The significance of this for a capacitor application would depend on the kinetics of decomposition at capacitor operating temperature. Annealing experiments at 300 to 600 °C were initiated. At 600 °C after only 2 to 3 hours additional phases of $SrNb_2O_6$ and $Sr_2Nb_{10}O_{27}$ form from the SNN1.0, indicating partial decomposition. At 400 °C there is evidence of decomposition in SNN0.8 after 24 weeks. Even at 300 °C, the upper working temperature of capacitors for some power electronics applications, there is tentative evidence of structural changes.

Contents

Acknowledgements……..ii

Abstract……..iii

List of Figures……x

List of Tables……..xix

List of Abbreviations……...xxii

List of Symbols……xxiv

Chapter 1 – Introduction……1

1.1 High temperature dielectrics……...1

1.2 Research problem……2

1.3 Aims and objectives……3

1.3.1 Objectives……3

Chapter 2 - Background science and literature review……..5

2.1 Introduction……5

2.2 Crystal structure……5

2.3 Dielectric materials and capacitors……7

2.4 Polarisation mechanisms……9

2.5 Ferroelectrics……..11

2.5.1 Perovskite crystal structure……...11

2.5.2 Ferroelectric domains……14

2.5.3 $BaTiO_3$, doping and temperature stability……16

2.6 Relaxor ferroelectrics……18

2.7 Tungsten Bronze structure……21

2.8 Relevant materials……24

2.8.1 $Sr_2NaNb_5O_{15}$ (SNN)……24

2.8.2 A-site doping……28

2.8.3 B-site doping and co-doping (A and B-sites)……31

2.8.4 A-site vacancies – “unfilled” tungsten bronze structures……..33

Chapter 3 - Experimental methods……37

3.1 Introduction……..37

3.2 Mixed-oxide synthesis route……37

3.2.1 Powder processing……37

3.2.2 Ball milling……38

3.2.3 Powder drying and sieving……39

3.2.4 Calcination……39

3.2.5 Pellet formation……39

3.2.6 Sintering……40

3.2.7 Density measurements and electrode application……41

3.3 Characterisation and analysis techniques……..42

3.3.1 X-ray diffraction (XRD)……...42

3.3.2 Permittivity vs temperature……44

3.3.3 Scanning electron microscope (SEM)……45

3.3.4 Energy dispersive X-ray spectroscopy (EDX)……47

3.3.5 Polarisation-electric field loops (P-E loops)……47

Chapter 4 - Results 1: Synthesis and properties of strontium niobate (SNN) ceramic system with simultaneous Ca^{2+}, Y^{3+}, and Zr^{4+} doping……..48

4.1 Introduction……..48

4.2 Strontium sodium niobate (SNN)……51

4.2.1 Phase analysis……51

4.2.2 Dielectric analysis……...55

4.2.3 Ferroelectric analysis……57

4.2.4 Microstructural analysis……58

4.2.5 Summary: Strontium sodium niobate (SNN)……59

4.3 Calcium modified strontium sodium niobate (SCNN) with Y^{3+} and Zr^{4+} doping (SCNN-YZ)……60

4.3.1 Phase analysis……61

4.3.2 Dielectric analysis……...64

4.3.3 Ferroelectric analysis……70

4.3.4 Microstructural analysis……72

4.3.5 Summary: Calcium modified strontium sodium niobate (SCNN) with Y^{3+} and Zr^{4+} doping (SCNN-YZ)……75

Chapter 5 - Results 2: Further doping studies relating to $Sr_2NaNb_5O_{15}$ and characterisation of sodium deficient phase $Sr_{2.1}Na_{0.8}Nb_5O_{15}$……81

5.1 Introduction……..81

5.2 Strontium sodium niobate (SNN) with single doping by yttrium (SNN-Y, Y^{3+} for Sr^{2+}) and single doping by zirconium (SNN-Z, Zr^{4+} for Nb^{5+})……...82

5.2.1 Phase analysis……83

5.2.2 Dielectric analysis……...86

5.2.3 Ferroelectric analysis……90

5.2.4 Microstructural analysis……92

5.2.5 Summary Section 5.2: (Y^{3+} for Sr^{2+}; Zr^{4+} for Nb^{5+} single dopants)……..95

5.3 Strontium sodium niobate co-doped with Y^{3+} (for Sr^{2+}) and Zr^{4+} (for Nb^{5+}) (SNN-YZ)……99

5.3.1 Phase analysis……99

5.3.2 Dielectric analysis……101

5.3.3 Ferroelectric analysis……...104

5.3.4 Microstructural analysis……...105

5.3.5 Summary section 5.3: (co-doping SNN, Y^{3+} for Sr^{2+}; Zr^{4+} for Nb^{5+})……..107

5.4 Strontium sodium niobate (SNN) with single doping by yttrium (SNN-Y, Y^{3+} for Na^{+})……109

5.5 Controlled Na^{+} deficiency $Sr_{2.1}Na_{0.8}Nb_5O_{15}$ (SNN0.8)……112

5.5.1 Phase analysis……..118

5.5.2 Dielectric analysis……120

5.5.3 Ferroelectric analysis……...123

5.5.4 Microstructural analysis……...124

5.6 SNN0.8 co-doped with Ca, Y (for Sr), and Zr (for Nb)……...126

5.7 Summary section 5.5 controlled Na^{+} deficiency $Sr_{2.1}Na_{0.8}Nb_5O_{15}$ (SNN0.8), and 5.6 co-doping SNN0.8 with Ca, Y, and Zr……...130

Chapter 6 - Results 3: Long term temperature stability of strontium sodium niobate (SNN) tetragonal tungsten bronzes……..132

6.1 Introduction……132

6.2 Phase analysis after annealing……..134

6.2.1 Methodology……..134

6.2.2 Overview of phase analysis reported in rest of Section 6.2…...136

6.2.3 SNN1.0 calcined powder – in-situ high temperature X-ray diffraction 600 ^{o}C……138

6.2.4 SNN1.0 calcined powder – in-situ high temperature X-ray diffraction 400 ^{o}C……145

6.2.5 Long term annealing at 600 °C and 300 °C……..146

6.2.6 Summary: SNN1.0 calcined powder and SNN0.8 sintered pellet annealing experiments……...152

6.3 Permittivity changes resulting from annealing at 300 to 600 °C……...154

6.4 Summary: Thermal related permittivity changes……...160

Chapter 7 - Conclusions and future work……..161

7.1 Final overview……...161

7.2 Conclusions……..164

7.3 Future work……...165

Chapter 8 – References……..166

Appendix A……180

Ferroelectric ageing experiment (Dr Jon Gardener, University of Leeds)

Appendix B……182

Brown et al. (2020). New high temperature dielectrics: Bi-free tungsten bronze ceramics with stable permittivity over a very wide temperature range. *Journal of the European Ceramic Society*, 41 (6), pp. 3416-3424.

List of figures

2.2.1 Lattice vector and interaxial angle designations of a unit cell (reproduced from Cullity and Stock, 2014)……6

2.2.2 The seven crystal systems and associated lattice parameters, plus illustrations of the fourteen Bravais lattices (reproduced from Cullity and Stock, 2014)……6

2.2.3 Points, vectors, and planes within a unit cell, identified through Cartesian coordinates with reference to an origin *O*……7

2.4.1 Different polarisation mechanisms found in dielectrics (reproduced from Moulson, 2003)……9

2.4.2 Phase angle between applied alternating current and resulting voltage in an ideal dielectric and a real dielectric (reproduced from Moulson, 2003)…..10

2.5.1 Perovskite crystal structure ABX_3 (ABO_3 in oxide perovskites). In $BaTiO_3$, A = Ba, B = Ti, and X = O (reproduced from Demic et al. 2017)……12

2.5.2 Formation of a tetragonal phase in perovskites resulting in a non-centrosymmetric structure across all unit cells……12

2.5.3 Unit cell distortions and preferred polarisation directions in $BaTiO_3$ on cooling from > 130 ^oC to < -90 ^oC (reproduced from Jaffe et al. 1971)……13

2.5.4 Polarisation versus applied electric field hysteresis loop in ferroelectric materials (reproduced from Draft 16….. IEEE transactions, 2003)……..15

2.5.5 Plot of relative permittivity for unmodified barium titanate (reproduced from Hennings, 1987)……...17

2.6.1 Frequency dependent relative permittivity as a function of temperature at T_m in relaxor ferroelectric $Ba_4Sr_{2-z}(Ba_{0.37}Ca_{0.63})_zGaNb_9O_{30}$, z = 0.5 (reproduced from Miller et al. 2015)……...18

2.6.2 P-E hysteresis loops for a) normal ferroelectric, b) relaxor ferroelectric, c) dielectric (reproduced from Yang et al. 2013)……..19

2.6.3 Temperature stable and frequency dependent relative permittivity plot for (1-x)$BaTiO_3$ – x$Bi(Mg_{0.5}Ti_{0.5})O_3$ (x = 0.1) (reproduced from Zeb et al. 2018)……...20

2.7.1 Tungsten Bronze (TB) structure……...21

2.7.2 Pseudocubic tetragonal primary cell of tungsten bronze structure…….23

2.8.1 Differential scanning calorimetry curve of mixed $SrNb_2O_6$ and $NaNbO_3$ powders (reproduced from Wei et al. 2010)…….25

2.8.2 Relative permittivity measured parallel to the *c* axis in SNN single crystal (1) showing three dielectric anomalies……..27

2.8.3 Relative permittivity as a function of temperature at 1 kHz for $Sr_{2-x}Ca_xNaNb_5O_{15}$ ceramics with increasing levels of x (reproduced from Xie et al. 2002 (2))…….29

2.8.4 Metastable phase diagram of $NaNbO_3$ – $SrNb_2O_6$ system (reproduced form Tang et al. 1979 with annotations by the author)……33

2.8.5 Equilibrium phase diagram of $NaNbO_3$ – $SrNb_2O_6$ system (reproduced form Tang et al. 1979 with annotations by the author)……34

2.8.6 a) Solid solution of weakly polar clusters in a polar matrix. b) Weakly polar clusters in a non-polar matrix (reproduced from Cao et al. 2021)……..35

3.2.1 Typical calcination scheme used throughout this research…….39

3.2.2 Typical sintering scheme used throughout this research…….40

3.3.1 Schematic representations of electronic transitions in an atom with the emission processes indicated by arrows (Cullity and Stock, 2014)……..42

3.3.2 Geometric representation of Bragg's law showing diffraction of x-rays from lattice planes with spacing d_{hkl} (Pecharsky et al. 2009) ……43

4.1.1 (a) 10 kHz relative permittivity versus temperature plot of $Sr_2NaNb_5O_{15}$ (reproduced from Garcia-Gonzalez et al. 2007). (b) multi-frequency relative permittivity versus temperature plot for $Sr_2NaNb_5O_{15}$ (reproduced from Torres-Pardo et al. 2011)…….49

4.1.2 Relative permittivity as a function of temperature at 1 kHz for $Sr_{2-x}Ca_xNaNb_5O_{15}$ ceramics with increasing levels of x (reproduced from Xie et al. 2002 (1))……50

4.2.1 12 h powder XRD plot of SNN $Sr_2NaNb_5O_{15}$. Indexed to ICDD 04-008-7203, tetragonal SNN, P4bm……..52

4.2.2 12 h powder XRD plot of SNN $Sr_2NaNb_5O_{15}$ showing raw data (black) and calculated data (red) after unit cell refinement using HighScore Plus software (Malvern Panalytical, UK)……54

4.2.3 Multi-frequency relative permittivity and dielectric loss tangent versus temperature plots for Sr2NaNb5O15……56

4.2.4 1 kHz relative permittivity and dielectric loss tangent versus temperature plot for $Sr_2NaNb_5O_{15}$. The dashed outline indicates the +/- 15 % limit…….56

4.2.5 Multi-field polarisation – electric field loop plots for $Sr_2NaNb_5O_{15}$ up to 40 kV cm^{-1}……57

4.2.6 Secondary electron (left) and back scattered electron (right) images of $Sr_2NaNb_5O_{15}$……..58

4.2.7 Back scattered electron image with associated EDX mapping of $Sr_2NaNb_5O_{15}$ showing darker grains to be Na^+ rich and Sr^{2+} deficient. Nb^{5+} has a homogenous distribution……..59

4.3.1 1 kHz comparison of permittivity and dielectric loss for $Sr_{2-x}Ca_xNaNb_5O_{15}$ with Ca^{2+} additions of x=0, 0.025, 0.05, and 0.075……61

4.3.2 12 h powder XRD plots of $Sr_{2-x-y}Ca_xY_yNaNb_{5-y}Zr_yO_{15}$ with a) x = 0.025, y = 0, b) x = 0.05, y = 0.05. Indexed to ICDD 04-008-7203, tetragonal SNN, P4bm……...62

4.3.3 Multi-frequency relative permittivity and dielectric loss tangent versus temperature plots showing relative permittivity variation for $Sr_{2-x-y}Ca_xY_yNaNb_{5-y}Zr_yO_{15}$ a) x = 0, y = 0 (SNN), b) x = 0, y = 0.025, c) x = 0.025, y = 0.025, d) x = 0.025, y = 0.05, e) x = 0.05, y = 0, f) x = 0.05, y = 0.025, g) x = 0.05, y = 0.05……66

4.3.4 1 kHz relative permittivity and dielectric loss tangent versus temperature plots for $Sr_{2-x-y}Ca_xY_yNaNb_{5-y}Zr_yO_{15}$ with a) x = 0.025, y = 0, 0.025, 0.05, and b) x = 0.05, y = 0, 0.025, 0.05……..67

4.3.5 1 kHz relative permittivity and dielectric loss tangent versus temperature plots for $Sr_{2-x-y}Ca_xY_yNaNb_{5-y}Zr_yO_{15}$ with x = 0.025, y = 0.025 sintered at 1300 ^oC and 1350 ^oC……..69

4.3.6 Polarisation – electric field loop plots at 40 kV cm^{-1} for $Sr_{2-x-y}Ca_xY_yNaNb_{5-y}Zr_yO_{15}$ with a) x = 0.025, y = 0, 0.025, and 0.05, b) x = 0.05, y = 0, 0.025, and 0.05. Unmodified SNN is also shown on both plots……70

4.3.7 Polarisation – electric field loop plots at 40 kV cm^{-1} for $Sr_{2-x-y}Ca_xY_yNaNb_{5-y}Zr_yO_{15}$ with x = 0.025, y = 0, 0.025, sintered at 1300 ^oC and 1350 ^oC……...72

4.3.8 Back scattered electron images of a) unmodified SNN, b) x = 0.025, y = 0, c) x = 0.025, y = 0.025, d) x = 0.05, y = 0, e) x = 0.05, x = 0.05……...73

4.3.9 Back scattered electron images of $Sr_{2-x-y}Ca_xY_yNaNb_{5-y}Zr_yO_{15}$ with x = 0.05, y = 0.05 showing grains up to 10 µm and darker sodium rich/strontium deficient grains. Small grains of unreacted ZrO_2 are also present. EDX mapping confirms sodium enrichment and presence of Zr……74

4.3.10 Back scattered electron image $Sr_{2-x-y}Ca_xY_yNaNb_{5-y}Zr_yO_{15}$ with x = 0.025, y = 0.025 (1350 ^oC) showing large grains of up to ~25 µm. Grains are generally larger than 1300 ^oC sample (Figure 4.3.7 c) and more rounded….75

5.2.1 12 hour powder XRD plots for a) $S_{2-3x}Y_{2x}NaNb_5O_{15}$ with x = 0.025, and b) $Sr_2Na_{1.0}Nb_{5-4y}Zr_{5y}O_{15}$ with y = 0.02. Indexed to ICDD 04-008-7203, tetragonal SNN, *P4bm*……84

5.2.2 Log plot of $Sr_2Na_{1.0}Nb_{5-4y}Zr_{5y}O_{15}$ with y = 0.02 for 22 – 34 $^o2\theta$……85

5.2.3 Multi-frequency permittivity and dielectric loss tangent versus temperature plots for a) SNN, $S_{2-3x}Y_{2x}NaNb_5O_{15}$ with b) x = 0.0125, c) x = 0.025, and $Sr_2NaNb_{5-4y}Zr_{5y}O_{15}$ with d) y = 0.01 and e) y = 0.02……88

5.2.4 1 kHz relative permittivity and dielectric loss tangent versus temperature plots for $S_{2-3x}Y_{2x}NaNb_5O_{15}$ with x = 0.0125, and 0.025, and $Sr_2NaNb_{5-4y}Zr_{5y}O_{15}$ with y = 0.01 and 0.02……..89

5.2.5 40 kV cm^{-1} polarisation – electric field loop plots for a) $S_{2-3x}Na_{1.0}Y_{2x}Nb_5O_{15}$ with x = 0.0125, and 0.025 b) $Sr_2NaNb_{5-4y}Zr_{5y}O_{15}$ with y = 0.01 and 0.02…….91

5.2.6 Back scattered scanning electron micrographs of a) unmodified SNN, b) $Sr_{2-3x}Na_{1.0}Y_{2x}Nb_5O_{15}$ with x = 0.025, and c) $Sr_2NaNb_{5-4y}Zr_{5y}O_{15}$ with y = 0.02…….93

5.2.7 SEM-EDX maps of $Sr_2NaNb_{5-4y}Zr_{5y}O_{15}$ with y = 0.02……94

5.2.8 Vacancy of the alkali metal ion sites versus Madelung energy of $K_3Li_2Nb_5O_{15}$ (reproduced from Jang et al. 2004)…….96

5.3.1 12 hour powder XRD plots of $Sr_{2-x}Y_xNaNb_{5-x}Zr_xO_{15}$ with x = 0.05. Indexed to ICDD 04-008-7203, tetragonal SNN, P4bm……100

5.3.2 Multi-frequency permittivity and dielectric loss tangent versus temperature plots for a) unmodified SNN, and $Sr_{2-x}Y_xNaNb_{5-x}Zr_xO_{15}$ with b) x = 0.025, and c) x = 0.05……102

5.3.3 1 kHz relative permittivity and dielectric loss tangent versus temperature plots for $Sr_{2-x}Y_xNaNb_{5-x}Zr_xO_{15}$ with x = 0.025, and 0.05……103

5.3.4 40 kV cm^{-1} polarisation – electric field loop plots for $Sr_{2-x}Y_xNaNb_{5-x}Zr_xO_{15}$ with x = 0.025, and 0.05……104

5.3.5 Back scattered scanning electron micrographs of $Sr_{2-x}Y_xNaNb_{5-x}Zr_xO_{15}$ with x = 0.05……105

5.3.6 SEM-EDX maps of $Sr_{2-x}Y_xNaNb_{5-x}Zr_xO_{15}$ with x = 0.05……..106

5.4.1 12 hour powder XRD plots of a) $Sr_{2-3x}Y_{2x}NaNb_5O_{15}$ with x = 0.025 (section 5.2), and b) $Sr_2Na_{1-3x}Y_xNb_5O_{15}$ with x = 0.05. Indexed to ICDD 04-008-7203, tetragonal SNN, P4bm……110

5.4.2 Multi-frequency permittivity and dielectric loss tangent versus temperature plots for a) $Sr_{2-3x}Y_{2x}NaNb_5O_{15}$ with x = 0.025 (Y^{3+} = 0.05) (section 5.2), and b) $Sr_2Na_{1-3x}Y_xNb_5O_{15}$ with x = 0.05…….111

5.5.1 a) XRD patterns from the SCNN ceramics with different x; b) enlarged view of the XRD patterns in the range from 31.7 to 33.6 $^o2\theta$. Both show second phase material in composition x ≥ 0.9. (Yang et al. 2017)……113

5.5.2 XRD patterns from the SCNN ceramics with different x, showing single phase material for all compositions (reproduced from Yang et al. 2019)…..114

5.5.3 Phase diagram of $NaNbO_3$ – $SrNb_2O_6$ system (reproduced from Tang et al. 1979 with annotations by the author)…….115

5.5.4 Phase diagram of $NaNbO_3$ – $SrNb_2O_6$ system (reproduced from Morin et al. 1973 with annotations by the author)…….116

5.5.5 12 h powder XRD plots of SNN0.8 (1450 ^{o}C, 91 %) and SNN1.0 (93 %)……..118

5.5.6 12 h powder XRD plot of SNN0.8 (ES, 95 %). Indexed to ICDD 04-008-7203, tetragonal SNN, *P4bm*……119

5.5.7 Multi-frequency relative permittivity and dielectric loss tangent versus temperature plots for a) SNN0.8 (1450 ^{o}C) and b) SNN0.8 (1240/1320 ^{o}C ES). c) 1kHz comparison plot including SNN1.0……121

5.5.8 40 kV cm^{-1} polarisation – electric field loop plots for SNN1.0, SNN0.8 (1450 ^{o}C) and SNN0.8 (1240/1320 ^{o}C, ES)……123

5.5.9 Back scatered scanning electron micrographs of a) SNN1.0, b) and c) SNN0.8 (1240/1320 ^{o}C, ES)…….125

5.6.1 12 hour powder XRD plots of $Sr_{2.1-2x}Ca_xY_xNa_{0.8}Nb_{5-y}Zr_yO_{15}$. Indexed to ICDD 04-008-7203, tetragonal SNN, *P4bm*……...126

5.6.2 Back scattered scanning electron micrograph of $Sr_{2.1-2x}Ca_xY_xNa_{0.8}Nb_{5-y}Zr_yO_{15}$ (SCNN-YZ 0.8)……...127

5.6.3 SEM-EDX maps of $Sr_{2.1-2x}Ca_xY_xNa_{0.8}Nb_{5-y}Zr_yO_{15}$ (SCNN-YZ 0.8) showing single phase material and homogenous distribution of elements...128

5.6.4 a) Multi-frequency relative permittivity and dielectric loss tangent versus temperature plots for $Sr_{2.1-2x}Ca_xY_xNa_{0.8}Nb_{5-y}Zr_yO_{15}$ x = 0.05, y = 0.05. b) 1 kHz comparison plot of $Sr_{2.1-2x}Ca_xY_xNa_{0.8}Nb_{5-y}Zr_yO_{15}$ against optimum composition from Chapter 4, $Sr_{2-2x}Ca_xY_xNaNb_{5-y}Zr_yO_{15}$, with permittivity-temperature variation of +/- 9 %, -55 to 300 ^oC……129

5.6.5 Multi-frequency relative permittivity and dielectric loss tangent versus temperature plots for $Sr_{2.1}Y_xNa_{0.8-3x}Nb_5O_{15}$, with Y^{3+} substituting for Na^+. An extra permittivity peak (T_3) is present just below T_2 (Gardener. J, University of Leeds)……...129

6.1.1 Figure 6.1.1. Metastable phase diagram of $NaNbO_3$ – $SrNb_2O_6$ system (reproduced from Tang et al. 1979 with annotations by the author)……..133

6.1.2 Equilibrium phase diagram of $NaNbO_3$ – $SrNb_2O_6$ system. SNN solid solution (labelled S_2N here) with formula $Sr_{2+x}Na_{1-2x}Nb_2O_6$ showing thermal instability of SNN below 1180 ^oC (reproduced from Tang et al. 1979 with annotations by the author)…….133

6.2.1 Temperature-dependent, in-situ powder X-ray diffraction data for $Sr_2NaNb_5O_{15}$ with some second phase $NaNbO_3$ (reported in and reproduced from Garcia-Gonzalez et al. 2007)……...135

6.2.2 Log plot of 30 min powder X-ray diffraction pattern for $Sr_2NaNb_5O_{15}$ calcined powder at 0 weeks ageing and acquired at room temperature. Indexed to orthorhombic *Im2a* (ICDD 04-018-2808) (Data acquired by Dr F. Esat, University of Leeds)……138

6.2.3 Log (intensity) plot of 30 min powder in situ X-ray diffraction pattern for $Sr_2NaNb_5O_{15}$ calcined powder at 50 h ageing at 600 ^oC. Indexed to tetragonal *P4mbm* (ICDD 04-014-7370) (Data acquired by Dr F. Esat, University of Leeds)……...140

6.2.4 Log (intensity) plot of 10 min in situ powder X-ray diffraction pattern for $Sr_2NaNb_5O_{15}$ calcined powder at 0 time on first reaching 600 ^oC (Data acquired by Dr F. Esat, University of Leeds)……..142

6.2.5 Log (intensity) plots of 30 min powder X-ray diffraction patterns for $Sr_2NaNb_5O_{15}$ calcined powder taken every hour at 600 ^oC: a) A third phase $SrNb_2O_6$, with peaks at approximately 19.65 $^o2\theta$, b) a fourth phase $Sr_2Nb_{10}O_{27}$ (Data acquired by Dr F. Esat, University of Leeds)……...143

6.2.6 Log (intensity) plot powder X-ray diffraction patterns of $Sr_2NaNb_5O_{15}$ calcined powder before heating (black), 600 ^oC for 50 h (red), and on returning to room temperature (blue): a) Enlarged 45.5 to 47.5 $^o2\theta$ region showing additional tetragonal peaks developed during heating (red) remains on cooling to room temperature (blue) (indexed to tetragonal *P4mbm* ICDD 04-014-7370 (Data acquired by Dr F. Esat, University of Leeds)……...144

6.2.7 Log (intensity) plot of 30 min powder X-ray diffraction patterns for $Sr_2NaNb_5O_{15}$ calcined powder at 0 time pre heating (black plot), 24 h at 400 ^oC (red plot), and after returning to room temperature (blue plot) (Data acquired by Dr F. Esat, University of Leeds)……..145

6.2.8 Log (intensity) plot of 12 h powder X-ray diffraction pattern for $Sr_2NaNb_5O_{15}$ calcined powder at 45 weeks and 600 ^oC……...147

6.2.9 Back scattered SEM image and SEM-EDX maps of SNN1.0 calcined powder held for 46 weeks at 600 ^oC……148

6.2.10 Log (intensity) plot of 24 min powder X-ray diffraction pattern for $Sr_2NaNb_5O_{15}$ calcined powder at 24 weeks and 300 ^oC……..149

6.2.11 Log (intensity) plot of 24 min powder X-ray diffraction pattern for $Sr_{2.1}Na_{0.8}Nb_5O_{15}$ calcined powder, 24 weeks at 400 ^oC……...150

6.2.12 Log (intensity) plot of 24 min powder X-ray diffraction pattern for $Sr_{2-x-y}Ca_xY_xNaNb_{5-y}Zr_yO_{15}$ x = 0.05, y = 0.05 calcined powder calcined, 20 weeks at 600 ^oC……...151

6.3.1 1 kHz high temperature relative permittivity versus temperature plots for SNN0.8 (ES) showing six consecutive measurements of the same sample up to ~600 ^oC……155

6.3.2 T_2 peak temperature and ε_r value for SNN0.8 (ES) at 1 kHz for six consecutive permittivity versus temperature measurements up to ~600 ^oC……...155

6.3.3 Log (intensity) plot XRD patterns of SNN0.8 (ER) whole sintered pellet before (red) and after six permittivity versus temperature measurements up to ~600 ^oC (black)……158

6.3.4 a) 1 kHz high temperature relative permittivity versus temperature plots for SNN0.8 (ES) showing ten consecutive measurements of the same sample up to ~300 ^oC, b) enlarged image illustrating some variation between consecutive runs…….159

6.3.5 Plot of T_2 peak temperature (T_c) with consecutive permittivity versus temperature measurements to ~300 ^oC……..160

Appendix A Figure 1 Long duration permittivity measurements at 250 ^oC for a) $Sr_{2-x-y}Ca_xY_yNaNb_{5-y}Zr_yO_{15}$, x = 0.05, y = 0.05 b) $Sr_{2.1}Na_{0.8}Nb_5O_{15}$ (ES) (data acquired and plots by Dr J. Gardener, University of Leeds)……180

List of Tables

2.5.1 Space groups based on crystal system and Laue class. Only space groups in bold are centrosymmetric (reproduced from Dept. of Chemistry & Biochemistry, University of Oklahoma, 2019)……..14

3.2.1 Carbonate and oxide reagents, purity and suppliers…….38

4.2.1 Crystallographic data of $Sr_2NaNb_5O_{15}$ from X-ray powder diffraction analysis……...55

4.2.2 1 kHz relative permittivity and dielectric loss tangent versus temperature data for $Sr_2NaNb_5O_{15}$……57

4.3.1 Crystallographic data for $Sr_{2-x-y}Ca_xY_yNaNb_{5-y}Zr_yO_{15}$ (x = 0.025, y = 0, 0.025, 0.05 and x = 0.05, y = 0, 0.025, 0.05) from X-ray powder diffraction unit cell refinements. Unmodified SNN is also included…….64

4.3.2 1 kHz relative permittivity and loss tangents versus temperature data for $Sr_{2-x-y}Ca_xY_yNaNb_{5-y}Zr_yO_{15}$ with x = 0.025 and x = 0.05 and increasing amounts of y……...68

4.3.3 Remnant polarisation (P_r) and coercive field (E_c) data at 40 kV cm^{-1} for $Sr_{2-x-y}Ca_xY_yNaNb_{5-y}Zr_yO_{15}$ with x = 0.025 and 0.05, and y = 0, 0.025 and 0.05. Unmodified SNN is also shown……..71

5.1.1 Ionic radii of utilised cations with coordination numbers……..82

5.2.1 Table of compositions in Section 5.2 showing solid solution formulas, dopant levels, and shorthand notation……..83

5.2.2 Crystallographic data for $S_{2-3x}Y_{2x}NaNb_5O_{15}$ with x = 0.0125, and 0.025, and $Sr_2NaNb_{5-4y}Zr_{5y}O_{15}$ with y = 0.01 and 0.02 from laboratory XRD measurements. Unmodified SNN data (Chapter 4.2) are also shown for comparison…….86

5.2.3 Permittivity and loss tangents versus temperature data for $Sr_{2-3x}Y_{2x}NaNb_5O_{15}$ with x = 0.0125, and 0.025, and $Sr_2NaNb_{5-4y}Zr_{5y}O_{15}$ with y = 0.01 and 0.02. Values for unmodified SNN are also listed…….90

5.2.4 Remnant polarisation (P_r) and coercive field (E_c) data at 40 kV cm^{-1} for $Sr_{2-3x}Na_{1.0}Y_{2x}Nb_5O_{15}$ with x = 0, 0.0125, and 0.025 and $Sr_2NaNb_{5-4y}Zr_{5y}O_{15}$ with y = 0.01 and 0.02……..91

5.3.1 Crystallographic data of $Sr_{2-x}Y_xNaNb_{5-x}Zr_xO_{15}$ with x = 0.025, and 0.05, from X-ray powder diffraction unit cell refinements. Unmodified SNN (Chapter 4.2) is also shown for comparison……101

5.3.2 Permittivity and loss tangents versus temperature data for $Sr_{2-x}Y_xNaNb_{5-x}Zr_xO_{15}$ with x = 0.025, and 0.05. Unmodified SNN is also shown……..104

5.3.3 Remnant polarisation (P_r) and coercive field (E_c) data at 40 kV cm^{-1} for $Sr_{2-x}Y_xNaNb_{5-x}Zr_xO_{15}$ with x = 0.025, and 0.05……...105

5.4.1 Permittivity and loss tangents versus temperature data for $Sr_{2-3x}Y_{2x}NaNb_5O_{15}$ with x = 0.025 (section 5.2), and $Sr_2Na_{1-3x}Y_xNb_5O_{15}$ with x = 0.05……...111

5.5.1 SNN0.8 sintering study data, showing maximum temperature, geometric and theoretical density……...117

5.5.2 Crystallographic data for SNN1.0, and SNN0.8 (1450 °C and extended sintering), from X-ray powder diffraction unit cell refinements……120

5.5.3 1 kHz relative permittivity and loss tangents versus temperature data for SNN0.8 (1450 °C), SNN0.8 (1240/1320 °C ES), and SNN1.0……122

5.5.4 Remnant polarisation (P_r) and coercive field (E_c) data at 40 kV cm^{-1} for SNN0.8 (1450 °C) and SNN0.8 (1240/1320 °C, ES)……124

6.2.1 Relative peak intensity in relation to the main SNN peak. N.B. complete absence of $Sr_2Nb_{10}O_{27}$ in some samples could be due to low scan quality making identification difficult. Comparable heat treatments and time lengths are highlighted for different compositions……...137

6.2.2 Full pattern comparison of SNN1.0 calcined powder at room temperature with orthorhombic *Im2a* structure (ICDD 04-018-2808). Second phase $NaNbO_3$ indexed to ICDD 04-009-3239……..139

6.2.3 Full pattern comparison of SNN1.0 calcined powder at 50 h ageing at 600 ^{o}C with tetragonal *P4mbm* structure (ICDD 04-014-7370). Second phase $NaNbO_3$ indexed to ICDD 04-009-3239. Third and fourth phase strontium niobates are indexed as: $SrNb_2O_6$ (ICDD04-011-3157) and $Sr_2Nb_{10}O_{27}$ (ICDD 04-0880-4392). Blue text indicates unique tetragonal peaks, distinguishing from orthorhombic *Im2a*……141

6.3.1 T_2 peak temperature and ε_r value for SNN0.8 (ES) at 1 kHz for six consecutive permittivity versus temperature measurements up to ~600 ^{o}C. The date of each measurement is also shown……..157

List of Abbreviations

$A1_2A2_4B1_2B2_2C_4O_{30}$	General formula for tungsten bronze oxides
ABO_3	General formula for a perovskite
AC	Alternating Current
BNN	$Ba_2NaNb_5O_{15}$
BSE	Back Scattered Electron
CN	Coordination Number
DC	Direct Current
DSC	Differential Scanning Calorimetry
EDX	Energy Dispersive X-ray
EPSRC	Engineering and Physical Sciences Research Council
EIA	Electronics Industries Alliance
EM	Electron Microscope
ES	Extended Sintering
FIB	Focused Ion Beam
FWHM	Full Width Half Maximum
ICDD	International Centre for Diffraction Data
KLN	$K_3Li_2Nb_5O_{15}$
MLCC	Multilayer Ceramic Capacitor
P-E	Polarisation-Electric Field
PNR	Polar Nano Region
SAED	Selected Area Electron Diffraction
SE	Secondary Electron

SEM	Scanning Electron Microscope
SNN	$Sr_2NaNb_5O_{15}$
SNN (1.0)	$Sr_2NaNb_5O_{15}$
SNN0.8	$Sr_{2.1}Na_{0.8}Nb_5O_{15}$
TTB	Tetragonal Tungsten Bronze
TEM	Transmission Electron Microscope
TB	Tungsten Bronze
XRD	X-Ray Diffraction

List of Symbols

a, b, c	Unit cell parameters
A	Area
Å	Angstrom (10^{-10} m)
c/a	Tetragonality
C	Capacitance
C_0	Capacitance with air as dielectric material
d	Distance or thickness
eV	Electron-volt
E	Electric field
E_c	Coercive field
f	Frequency
I	Current
j	$\sqrt{-1}$
m	Mass
M	Molecular mass
N_A	Avogadro's number (6.023×10^{23})
P	Polarisation
P_{max}	Maximum polarisation
P_r	Remnant polarisation
q	Charge
r	Radius
r_A	Ionic radius A-site ion
r_B	Ionic radius B-site ion

r_O	Ionic radius oxygen anion
R_{WP}	Weighted profile R-factor
t	Thickness
t_G	Goldschmidt tolerance factor
T	Temperature
T_1	See T_m
T_2	See T_c
T_3	Space charge related dielectric anomaly
T_0	Curie-Weiss temperature
T_B	Burns temperature
T_c	Curie point
T_f	Dipole freezing temperature
T_m	Low temperature dielectric anomaly
tan δ	Dielectric loss factor
v	Volume
V	Voltage
Z	Number of formula unit per unit cell
β	Semi-angle of collection
δ	Smallest observable distance
ε_r	Relative permittivity
ε_r'	Real permittivity
ε_r''	Imaginary permittivity
ε_0	Permittivity of free space (8.854×10^{-12} F/m)
θ	Angle in degrees

λ	Wavelength
μ	Dipole moment
μ	Refractive index
ρ	Density
ρ_t	Theoretical density
χ_E	Electric susceptibility
□	Vacancy

Chapter 1. Introduction

1.1 High temperature dielectrics

Multilayer ceramic capacitors (MLCC) store electrical energy within an electrical field and are one of the most widely used and produced electrical components. They have the advantage of being small, cheap and useful for high frequency applications (Bell, 2008).

Their applications are many and varied, and include:

- Energy storage
- Digital memory
- Pulsed power applications (e.g. radar)
- Power conditioning (e.g. charge pump circuits)
- Signal coupling (splitting AC and DC currents)
- Decoupling (protecting circuit parts from each other).

There is currently an industry demand for progress in the field of high temperature dielectrics for use in the production of MLCC that operate at higher temperatures than those currently available, largely driven by:

- Automotive and aerospace industries, e.g. distributed engine control systems in which electronic components are placed closer to the engine, giving weight/fuel/cost savings.
- Power electronics, e.g. heat dissipation in the control of electrical energy in the integration of renewable energy sources into the grid. High temperature electronics that exploit wide bandgap active components (semiconductors, transistors) have been developed. Similar advances in passive components such as capacitors have not been similarly exploited (Zeb and Milne, 2015).

Industry standard X7R Class II capacitors are manufactured from high relative permittivity (ε_r) ferroelectric ceramic dielectrics which provide a high volumetric

efficiency of capacitance. Class II refers to the attributes of offering very high permittivity and therefore a better volumetric efficiency than class 1 capacitors, but lower accuracy and stability, and a nonlinear change of capacitance over temperature range such that the capacitance will drop off sharply outside the prescribed temperature range. Capacitors and the prefixes are coded according to the Electronics Industries Alliance Codes as follows:

- 1st character – lowest functional temperature, X = -55°
- 2nd character – highest functional temperature, 7 = 125°C
- 3rd character – maximum capacitance change over temperature range, R = +/- 15 %

Barium titanate $BaTiO_3$, compositionally and structurally modified, is the industry base material of choice which achieves stable class II capacitance from -55 to 125 °C. Variations in composition have pushed the maximum operating temperature to 200 °C. But this is still insufficient for emerging applications. A good dielectric material should also possess a low level of dielectric loss across the full temperature range. A tan δ value of < 0.025 across this range is a reasonable target specification of any new dielectric. Over the past 10 years researchers have demonstrated a range of dielectric ceramic formulations, classified as relaxor ferroelectrics with R-type stability to > 200 °C. However, they all contain bismuth and are of low interest to capacitor manufacturing companies due to the incompatibility of Bi with base metal electrodes during the firing process. That is, the Bi component is thermodynamically incompatible with Ni electrodes which must be fired at high temperatures and low oxygen partial pressure (< 10^{-8} atm) to avoid oxidation. Oxidation of the Ni would reduce its electrical conductivity. Under these reducing conditions, the similarity in Gibbs free energies of Ni/NiO and $Bi/BiO_{1.5}$ would lead to oxidation of Ni and reduction of Bi, ultimately making the ceramic too conducting.

1.2 Research Problem

Investigation into new high temperature ceramic dielectrics with stability in electrical properties to 250 °C or 300 °C (dependent on application) and the capability of operating at high voltages (up to 600 V) on a dielectric layer a few

microns thick are underway. For some applications this would require a ceramic with electric breakdown field strengths of >> 100 kV/mm. These must be free from Pb and Bi in order to be compatible with MLCC industrial manufacturing processes.

The introduction of a viable, industry-compatible material exhibiting these properties would have a huge impact on the capacitor industry. Capacitors are found widely in all electronic devices and systems and the lack of a reliable high temperature; high value capacitor has limited growth in many applications. Their utilisation is critical to meet the increasing demand of more efficient electrical energy storage and power conditioning (the delivery of voltage of the proper level and characteristics) in extreme conditions.

The prospective material investigation described in this work involving standard ceramic processing, has moved away from the traditional perovskite route and focused on the tungsten bronze (TB) structures. The intention is to take advantage of this structures inherent compositional flexibility to optimise dielectric properties.

1.3 Aims and objectives

The aim of this research was to develop a new Bi and Pb free high temperature dielectric material, primarily for application in the capacitor industry. Research focused on the tetragonal tungsten bronze system $Sr_2NaNb_5O_{15}$ (SNN) and its aliovalent substitution.

1.3.1 Objectives

- To investigate the properties of the tungsten bronze (TB) crystal system $Sr_2NaNb_5O_{15}$ (SNN) and compositional variants in relation to producing a wide temperature stable dielectric (+/- 15 % stability in ε_r from -55 to 300 °C) with low dielectric loss.
- Understand composition-structure-property relationships of $Sr_2NaNb_5O_{15}$ and compositional variants as a means of achieving these aims. Charge disorder will be altered whilst size disorder kept to a minimum.

- Understand the role various stages of conventional mixed oxide fabrication have on the structure and properties of the final material.
- Powder/sintered pellet X-ray diffraction measurements to determine phase purity of the compositions.
- Relative permittivity and dielectric loss tangent measurements as a function of temperature and at frequencies 1kHz to 1 MHz, to achieve temperature limits of +/- 15 % stability.
- Polarisation-electric field measurements to determine the ferroelectric nature of the compositions.
- Investigation of ceramic microstructure using scanning electron microscopy (SEM).
- The +/- 15 % specification could be relaxed slightly provided other properties were satisfactory (including grain size < 2 μm). Extending the lower temperature limit from -55 to -60 C would also be of interest.

Chapter 2. Background science and literature review

2.1 Introduction

This chapter outlines the basic scientific concepts of dielectric and ferroelectric ceramic materials, including their structure, properties, and polarisation mechanisms. Following this will be a brief review of ceramics with the tetragonal tungsten bronze structure, materials of this type being the research interest of this study. A review of key published research, focusing on $Sr_2NaNb_5O_{15}$ (SNN) and structurally similar material will make up the final part of this chapter.

2.2 Crystal Structure

Cullity and Stock (2014) define a crystal as 'a solid composed of atoms, ions or molecules arranged in a pattern periodic in three dimensions'. The three-dimensional geometry of this periodic structure forms a lattice, and can be imagined, without the atoms, ions or molecules, as extending to infinity. The simplest repeating unit of a lattice is referred to as the unit cell and is defined by the vectors *a*, *b* and *c*, and the angles *α*, *β* and *γ* (lattice parameters, Figure 2.2.1). Variations of these, result in seven crystal systems (cubic, tetragonal, orthorhombic, rhombohedral, hexagonal, monoclinic, and triclinic), one of which all crystal systems must display. Further arrangement of points within these seven unit cells is possible whilst continuing to maintain the critical condition for a crystal, that each lattice point has identical surroundings. In this way, Auguste Bravais demonstrated in the 19th century that a total of 14 Bravais lattice are possible from the original seven crystal systems (Cullity and Stock, 2014, Figure 2.2.2).

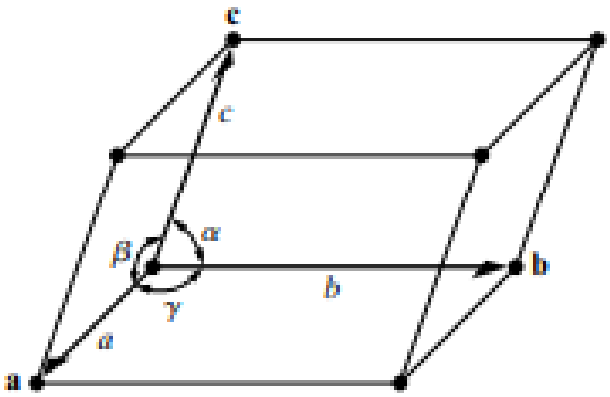

Figure 2.2.1. Lattice vector and interaxial angle designations of a unit cell (reproduced from Cullity and Stock, 2014)

System	Axial lengths and angles	Bravais lattice	Lattice symbol
Cubic	Three equal axes at right angles $a = b = c$, $\alpha = \beta = \gamma = 90°$	Simple Body-centered Face-centered	P I F
Tetragonal	Three axes at right angles, two equal $a = b \neq c$, $\alpha = \beta = \gamma = 90°$	Simple Body-centered	P I
Orthorhombic	Three unequal axes at right angles $a \neq b \neq c$, $\alpha = \beta = \gamma = 90°$	Simple Body-centered Base-centered Face-centered	P I C F
Rhombohedral*	Three equal axes, equally inclined $a = b = c$, $\alpha = \beta = \gamma \neq 90°$	Simple	R
Hexagonal	Two equal coplanar axes at 120°, third axis at right angles $a = b \neq c$, $\alpha = \beta = 90°$ $(\gamma = 120°)$	Simple	P
Monoclinic	Three unequal axes, one pair not at right angles $a \neq b \neq c$, $\alpha = \gamma = 90° \neq \beta$	Simple Base-centered	P C
Triclinic	Three unequal axes, unequally inclined and none at right angles $a \neq b \neq c$, $(\alpha \neq \beta \neq \gamma \neq 90°)$	Simple	P

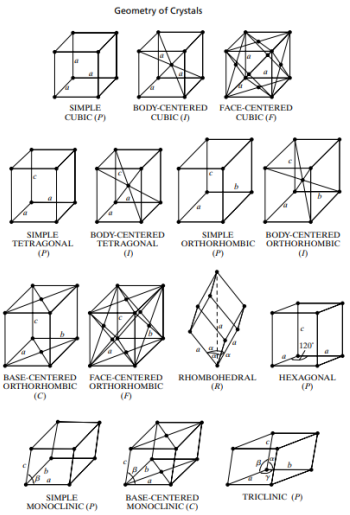

Figure 2.2.2. The seven crystal systems and associated lattice parameters, plus illustrations of the fourteen Bravais lattices (reproduced from Cullity and Stock, 2014)

Further permutations through translations (glides) and symmetry operation of lattice points (e.g. rotations, mirror planes and reflections) result in 230 space groups (combinations of translations and symmetries) (Hammond, 2015).

Points representing atoms, or planes of atoms can be identified within a unit cell using Cartesian coordinates relative to an origin *O* (Figure 2.2.3). Therefore the position of a point *P* relative to the origin *O* is described by steps of unit length along the appropriate combination of unit cell vectors e.g. for Figure 2.2.3, P is at the point with Cartesian coordinates 0,1,1 relative to O, and represented by the directional vector [011]. The specific vector *OQ* (red arrow) is represented by [111]. The

notation $\langle 001 \rangle$ would represent the family of directions related to $[001]$ by symmetry (which for a cubic unit cell would be $[001]$, $[010]$, $[100]$). The plane *R* (blue plane) is represented by (100), with $\{100\}$ representing the family of planes related to (100) by symmetry (which again for a cubic unit cell would be (001), (010), (100)).

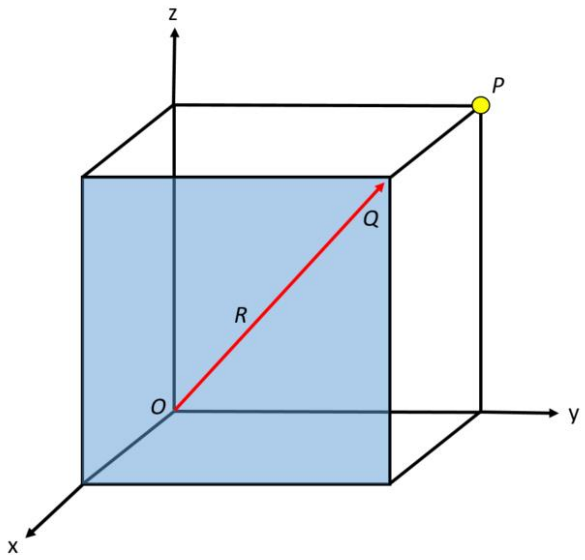

Figure 2.2.3. Points, vectors, and planes within a unit cell, identified through Cartesian coordinates with reference to an origin *O* (T. Brown).

There are many categories of defects that can occur within a crystal structure which may affect the mechanical and electrical properties of the material. In this study however, the focus is on the influence of point defects, that is, a defect at a single atom site. These can include missing atoms (vacancy defects), substitution of atoms with an external ion (substitutional defects), and the occupation of an otherwise empty site within the crystal structure (interstitial defects) (Moulson, 2003).

2.3 Dielectric materials and capacitors

Dielectric materials are electrically insulating materials (those with a large band gap requiring high levels of energy for conduction) which under an applied electric field will display a polarisation *P*, a value representing an electrostatic dipole moment per unit volume, *v* (Equation 2.3.2) (Moulson, 2003). A dipole moment (μ) is expressed as the product of two equal but opposite charges (q), and the distance

between them (*d*) (Equation 2.3.1) (Raju, 2003). Polarisation is linearly related to any applied electric field by Equation 2.3.3.

$$\mu = q \cdot d \quad \text{(Equation 2.3.1)}$$

$$P = \frac{\mu}{v} \quad \text{(Equation 2.3.2)}$$

$$P = \varepsilon_0 . \chi_E . E \quad \text{(Equation 2.3.3)}$$

Where *P* is the polarisation, ε_0 is the permittivity of free space (8.85 x 10^{-12} F.m^{-1}), χ_E the electric susceptibility and *E* the electric field.

The applied field causes short range charge displacements (dipole moments) within the material creating the polarisation, but the absence of long-range movement of charge carriers results in no conductivity. Positive charges will be displaced in the direction of the field and negative charges away from it, developing opposing charges across opposite surfaces of a material. This results in a materials ability to store charge, represented by its relative permittivity, ε_r, and can allow utilisation in, for example, capacitor applications, although all dielectric materials will break down and begin to conduct under conditions of sufficient temperature or electrical field strength (Moulson, 2003). The relative permittivity of a material (ε_r) is related to its permittivity (ε) and the permittivity of free space (ε_0) by Equation 2.3.4.

$$\varepsilon_r = \frac{\varepsilon}{\varepsilon_0} \quad \text{(Equation 2.3.4)}$$

A parallel plate capacitor consists of an insulating dielectric material between a pair of parallel conducting plates separated by a distance *d*, that is small in comparison to the plates, with a potential difference *V* applied between them (West, 2014). The electric field (*E)* and capacitance (*C*) of this arrangement is given by Equations 2.3.5 and 2.3.6, and the stored charge (*Q*) by Equation 2.3.7. The relative permittivity of the material is related to the increase in overall capacitance by Equation 2.3.8 (Moulson, 2003 and West, 2014).

$$E = \frac{V}{d}$$ (Equation 2.3.5)

$$C = \varepsilon_r \cdot \varepsilon_0 \cdot \frac{A}{d}$$ (Equation 2.3.6)

$$Q = C \cdot V$$ (Equation 2.3.7)

$$\varepsilon_r = \frac{C}{C_0}$$ (Equation 2.3.8)

Where *A* is the area of the electrode plates, *d* is the thickness of the dielectric layer, and C_0 is the capacitance with air as the dielectric material.

2.4 Polarisation mechanisms

The four main charge displacement mechanisms that contribute to polarisation under the application of an electric field are atomic, ionic, dipolar, and space charge (Moulson, 2003) (Figure 2.4.1). The speed by which each can follow an AC field means that the response of each will begin to drop off as the frequency is increased.

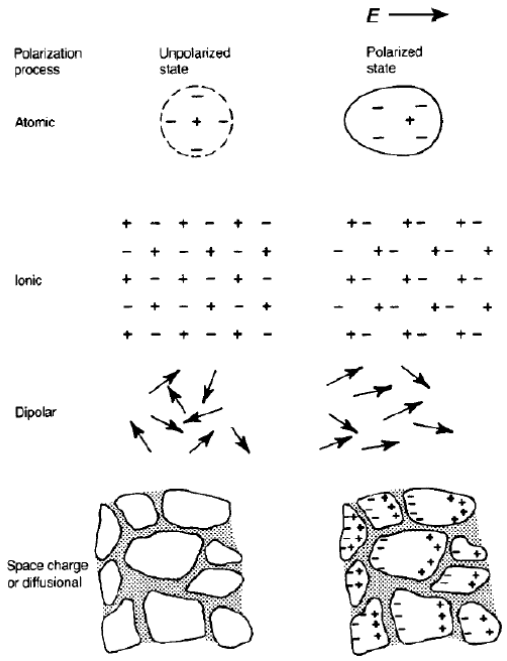

Figure 2.4.1. Different polarisation mechanisms found in dielectrics (reproduced from Moulson, 2003).

Atomic polarisation involves the displacement of the negative charge of the electron cloud of an atom in an electric field to behave like a dipole. This occurs up to frequencies of ~10^{17} Hz. Ionic polarisation is the relative displacement of positive and negative ions in an ionic material under an applied field and occurs up to frequencies of ~10^{13} Hz. Atomic and ionic polarisation are the main contributors to polarisation in dielectrics. Dipolar polarisation occurs in materials where polarisation already exists. Under no electric field the dipoles are randomly orientated and result in a net polarisation of zero. When an electric field is applied the dipoles align in the direction of the field, resulting in net polarisation. This occurs up to frequencies of ~10^{10} Hz. In space charge polarisation, charge carriers migrating because of the application of an electric field are stopped at material grain boundaries, creating a dipole moment. This occurs up to frequencies of ~10^{3} Hz. (Moulson, 2003).

In an ideal dielectric, a phase angle of 90° exists between the applied alternating current and the resulting voltage. However, in reality, the current consists of two components, the capacitive component at 90° from the voltage, and the lossy component which is at an angle δ from the capacitive component and $90° - \delta$ from the voltage (Figure 2.4.2). As a result of this the relative permittivity (ε_r) is expressed as a complex value with a real and imaginary part (Equation 2.4.1) (Hass and Wadley, 2011).

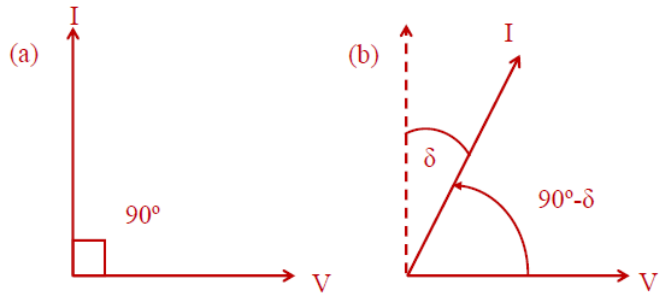

Figure 2.4.2. Phase angle between applied alternating current and resulting voltage in a) an ideal dielectric where the angle is 90°, and b) a real dielectric where the current consists of two components (reproduced from Moulson, 2003).

$$\varepsilon_r = \varepsilon_r' - j\varepsilon_r'' \quad \text{(Equation 2.4.1)}$$

Where ε_r' is the real part (corresponding to the charge storage ability and therefore, energy stored), ε_r'' is the imaginary part (corresponding to the energy loss of the process) of the relative permittivity, and $j = \sqrt{-1}$.

The dielectric loss tangent (tan δ) is a measure of the dielectric loss in a material. The dielectric loss tangent is defined as the ratio between energy lost (ε_r'') to the energy stored (ε_r') (Equation 2.4.2) (Hass and Wadley, 2011).

$$tan\delta = \frac{\varepsilon_r''}{\varepsilon_r'} \text{ (Equation 2.4.2)}$$

Both ε_r' and ε_r'' are frequency dependent due to the fact that, as mentioned above, all polarisation mechanisms will not be able to respond when certain frequencies are reached, the exact frequency being specific to each polarising mechanism. That mechanisms contribution to the real permittivity will then cease and can be seen at this frequency as a peak in the imaginary part of the permittivity (ε_r'') (Moulson, 2003).

2.5 Ferroelectrics

Ferroelectric materials possess a spontaneous polarisation that can be reoriented and reversed by the application of an electric field. The polarisation occurs due to the ordering of dipoles through internal processes, independent of external factors. The dipoles are usually orientated randomly, resulting in a zero-net polarisation. The fact that this polarisation exists in the absence of an electric field, but then can be ordered by one, works as an additional polarisation mechanism. This gives ferroelectrics a higher value of relative permittivity ε_r, and therefore capacitance, than other dielectric materials (West, 2014). The reorientation of ferroelectric polarisation is demonstrated in polarisation-electric field (P-E) loops which show a characteristically broad S shape, as seen in Figure 2.5.4. The polarisation can be aligned by the applied electric field, and then reversed by inverting the field (with some losses or hysteresis). The time taken for this realignment is the relaxation time and switching at higher frequencies will cease as the contribution from those mechanisms become unable to match it (Bell, 2008).

2.5.1 Perovskite crystal structure

The atomic origin of ferroelectricity can be illustrated by looking at the perovskite crystal structure as seen in capacitor materials such as $BaTiO_3$. These

materials have the general chemical form ABO_3 where the valence of the A cations is +1 to +3 and the B cations +3 to +6. This structure consists of a unit cell with A ions at the corners and the B ion at the centre surrounded by an oxygen octahedral cage (Figure 2.5.1) (Sebastian, 2010).

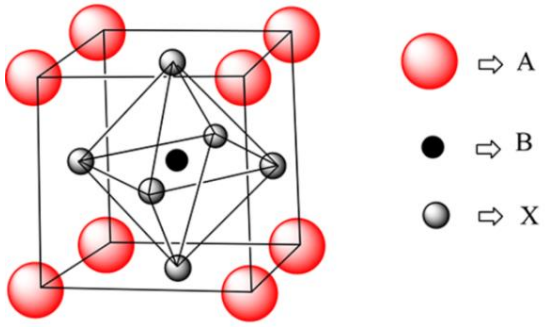

Figure 2.5.1. Perovskite crystal structure ABX_3 (ABO_3 in oxide perovskites). In $BaTiO_3$, A = Ba, B = Ti, and X = O (reproduced from Demic et al. 2017).

In this simple (cubic) structure that exists at high temperature, a high level of symmetry (centrosymmetric structure) is present and consequently no polarisation occurs and the material is said to be paraelectric. On cooling to below a critical temperature (the Curie point, T_c, ~130 °C for $BaTiO_3$), a tetragonal phase forms and the centres of the positive and negative charges no longer coincide (non-centrosymmetric structure), creating a dipole or ionic polarisation. This occurs in every unit cell so the material develops a polarisation (Figure 2.5.2).

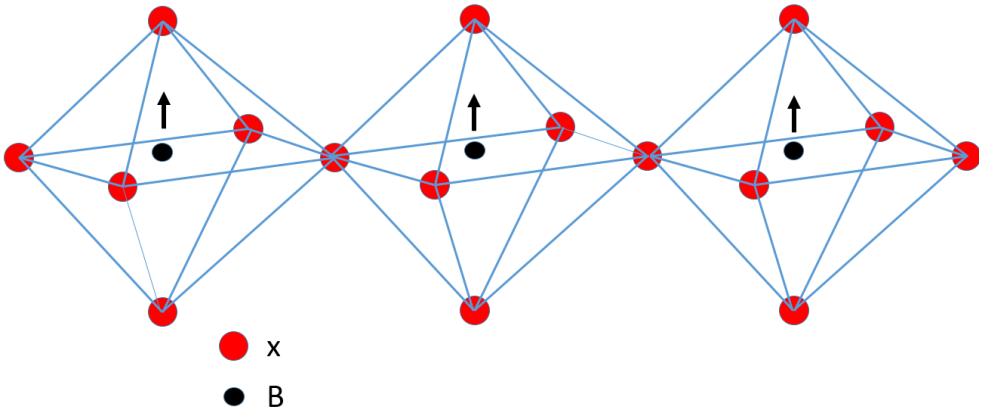

Figure 2.5.2. Formation of a tetragonal phase in perovskites resulting in a non-centrosymmetric structure across all unit cells. This causes a polarisation to develop in the material through the permanent displacement of the central cation, indicated by the arrow (T. Brown).

The vast majority of perovskite ferroelectric materials show this structural phase change from a high temperature paraelectric phase (or non-ferroelectric) when a cubic structure, into a ferroelectric phase (with spontaneous polarisation) at lower temperatures. In $BaTiO_3$ the cubic phase initially transforms to tetragonal phase. Further phase transitions can also occur below T_c resulting in a change in preferred polarisation orientation (Jaffe et al. 1971). With $BaTiO_3$ the tetragonal phase with polarisation along $\langle 001 \rangle$ changes at 0 °C to an orthorhombic phase with polarisation along the $\langle 011 \rangle$ direction. Further cooling to -90 °C sees a transition to a rhombohedral phase and polarisation along the $\langle 111 \rangle$ direction (Figure 2.5.3) (Moulson, 2003).

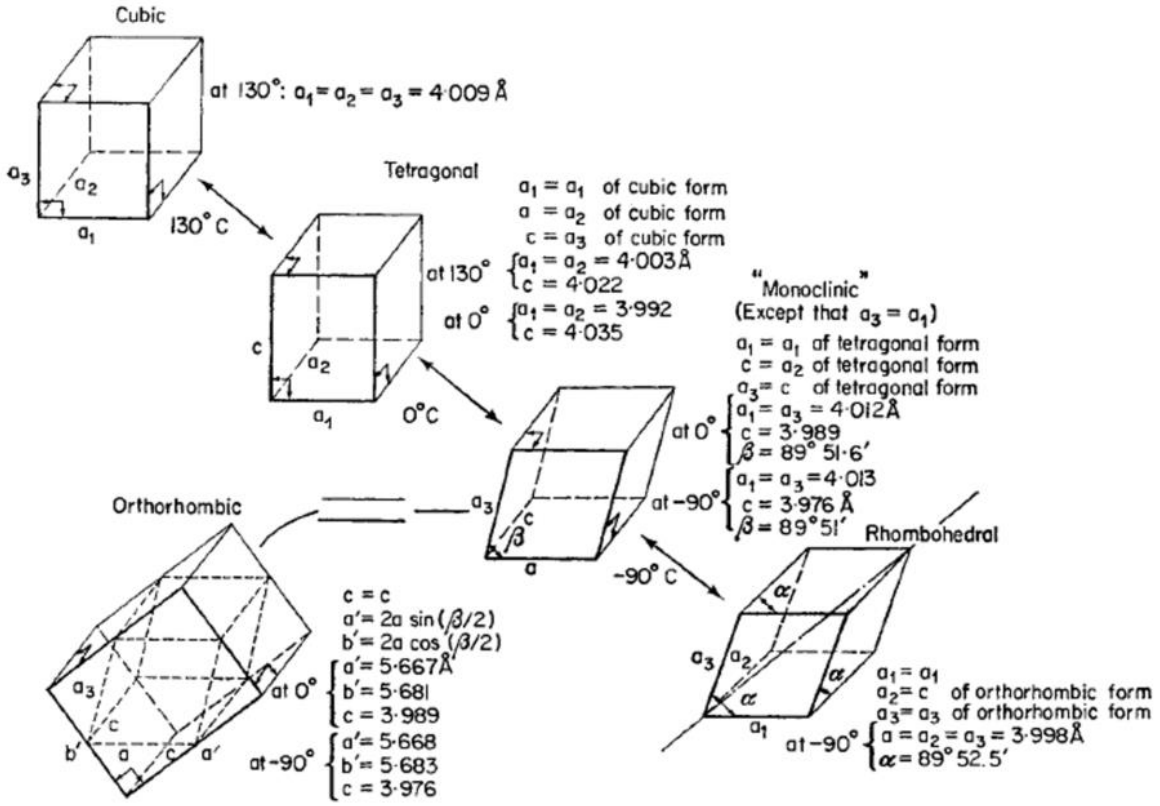

Figure 2.5.3. Unit cell distortions and preferred polarisation directions in $BaTiO_3$ on cooling from > 130 °C to < -90 °C (reproduced from Jaffe et al. 1971).

Many oxide perovskites will also adopt symmetries relating to the relative size of the constituent ions (Ishihara, 2009), and this structural stability can be quantified using the Goldschmidt tolerance factor t_G (Equation 2.5.1) (Sebastian, 2010).

$$t_G = \frac{r_A + r_O}{\sqrt{2}(r_B + r_O)} \quad \text{(Equation 2.5.1)}$$

Where r_A, r_B and r_O are the ionic radii of the A and B-site cations and oxygen anion respectively. When $t_G = 1$ a perfect cubic perovskite will form, whilst $t_G > 1$ will result in a tetragonal structure and $t_G < 1$ an orthorhombic one. The perovskite structure is generally stable in the region $0.880 < t_G < 1.090$ (Lee et al. 2009).

A variety of space groups for each crystal structure are non-centrosymmetric and could therefore be ferroelectric. Others are centrosymmetric and so could not be (Table 2.5.1)

Table 2.5.1. Space groups based on crystal system and Laue class. Only space groups in **bold** are centrosymmetric (reproduced from Dept. of Chemistry & Biochemistry, University of Oklahoma, 2019).

Crystal System	Laue Class	Space Group
triclinic	$\bar{1}$	*P*1, ***P*$\bar{1}$**
monoclinic	2/*m*	*P*2, *P*2$_1$, *C*2, *Pm*, *Pc*, *Cm*, *Cc*, ***P*2/*m***, ***P*2$_1$/*m***, ***C*2/*m***, ***P*2/*c***, ***P*2$_1$/*c***, ***C*2/*c***
orthorhombic	*mmm*	*P*222, *P*222$_1$, *P*2$_1$2$_1$2, *P*2$_1$2$_1$2$_1$, *C*222$_1$, *C*222, *F*222, *I*222, *I*2$_1$2$_1$2$_1$, *Pmm*2, *Pmc*2$_1$, *Pcc*2, *Pma*2, *Pca*2$_1$, *Pnc*2, *Pmn*2$_1$, *Pba*2, *Pna*2$_1$, *Pnn*2, *Cmm*2, *Cmc*2$_1$, *Ccc*2, *Amm*2, *Aem*2, *Ama*2, *Aea*2, *Fmm*2, *Fdd*2, *Imm*2, *Iba*2, *Ima*2, ***Pmmm***, ***Pnnn***, ***Pccm***, ***Pban***, ***Pmma***, ***Pnna***, ***Pmna***, ***Pcca***, ***Pbam***, ***Pccn***, ***Pbcm***, ***Pnnm***, ***Pmmn***, ***Pbcn***, ***Pbca***, ***Pnma***, ***Cmcm***, ***Cmce***, ***Cmmm***, ***Cccm***, ***Cmme***, ***Ccce***, ***Fmmm***, ***Fddd***, ***Immm***, ***Ibam***, ***Ibca***, ***Imma***
tetragonal	4/*m*	*P*4, *P*4$_1$, *P*4$_2$, *P*4$_3$, *I*4, *I*4$_1$, ***P*$\bar{4}$**, ***I*$\bar{4}$**, ***P*4/*m***, ***P*4$_2$/*m***, ***P*4/*n***, ***P*4$_2$/*n***, ***I*4/*m***, ***I*4$_1$/*a***
tetragonal	4/*mmm*	*P*422, *P*42$_1$2, *P*4$_1$22, *P*4$_1$2$_1$2, *P*4$_2$22, *P*4$_2$2$_1$2, *P*4$_3$22, *P*4$_3$2$_1$2, *I*422, *I*4$_1$22, *P*4*mm*, *P*4*bm*, *P*4$_2$*cm*, *P*4$_2$*nm*, *P*4*cc*, *P*4*nc*, *P*4$_2$*mc*, *P*4$_2$*bc*, *I*4*mm*, *I*4*cm*, *I*4$_1$*md*, *I*4$_1$*cd*, ***P*$\bar{4}$2*m***, ***P*$\bar{4}$2*c***, ***P*$\bar{4}$2$_1$*m***, ***P*$\bar{4}$2$_1$*c***, ***P*$\bar{4}$*m*2**, ***P*$\bar{4}$*c*2**, ***P*$\bar{4}$*b*2**, ***P*$\bar{4}$*n*2**, ***I*$\bar{4}$*m*2**, ***I*$\bar{4}$*c*2**, ***I*$\bar{4}$2*m***, ***I*$\bar{4}$2*d***, ***P*4/*mmm***, ***P*4/*mcc***, ***P*4/*nbm***, ***P*4/*nnc***, ***P*4/*mbm***, ***P*4/*mnc***, ***P*4/*nmm***, ***P*4/*mcc***, ***P*4$_2$/*mmc***, ***P*4$_2$/*mcm***, ***P*4$_2$/*nbc***, ***P*4$_2$/*nnm***, ***P*4$_2$/*mbc***, ***P*4$_2$/*mnm***, ***P*4$_2$/*nmc***, ***P*4$_2$/*ncm***, ***I*4/*mmm***, ***I*4/*mcm***, ***I*4/*amd***, ***I*4/$_1$*acd***
trigonal	$\bar{3}$	*P*3, *P*3$_1$, *P*3$_2$, *R*3, ***P*$\bar{3}$**, ***R*$\bar{3}$**,
trigonal	$\bar{3}m$	*P*312, *P*321, *P*3$_1$12, *P*3$_1$21, *P*3$_2$12, *P*3$_2$21, *R*32, *P*3*m*1, *P*31*m*, *P*3*c*1, *P*31*c*, *R*3*m*, *R*3*c*, ***P*$\bar{3}$1*m***, ***P*$\bar{3}$1*c***, ***P*$\bar{3}$*m*1**, ***P*$\bar{3}$*c*1**, ***R*$\bar{3}$*m***, ***R*$\bar{3}$*c***
hexgonal	6/*m*	*P*6, *P*6$_1$, *P*6$_5$, *P*6$_2$, *P*6$_4$, *P*6$_3$, ***P*$\bar{6}$**, ***P*6/*m***, ***P*6$_3$/*m***
hexagonal	6/*mmm*	*P*622, *P*6$_1$22, *P*6$_5$22, *P*6$_2$22, *P*6$_4$22, *P*6$_3$22, *P*6*mm*, *P*6*cc*, *P*6$_3$*cm*, *P*6$_3$*mc*, ***P*$\bar{6}$*m*2**, ***P*$\bar{6}$*c*2**, ***P*$\bar{6}$2*m***, ***P*$\bar{6}$2*c***, ***P*6/*mmm***, ***P*6/*mcc***, ***P*6$_3$/*mcm***, ***P*6$_3$/*mmc***
cubic	$m\bar{3}$	*P*23, *F*23, *I*23, *P*2$_1$3, *I*2$_1$3, ***Pm*$\bar{3}$**, ***Pn*$\bar{3}$**, ***Fm*$\bar{3}$**, ***Fd*$\bar{3}$**, ***Im*$\bar{3}$**, ***Pa*$\bar{3}$**, ***Ia*$\bar{3}$**
cubic	$m\bar{3}m$	*P*432, *P*4$_2$32, *F*432, *F*4$_1$32, *I*432, *P*4$_3$32, *P*4$_1$32, *I*4$_1$32, ***P*$\bar{4}$3*m***, ***F*$\bar{4}$3*m***, ***I*$\bar{4}$3*m***, ***P*$\bar{4}$3*n***, ***F*$\bar{4}$3*c***, ***I*$\bar{4}$3*d***, ***Pm*$\bar{3}$*m***, ***Pn*$\bar{3}$*n***, ***Pm*$\bar{3}$*n***, ***Pn*$\bar{3}$*m***, ***Fm*$\bar{3}$*m***, ***Fm*$\bar{3}$*c***, ***Fd*$\bar{3}$*m***, ***Fd*$\bar{3}$*c***, ***Im*$\bar{3}$*m***, ***Ia*$\bar{3}$*d***

2.5.2 Ferroelectric domains

As a ferroelectric material cools through its Curie point (T_c), as well as changes in the electrical properties of the material (spontaneous polarisation), a change in dimensions known as spontaneous strain will take place too. A ferroelectric must possess at least two stable polarisation states. These occur in regions within the material that possess a polarisation vector (dipole) that differs from another region, called domains, and are separated by domain walls (Guyonnet, 2014). These micron-sized domains of ferroelectric polarisation will begin to be lost if the temperature increases beyond the Curie point, since the crystal structure changes to a higher symmetry phase. This lack of asymmetry robs the material of its polarisation. If the adjacent domains have polarisation in the opposite direction these are separated by 180 ° walls. If the domains are perpendicular, then they are separated by 90 ° walls (Bell, 2008).

Application of an electric field to ferroelectric domains can cause changes in overall polarisation and with sufficient field strength, polarisation reversal or switching. In a ceramic this polarisation alignment has the effect of greatly reducing the number of domain walls, movement of which result in ferroelectric hysteresis (Figure 2.5.4). The breadth of the P-E loop being due to domain movement time lag. This contrasts to the linear polarisation-applied field plot seen in dielectric materials (Figure 2.6.2 c). For a ferroelectric, as an electric field is applied the polarisation begins to increase linearly to align domains but is not strong enough to switch domains that are oppositely aligned. As the field increases, the energy becomes sufficient to switch and all the domains move as close as possible to the field direction. The 180 ^{o} domains will switch first, followed by the 90 ^{o} ones which will cause strain within the material. This continues until a saturation point is reached at the top right-hand point (P_s). On reduction of the field some domains will turn back but in the absence of any restoring force, when the field reaches zero a remnant polarisation remains (P_r). In order for the polarisation to reach zero the field must be applied in the reverse direction. This is termed the coercive field E_c. A continuation of this reverse field will produce an alignment in the opposite direction. The intercepts of the x axis therefore represent the coercive field, which is that needed to bring the polarisation back to zero. Ferroelectric coercivity can be said to be the ability of a ferroelectric material to withstand an external electric field without becoming depolarised (West, 2014).

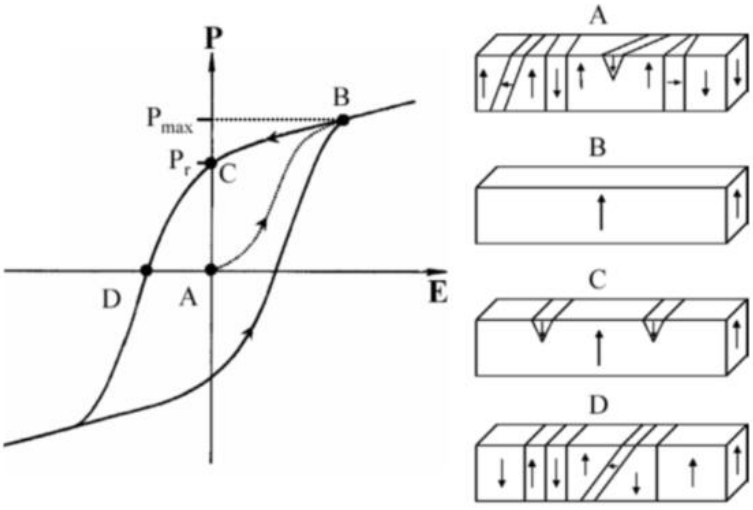

Figure 2.5.4. Polarisation versus applied electric field hysteresis loop in ferroelectric materials showing an example of possible domain structures in the material at points in the loop A, B

(P_{max}), C (P_r), and D ($-E_c$) (IEEE standard definitions of terms associated with ferroelectric and related materials, 2003).

In normal ferroelectrics the dependence of relative permittivity on temperature can be predicted using the Curie-Weiss law (Equation 2.5.2) when the material is in the paraelectric state (above T_c).

$$\varepsilon_r = \frac{C}{T - T_0} \quad \text{(Equation 2.5.2)}$$

Where C is the Curie constant and T_0 is the Curie-Weiss temperature, which is usually different from T_c (Curie point). The relative permittivity ε_r will become very large close to T_0. If T_0 is far from T_c then the phase transition will be first order (discontinuous change in entropy corresponding to latent heat). If it is far away, then it will be second order (continuous change in entropy resulting in no latent heat) (Moulson, 2003).

2.5.3 $BaTiO_3$, doping and temperature stability

Barium titanate ($BaTiO_3$) was the first ceramic material in which ferroelectric behaviour was observed, and was developed into a high permittivity dielectric in the 1940's (Moulson, 2003). It has become the industry material of choice for multilayer ceramic capacitors (MLCC's) due to its stable capacitance between -55 to 125 °C (Hennings, 1987). As stated in Section 2.5.1, $BaTiO_3$ has three phase transitions which are represented as peaks in the relative permittivity versus temperature plot (Figure 2.5.5), with the largest of these (T_c, 130 °C) representing the ferroelectric to paraelectric phase transition (Moulson, 2003).

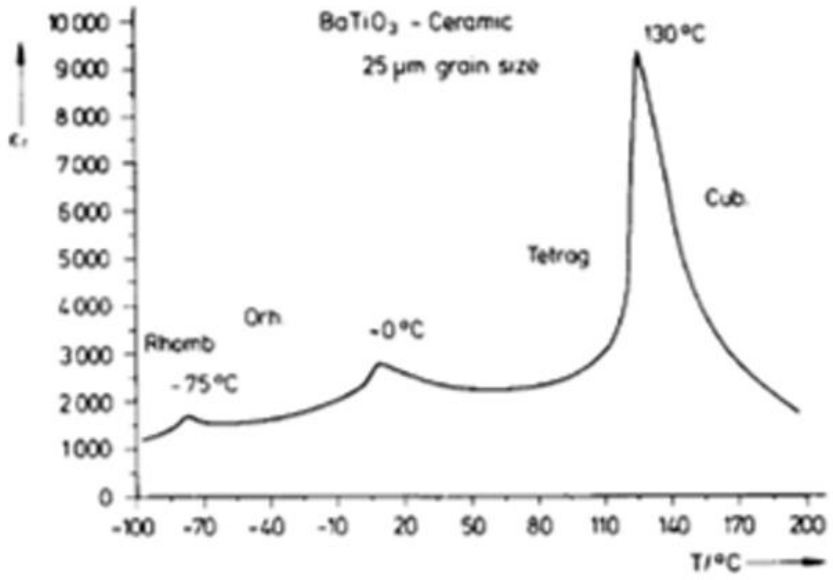

Figure 2.5.5. Plot of relative permittivity for unmodified barium titanate (reproduced from Hennings, 1987).

As this temperature dependent variation in permittivity would make it unsuitable for use as a capacitor material, there is a need to flatten out the permittivity response. The temperature value of T_c is controlled by the degree of chemical heterogeneity, whilst the ε_r value is affected by the grain size. Control of both is therefore required to produce a temperature stable $BaTiO_3$ material (Hennings, 1987). Chemical heterogeneity is achieved through doping, i.e. substitution by small amounts of alternative cations to those in the stoichiometric formula, to alter the composition and properties of the material (Moulson, 2003). A combination of two dielectric materials to achieve this would be unsuitable due to different materials displaying inconsistent thermal expansion coefficients and differing shrinkage behaviour (Henning, 1987).

Broadening of the ε_r – T profile can be achieved by instigating a so called “core-grain structure” by cation substitutions that result in regional variations in composition and a range of Curie points. In this way, the high temperature permittivity is spread across a wider temperature range but at a lower level of permittivity (Moulson, 2003). Structurally, the grains now usual in capacitors consist of two regions at room temperature, with the core being nearly pure $BaTiO_3$ and containing typical ferroelectric domain patterns. The surrounding shell contains dopants such as Sn or Zr for Ti, or Sr for Ba (Henning, 1987) and is paraelectric at

room temperature (Moulson, 2003). In that way a core-shell grain structure induced by additional oxides is responsible for inducing a temperature stable response (-55 to 125 °C) for $BaTiO_3$ capacitor applications.

2.6 Relaxor Ferroelectrics

Relaxor ferroelectrics are a sub-group of compositionally disordered ferroelectric materials that show a broad, *frequency dependent* dielectric relaxation peak, at temperatures T_m (Ravez and Simon, 2001), Figure 2.6.1. In a normal ferroelectrics there is a structural phase transition at the Curie point T_c from a paraelectric to ferroelectric state (on cooling), for example in $BaTiO_3$ from cubic (paraelectric) to tetragonal (ferroelectric) crystal system. Polar domains form below T_c, and typically these are in the micrometre size range (Cross, 1994). In normal ferroelectrics, T_c is seen as a sharp peak in the relative permittivity temperature profile at a well-defined transition temperature (Figure 2.5.5).

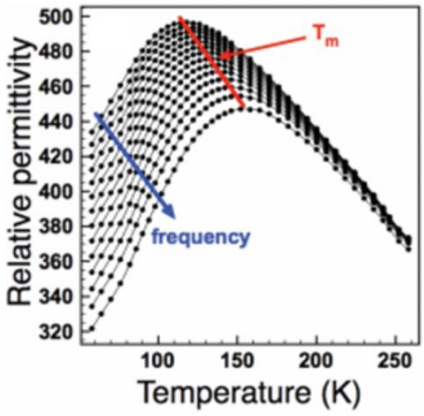

Figure 2.6.1. Frequency dependent relative permittivity as a function of temperature at T_m in relaxor ferroelectric $Ba_4Sr_{2-z}(Ba_{0.37}Ca_{0.63})_zGaNb_9O_{30}$, z = 0.5 (reproduced from Miller et al. 2015).

Relaxor ferroelectrics are often described as ‘frustrated ferroelectrics’ and theories to explain their properties are based on compositional fluctuations and the formation of polar nanoregions (nano-scale domains, as opposed to micrometre-scale domains) (Bokov, 1992). Compositional disorder on A or B-sites creates fluctuating electrostatic and stress fields that inhibit long range polar order across

many unit cells. As a result, no bulk structural phase transition occurs in relaxor ferroelectrics. Randomly polarised nanoregions begin to form on cooling at the Burn's temperature (T_B) and are initially mobile and transient. On cooling, the reduction in thermal energy causes the regions to increase in size but this makes then more sluggish in responding to an electric field. Differing sizes of regions will also result in a range of relaxation times. These factors create a broad frequency dependent permittivity peak at T_m (Figure 2.6.1). The peak represents a tipping point' whereby on cooling further a slowing in dipole re-orientation overcomes the trend of increasing polarisation expected from an increase in dipole magnitude on cooling. As the dielectric peak at T_m originates from dipole dynamics (dipole reorientation can no longer keep up with the field) T_m is frequency dependent. Eventually, the dipoles will freeze on cooling at a temperature T_f (dipole freezing temperature), the mobility is stopped, and the material may spontaneously, or under application of an appropriate electric field, become ferroelectric (Shvartsman et al. 2011).

Relaxor ferroelectrics show high levels of polarisation in the form of a narrow P-E hysteresis loop due to the orientation of polar domains or polar nanoregions. In relaxor ferroelectrics, on removal of the field, most of the polar nanoregions will revert to a random orientation, leading to only a small remnant polarisation (the polarisation when the electric filed is reduced to zero). This also results in a characteristic slim P-E hysteresis loop (Figure 2.6.2 b) in comparison to that of a normal ferroelectric (Cross, 1994).

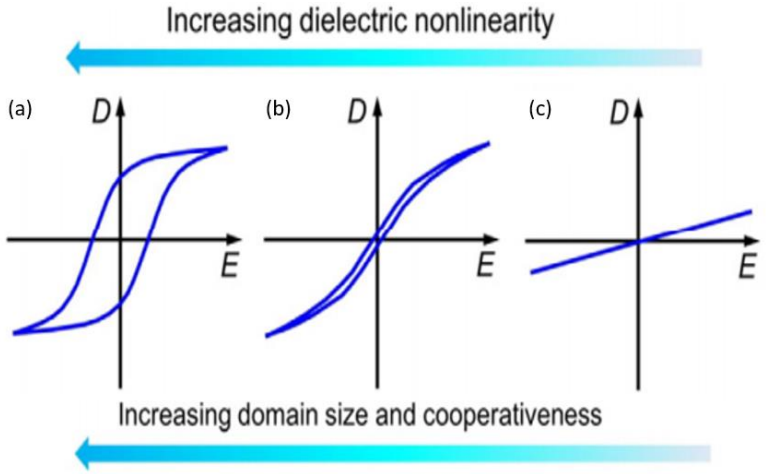

Figure 2.6.2. P-E hysteresis loops for a) normal ferroelectric, b) relaxor ferroelectric, c) dielectric (reproduced from Yang et al. 2013)

The relative permittivity peaks of a relaxor ferroelectric can be further supressed and broadened by cation substitutions on to the A and B sites (e.g. in ABO_3 of perovskites), creating broad, flattened, frequency dependent peaks in the relative permittivity temperature profile, often over a narrow compositional range. These are then termed temperature stable relaxors, an example being the binary system $(1-x)[0.85Na_{0.5}Bi_{0.5}TiO_3–0.15Ba_{0.8}Ca_{0.2}Ti_{1-y}Zr_yO_3]–xNaNbO_3$.

A relative permittivity plot for x = 0.3, y = 0.2 of this system is shown in Figure 2.6.3 (Zeb et al. 2018), displaying temperature stability *and* frequency dependence. One potential explanation for this behaviour is the presence of chemical immiscibility whereby weakly polar regions form and act to block the thermally induced increased in dipole size and coupling between dipoles that occurs in a normal relaxor when forming domains (Zeb and Milne, 2015). This supresses the temperature dependence of the relaxor, making it temperature stable and therefore a good capacitor material, i.e. this flat response makes relaxor ferroelectrics particularly interesting for capacitor applications, especially when combined with a second dielectric peak at higher temperature. To achieve a permittivity response similar to that seen in $BaTiO_3$, in terms of selective doping to control electrical properties, in the relaxor class of material would have great potential for the development of high temperature capacitors.

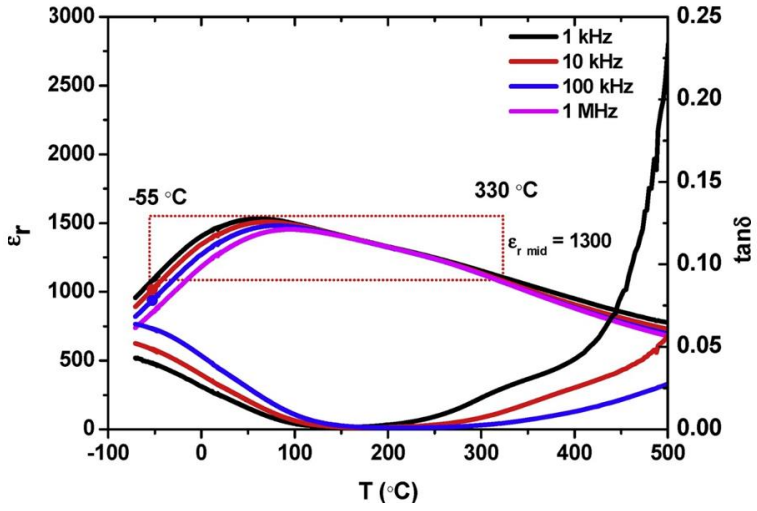

Figure 2.6.3. Temperature stable and frequency dependent relative permittivity plot for $(1-x)BaTiO_3 – xBi(Mg_{0.5}Ti_{0.5})O_3$ (x = 0.1) (reproduced from Choi et al. 2013).

2.7 Tungsten Bronze Structure

The tungsten bronze structures are related to ABO_3 perovskites, being also built up of corner sharing BO_6 octahedra but in such a way that a more complex structure and bigger unit cell is formed. They are able to contain a greater multiplicity of crystallographic sites, with the general formula for the tungsten bronze oxides under consideration in this work being $A1_2A2_4B1_2B2_8C_4O_{30}$ (Gardener et al. 2016). Blocks of octahedra which form four-membered rings are rotated within the unit cell, relative to the parent structure to form square (A_1, coordination number 12), pentagonal (A_2, coordination number 15), and triangular (C, coordination number 9) channels, when looking down the $[001]$ direction (Figure 2.7.1) (West, 2014). The nomenclature in the published literature relating to the A sites is variable, here I have used the most common assignments of A_1 (square) and A_2 (pentagonal). The tungsten bronze structure also contains two distinct B ion sites (B_1 and B_2, coordination number 6), occupied by small and highly charged ions (e.g. Nb^{5+}) located at the centre of the oxygen octahedra (Simon et al. 2006). The basic unit cell in the *c* direction is only one octahedron thick (Figure 2.7.1) (West, 2014).

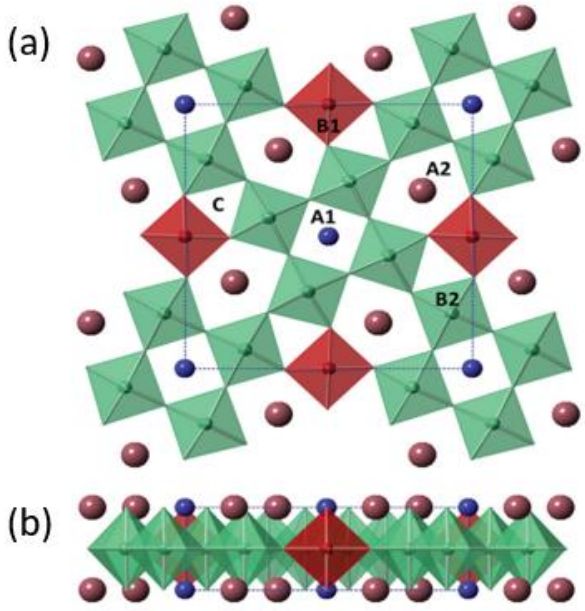

Figure 2.7.1. Tungsten Bronze (TB) structure. The dashed blue lines show the basic unit cell. The sharing BO_6 octahedra are arranged in columns along the c-axis. a) $[001]$ direction, b) $[100]/[010]$ direction (reproduced from Gardener, 2016).

Variable occupancy of these sites result in additional compositional degrees of freedom and structural complexity (Gardener et al. 2016). The C-cite can only be filled by small low charge species (e.g. Li^+) but is often vacant. When this is vacant, but all A and B-sites are occupied, the structure is described as “filled”. In the same situation but with vacancies present on the A-sites, the structure is “unfilled”. Less common is a structure with full occupancy of all sites (A, B and C) which is referred to as “stuffed” (Rotaru et al. 2014). In practice, larger A-site ions will occupy the pentagonal (A_2) channels and smaller ones the square (A_1) channels (West, 2014). However there can be cross occupancy of the A_1 and A_2 sites, for example in $Sr_4Na_2Nb_{10}O_{30}$ ($Sr_2NaNb_5O_{15}$) Sr and Na each occupy A_1 and A_2 sites.

The presence of these various crystallographic non-equivalent sites offers the potential for large compositional flexibility, superstructures and a complex/larger unit cell. The dielectric properties of the material can be greatly varied by the size and type of ions substituted onto the A and B sites, and the amount of disorder created. Cation coexistence is possible on both A and B sites and disorder in the sites they occupy (A_1/A_2 or B_1/B_2) is directly linked to relaxor behaviour (Garcia-Gonzalez et al. 2007).

The high temperature tungsten bronze structure is tetragonal and centrosymmetric, with dimensions $a_{TTB} = b_{TTB} \approx 12.5$ Å, $c_{TTB} \approx 4$ Å, and space group *P4/mbm* (Brown et al. 2020), Figure 2.7.2. The actual symmetry is often lower due to displacement and disorder of cations or rotation and tilting of the BO_6 octahedra (Whittle et al. 2021). Aamlid et al. (2020) and Whittle et al. (2021) studying $Ba_2NaNb_5O_{15}$ (BNN) reported that on cooling through T_c (~590 °C), a first order ferroelectric transition to a non-centrosymmetric (ferroelectric) tetragonal structure takes place. This has space group *P4bm* and similar cell dimensions to the *P4mbm* (Gardener et al. 2016). This tetragonal region continues down to ~280 °C (in BNN), where a second order ferroelastic transition to an orthorhombic structure occurs that remains at room temperature (Geuisic et al. 1967). This is consistent with high temperature X-ray diffraction data obtained by Aamlid et al. (2020). Similar structural changes to this are thought to be likely in $Sr_2NaNb_5O_{15}$ (SNN), the material of interest in this study. The exact crystallographic structure at this lower temperature transition for SNN (at -15 °C) has proved harder to discern and is not fully understood.

It is common to see orthorhombic distortions of the tetragonal structure, the simplest being a 45 degree rotation and $\sqrt{2}$ expansion in the *ab* plane so that $a \approx b \approx \sqrt{2}a_{TTB}$. For SNN, Torres-Pardo found a room temperature *Im2a* unit cell with a further doubling of *a, b* and *c* $\left(2\sqrt{2}a_{TTB} \times 2\sqrt{2}b_{TTB} \times 2c_{TTB}\right)$ (Garcia-Gonzalez et al. (2007) and Torres-Pardo et al. (2011)) and it is suggested this could result from changes in the oxygen positioning from octahedral tilting out of the *ab* plane (Gardener et el. 2016). It is proposed this occurs due to the small size of cations on the A-sites in comparison with the interstitial region between the octahedra, and this instability leads to the formation of lower symmetry structures (Gao et al. 2021). The orthorhombic supercells of this nature have been attributed to a *Bbm2* structure by Whittle et al. (2021) in BNN. They reported that those in which all octahedra tilt through the same angle are the most plausible and therefore assigned the structure of BNN to *Bbm2* (*Ama2* in standard setting). For SNN, weak superlattice reflections reported by Garcia-Gonzalez et al. (2007) and Torres-Pardo et al. (2011) confirm the presence of an orthorhombic phase. However, the signal to noise ratio of laboratory X-ray diffraction is not expected to be good enough to detect these, meaning high resolution X-ray data would be required.

These lower symmetry structures (whether commensurate or incommensurate) have been linked to ferroelectricity in tungsten bronzes (Olsen et al. 2017) and the onset of relaxor behaviour (Levin et al. 2006).

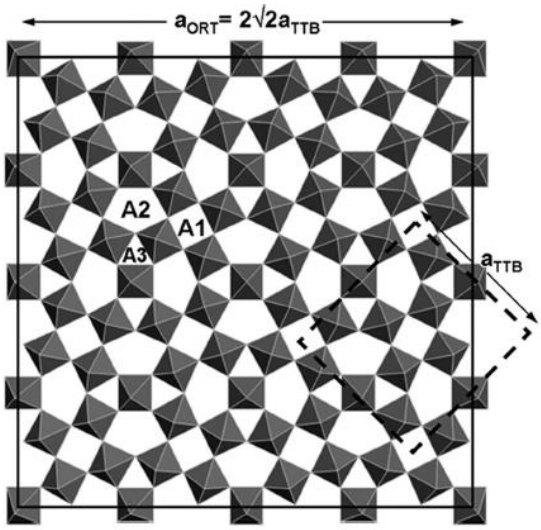

Figure 2.7.2. Schematic representation of TTB-type structure projected on the *ab* plane. The unit cell of both the basic tetragonal substructure (dotted) as well as the orthorhombic superstructure (solid) have been outlined (reproduced from Torres-Pardo et al. 2011).

2.8 Relevant materials

2.8.1 $Sr_2NaNb_5O_{15}$ (SNN)

The formula $Sr_2NaNb_5O_{15}$ represents an alkali and alkaline earth niobate with a “filled” tungsten bronze type structure (Lanfredi et al. 2011, Wei et al. 2010). Within this ideal structure, the A-sites are occupied by monovalent alkali metal Na^+ and divalent alkaline earth metal Sr^{2+}, whilst the B-site contains Nb^{5+} (Li et al 2019). However, as stated above, mixed occupancy is probable. It has been suggested that the size and type of these cations is of particular significance to the dielectric properties of the material due to their effect on tilting the oxygen octahedra out of the *ab* plane and causing structural distortion leading to polarisation (Lanfredi et al. 2011). The substitution of these cations with dopants of differing ionic radii forms the basis of the main part of this study.

Processing routes

The fabrication routes for SNN synthesis listed in the literature are varied, ranging from conventional mixed-oxide techniques to more sophisticated multi-stage routes and nanostructured powders. The conventional mixed-oxide method with calcination at 900 ^oC for 24 h and sintering at 1250 ^oC for 2 days was utilised by Garcia-Gonzalez et al. (2007) and Torres-Pardo et al. (2011), both reporting material of > 95 % density containing second phase Sr modified $NaNbO_3$. An orthorhombic *Im2a* space group was assigned by both groups. Selected Area Electron Diffraction (SAED) revealed extra diffraction maxima at room temperature, indicating the formation of a commensurate superstructure (Garcia-Gonzalez et al. 2007).

A two-stage solid-state reaction was used by Wei et al. (2010) where niobates of Sr and Na are formed first (calcined at 1100 ^oC and 900 ^oC respectively) before being mixed and calcined at 1200 ^oC. The final samples were then sintered at 1340 ^oC and a density of 98.5 % was reported by the Archimedes method. A uniform grain size with no abnormal grain growth (i.e. all grains < 50 µm) and few pores was also seen, abnormal grain growth was reported as being a particular problem in producing SNN. Wei et al. described the material as tetragonal at room temperature,

and single phase, although this is difficult to verify from the reproduced X-ray diffraction patterns. It is possible that the tetragonal to orthorhombic transition could be suppressed with rapid cooling (Xie et al. 2002 (2)). Differential scanning calorimetry (DSC) suggested that SNN can exist stably between 1100 and 1360 ^{o}C, although abnormal grain growth could occur above 1340 ^{o}C due to the formation of a liquid phase (Matsuo et al. 2002). DSC heating profiles show a first heat flow dip at 1221 ^{o}C which may correspond to the reaction between $SrNb_2O_6$ and $NaNbO_3$ to form SNN, whilst a dip at 1390 ^{o}C may be the breakdown of SNN (Figure 2.8.1) (Wei et al. 2010).

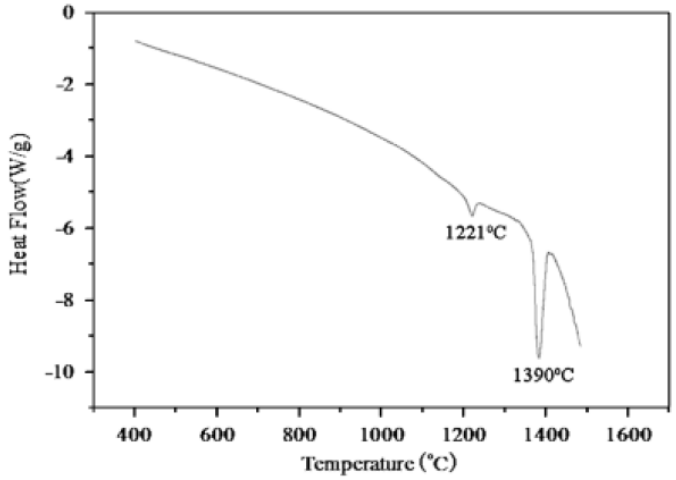

Figure 2.8.1. Differential scanning calorimetry curve of mixed $SrNb_2O_6$ and $NaNbO_3$ powders (reproduced from Wei et al. 2010).

The work of Lanfredi et al. (2011) attempted something slightly different, producing SNN from a nanostructured powder. Although this synthesis technique was unavailable for this current study, it is interesting that both calcination (12 h) and sintering (2 h) were carried out at the same temperature of 1150 ^{o}C. The material was indexed to a tetragonal *P4bm* spacegroup.

A comparison of fabrication methods was undertaken by Li et al. (2019) looking at conventional mixed-oxide, two-step sintering, reactive sintering, and molten salt sintering. Details of these will not be outlined here except that the outcome was that the conventional mixed-oxide route SNN ceramic was found to contain second phase $Sr_{0.25}Na_{0.5}NbO_3$, whilst the others were described as single phase. Other work on doped SCNN (substitution of Na^+ by rare earth ions) by Hao et

al. (2017 and 2019) reported high density single phase material from a conventional mixed-oxide fabrication route.

It should be noted here that the main focus of this project was improving the variation of permittivity of SNN-based ceramics over a large temperature range (-55 to 300 ^{o}C), with the SNN starting point optimised through the addition of dopants. Therefore, this was the main consideration when deciding on which fabrication method to use throughout this study, and so the simple mixed-oxide route was selected.

Dielectric properties

The work of Garcia-Gonzalez (2007), Torres-Pardo (2011), and Wei (2010) all showed relative permittivity versus temperature responses displaying two dielectric anomalies. A frequency indepedent high temperature peak (attributed to the materials T_C), between 245 and 280 ^{o}C, and a frequency dependent (relaxor like) low temperature peak (T_m) at approximately -43 ^{o}C (1 kHz). The high temperature peak obeys a Curie-Weiss law above T_c and represents the ferroelectric to paraelectric displacive phase transition (Garcia-Gonzalez et al. 2007). The low temperature peak is broader, and shows frequency dependence of T_m, indicating the material behaves as a relaxor (i.e. relaxation of the polar nanoregions) (Torres-Pardo et al. 2011). A third anomaly was observed in SNN single crystals at approximately 184 ^{o}C by Van Uitert et al. (1968) but was generally not seen in polycrystalline ceramics from other studies (Figure 2.8.2). One exception was reported by Cao et al. (2021) at 70 ^{o}C in $Sr_{2-x}Gd_xNaNb_{5-x}Ti_xO_{15}$ (x = 0.05 and 0.08). Its presence at low frequencies only, indicates the anomaly undergoes slow polarisation mechanisms such as space charge polarisation (up to ~10^3 Hz, Section 2.4).

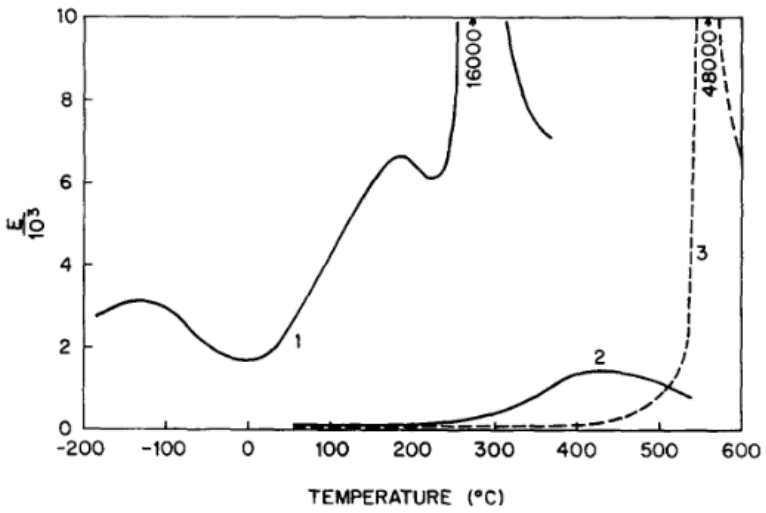

Figure 2.8.2. Relative permittivity measured parallel to the *c* axis in SNN single crystal (1) showing three dielectric anomalies. The anomaly located at approximately 184 °C is usually missing from polycrystalline compositions. Materials $K_3Li_2Nb_5O_{15}$ (2) and $Ba_2NaNb_5O_{15}$ (3) are also shown (reproduced from Van Uitert et al. 1968).

The ferroelectric response of SNN is probably the result of two contributions, the first being a displacive component as the B-site Nb^{5+} ion is shifted away from the centre of the oxygen octahedra when a lower symmetry structure forms on cooling through T_c (Simon et al. 2006). This displacement is caused by a conventional Jahn-Teller mechanism as symmetry decreases, causing polarisation along the *c* axis (Aamlid et al. 2020). The second is related to an order-disorder effect of A-site occupancy, where ions are preferentially positioned within the polar phase and gives rise to local polarisation (Simon et al. 2006). A disordered distribution on the A-sites of Na^+ and Sr^{2+} ions due to size similarity (1.39 Å and 1.44 Å respectively with coordination number (CN) XII, Shannon, 1976) was suggested by Garcia-Gonzalez (2007) and Torres-Pardo (2011). This occupancy is initially on the square A_1 sites, with the remaining ions then occupying the larger, pentagonal A_2 sites once these are filled. These secondary distortions result in rotation and tilting of the NbO_6 octahedran causing structural distortions in the *ab* plane (Garcia-Gonzalez et al. 2007). This is in contrast to $Ba_2NaNb_5O_{15}$, where the much larger barium ions (1.61 Å with CN XII, Shannon, 1976) will always preferentially sit in the larger A_2 site, with sodium occupying the A_1 sites (Garcia-Gonzalez et al. 2007). Torres-Pardo (2011) suggest that the low temperature anomaly (T_m) is created on cooling by this disordered A-site occupation and associated structural distortions, creating a

ferroelastic transition. Thermal parameters from analysis of neutron diffraction data show an in-site localisation of Sr and Na at lower temperatures where this slight structural change could result in local variations to dipole strength and reduce its long range interaction. The charge disorder also leads to the correlation of quenched random fields and the formation of polar nanoregions. These are suppressed at higher temperatures but their formation at lower temperatures reduces the long range ferroelectric correlation and promotes the onset of relaxor behaviour (Torres-Pardo et al. 2011). Broad agreement seems to be on the low temperature T_m peak being related to freeze out of polarisibility rather than a structural phase transition (Zhu et al, 2014).

2.8.2 A-site doping

Substituion of dopants on to the A-sites of SNN constitutes one of the main parts of this study. The likely effect that any substitutions might have was considered in determining which dopants to use. $Sr_{2-x}Ca_xNaNb_5O_{15}$ (SCNN) has been the subject of a number of publications and involves substitution of the A-site of Sr^{2+} (1.44 Å CN XII) by the smaller Ca^{2+} (1.34 Å CN XII, Shannon, 1976). Xie et al. (2002 (2)) reported that increasing amounts of Ca^{2+} led to XRD peak broadening and peak splitting at x = 0.35, indicating structural distortion and a possible solubility limit. They also described that the *a* and *c* parameters, and unit cell volume decreased with increasing Ca content, consistent with the smaller size of the Ca^{2+} cation. This size difference was related to an increase in T_c with increasing Ca^{2+}, indicating also that the ferroelectric transition was effected. This increase was thought to be related to an increase in ionic displacement, resulting from the additional “rattling space” a Ca^{2+} ion would have in an A-site (Xie et al. 2002 (2)). Similar effects were reported by Wei et al. (2012) for both the T_c and T_m peaks. A change in polarisation relating to this effect was not discussed, but it could be assumed that an increase would result due to the larger displacement causing a greater dipole moment. However, a structural distortion leading to reduced spontaneous polarisation (a reduction in $\varepsilon_{r\,max}$ value) because of a reduction in ionic polarisation, was reported. The justification for this is that althought there is an increase in distortion, it is within a smaller unit cell and so the net volume reduction causes a net drop in polarisation (Xie et al. 2002 (2)), Figure 2.8.3.

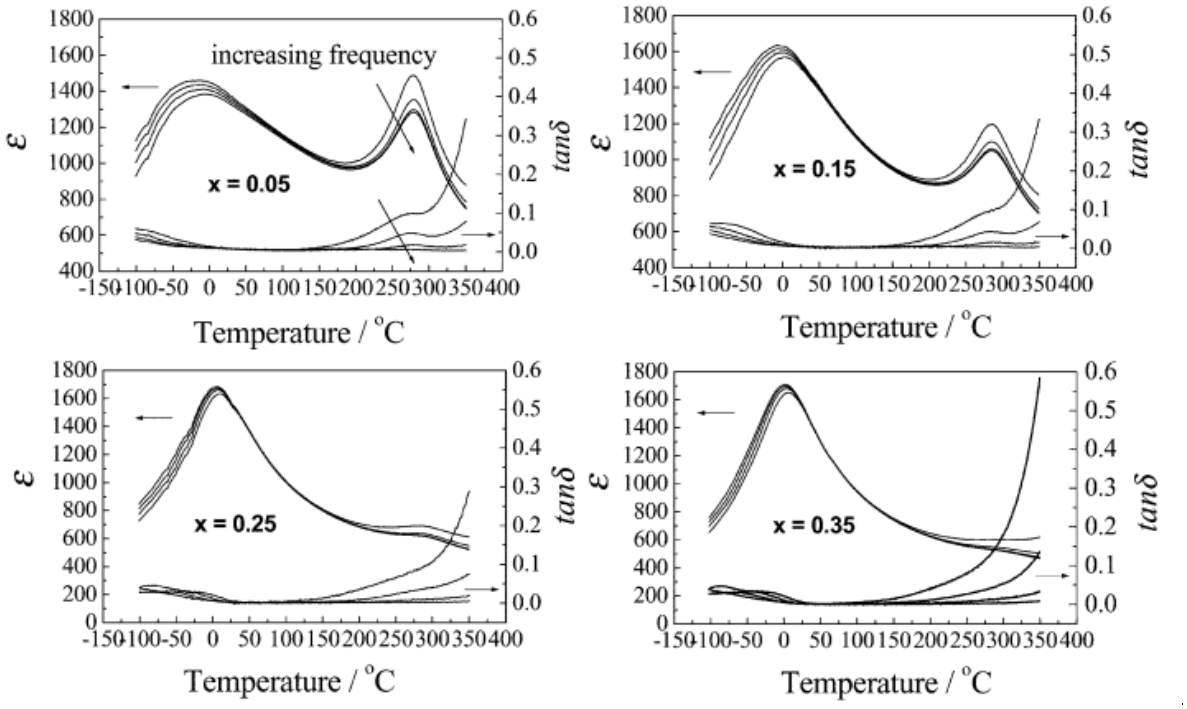

Figure 2.8.3. Relative permittivity as a function of temperature at 1 kHz for $Sr_{2-x}Ca_xNaNb_5O_{15}$ ceramics with increasing levels of x. Composition x=0.05 has a permittivity variation of approximately +/-20% from -55 to 300°C (estimated from the published permittivity-temperature plots) (reproduced from Xie et al. 2002 (2))

Both T_c and T_m anomalies are thought by Zhu et al. (2014) to be dominated by compositional and radii differences of cations on the A_1 and A_2 sites, with the B-site occupancy of less importance. The difference between A-site ionic radii are considered the dominant factor affecting T_c, whilst structural modulations due to order/disorder on both A and B-sites are more important for T_m (Zhu et al. 2014).

Levin et al. (2006), reporting on barium niobates, showed the ferroelecrtric nature and structural modulation were connected to the size of the A-site cation. Smaller cations were associated with a commensurate modulation and a ferroelectric nature, whilst larger cations with an incommensurate modulation and relaxor behaviour. In contrast to Xie, (2002 (2)), they reported a decrease in $\varepsilon_{r\,max}$ value at T_c and T_m with increasing rare earth ionic radius $Ba_2MTi_2Nb_3O_{15}$ (M = Bi, La, Nd, Sm, Gd). It is suggested that a larger A-site cation size increases the O-B-O bond length in the oxygen ochtahedron, enhancing the polarisibility of the B-site cation and promoting long range ferroelectric ordering, whilst with a smaller cation the scale of polar order diminishes and results in relaxor beahviour (Zhu et al. 2015). The A_1 tolerance factor in tungsten bronzes (the same as that which describes

perovskites, Section 2.5.1) is related to the driving force of the octahedral tilt system. A low value will favour ferroelectric behaviour, but paradoxically, will also decrease the average A-site ion size which favours relaxor behaviour by frustrating the ferroelectricity, and vice versa. The two mechanisms are therefore dependent but competing, with the tolerance factor being the dominant one (Zhu et al. 2015).

Zhu et al. (2014) indicate that the ferroelectric nature is also effected by the difference in ionic radius between the two A-sites (Δr), with this being reported as the critical factor. They suggest this value as being of importance to the type of tilting modulation the NbO_6 octadra in the material displays, and that it effects the coordination environments of the cation sites in the three types of cation tunnels. Therefore, the nature of the tilting and its periodicity is determined by the bonding requirements of the cations in the A-sites, and changes to this causes variation to the ferroelectric or relaxor ferroelectric nature of the material (Zhu et al. 2014). A larger Δr represents a significant distortion to the octahedra as it strongly couples to the polar cation displacements. This induces a commensurate modulation, and encourages long-range ferroelectric ordering, resulting in a ferroelectric nature. With a smaller Δr, the modulation will remain incommensurate and relaxor behaviour is seen. T_c and T_m are reported to decrease with decreasing Δr (Zhu et al. 2014). This effect is believed to be particularly true for compositions with a single B-site species with high polarisibility such as Nb^{5+} (Zhu et al. 2015).

A-site doping of SCNN with rare earth elements Sm^{3+} and Eu^{3+} substituting for Na^{+} (1.24 Å, 1.12 Å, 1.39 Å, CN XII, IX, XII repectively, Shannon, 1976) was undertaken by Hao et al. (2017 and 2019). In both materials the introduction of smaller cations had the effect of increasing the frequency dispersion at T_m, whilst retaining normal ferroelectric properties at T_c. The increase in relaxor behaviour was attributed to greater NbO_6 octahedra distortion and the creation of random A-site occupancy linked to the addition of smaller cations. Their introduction into the crystal lattice was also reported to necessitate higher sintering temperatures for phase formation. The Sm and Na ions are both thought to preferentially occupy A_1 sites, but as Sm coontent increases, the remaining Na is forced to occupy A_2 sites with Sr (Hao et al. 2019). At high levels of Eu (x = 0.1), the T_c peak was suppressed and a third dielectric anomaly was seen at 100 ^{o}C, thought to be related to the size difference between Sr and Eu (Hao et al. 2017). Both compositions initially saw an

increase in $\varepsilon_{r\,max}$ value at T_c and T_m with the introduction of dopants, followed by a decrease at higher levels. Doping with increased Sm reduced T_m temperature, whilst T_c remained unchanged. For Eu, both T_c and T_m decreased with increased doping. It was observed that when T_m was above room temperature, an orthorhombic phase dominated, changing to tetragonal on T_m falling below room temperature. As such, high levels of Eu resulted in a tetragonal phase.

No literature relating exclusively to the aliovalent doping of the A-site alkali rare earth cation in SNN/SCNN (Sr^{2+}) was found, suggesting that this could be a novel area of research.

2.8.3 B-site doping and co-doping (A and B-site)

The effect of B-site only doping on the properties of TTBs has not been explored at great depth. Fan et al. (2015) studied SNN with Sb^{5+} (0.6 Å, CN VI) substituting for Nb^{5+} (0.64 Å, CN VI) on B-sites ($Sr_2NaNb_{5-x}Sb_xO_{15}$). Increasing x resulted in a decreasing of T_c, attributed to a higher degree of structural distortion and the evolution of the microstructure. A wider range of grain size was reported as giving a higher value of T_c, whilst the grain size reduced with increasing x. Low tan δ below T_c was described as being linked to “an improvement in the domain wall during the paraelectric to ferroelectric phase transition” (Fan et al. 2015). T_m displayed the typical frequency dependent relaxor behaviour, becoming more pronounced with increasing x, and is partially induced by disorder on the B-site by cations of similar size. A defect associated octahedral tilting into the *ab* plane results, causing delocalisation of small A-site cations. This in turn induces an incommensurate superstructure and relaxor behaviour (Fan et al. 2015).

Co-doping of SNN on both the A and B-sites was reported by Cao et al. (2020), with La^{3+} (1.36 Å CN XII) or Ho^{3+} (1.18 Å CN XII) substituting for Sr^{2+}, and Ti^{4+} (0.74 Å, CN VIII) for Nb^{5+} (ionic radii Shannon, 1976, and Cao et al. 2020) to form $Sr_{2-x}M_xNaNb_{5-x}Ti_xO_{15}$ (where M = La^{3+} or Ho^{3+}). *Note: the Cao work was reported after the commencement of this thesis*. The effects seen by doping were more pronounced in the Ho^{3+} compositions due to its smaller ionic radius compared to Sr^{2+}, although both A-site dopants were small enough to display A_1 site preference. Both compositions showed the two dielectric peaks associated with

SNN, with a third appearing ≥ x = 0.08 at approximately 80 ^{o}C. This disappears at higher frequency due to the dropping off of polarisation mechanisms. Increasing amounts of both La^{3+} and Ho^{3+} caused a decrease in T_c and $\varepsilon_{r\,max}$ value, the permittivity eventually becoming diffuse and relaxor like. It was concluded that both dopants, in conjunction with Ti^{4+}, cause a transition in SNN from normal ferroelectric to relaxor behaviour. This effect was more pronounced with Ho^{3+}, indicating greater loss of polarity/relaxor behaviour at similar doping levels. This was consistent with P-E loops showing all of reduced slope, maximum polarisation, and residual polarisation (Cao et al. 2020). The smaller ionic radius and A_1-site tolerance factor of Ho^{3+} was linked to a higher second phase $NaNbO_3$ content in these compositions. Others have reported the difficulty of producing single phase TTBs with very small cations, stating that a large number of heterophases usually result (Gardener et al. 2014). On the likely causes of the observed relaxor behaviour, Cao et al. ruled out an incommensurate modulation through lack of evidence. Instead they suggested disorder from site occupancy by ions with different valence, destroying long range ferroelectric ordering and the introduction of polar nanoregions i.e. charge effects.

Work on SNN containing K^+, and B-site doped with Ta^{5+} ($Sr_2K_{0.1}Na_{0.9}Nb_{5-x}Ta_xO_{15}$) was conducted by Wei et al. (2010). The presence of K^+ lessens the relevance of this material to this study, but the substitution of B-site cations with identical charge and ionic radius is of interest (0.64 Å, CN VI for Ta^{5+} and Nb^{5+}). Despite this, peak splitting with increasing x in XRD patterns suggest a change in structure is occurring. Only one dielectric peak (T_c) was reported for this material and this decreases drastically with doping, from 269 ^{o}C at x = 0, to -35 ^{o}C at x = 2.0. This is such that at room temperature, x = 2.0 can be described as paraelectric, and is consistent with the residual polarisation and coercive field disappearing in P-E loops at high values of x (Wei at al. 2010). Given the similarities of the cations involved in the substitution, this reduction in T_c is thought to be linked to the covalence of the M-O bond (M = Ta^{5+} or Nb^{5+}). An increase in covalence occurs with Ta^{5+} due to the nature of the electron wave function being more diffuse, so the electron density spills out from the main occupied orbitals. This results in a larger M-O overlap when M = Ta^{5+} and a hardening of the crystalline structure which cancels the ferroelectric distortion and reduces T_c (Wei et al. 2010).

2.8.4 A-site vacancies – “unfilled” tungsten bronze structures

Binary phase diagrams found in a translated Chinese language paper part way through this study (Tang et al. 1979), provided insight into the SNN system and the implications of introducing compositional vacancies to the material. The metastable $NaNbO_3$-$SrNb_2O_6$ phase diagram (cooled from sintering temperature 1300 ^oC, 50 h) (Figure 2.8.4) indicated that $Sr_2NaNb_5O_{15}$ lies outside the single phase region below ~1400 ^oC. A Na^+ deficient composition ($Sr_{2.1}Na_{0.8}Nb_5O_{15}$) with vacancies is situated in the centre of the single phase field and it is suggested that it will remain single phase down to room temperature with sufficient cooling. This will be investigated in Chapter 5. The equilibrium phase diagram (samples annealed at 900 to 1300 ^oC for ~300 h) (Figure 2.8.5) indicates that a single phase will never be formed below ~1180 ^oC, but will fully break down into $SrNb_2O_6$ and Sr modified $NaNbO_3$. The temperature stability of SNN will be investigated in Chapter 6.

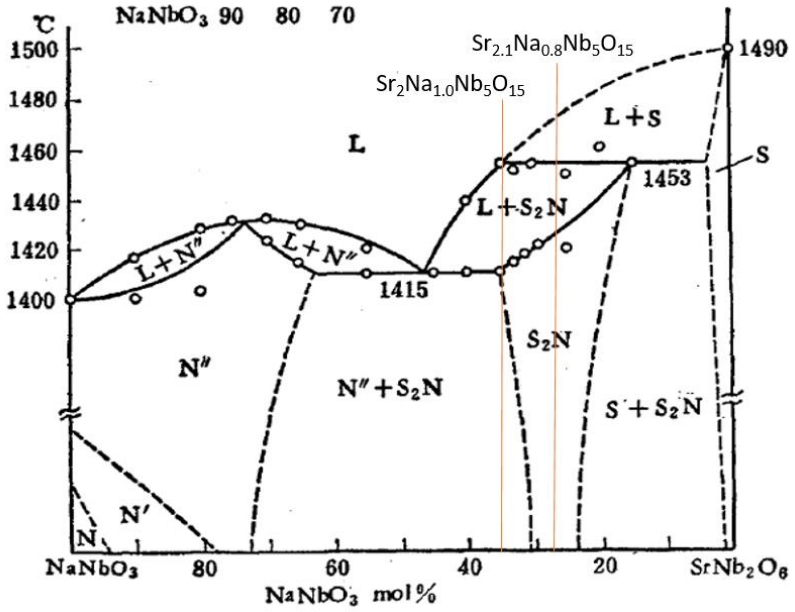

Figure 2.8.4. Metastable phase diagram of $NaNbO_3$ – $SrNb_2O_6$ system (reproduced form Tang et al. 1979).

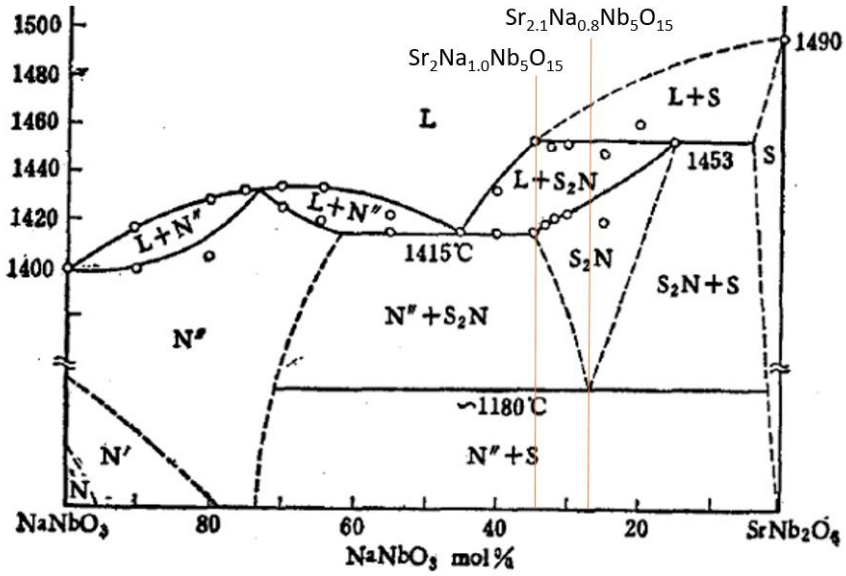

Figure 2.8.5. Equilibrium phase diagram of $NaNbO_3$ – $SrNb_2O_6$ system (reproduced form Tang et al. 1979).

"Unfilled" tungsten bronze structures contain structural vacancies on the A-sites which are thought to add to the degree of distortion and promote relaxor behaviour (by being destructive to the order of long-range ferroelectrics, Cao et al. 2021), but they can also have a subtle effect on the incommensurate/commensurate modulation (Zhu et al. 2015). Work by Gardener et al. (2014) found they strongly affected the ferroelectric properties of $Ba_4R_{0.67}\square_{1.33}Nb_{10}O_{30}$ (R = La, Nd, Sm, Gd, Dy and Y; □ = vacancy). It was reported that although the size of these vacancies was hard to quantify, they were likely to create a larger effective A_1:A_2 size difference in comparison to a filled TTB. This causes a stabilisation of the ferroelectric distortion within the structure, and so, a sufficient number of vacancies will stabilise the ferroelectric phase over the relaxor ferroelectric phase. This is consistent with the fact that the "filled" analogue of this material displays relaxor ferroelectric behaviour (Gardener et al. 2014). However, other work by Gardener et al. 2016 on $Ba_4(La_{1-x}Nd_x)_{0.67}Nb_{10}O_{30}$ (x = 0, 0.25, 0.5, 0.75, and 1) suggested that a sufficient quantity of A-site vacancies can produce significant structural relaxation to destabilise long range polar ordering, thus making it more relaxor like. The A_1 vacancies create additional lattice disruption to that found in the "filled analogue" and so in this case create a stronger relaxor (Gardener et al. 2016). This is consistent with the work of Cao et al. (2021) who investigated $Sr_{2-1.5x}Gd_x\square_{0.5x}NaNb_5O_{15}$ (□ =

vacancy), where for every Gd cation added to SNN, half a vacancy is created. They report that vacancies are destructive to long range ordering in ferroelectrics and that they provide an additional distortion to create a ferroelectric to relaxor ferroelectric crossover. At higher levels of vacancies, the ferroelectric response will be flattened as the long range order breaks down from a solution of weakly polar clusters in a polar matrix (as in SNN, Figure 2.8.6 a), to a distribution of weakly polar cluster in a non-polar matrix (Figure 2.8.6 b).

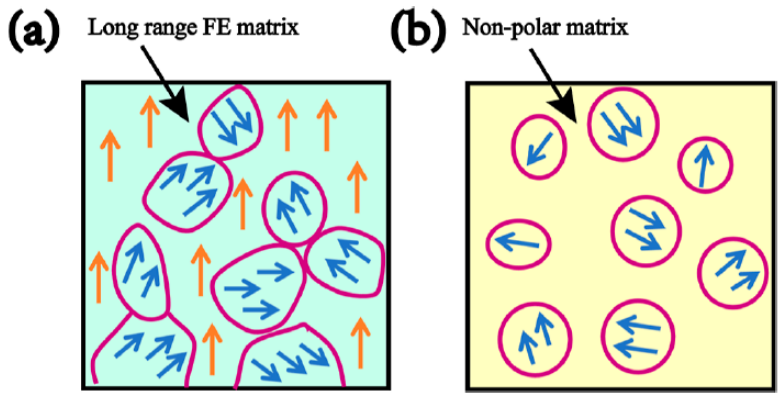

Figure 2.8.6. a) Solid solution of weakly polar clusters in a polar matrix. b) Weakly polar clusters in a non-polar matrix (reproduced from Cao et al. 2021).

The structure, with low levels of doping and vacancies, was similar to pure SNN and was assigned as orthorhombic using selected area electron diffraction (SAED). With higher doping and vacancies, all additional diffraction spots were not visible indicating a tetragonal structure was obscuring them. The structural vacancies were suppressing the structural distortions, although it was noted that this is not universal and is dependent on the chemical environment (Cao et al. 2021). It was also evident that the ubiquitous second phase $NaNbO_3$ found in SNN was absent in the “unfilled” structure. It is thought that the introduction of more vacancies into the crystal promotes electrostatic stability of the tungsten bronze structure, as the second phase is formed in “filled” structures through electrostatic instability (Jang et al. 2004). Zhu et al. (2015) report that the presence of significant vacancies prevents normal ferroelectric behaviour by suppressing the incommensurate to commensurate transition in tungsten bronzes. The vacancies cause the “frustrated” incommensurate tilt system to relax and become stable as they relieve local strain at octahedral apexes. They also inhibit rotations of the oxygen octahedral which are required for transition to a ferroelectric state (Zhu et al. 2015).

The targets of this study were therefore to maintain high Class II permittivity whilst achieving a stable response over as a temperature range as wide as possible (-55 to 300 °C) to meet the demands of power electrics and harsh environment electronics. The permittivity variation would need to meet R-type industry specifications set by the Electronics Industries Alliance Codes as +/- 15 %, with tan δ values < 0.025, both over the whole temperature range.

This was approached through introducing compositional heterogeneity via doping on both A and B-sites initially, selecting dopants Y^{3+} and Zr^{4+}, based on similarities in ionic radii to the host ions. The inclusion of Ca^{2+} substitution was based on permittivity- temperature data reported by Xie et al. (2002), Figure 2.8.3, where it was shown that both permittivity peaks became balanced through Ca^{2+} substitution.

Chapter 3. Experimental Methods

3.1 Introduction

Both the electrical and physical properties of a ceramic material will depend greatly on the processing methods used in the fabrication. The aim here was to produce a dense and chemically homogenous material. Further additions to this base ceramic could be made later to optimise electrical properties. An explanation of the mixed oxide synthesis route used throughout this study is given in Section 3.2.

Various methods of characterisation and analysis were used to determine the nature and properties of the finished ceramics. These are listed with a brief explanation of how they work and their operation in Section 3.3

3.2 Mixed-oxide synthesis route

3.2.1 Powder processing

A single-stage mixed-oxide synthesis route was used throughout the majority of this work. The powders used were reagent grade carbonates and oxides and are listed in Table 3.2.1 along with suppliers and purity. These were either dried overnight at 300 °C or stored permanently in drying ovens at 100 °C (Na_2CO_3 required storing at 300 °C due to its highly hygroscopic nature) and then allowed to cool in a vacuum desiccator before weighing and mixing. Stoichiometric measurements were made of the relevant powders for a particular composition using a Sartorius electronic balance (Sartorius UK Ltd, UK) to a precision of +/- 0.001 g.

Table 3.2.1. Carbonate and oxide reagents, purity and suppliers.

Raw powder	Purity	Supplier	CAS Code
$SrCO_3$	≥99.9%	Aldrich	1633-05-2
$CaCO_3$	≥99%	Aldrich	23-921-6
Na_2CO_3	≥99.95%	Sigma-Aldrich	497-19-8
Nb_2O_5	99.9%	Alfa-Aesar	1313-96-8
ZrO_2	99%	Aldrich	1314-23-4
Y_2O_3	99.9%	Alfa-Aesar	1314-36-9

Quantities of powder were calculated by multiplying the formula mass of the starting compounds by the atomic fraction of each element in the intended formula, and then added together. So for $Sr_{1.95}Ca_{0.05}NaNb_5O_{15}$:

$SrCO_3$ 147.628 g mol^{-1} x 1.95 mol = 287.875 g

$CaCO_3$ 100.086 g mol^{-1} x 0.05 mol = 5.004 g

Na_2CO_3 105.987 g mol^{-1} x 0.5 mol = 52.994 g

Nb_2O_5 265.808 g mol^{-1} x 2.5 mol = 664.519 g

Total – 1010.392 g

Each product was then divided by this total and then multiplied by the quantity in grams to be produced. Therefore, for 50 g of powder, the quantity of $SrCO_3$ would be:

$$\frac{287.875\ g}{1010.392\ g} \times 50\ g = 28.492\ g$$

3.2.2 Ball milling

The powders were then mixed by conventional ball milling using 0.5 litre plastic bottles two thirds full of zirconia grinding media (cylindrical ~1 cm length). The powder and grinding medium were then just covered in isopropyl alcohol (propan-2-ol ≥ 99.8 %, Fisher Chemicals) and ball milled for 24 h on horizontal mechanical rollers at 150 rpm. This was not intended to effect the particle size, but to mix the chemicals and remove clumps of material, forming a smooth slurry.

3.2.3 Powder drying and sieving

The slurry was dried using a Kenwood food mixer with heating element (cooking chef major with induction technology) at ~90 °C (lowering to ~65 °C towards the end of the process) until a dry powder was achieved. This raw powder was passed through a 300 µm gauze to break up agglomerates and then stored in sealed plastic containers.

3.2.4 Calcination

Calcination is a thermal treatment that causes interdiffusion of ions and can be regarded as part of the mixing process. The final phases may or may not be formed on completion of calcination (Moulson, 2003). This was performed in a covered crucible with a heating/cooling ramp rate of 5 °C/min, a dwell time of 6 h and at a temperature of 1200 °C in a conventional furnace with a hot zone considerably larger than the sample size (Figure 3.2.1).

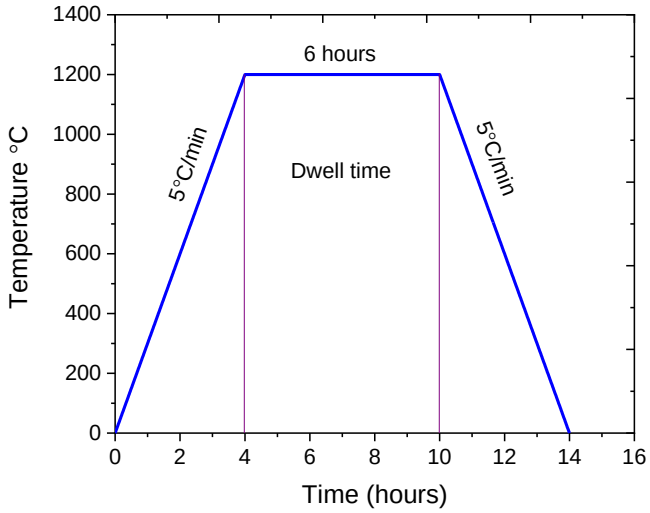

Figure 3.2.1. Typical calcination scheme used throughout this research.

3.2.5 Pellet formation

Following calcination, the powder was sieved before milling again for 24 h with 1-2 % Optapix (AC112, Zshimmer and Schwarz, Lahnstein, Germany) binder

and distilled water (instead of isopropyl alcohol). The addition of binder enables compaction into pellets. After further drying (as per Section 3.2.3) pellets were pressed with a 10 mm diameter steel die on a uniaxial press at a pressure of 100 MPa for 90 s. Isostatic pressing was then performed at 200 MPa for 5 minutes (Stanstead fluid power, Essex, UK).

3.2.6 Sintering

Sintering is a process widely used in ceramic production. Malič et al. (2015) describe it as “an irreversible thermodynamic process in which powder compacts are consolidated using thermal energy to obtain dense, polycrystalline ceramics”. It can be seen as a combination of grain growth and densification. Sintering was performed in a covered powder bed of calcined powder (atmosphere powder) and enclosed within an upturned crucible to minimise Na^+ losses which could lead to specific site vacancies in the final structure. A typical sintering heating regime is shown in Figure 3.2.2.

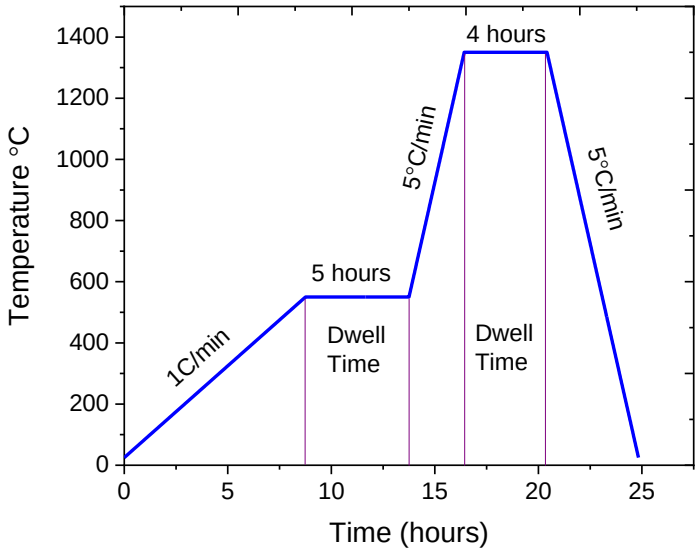

Figure 3.2.2. Typical sintering scheme used throughout this research.

The pellets were heated from room temperature to 550 °C in a conventional furnace (with a hot zone considerably larger than the sample size) at 1 °C/min with a dwell of 5 h to allow the binder material to burn out. The temperature was then

increased from 550 – 1300 °C at 5 °C/min with a dwell of 4 h, before cooling at the same rate to room temperature. 1300 °C was a typical sintering temperature used in this study, although others were used and will be stated in the text where necessary.

3.2.7 Density measurements and electrode application

On completion the pellets were cleaned, and geometric density measurements taken. The diameter, and thus radius *r*, and thickness *t* of each pellet was measured on a micrometre screw gauge and used to find the volume *V*. The sample mass *m* was measured on a Sartorius electronic balance (Sartorius UK Ltd, UK). The density (ρ) was then calculated using Equation 3.2.1.

$$\rho = \frac{m}{V} = \frac{m}{\pi(r)^2 t} \quad \text{(Equation 3.2.1)}$$

Theoretical densities of the materials was calculated using unit cell parameters acquired from basic unit cell refinement of X-ray diffraction data to calculate unit cell volume *V* (Chapter 4, Section 4.2.1). This was then used in Equation 3.2.2 to calculate the theoretical density ρ_t.

$$\rho_t = \frac{ZM}{VN_A} \quad \text{(Equation 3.2.2)}$$

Where *Z* is the number of formula unit per unit cell, *M* is the molecular mass, and N_A is Avogadro's number (6.023×10^{23}).

The ratio of the calculated geometric density to the theoretical density gives a relative density that indicates the percentage of sample densification.

For electrical measurements the pellets were ground down to ~1 mm and silver electrode paste added to the faces (Sun Chemical, Gwent electronic materials Ltd, Pontypool, UK). They were then fired at 550 °C at 5 °C/min for 30 m). After, the edges were cleaned of any electrode paste and measurements of diameter and thickness were taken. The pellets were then ready for electrical testing to be carried out.

3.3 Characterisation and analysis techniques

3.3.1 X-ray diffraction (XRD)

Powder X-ray diffraction is used to identify phase purity, structural transitions, determine lattice parameters and resolve the internal arrangement of atoms in a crystal structure. It was routinely performed on samples throughout this study.

The technique works by detecting interference patterns created by diffracted X-rays (wavelength from ~0.1 to ~100 Å) scattered by crystals. The X-rays most commonly used in crystallography are between ~0.5 and ~2.5 Å, having a similar wavelength to the smallest interatomic/molecular spacing.

X-rays are created by accelerating electrons at a Cu target which can knock other electrons out of the *K*-shell orbitals. An electron from a higher (outer shells *L* or *M*) energy level will then drop down to fill this gap, releasing energy in the form of X-rays as it does so. This creates a series of *K* α or β X-rays when electrons fall from the *L* or *M* shells respectively (Cullity and Stock, 2014) (Figure 3.3.1)

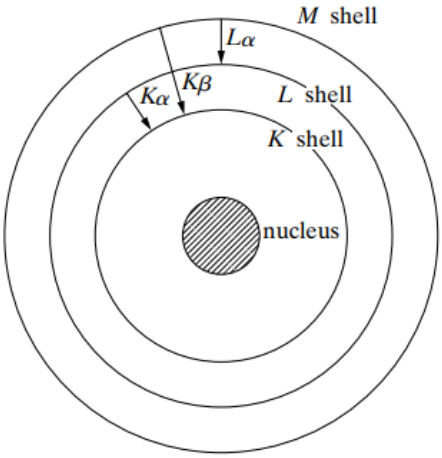

Figure 3.3.1. Schematic representations of electronic transitions in an atom with the X-ray emission processes indicated by arrows (Cullity and Stock, 2014).

Since it is more likely the *K*-shell vacancy will be filled by an *L* electron, the K_α is the more intense of the two, with the K_β radiation filtered out by the diffractometer. The L shell actually consists of two sub energy levels, so the resulting radiation is

split into $K_{\alpha 1}$ (λ = 1.5406 Å) and $K_{\alpha 2}$ (λ = 1.5443 Å). For clearer data, the $K_{\alpha 2}$ radiation is stripped out at a later point by computer software.

Beams of parallel, monochromatic, in phase X-rays strike the sample surface at an angle of θ. The sample is in effect a series of atomic planes with lattice plane spacing d_{hkl} that diffract the X-rays. The extra distance travelled by a diffracted X-ray from a lower atomic layer is thus calculated by $2d_{hkl}\sin\theta$. If this value is equal to a whole number of wavelengths, *nλ* then Bragg's law is satisfied and the two waves will interfere constructively (Equation 3.3.1). Constructive interference of these emissions creates an interference pattern through the supposition of peaks that a detector can pick up. (Figure 3.3.2) (Pecharsky et al. 2009).

$$n\lambda = 2d_{hkl}sin\theta \text{ (Equation 3.3.1)}$$

Where *λ* is the known incident X-ray wavelength, *d* is the atomic layer distance, *θ* is the angle of incidence.

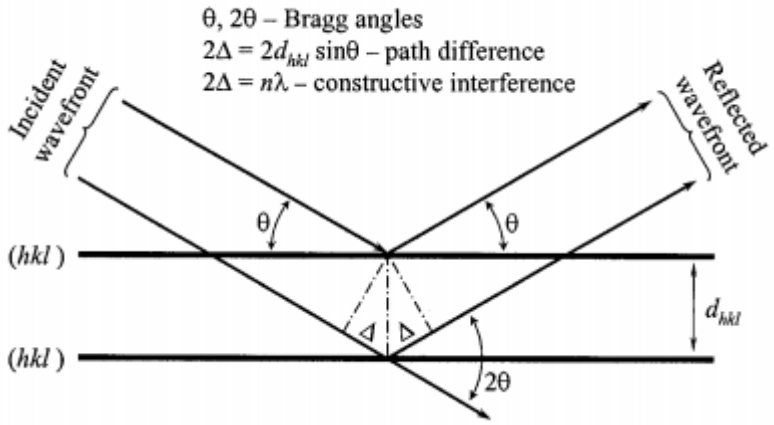

Figure 3.3.2. Geometric representation of Bragg's law showing diffraction of X-rays from lattice planes with spacing d_{hkl} (Pecharsky et al. 2009).

This result is a pattern of peaks in intensity at certain positions recorded against values of 2θ. The structure of the material can be interpreted from the height (intensity, relating to the atomic parameters or distribution of atoms in the unit cell), width (microstructure, wider peaks equate to smaller grain sizes) and position

(related to unit cell parameters, altered by any change in interatomic spacing (e.g. by doping) of these peaks. The space between diffracting planes of atoms will determine the peak positions, whilst the atoms present in the plane will determine the peak intensity. Thus, an indexed XRD pattern permits information on unit cell parameters to be obtained. More advanced structural information (atom positions) may be obtained by further advanced analysis of the data.

X-ray diffraction was performed on crushed sintered pellets to assess the phase purity and crystal structure using a Bruker D8 diffractometer (Cu, Kα ~ 1.5406Å, Karlsruhe, Germany) with a step size of 0.2 °2θ and range of angles from 10 to 80 °2θ (although 10 to 60 °2θ was deemed suitable for most plots within this work). Initially, scans of 24 min were used to check phase purity. Then longer 12 h scans were performed on selected samples for higher resolution data which allowed more detailed analysis and basic unit cell refinements.

Data analysis was performed on the PANalytical X'pert Highscore Plus software in the form of peak profile fitting and comparison to data in the International Centre for Diffraction Data (ICDD) database. Matched profiles were then fitted manually to confirm the phases present. A basic form of unit cell refinement was performed to determine unit cell parameters and volume and thus theoretical density of the samples (See Chapter 4, Section 4.2.1).

3.3.2 Permittivity vs temperature

The dielectric permittivity of a sample was calculated with an impedance analyser measuring capacitance and loss values at varying frequencies and as a function of temperature. Relative permittivity can then be found using Equation 3.3.2.

$$\varepsilon_r = \frac{Ct}{A\varepsilon_0} \quad \text{(Equation 3.3.2)}$$

Where ε_r is relative permittivity, C is capacitance, t is thickness of the sample, A is the area of the electrode and ε_0 is the permittivity of free space (8.854×10^{-12} F/m).

Dielectric properties at low and high temperatures were recorded on a Agilent HP4284 LCR meter (Agilent/Hewlett Packard, USA), using a conventional furnace (25 °C to 450 °C) and a Tenney environmental chamber (-70 °C to 180 °C) (TJR; Tenney Environmental-SPX, White Deer, CA). A heating and cooling rate of 3 °C/min was used. These were at selected frequencies between 10^2 and 10^6 Hz on disc shaped specimens of < 1 mm thickness and < 9 mm diameter placed between platinum wires. The measurement of capacitance combined with the sample dimensions were automatically converted to relative permittivity values. A K-type thermocouple was positioned close to the sample and recorded with a USB-TC01 device (National Instruments, UK).

3.3.3 Scanning electron microscope (SEM)

A scanning electron microscope (SEM) was used to study grain size, grain morphology and density properties. The existence of second phases can also be determined, particularly using Energy Dispersive X-ray (EDX) to gain compositional information. Sintered samples were set in epoxy resin and then ground and polished on progressively finer grade silicon carbide paper to reveal a stress free surface and eliminate scratches. Etching of the polished surfaces was performed with a 2:1 ration hydrogen fluoride and nitric acid for 90 s to reveal grain structure.

Using the wavelike properties of an electron, an electron microscope (EM) works in a similar fashion to light microscopy, where the maximum resolution (smallest distinguishable distance between two points) is proportional to the wavelength of the illuminating radiation as shown by the Rayleigh criterion for visible-light microscopy (Equation 3.3.3).

$$\delta = \frac{0.61\lambda}{\mu sin\beta} \quad \text{(Equation 3.3.3)}$$

Where δ is the smallest observable distance, λ is wavelength of radiation, μ is the refractive index of the viewing medium, and β is the semi-angle of collection.

An approximation for the Rayleigh criterion for an electron microscope is 1.22 λ/β, where β is limited by the spherical aberration of the electron lens. (Williams and Carter, 2009). Since visible light has a wavelength of ~400-700 nm and a high kV

electron has a wavelength of 0.001-0.01 nm, the electron microscope has much greater resolving power. Electromagnets are used to focus the beam (instead of refracting lenses in an optical microscope) and spherical aberrations in these lenses typical reduce the resolution from the optimum value. An SEM can usually image to a few nanometres. An advantage of the limited collection angle (due to spherical aberration of the EM lenses) is the excellent depth of field attainable. This is the ability to maintain focus on topographical features of different elevation in SEM or the whole thin section in focus for transmission electron microscopy (TEM). With a SEM, the working distances and apertures make this depth of field tens of μm.

With the SEM, two types of electrons are detected, which carry different information about the sample. Secondary electrons (SE) originate from near the surface (a few nm) of the sample and reveal most about the topographical features of a sample. As such, they are most often used for imaging. SE are low energy (<50 eV) and are produced by inelastic collisions between the electron beam and the sample. In contrast back-scattered electrons (BSE) occur as a result of elastic collisions (kinetic energy conserving) that change the trajectory of the incoming electron i.e. they are primary incident electrons. They originate from deeper within the sample and have an energy of >≥ 50 eV. Because larger atoms will scatter more, the backscattered signal at the detector is proportional to the Z number of the atom (assuming the specimen is flat). So qualitative compositional information can be determined, with heavier elements showing as lighter on the BSE images (Williams and Carter, 2009).

In order to prepare specimens for microstructural characterisation by scanning electron microscopy, ceramic pellets were mounted in epoxy resin (Epothin, Buehler) and ground with P240, P600 and P2500 silicon carbide paper. Subsequent sequential polishing was carried out using Texmet P microcloths with MetaDi 2 diamond suspensions of decreasing particle size of: 9 μm, 3 μm and 1 μm. A final polish was carried out with ChemoMet and MasterMet 0.06 μm colloidal silica on a Buehler EcoMet 300 grinder/polisher. Chemical etching was carried out with a 2:1 ratio of hydrofluoric acid and concentrated nitric acid for 90 s at room temperature.

Scanning electron microscopy (SEM) was performed at 15 keV using a Hitachi SU8230 high performance cold field emission instrument fitted with an Oxford

Instruments energy dispersive X-ray analysis (EDX) system with 80 mm^2 X-Max Silicon Drift detector and Aztec analysis software.

3.3.4 Energy Dispersive X-ray Spectroscopy (EDX)

Working in conjunction with SEM or TEM, this technique captures X-rays from the sample which are generated by primary or incident electrons exciting electrons in the specimen to higher energy states such that when these atomic electrons decay back to the ground state, they release an X-ray. The generated X-rays have an energy characteristic of the element they are generated in and by measuring the energy dispersion of the X-rays generated with a spectrometer, compositional data may be gathered and nominally quantified.

3.3.5 Polarisation-electric field loops (P-E loops)

A reversible spontaneous electric polarisation determines whether a ferroelectric material has been produced and is represented by the formation of a hysteresis loop on application of an electric field (Chapter 2, Section 2.5.2).

Polarisation-electric field (P-E) hysteresis loops were obtained using a modified Sawyer-Tower circuit, where a current is induced in the sample by an applied field. The voltage is incrementally increased in order to increase the field. The equipment used was a 5 kV amplifier source (Model 5/80, Trek Inc., Medina, NY) and data acquisition hardware controlled by Vision software package (Radiant Technologies, Albuquerque, New Mexico). The samples were ground to <1 mm to maximise the amount of available electric field and were submerged in silicone oil in order to increase the dielectric breakdown voltage and prevent arcing around the edges of the pellet. All measurements were carried out at room temperature.

Chapter 4. Synthesis and properties of strontium sodium niobate (SNN) ceramic system with simultaneous Ca^{2+}, Y^{3+}, and Zr^{4+} doping

4.1 Introduction

This chapter investigates the synthesis and properties of the parent niobate phase $Sr_4Na_2Nb_{10}O_{30}$ (for convenience expressed as $Sr_2NaNb_5O_{15}$ (SNN)) and its doping with Ca^{2+}, Y^{3+}, and Zr^{4+} to form a ceramic system with the assumed solid solution formula $Sr_{2-x-y}Ca_xY_yNaNb_{5-y}Zr_yO_{15}$ (SCNN-YZ). The following assumptions, due to similarities in ionic radii, were made in the first instance; that Ca^{2+} and Y^{3+} substitute for Sr^{2+} on the A1/A2 sites, Zr^{4+} substitutes for Nb^{5+} on the B sites. C sites were assumed to remain empty. Y^{3+} and Zr^{4+} were chosen for co-dopants as a way of maintaining charge balance. Dopant levels were calculated as such, as illustrated in Chapter 3.

SNN was of interest due to the presence of high and low temperature dielectric peaks located at the limits of the target temperature range (-55 to 300 °C), while having a high baseline permittivity at room temperature. Previous work on SNN by Garcia-Gonzalez et al. (2007) (Figure 4.1.1) and Torres-Pardo et al. (2011) (Figure 4.1.2) had produced dense SNN ceramics (> 95 %) which contained a small amount of second phase Sr modified $NaNbO_3$ (3 % reported in both). Calcination was 900 °C for 24 h and sintering was 1300 °C for two days then quenched to room temperature for both studies. The samples displayed two dielectric anomalies: one at -20 °C and another at 250 °C (Figure 4.1.1 a-b) (Garcia-Gonzalez et al. 2007, and Torres-Pardo et al. 2011).

Permittivity variations were shown to be approximately +/- 23 % ($\varepsilon_{r\,max}$ 1450, $\varepsilon_{r\,min}$ 900 at 10 kHz) and +/- 30 % ($\varepsilon_{r\,max}$ 1750, $\varepsilon_{r\,min}$ 875 at 1 kHz) (-55 to 300 °C), estimated from the published permittivity-temperature plots for Garcia-Gonzalez and Torres-Pardo respectively. Both publications reported a commensurate superstructure in the ferroelectric phase from superlattice reflections, first identified

in Selected Area Electron Diffraction (SAED) patterns, then in the X-ray diffraction patterns.

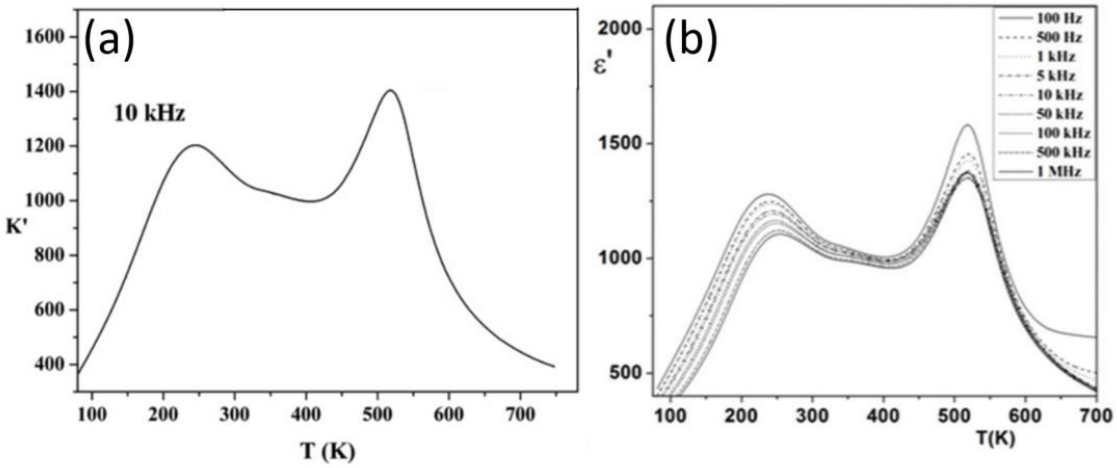

Figure 4.1.1 a-b. (a) 10 kHz relative permittivity versus temperature plot of $Sr_2NaNb_5O_{15}$ (reproduced from Garcia-Gonzalez et al. 2007). (b) multi-frequency relative permittivity versus temperature plot for $Sr_2NaNb_5O_{15}$ (reproduced from Torres-Pardo et al. 2011). Both show high and low temperature dielectric anomalies with relative permittivity variations of approximately +/- 23 % and +/- 30 % (-55 to 300 ºC) respectively. Both densities were reported as > 95 % of calculated theoretical values.

Evidence was seen in the literature that Ca^{2+} modification of SNN ($Sr_{2-x}CaNaNb_5O_{15}$, SCNN) produced high and low permittivity peaks of comparable ε_r values to each other (Figure 4.1.2) at levels of x = 0.05 (Xie et al. 2002 (1), (synthesis by spark plasma sintering at 1200 ºC 5 min under 35 MPa in a vacuum, followed by annealing 1000 ºC 10 h in air)), with a permittivity variation of approximately +/- 25 %, -55 to 300 ºC (Figure 4.1.2). This was considered a useful starting point in the attempt to reduce relative permittivity variation to within +/- 15 %, the R-type EIA specification required for high temperature capacitor material. It is noted that differences in the fabrication routes and the relative density of the SNN/SCNN ceramics reported in the literature (> 97 % for SCNN, Xie et al. 2002 (1), > 95 % for SNN, Torres Pardo, 2011 and Garcia Gonzalez, 2007) may contribute to the reported differences in $\varepsilon_{r\,max}$ value of each dielectric peak and to differences in the % change in relative permittivity from -55 to 300ºC.

Since literature values of relative permittivity were used in this scoping assessment, a preliminary analysis of Ca^{2+} only doping of SNN was performed

(Section 4.3). This agreed with the published work, that increasing Ca^{2+} would increase the intensity of the low temperature permittivity peak and showed the high and low temperature peaks were approximately of equal intensity at $Ca^{2+} = 0.05$ (Figure 4.3.2).

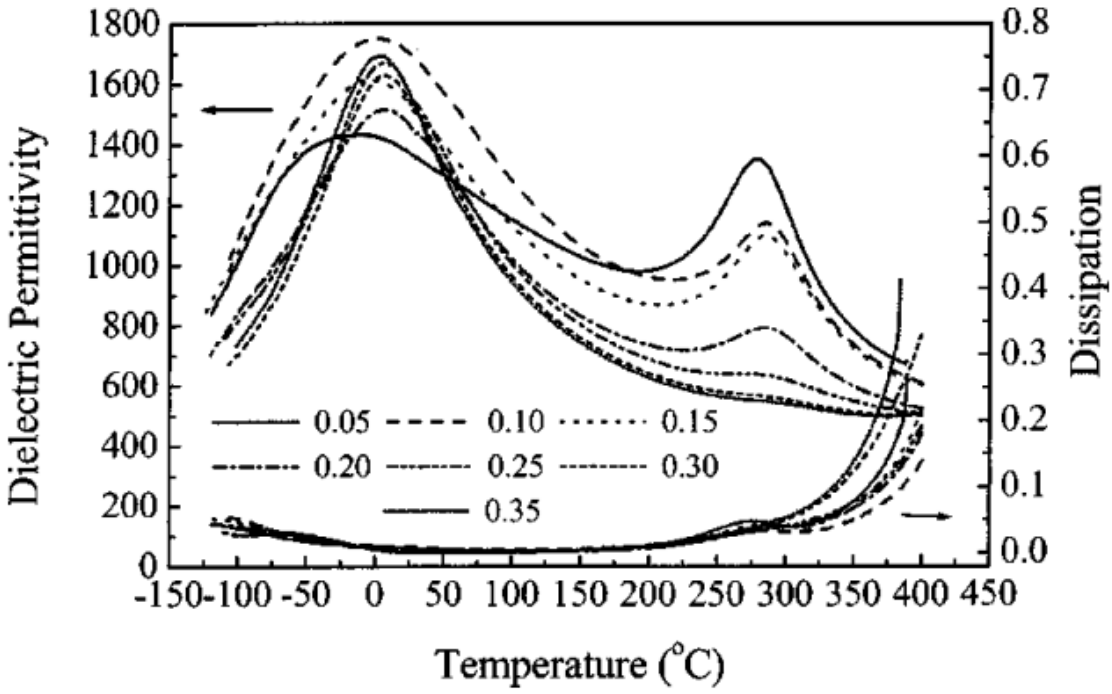

Figure 4.1.2. Relative permittivity as a function of temperature at 1 kHz for $Sr_{2-x}Ca_xNaNb_5O_{15}$ ceramics with increasing levels of x. Composition x = 0.05 has a permittivity variation of approximately +/- 25 % from -55 to 300 °C (estimated from the published permittivity-temperature plots). Reported densities were > 97 % of calculated theoretical values. The high temperature dielectric anomaly was suppressed with increasing x, whilst the low temperature anomaly followed no systematic trend (reproduced from Xie et al. 2002 (1)).

In this chapter, production of SNN (Section 4.2), is followed by compositions modified with Ca^{2+}, Y^{3+} and Zr^{4+} prepared according to the formula $Sr_{2-x-y}Ca_xY_yNaNb_{5-y}Zr_yO_{15}$ (Section 4.3). The assumption was that Ca^{2+} and Y^{3+} would substitute on Sr^{2+} sites, although in practice it was recognised that substitution of Na^+ may also occur. Indeed for SNN there may be split occupancy of Sr^{2+} and Na^+ sites, giving a formula $Sr_{2+x}Na_{1-2x}Nb_5O_{10}$ (Yang et al. 2019). Promising results in terms of permittivity-temperature response were produced using the formulations: $Sr_{2-x-y}Ca_xY_yNaNb_{5-y}Zr_yO_{15}$ (x = 0.025, and 0.05, y = 0, 0.025, and 0.05). These doped compositions represent a very low level of substitution. Only 1.25 at. % of the Sr^{2+} (A) sites are substituted by Y^{3+} in compositions with y=0.025; and 2.5 at. % for

y=0.05. For B sites, the Zr^{4+} for Nb^{5+} levels are 0.05 at. %, and 1 at. % for compositions with y = 0.025, and 0.05 respectively. Fabrication was carried out as outlined in Chapter 3, unless otherwise stated. No evidence of previous doping of TTBs with Y^{3+} and Zr^{4+} could be found in the literature, hence it was hoped that this novel approach would yield interesting results.

4.2 Strontium sodium niobate (SNN)

SNN was produced with composition $Sr_2NaNb_5O_{15}$, as outlined in Chapter 3. The powder was calcined for 6 h at 1200 ^oC in air, then pellets were sintered for 4 h at 1300 ^oC in air, covered with 2 g of calcined SNN powder. These times were much shorter than those employed by Garcia-Gonzalez et al. (2007) (Figure 4.1.1) and Torres-Pardo et al. (2011) (Figure 4.1.2) (calcination 24 h at 900 ^oC, sintering 2 days at 1300 ^oC) in order to simplify the sintering process. Shorter sintering times produced densities of > 90 % which were considered acceptable for this permittivity profiling.

4.2.1 Phase analysis

Figure 4.2.1 shows the room temperature, 12 h X-ray powder diffraction pattern for $Sr_2NaNb_5O_{15}$. This was obtained for crushed, sintered pellets in order to confirm the formation of a crystalline TTB structure and to detect the presence of any impurity phases. The pattern was indexed to a tetragonal SNN (*P4bm* space group (ICDD 04-008-7203)), with the main peaks found to match the reference file within ≤ 0.1 $^o2\theta$ (Figure 4.2.1 shows 10 to 60 $^o2\theta$ range). No evidence of weak extra super lattice reflections at 20 $^o2\theta$ or 37 $^o2\theta$ were observed (Garcia-Gonzalez, 2007).

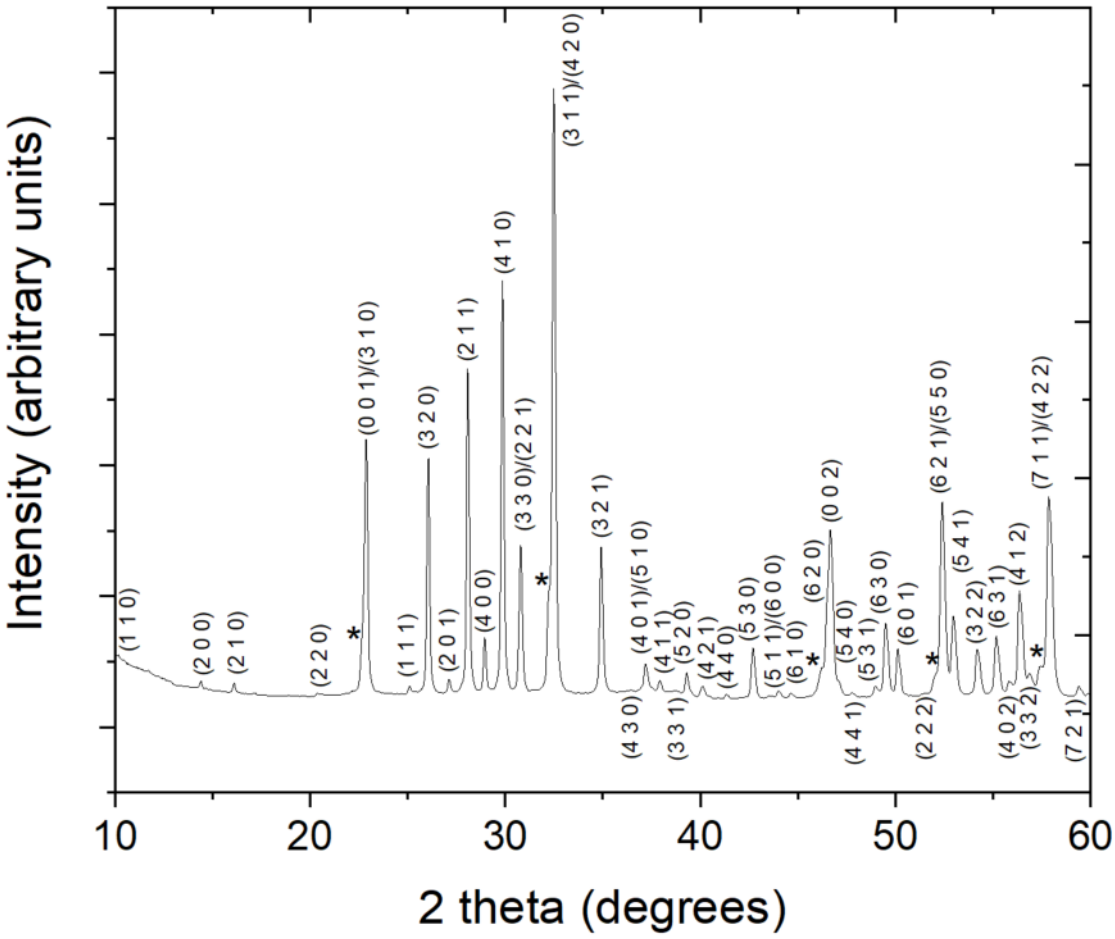

Figure 4.2.1. 12 h powder XRD plot of SNN $Sr_2NaNb_5O_{15}$. Indexed to ICDD 04-008-7203, tetragonal SNN, *P4bm*. Second phase orthorhombic $NaNbO_3$ (*) was also present (ICDD 04-009-3239).

Second phase orthorhombic $NaNbO_3$ was present, as has been reported by others for SNN (Garcia-Gonzalez, 2007 and Torres-Pardo, 2011), although it has been suggested this phase may contain small amounts of Sr^{2+} (Garcia-Gonzalez et al. 2007). Peaks for this second phase were found at 22.64, 32.24, 46.09/46.23, 52.02, and 57.41 °2θ and are within 0.1 °2θ of those found in $NaNbO_3$ reference file ICDD 04-009-3239. The persistence of this extra phase (or possibly Sr modified $NaNbO_3$) suggested that for unmodified SNN the notional formula $Sr_2NaNb_5O_{15}$ may be inaccurate: for example, the Na rich secondary phase may be due to Sr^{2+} occupancy of a fraction of the nominal Na^+ sites, giving a formula $Sr_{2+x}Na_{1-2x}Nb_5O_{10}$ (Yang et al. 2019). However, at the outset of this project this information was not available. Subsequent TEM results discussed in the summary do suggest the second phase contains Sr, consistent with $Sr_2NaNb_5O_{15}$ reported by Torres-Pardo, 2011.

A simple unit cell refinement was carried out on the SNN using HighScore Plus (Malvern Panalytical, UK). This software uses a least-square fitting method to reduce error in fitting to a known reference patterns from the International Centre of Diffraction Data (ICDD) database and ascertain the structural phases present. Once the unit cells were refined for all structures present, the relative intensities were used to calculate phase fraction, a semi-quantitative value for the percentage mass of each component. A full Rietveld refinement was not performed at this stage, and was only employed later and carried out at the University of Manchester for selected compositions (Y Li, University of Manchester, published in Brown et al. 2020). The basic unit cell refinement reported here involved a least square fit on a rigid model of 2θ values to give unit cell measurements. Like Rietveld, a goodness of fit value (R_{WP}), is employed to evaluate the conformity between the measured data and the reference pattern. This is a weighted residual of least-square refinements and compares the raw data with the reference file model in relation to the difference in height, width, and position of X-ray peaks. An R_{WP} value of ≤ 10 % is usually considered a good fit, although it can be expected to be higher when applied to more complex structures and when secondary phases are present (HighScore Plus user manual, Malvern Panalytical). Any compositional differences between experimental samples and the reference material clearly will also contribute to a higher value of $R_{WP.}$ Once a pattern is sufficiently fitted to the model, crystallographic data such as unit cell parameters can be obtained. The HighScore data for SNN is shown in Figure 4.2.2 with raw data (black) and model data (red) and visually appears to be a good match. Lattice parameters for SNN using this approach were shown to be a = 12.3657(4) Å and c = 3.8963(2) Å. This indicates a very high level of precision in the measurement yet the R_{WP} value of 12 % (Table 4.2.1) suggests the fit is not as good. It was therefore decided to use an error of +/- 0.005 Å in the lattice parameter measurements, or in many cases four significant figures. We believe this to be a cautious estimate of accuracy (Table 4.2.1). It is important to appreciate the limitations of the HighScore software when performing a very basic unit cell refinement. This is mainly the inability to alter any parameters such as occupancies and thermal parameters in the structural model in order to match simulated positions and intensities of X-ray peaks to the experimental data. These ‘full’ fitting parameters are included in a rigorous Rietveld refinement such as that shown in Brown et al. (2020).

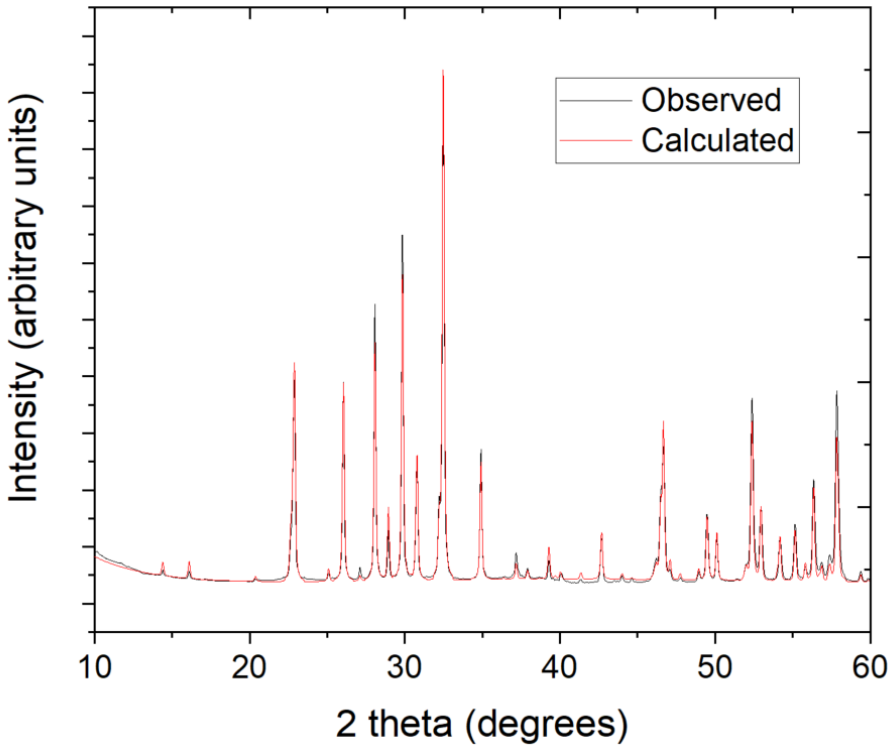

Figure 4.2.2. 12 h powder XRD plot of SNN $Sr_2NaNb_5O_{15}$ showing raw data (black) and calculated data (red) after unit cell refinement using HighScore Plus software (Malvern Panalytical, UK).

Lattice parameters based on *P4bm* and other data are summarised in Table 4.2.1. Geometric densities of the sample pellets were measured to be 93 % of theoretical density, as calculated from the X-ray derived unit cell parameters. The mass proportion of second phase was found to be 6 wt.% Sr modified $NaNbO_3$. The R_{WP} value for the refined laboratory XRD pattern for this SNN composition was 11.5 %, and values for the doped compositions are typically 13 to 14 % throughout this study. This is higher than the usual threshold of 10 % for a full Rietveld refinement and reflects the approximation due to the complexity of the system and the lack of detailed refinement. A full Rietveld refinement carried out in Manchester shows improved R_{WP} values of < 10 % when still fitting to the tetragonal structure (Y Li, University of Manchester, Brown et al. 2020).

Table 4.2.1. Crystallographic data of $Sr_2NaNb_5O_{15}$ from X-ray powder diffraction analysis.

Composition	*a* = *b* Å	*c* Å	Volume Å^3	Geometric density g/cm^3	Percentage theoretical density	Tetragonality c/a	2nd phase wt.%	R_{WP} %
$Sr_2NaNb_5O_{15}$	12.37	3.896	596.2	4.68	93 %	0.32	5.8 $NaNb0_3$	11.5

4.2.2 Dielectric analysis

Figure 4.2.3 shows the temperature dependence of the relative permittivity and dielectric loss tangent for $Sr_2NaNb_5O_{15}$. Frequencies of 1 kHz, 10 kHz, 100 kHz, and 1 MHz were measured and data are summarised in Table 4.2.2. The plot shows the presence of the main ferroelectric to paraelectric phase transition peak at 310 ^oC (T_2), as well as a broad second peak with a maximum at -15 ^oC (T_1). T_1 exhibited relaxor character, with $\varepsilon_{r\,max}$ moving to higher temperature on increasing frequency, from -15 ^oC at 1 kHz to -10 ^oC at 1 MHz.

Peak T_1 at a temperature of -15 ^oC had an $\varepsilon_{r\,max}$ value of 1710, whilst peak T_2 at 310 ^oC had an $\varepsilon_{r\,max}$ value of 2150 at 1 kHz. Dielectric loss tangents, tan δ at 1 kHz were ≤ 0.025 from temperatures of -30 to 220 ^oC, ≤ 0.03 from -65 to 240 ^oC, and ≤ 0.035 from -65 to 250 ^oC. However at T_2 the tan δ values increased, for example to ~ 0.06 at 300 ^oC (1 kHz).

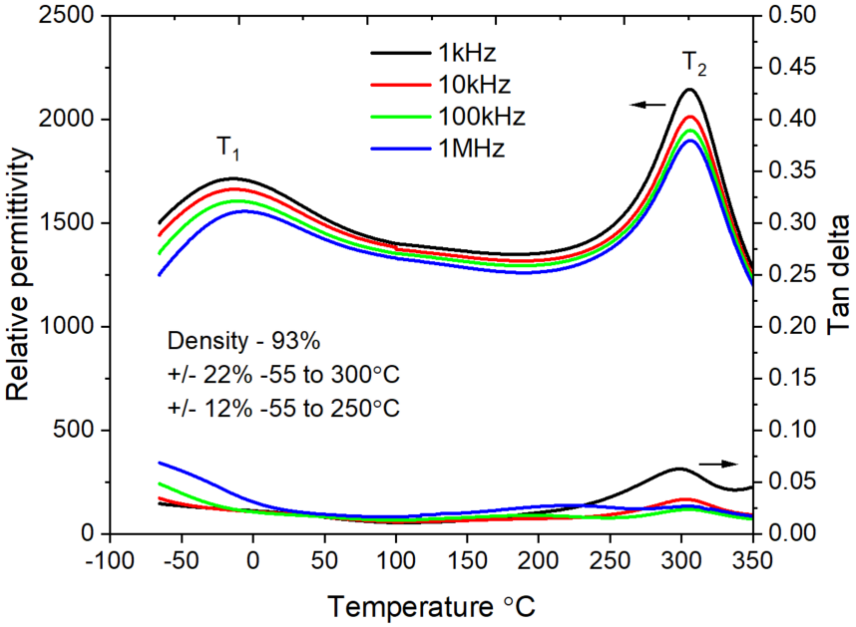

Figure 4.2.3. Multi-frequency relative permittivity and dielectric loss tangent versus temperature plots for $Sr_2NaNb_5O_{15}$.

The permittivity variation was measured as +/- 22 % about the median value from -55 to 300 °C, and +/- 12 % from -55 to 250 °C at 1 kHz. Figure 4.2.4 shows the 1 kHz plots for relative permittivity and dielectric loss, with the dashed limits representing the +/- 15 % variation in permittivity we were looking to achieve in this project.

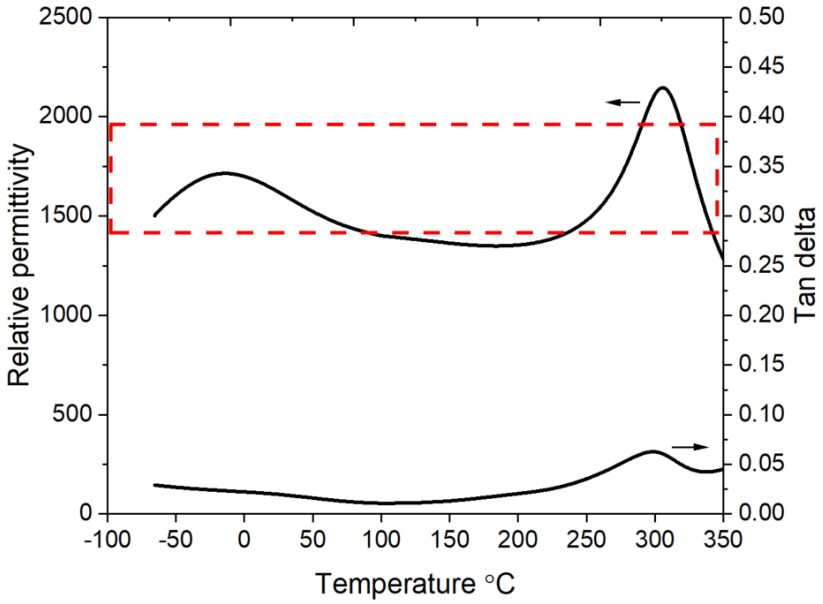

Figure 4.2.4. 1 kHz relative permittivity and dielectric loss tangent versus temperature plot for $Sr_2NaNb_5O_{15}$. The dashed outline indicates the +/- 15 % limit.

Table 4.2.2. 1 kHz relative permittivity and dielectric loss tangent versus temperature data for $Sr_2NaNb_5O_{15}$.

Composition	T_1 °C ($\varepsilon_{r\ max}$)	T_2 °C ($\varepsilon_{r\ max}$)	+/- % (-55 – 250°C)	+/- % (-55 - 300°C)	tan δ ≤0.025 °C	tan δ ≤0.030 °C	tan δ ≤0.035 °C
$Sr_2NaNb_5O_{15}$ 93 % density	-15 (1714)	306 (2146)	12 %	22 %	-32 to 223	-65 to 238	-65 to 249

4.2.3 Ferroelectric analysis

Hysteresis measurements up to 40 kV cm^{-1} confirmed the ferroelectric nature of SNN. The reversibility of the polarisation, indicated by non-linear hysteresis behaviour was observed, and is characteristic of ferroelectric behaviour (Figure 4.2.5). P-E hysteresis loops for SNN showed higher maximum polarisation (P_{max}) values as the electric field increased although were not fully saturated. Maximum polarisation was 13 µC cm^{-2}, whilst remnant polarisation (P_r) was approximately 5.5 µC cm^{-2} and the coercive field (E_c) approximately 12 kV cm^{-1} (all at 40 kV cm^{-1} with reading errors of +/- 0.5).

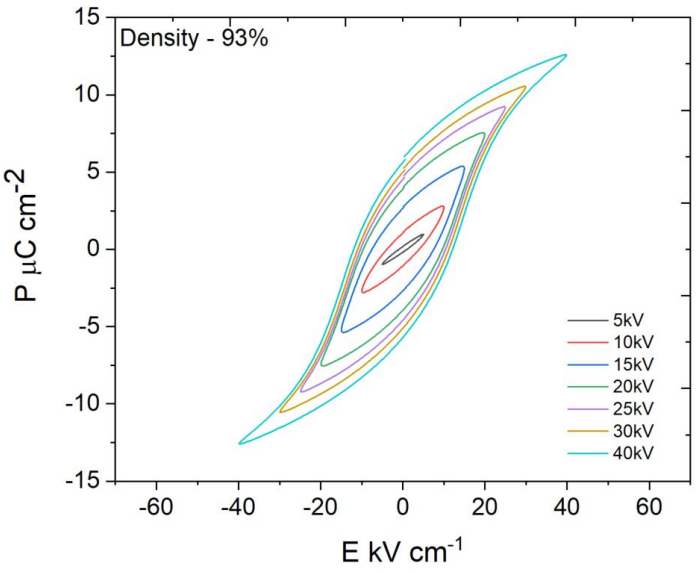

Figure 4.2.5. Multi-field polarisation – electric field loop plots for $Sr_2NaNb_5O_{15}$ up to 40 kV cm^{-1}.

4.2.4 Microstructural analysis

Scanning electron micrographs of $Sr_2NaNb_5O_{15}$ using secondary electron and back scattered electron imaging techniques were taken to analyse the samples microstructure (Figure 4.2.6). Images revealed a dense microstructure with a maximum, near equiaxed grain size of 17 µm. The grains were mostly between the sizes of 2 -10 µm and were facetted in nature. A number of darker grains were observed evenly distributed throughout the whole structure and with a similar grain size to the lighter ones. SEM-EDX analysis (Figure 4.2.7) revealed that these grains were rich in Na^+ (approximately 10 at. % compared to 4 at. % in lighter grains) and correspondingly deficient in Sr^{2+} providing evidence of the second phase $NaNbO_3$ (possibly containing Sr) as seen in the XRD patterns (Figure 4.2.1). Although some Sr^{2+} was detected within these areas (approximately 5 at. %) this could be from the electron beam interaction volume extending below the grain (at. % values obtained from point spectra are standardless quantification with ZAF correction using all elements including oxygen). The Nb^{5+} was seen to be homogenously distributed throughout the material. The EDX analysis showed no elemental gradation within the grains.

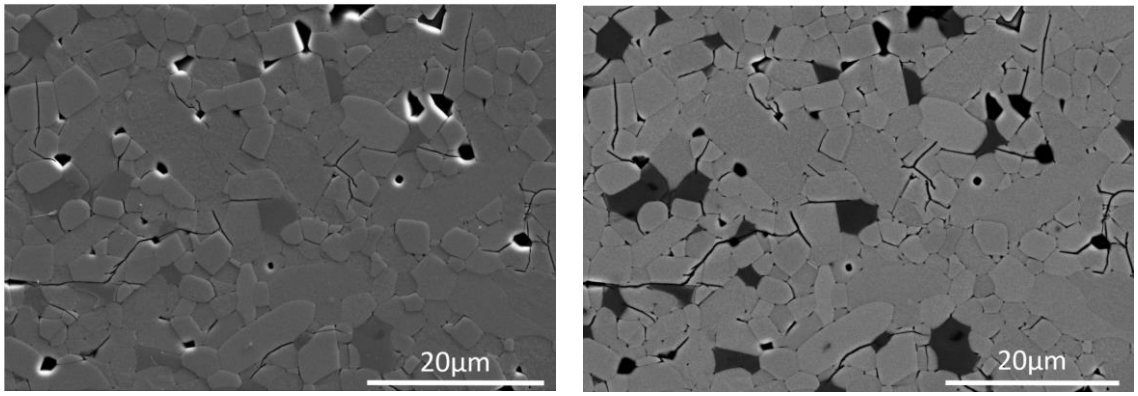

Figure 4.2.6. Secondary electron (left) and back scattered electron (right) images of $Sr_2NaNb_5O_{15}$.

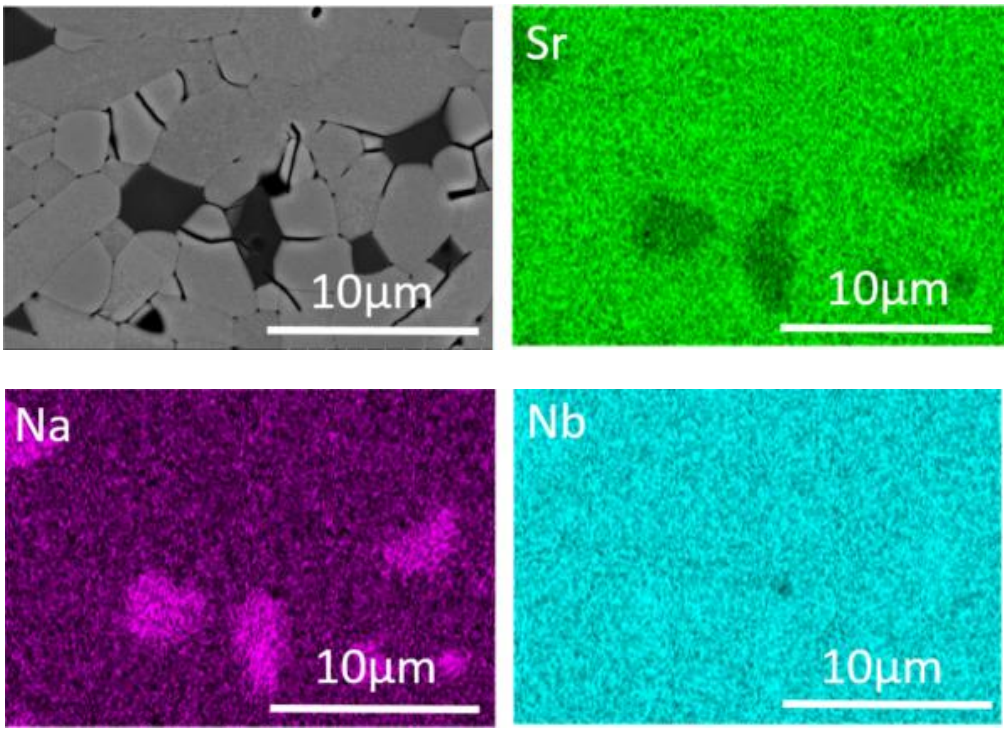

Figure 4.2.7. Back scattered electron image with associated EDX mapping of $Sr_2NaNb_5O_{15}$ showing darker grains to be Na^+ rich and Sr^{2+} deficient. Nb^{5+} has a homogenous distribution.

4.2.5 Summary: Strontium sodium niobate (SNN)

SNN ($Sr_2NaNb_5O_{15}$) was produced to replicate and confirm the findings of Garcia-Gonzalez (2007) and Torres-Pardo (2011). The sintering and calcination temperatures were modified to shorter times to simplify this stage (see section 4.1). A density of 93 % was produced but was of a lower density than that in the literature (> 95 %). XRD patterns revealed the presence of second phase Sr modified $NaNbO_3$, in line with the prior reports but at higher values (6 wt.% compared to 3 wt.%). The permittivity response at 1 kHz was of a similar nature to published work, with a high (T_2) and a low (T_1) temperature dielectric anomaly, the high temperature (T_2) representing the ferroelectric to paraelectric phase transition (Curie peak). However, the absolute permittivity values were higher for both peaks than in those prior reports, with T_1 at 1710 compared to approximately 1200, and T_2 at 2150 compared to approximately 1450 (Garcia-Gonzalez, 2007, Torres-Pardo, 2011). The temperatures of these peak maxima were also found to be higher than the prior reports with T_1 at -15 ^oC compared to -20 ^oC, and T_2 at 310 ^oC compared to 250 ^oC. The higher temperature value of T_2 in the current sample resulted in a superior

permittivity variation over the temperature range -55 to 300 ^{o}C, +/- 22 % compared to the prior report of +/- 30 %. Although un-modified SNN met the R-type EIA specification required for high temperature capacitor material from -55 to 250 ^{o}C, a similar response up to 300 ^{o}C is desired for use in power electronic applications using wide-bandgap semiconductors, where the high switching speeds involve passive and active components to be in close proximity (Case for Support for EPSRC grant EP/V053361/1https://gow.epsrc.ukri.org/NGBOViewGrant.aspx?GrantRef=EP/V053361/1) . An investigation into doping SNN with Ca^{2+}, Y^{3+}, and Zr^{4+} was therefore undertaken in an attempt to flatten the permittivity further through induced chemical heterogeneity.

4.3 Calcium modified strontium sodium niobate (SCNN) with Y^{3+} and Zr^{4+} doping (SCNN-YZ)

Compositions of $Sr_{2-x-y}Ca_xY_yNaNb_{5-y}Zr_yO_{15}$ (SCNN-YZ) were made with constant x = 0.025 or 0.05 and increasing levels of dopant y = 0, 0.025, and 0.05 to investigate the effect of increasing Y^{3+} and Zr^{4+} doping combined with calcium modification (Ca^{2+} was added to equalize the peak ε_r values of the two dielectric anomalies in SNN (T_1 and T_2), see section 4.1: the effect of Ca^{2+} on SCNN dielectric properties was briefly investigated and found to be in general agreement with prior reports, Figure 4.3.1). Fabrication of all samples was carried out using the methodology outlined in Chapter 3, unless stated otherwise. Most samples were sintered at 1300 ^{o}C as standard although some required a temperature of 1350 ^{o}C to achieve appropriately dense samples (target density ≥ 93 %). Composition x = 0.025, y = 0.025 was sintered at both temperatures by way of a direct comparison.

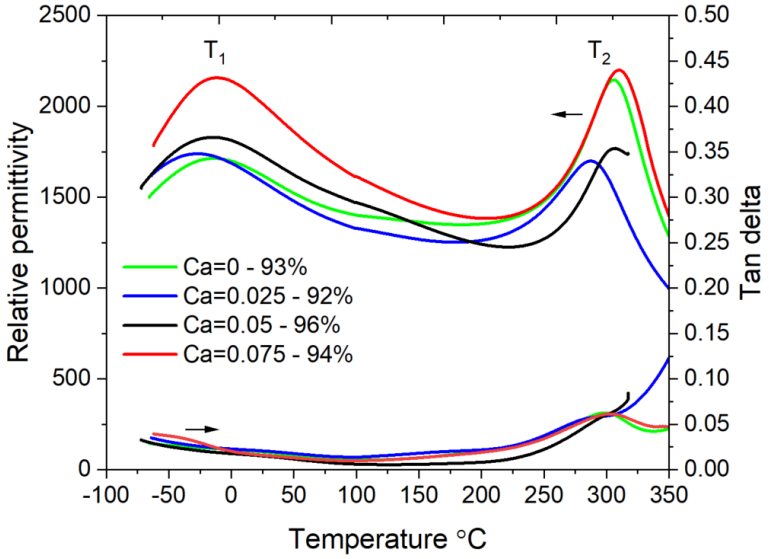

Figure 4.3.1. 1 kHz comparison of permittivity and dielectric loss for $Sr_{2-x}Ca_xNaNb_5O_{15}$ with Ca^{2+} additions of x=0, 0.025, 0.05, and 0.075. Composition x=0.05 has a permittivity variation of +/- 20 % from -55 to 300 °C (Figure legend includes percentage theoretical densities of sintered pellets).

4.3.1 Phase analysis

Room temperature, 12 h X-ray powder diffraction plots were produced and found to show similar phases to unmodified SNN (Figure 4.2.1) for most compositions. Figure 4.3.2 a-b show the patterns for $Sr_{2-x-y}Ca_xY_yNaNb_{5-y}Zr_yO_{15}$ with x = 0.025, y = 0, and x = 0.05, y = 0.05 respectively. Patterns for all compositions were indexed to tetragonal *P4bm* space group (ICDD 04-008-7203), and were found to match the reference file within 0.1 °2θ for y = 0 to 0.05 for both levels of x. Hence there was no measurable change in lattice parameters. Reports in the literature (Wei et al. 2012, and Xie et al. 2002 (1 and 2)) found that the addition of Ca^{2+} either decreased the unit cell parameters and cell volume (Xie et al. 2002 1 and 2), or increased *a,* whilst reducing the other parameters (Wei et al. 2012). This was seen at dopant levels x = 0.05 to 0.35 and suggests that the low levels presented here (x = 0.025 and 0.05) were not high enough to have a significant effect.

Second phase Sr modified $NaNbO_3$ was present, and composition x = 0.05, y = 0.05 showed impurity peaks possibly matching ZrO_2, reference file ICDD 00-037-1484, within ~0.1 °2θ.

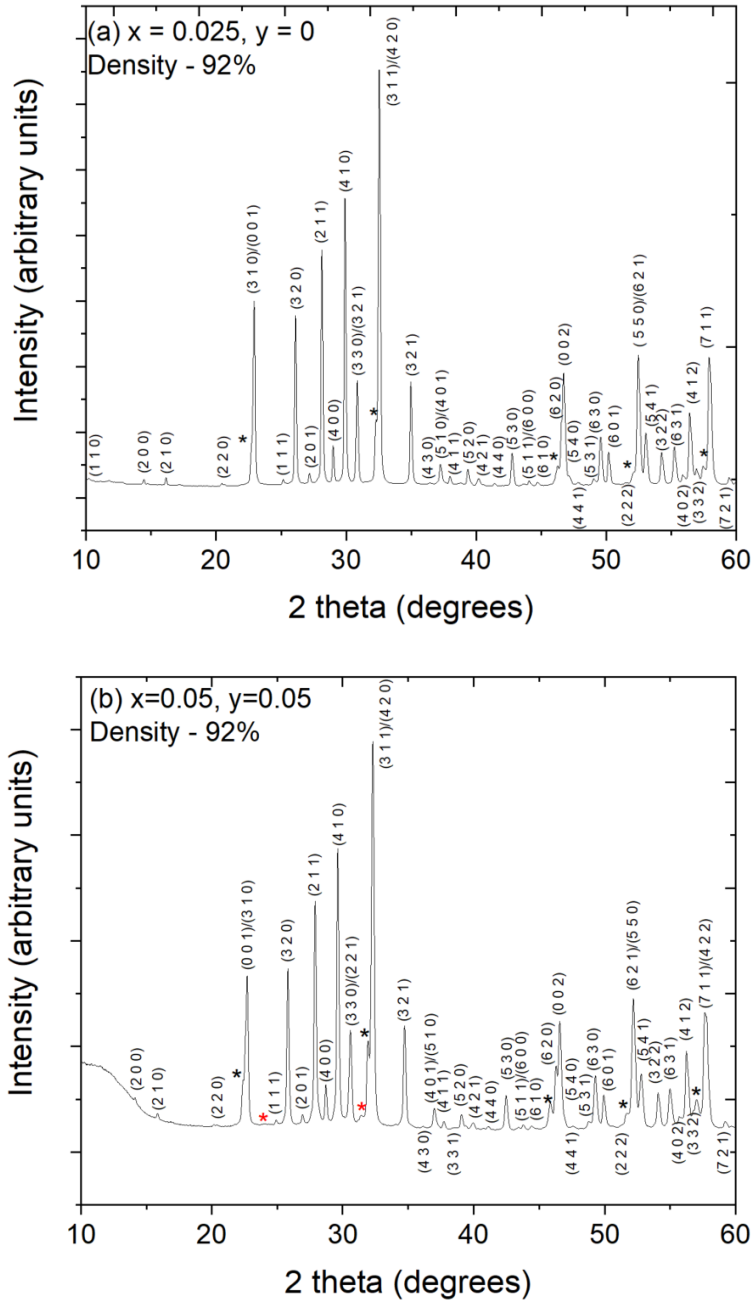

Figure 4.3.2 a-b. 12 h powder XRD plots of $Sr_{2-x-y}Ca_xY_yNaNb_{5-y}Zr_yO_{15}$ with a) x = 0.025, y = 0, b) x = 0.05, y = 0.05. Indexed to ICDD 04-008-7203, tetragonal SNN, *P4bm*. Second phase Sr modified $NaNbO_3$ (*) was present in all samples (ICDD 04-009-3239). Evidence of second phase ZrO_2 (*) was found in composition x = 0.05 and y = 0.05 (ICDD 00-037-1484).

Unit cell refinements were performed for *P4bm* with R_{WP} fitting errors between 13 and 16 %. Higher values were expected since the standard SNN pattern was a different composition to the experimental composition, but the value is recorded as a

figure of merit. The crystallographic data are summarised in Table 4.3.1. Geometric densities of the sample pellets were measured to be between 92 and 96 % of theoretical density. The theoretical density was estimated from lattice parameters obtained by XRD and the nominal composition. At x = 0.025 the geometric density remained relatively constant with a maximum of 95 % at y = 0.025. At x = 0.05, density decreased with increasing y from 96 % at y = 0 to 92 % at y = 0.05, although further work would be required to determine if this a general trend due to doping or a consequence of processing differences. The proportion of second phase Sr modified $NaNbO_3$ was found to be 5-7 wt.% for x = 0.025 compositions, with 7 wt.% seen in x = 0.05 compositions, with the exception of y = 0.025 at 3 wt.%. In addition to this composition x = 0.05, y = 0.05 contained ZrO_2 second phase at 1.5 wt.% (Figure 4.3.2 b, confirmed by SEM-EDX, Figure 4.3.10)

The unit cell parameters derived from the HighScore refinement showed no conclusive change in lattice parameters, except possibly for x = 0.05, y = 0.05 for which there was a slight contraction in cell volume. A robust full pattern refinement (Y Li, University of Manchester) for SNN and for compositions x = 0.025, y = 0.025 and x = 0.05, y = 0.05 pointed to a very slight reduction in unit cell volume (Brown et al. 2020).

Composition x = 0.025, y = 0.025, sintered at 1350 ^oC (not shown in Table 4.3.1) showed similar lattice parameters (*a*,*b* = 12.35 Å, *c* = 3.890 Å) and was the same density (95 %) as the same composition sintered at 1300 ^oC (Table 4.3.1). The unit cell volume at 1350 ^oC was slightly reduced to 593.3 $Å^3$, from 595.5 $Å^3$ at 1300 ^oC, or could be unchanged and the determined value gives an indication of the level of uncertainty in the measurements (+/- 2 $Å^3$). Second phase Sr modified $NaNbO_3$ was present at similar levels of 6 to 6.5 wt. %.

Table 4.3.1. Crystallographic data for $Sr_{2-x-y}Ca_xY_yNaNb_{5-y}Zr_yO_{15}$ (x = 0.025, y = 0, 0.025, 0.05 and x = 0.05, y = 0, 0.025, 0.05) from X-ray powder diffraction unit cell refinements. Unmodified SNN is also included.

Composition	*a* = *b* Å	*c* Å	Volume Å^3	Geometric density g/cm^3	Percentage theoretical density	Tetragonality c/a	2nd phase wt.%	R_{WP} %
SNN	12.37	3.896	596.2	4.68	93 %	0.31	5.8 $NaNb0_3$	11.5
x = 0.025 y = 0 (sintered 1300 ^oC)	12.36	3.894	594.9	4.61	92 %	0.32	5.3 $NaNb0_3$	13.9
x = 0.025 y = 0.025 (sintered 1300 ^oC)	12.37	3.892	595.5	4.81	95 %	0.31	6.1 $NaNb0_3$	14.8
x = 0.025 y = 0.05 (sintered 1300 ^oC)	12.37	3.891	595.4	4.69	92 %	0.31	6.3 $NaNb0_3$	16.2
x = 0.05 y = 0 (sintered 1350 ^oC)	12.36	3.896	595.2	4.84	96 %	0.32	6.7 $NaNbO_3$	13.5
x = 0.05 y = 0.025 (sintered 1350 ^oC)	12.36	3.892	594.6	4.71	93 %	0.31	3.1 $NaNb0_3$	13.4
x = 0.05 y = 0.05 (sintered 1300 ^oC)	12.35	3.883	592.2	4.67	92 %	0.31	7.2 $NaNb0_3$ 1.4 ZrO_2	12.7

4.3.2 Dielectric analysis

Figure 4.3.3 a-g shows the temperature dependence of the relative permittivity and loss tangents for $Sr_{2-x-y}Ca_xY_yNaNb_{5-y}Zr_yO_{15}$ with x = 0.025, y = 0, 0.025, 0.05 and x = 0.05, y = 0, 0.025, 0.05, respectively. Frequencies of 1 kHz, 10 kHz, 100 kHz, and 1 MHz were measured and data are summarised in Table 4.3.2. High and low temperature dielectric anomalies were seen in all compositions with T_1 exhibiting relaxor character by moving to higher temperature with increasing frequency.

A 1 kHz comparison plot for both sets of samples are shown in Figure 4.3.4 a-b. Dielectric data for these samples are summarised in Table 4.3.2. Increasing y led to the suppression of the T_2 peak, with ε_r values dropping from 2150 for unmodified SNN (93 % density), to 1700 at y = 0 (92 %), through 1580 at y = 0.025 (95 %), to 1490 at y = 0.05 (92 %) (x = 0.025). At x = 0.05 T_2 dropped to 1770 at y = 0 (96 %), through 1450 at y = 0.025 (93 %), then 1310 at y = 0.05 (92 %). No similar trend was shown in T_1 peak ε_r values, although lower intensities (1430) were seen at the highest doping levels (x = 0.05, y = 0.05) (Table 4.3.2). It was unclear whether this variation in T_1 intensity was an effect of density, doping, or a combination of the two.

For compositions with x = 0.025 the temperature of the T_1 and T_2 peaks showed no consistent change with doping. For compositions with x = 0.05, the T_1 and T_2 peak temperatures remained constant from unmodifed SNN (T_1 -15 ^{o}C, T_2 306 ^{o}C) to SCNN (x = 0.05, y = 0) (T_1 -15 ^{o}C, T_2 307 ^{o}C). Further doping with Y^{3+} and Zr^{4+} at x = 0.05 displayed a decrease in both T_1 and T_2 temperature at y = 0.025 (T_1 -31 ^{o}C, T_2 277 ^{o}C), and y = 0.05 (T_1 -49 ^{o}C, T_2 254 ^{o}C) (Table 4.3.2).

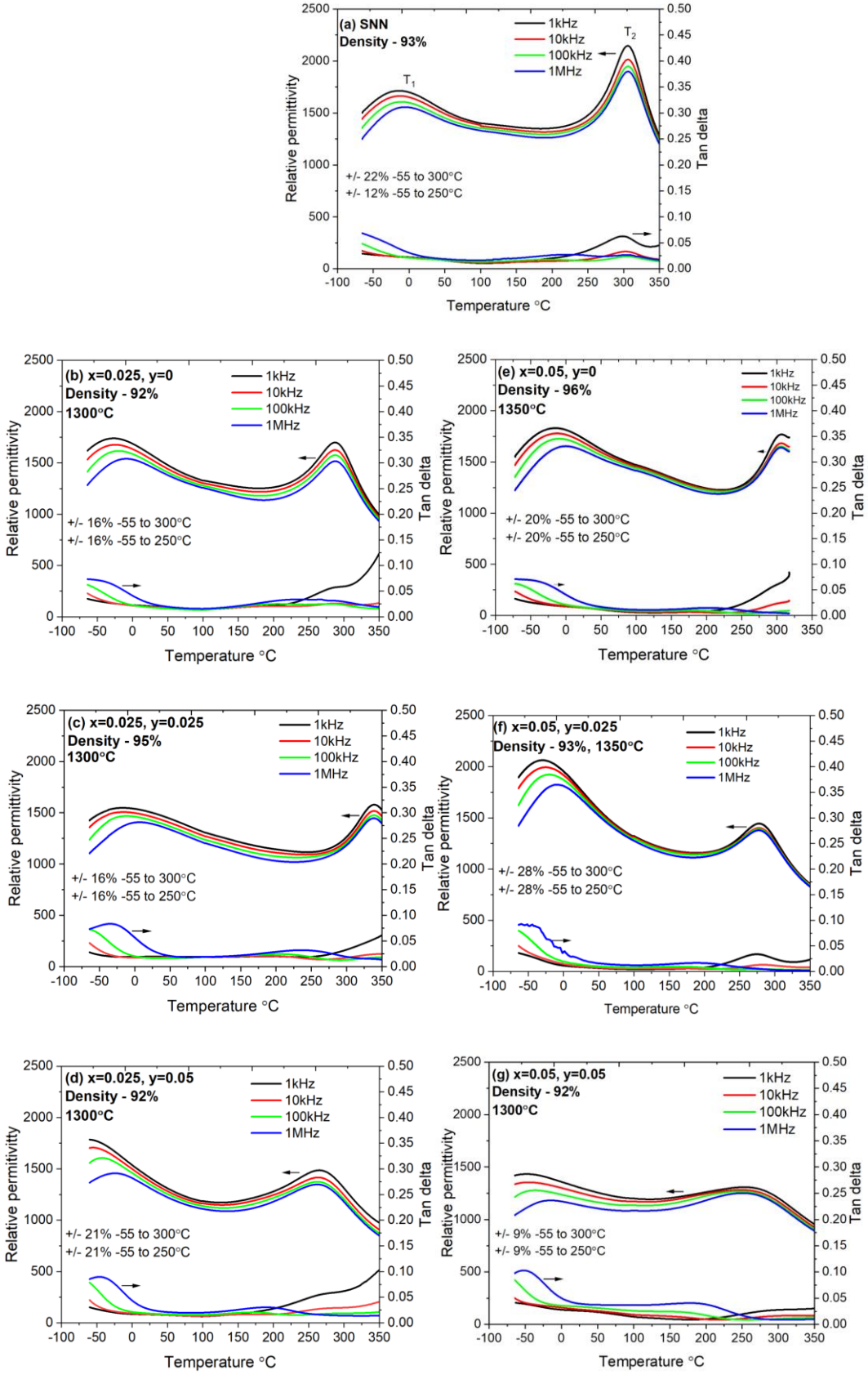

Figure 4.3.3 a-g. Multi-frequency relative permittivity and dielectric loss tangent versus temperature plots showing relative permittivity variation for $Sr_{2-x-y}Ca_xY_yNaNb_{5-y}Zr_yO_{15}$ a) x =

0, y = 0 (SNN), b) x = 0, y = 0.025, c) x = 0.025, y = 0.025, d) x = 0.025, y = 0.05, e) x = 0.05, y = 0, f) x = 0.05, y = 0.025, g) x = 0.05, y = 0.05.

The permittivity variation response for compositions with x = 0.025 and 0.05 fluctuated with increasing doping, although was generally lower than unmodified SNN from -55 to 300 °C. A substantial drop to +/- 9 % for temperature ranges -55 to 300 °C and -55 to 250 °C was not seen until the highest doping level was reached (x = 0.05, y = 0.05). Unmodified SNN showed values of +/- 22 % and +/- 12 % for these temperature ranges respectively (Table 4.3.2).

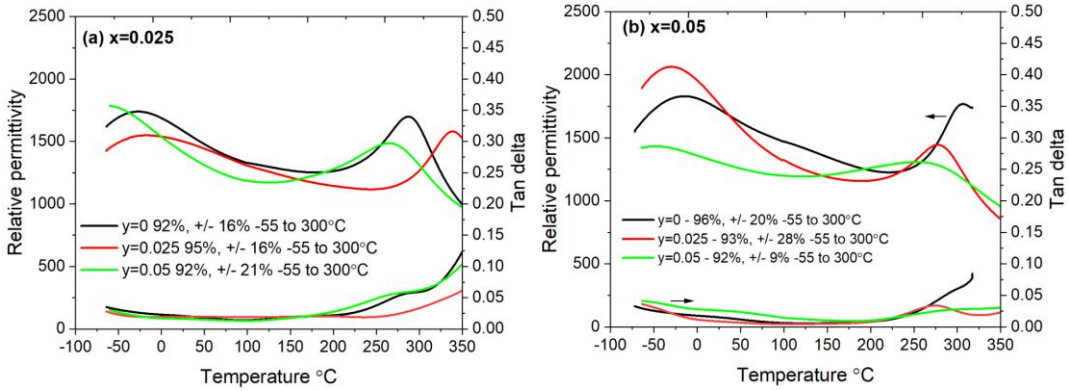

Figure 4.3.4 a-b. 1 kHz relative permittivity and dielectric loss tangent versus temperature plots for $Sr_{2-x-y}Ca_xY_yNaNb_{5-y}Zr_yO_{15}$ with a) x = 0.025, y = 0, 0.025, 0.05, and b) x = 0.05, y = 0, 0.025, 0.05.

The low-field dielectric loss tangents at 1 kHz are presented in Table 4.3.2 and show that 1 kHz tan δ increases to above 0.025 > ~250 °C. At x = 0.025, y = 0.025 the values were ≤ 0.035 -65 to 304 °C, whilst x = 0.05, y = 0.025 was ≤ 0.035 from -60 to 350 °C, and x = 0.05, y = 0.05 was ≤ 0.035 from -34 to 378 °C.

Table 4.3.2. 1 kHz relative permittivity and loss tangents versus temperature data for $Sr_{2-x-y}Ca_xY_yNaNb_{5-y}Zr_yO_{15}$ with x = 0.025 and x = 0.05 and increasing amounts of y.

Composition	T_1 °C ($\varepsilon_{r\ max}$)	T_2 °C ($\varepsilon_{r\ max}$)	+/- % (-55 - 250°C)	+/- % (-55 - 300°C)	tan δ ≤0.025 °C	tan δ ≤0.030 °C	tan δ ≤0.035 °C
SNN	-15 (1714)	306 (2146)	12 %	22 %	-32 - 223	-65 - 238	-65 - 249
x = 0.025 y = 0 density 92 %	-27 (1740)	287 (1699)	16 %	16 %	-20 to 220	-49 to 235	-63 to 244
x = 0.025 y = 0.025 density 95 %	-18 (1549)	339 (1580)	16 %	16 %	-57 to 278	-65 to 293	-65 to 304
x = 0.025 y = 0.05 density 92 %	-60 (1785)	264 (1486)	21 %	21 %	-44 to 190	-60 to 208	-60 to 220
x = 0.05 y = 0 density 96 % (sintered 1350 °C)	-15 (1830)	307 (1769)	20 %	20 %	-47 to 254	-67 to 263	-72 to 269
x = 0.05 y = 0.025 density 93 % (sintered 1350 °C)	-31 (2063)	277 (1445)	28 %	28 %	-36 to 249, 299 to 350	-48 to 259, 288 to 350	-60 to 350
x = 0.05 y = 0.05 density 92 %	-49 (1433)	254 (1308)	9 %	9 %	38 to 276	-13 to 345	-34 to 378

Composition x = 0.025, y = 0.025 was sintered at 1300 °C and 1350 °C for comparison. Figure 4.3.5 shows the 1 kHz relative permittivity and dielectric loss tangent versus temperature plots for the composition under diffrerent sintering conditions. The density was found to be identical for both sintering temperatures (95 %), as were T_1 and T_2 temperature (-18 °C and 340 °C respectively). Relative permittivity variation was +/- 16 % for both sintering temperature and dielectric losses were similar across both temperature ranges (-55 to 300 °C and -55 to 250 °C). This result gives a reasonable indication of the reproducability of the ceramics using this fabrication method. The main difference was the absolute values of ε_r were approximately 300 higher for the 1350 °C sample, possibly related to differing microstructure due to thermal history (Section 4.3.4).

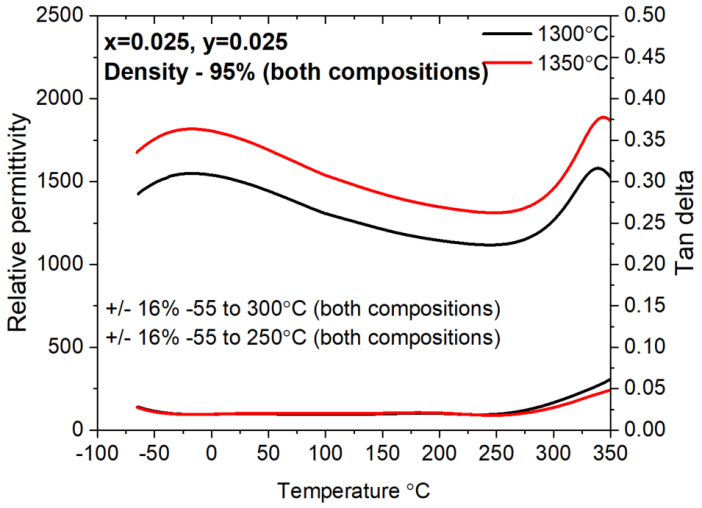

Figure 4.3.5. 1 kHz relative permittivity and dielectric loss tangent versus temperature plots for $Sr_{2-x-y}Ca_xY_yNaNb_{5-y}Zr_yO_{15}$ with x = 0.025, y = 0.025 sintered at 1300 °C and 1350 °C.

4.3.3 Ferroelectric analysis

Typical ferroelectric P-E hysteresis loops for SNN and $Sr_{2-x-y}Ca_xY_yNaNb_{5-y}Zr_yO_{15}$ with x = 0.025, y = 0, 0.025, 0.05 and x = 0.05, y = 0, 0.025, 0.05 are shown in Figure 4.3.6 a-b. Measurements were taken up to 40 kV cm^{-1} (composition x = 0.05, y = 0 suffered dielectric breakdown at 35 kV cm^{-1} so values shown are lower than expected). Maximum polarisation (P_{max}), remnant polarisation (P_r) and coercive field (E_c) data are summarised in Table 4.3.3. Figure 4.3.5 a-b clearly illustrate ferroelectricity in SCNN and SCNN-YZ ceramics, but with less saturation than unmodified SNN. Higher values of P_{max} is generally regarded to be related to increased maximum relative permittivity at T_2 (Li et al. 2020). This trend was observed with maximum polarisation in SNN (P_{max} 13 µC cm^{-2}, T_2 ε_r 2150) decreasing with doping to x = 0.025, y = 0.05 (P_{max} 8 µC cm^{-2}, T_2 ε_r 1490), and x = 0.05, y = 0.05 (P_{max} 8 µC cm^{-2}, T_2 ε_r 1310). Residual polarisation (P_r) also decreased with increasing doping with the exception of composition x = 0.025, y = 0.025, where an increase was seen. Values fell from 5.5 µC cm^{-2} for SNN to 3 µC cm^{-2} at x = 0.025, y = 0.05, and 2.5 µC cm^{-2} at x = 0.05, y = 0.05. Values of E_c increased from unmodified SNN (12 kV cm^{-1}) to between 13 and 16 kV cm^{-1}. The exception was composition x = 0.05, y = 0.05 where the value decreased to 11 kV cm^{-1}.

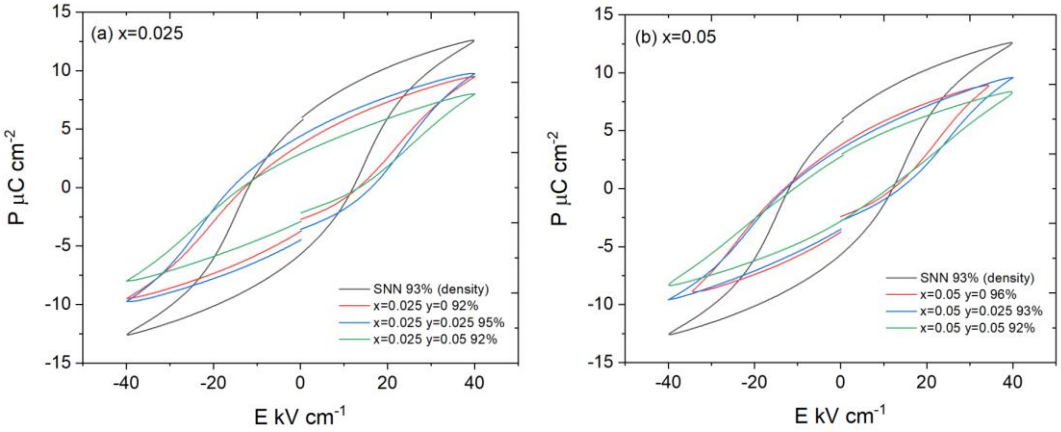

Figure 4.3.6. a-b. Polarisation – electric field loop plots at 40 kV cm^{-1} for $Sr_{2-x-y}Ca_xY_yNaNb_{5-y}Zr_yO_{15}$ with a) x = 0.025, y = 0, 0.025, and 0.05, b) x = 0.05, y = 0, 0.025, and 0.05. Unmodified SNN is also shown on both plots.

Table 4.3.3. Remnant polarisation (P_r) and coercive field (E_c) data at 40 kV cm^{-1} for $Sr_{2-x-y}Ca_xY_yNaNb_{5-y}Zr_yO_{15}$ with x = 0.025 and 0.05, and y = 0, 0.025 and 0.05. Unmodified SNN is also shown.

Composition	P_r µC cm^{-2} (+/- 0.5)	E_c kV cm^{-1} (+/- 0.5)	P_{max} µC cm^{-2} (+/- 0.5)
SNN (density 93 %)	5.5	12	13
x = 0.025, y = 0 (density 92 %)	3.5	13	9.5
x = 0.025, y = 0.025 (density 95 %)	4.5	16	9.8
x = 0.025, y = 0.05 (density 92 %)	3.0	14	8.0
x = 0.05, y =0 (density 96 %) (sintered 1350 °C) P-E loop only up to 35 kV cm^{-1}	3.8	12.5	9.0
x = 0.05, y = 0.025 (density 93 %) (sintered 1350 °C)	3.5	14	9.5
x = 0.05, y = 0.05 (density 92 %)	2.5	11	8.0

P-E loop for composition x = 0.025, y = 0.025 sintered at 1350 °C is shown in Figure 4.3.7 alongside that of the 1300 °C version. The plots are similar in appearance with the 1350 °C sample having a higher P_{max} than the 1300 °C (12 µC cm^{-2} compared to 10 µC cm^{-2}). This possibly reflects the higher relative permittivity observed in this sample (Figure 4.3.5). The 1350 °C sample showed a slightly lower P_r (4 µC cm^{-2}), whilst E_c remained constant at 16 Kv cm^{-1}.

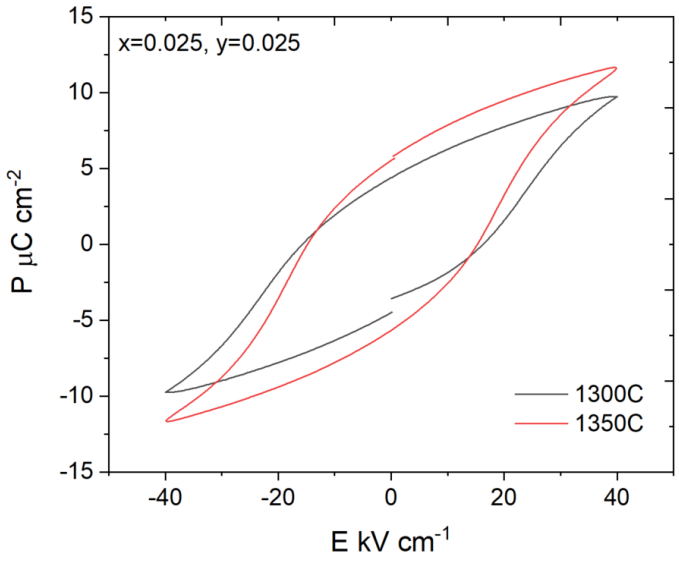

Figure 4.3.7. Polarisation – electric field loop plots at 40 kV cm^{-1} for $Sr_{2-x-y}Ca_xY_yNaNb_{5-y}Zr_yO_{15}$ with x = 0.025, y = 0, 0.025, sintered at 1300 °C and 1350 °C.

4.3.4 Microstructural analysis

Back scattered scanning electron micrographs showed similar phases to those present in unmodified SNN (Figure 4.3.8 a, and Section 4.2, Figures 4.2.6 and 4.2.7) for most compositions (Figure 4.3.8 b-e), with darker Na^+ rich grains corresponding to second phase $NaNbO_3$ seen in XRD patterns (Figure 4.3.2) confirmed by SEM-EDX mapping (Figure 4.3.9). Sr^{2+} was possibly present in these areas but detection could be the result of the X-ray interaction volume extending to material below the visible grain. The Ca^{2+}, Y^{3+}, and Nb^{5+} was seen to be homogenously distributed throughout each relevant material. No evidence of elemental gradation within grains was shown by SEM-EDX analysis for any of the compositions. Composition x = 0.05, y = 0.05 (Figure 4.3.8 e) also, uniquely, contained smaller white grains of approximately 1 to 2 µm. SEM-EDX mapping (Figure 4.3.9) revealed these to be Zr from ZrO_2, as identified in the XRD pattern (Figure 4.3.2 b). These grains were often associated with micro cracking around the perimeter, and affecting the surrounding structure.

Maximum grain size in all the compositions was similar, being 17 µm in SNN (Figure 4.3.8 a), 15 µm in x = 0.025 (b), and 20 µm in x = 0.05, x = 0.025 y = 0.025, and x = 0.05 y = 0.05 (c-e). An approximation of the majority of grains however,

showed that grain size increased from SNN (~2 to 4 µm) with the addition of Ca^{2+} to x = 0.025 (~3 to 9 µm) and x = 0.05 (~5 to 12 µm). A slight decrease was then seen with the addition of Y^{3+}/Zr^{4+} to x = y = 0.025 (1 to 5 µm) and x = y = 0.05 (3 to 9 µm)

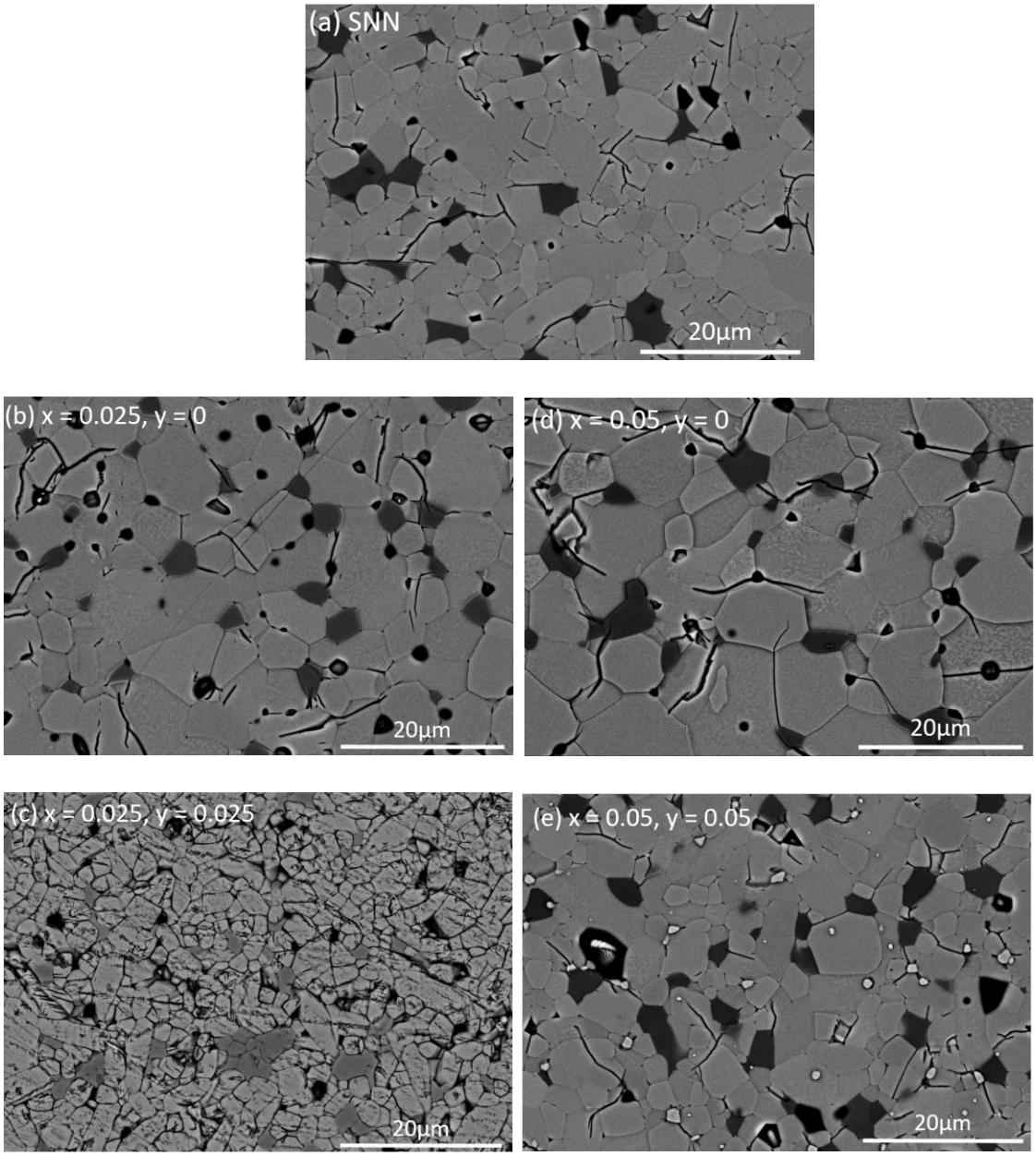

Figure 4.3.8. Back scattered electron images of a) unmodified SNN, b) x = 0.025, y = 0, c) x = 0.025, y = 0.025, d) x = 0.05, y = 0, e) x = 0.05, x = 0.05.

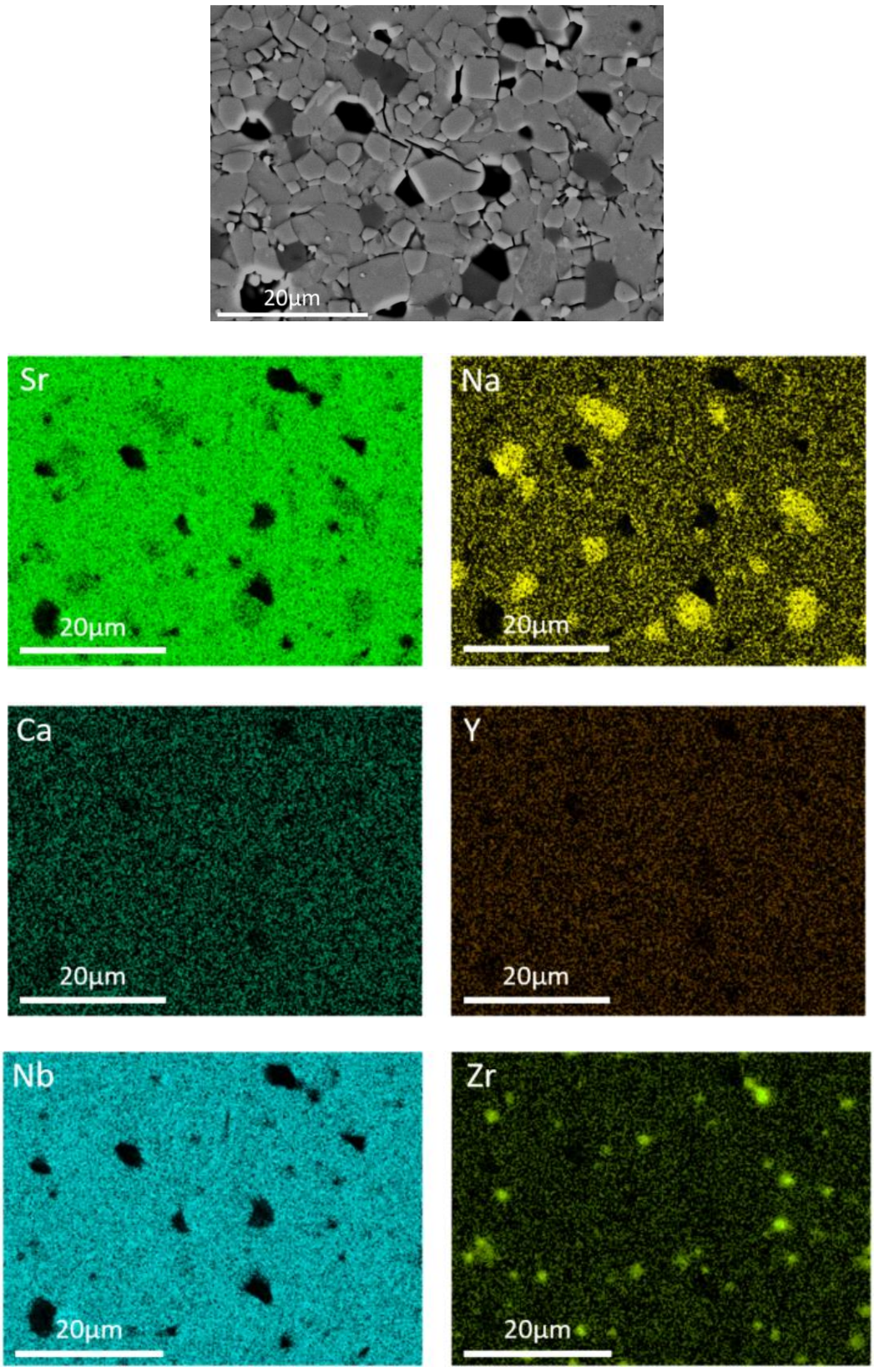

Figure 4.3.9. Back scattered electron images of $Sr_{2-x-y}Ca_xY_yNaNb_{5-y}Zr_yO_{15}$ with x = 0.05, y = 0.05 showing grains up to 10 µm and darker sodium rich/strontium deficient grains. Small grains of unreacted ZrO_2 are also present. EDX mapping confirms sodium enrichment and presence of Zr.

Composition x = 0.025, y = 0.025 (sintered 1350 ◦C, Figure 4.3.10) contained abnormal grains of up to 25 µm, although generally most grains were smaller than this. Overall, the average grain size appeared larger than the 1300 ◦C sample and the grains were rounder in appearance, raising the possibility of a liquid phase being present at the higher sintering temperature

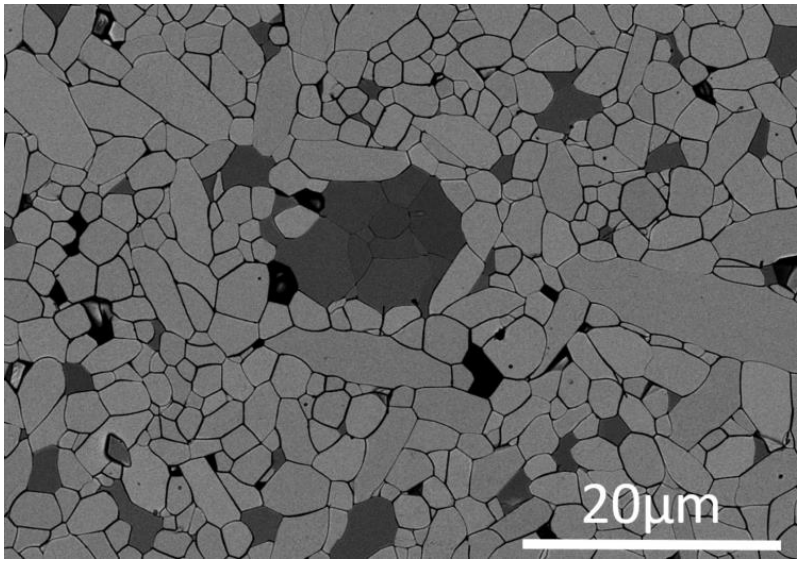

Figure 4.3.10. Back scattered electron image $Sr_{2-x-y}Ca_xY_yNaNb_{5-y}Zr_yO_{15}$ with x = 0.025, y = 0.025 (1350 ºC) showing large grains of up to ~25 µm. Grains are generally larger than 1300 ºC sample (Figure 4.3.7 c) and more rounded.

4.3.5 Summary: Calcium modified strontium sodium niobate (SCNN) with Y^{3+} and Zr^{4+} doping (SCNN-YZ)

Dense $Sr_{2-x-y}Ca_xNaY_yZr_yNb_{5-y}O_{15}$ formulations were made with x=0.025 and 0.05, and y = 0, 0.025, 0.05. Unmodified SNN and two optimised doped compositions (x = 0.025, y = 0.025 (sintered 1350 ºC), and x = 0.05, y = 0.05) were taken forward for publication on the basis of their relative permittivity response from -55 to 300 ºC (Brown et al. 2020). Due to the fact the levels of Ca^{2+} and Y^{3+}/Zr^{4+} were equal in both these compositions, they were referred to as z = 0.025 and z = 0.05 in the publication (See Appendix B).

Geometric densities were found to be between 92 and 96 % of the calculated theoretical density. Because of this broad range of densities, it was recognised that its role in determining the electrical properties of the materials could not be resolved. Second phase $NaNbO_3$ was present in all compositions between 3 to 8 %, as was expected from the literature, although it was possible this was Sr modified $NaNbO_3$ ($Sr_{2+x}Na_{1-2x}Nb_5O_{10}$) as identified by Garcia-Gonzalez (2007) and Torres-Pardo (2011). ICDD reference files for $NaNbO_3$ and $Sr_{0.25}Na_{0.5}NbO_3$ are virtually identical, reinforcing the fact that they are difficult to distinguish by X-ray diffraction at these second phase levels. In addition to this, 1.5 % ZrO_2 was found in composition x = 0.05, y = 0.05 but not in the corresponding x = 0.025, y = 0.05 composition. There was a broad trend of second phase Sr modified $NaNbO_3$ increasing with increased doping, from approximately 5.5 % in unmodified SNN and x = 0.025, y = 0, to ~7 % in x = 0.05, y = 0.05, which was the only composition to also contain ZrO_2 (~1.5 %). Unit cell volume was seen to decrease in doped samples in comparison to unmodified SNN (596.2 $Å^3$), due to substitution by smaller cations (Ca^{2+}, 1.34 Å) onto Sr^{2+} (1.44 Å), dropping to ≤ 595.5 $Å^3$ at x = 0.05, y = 0.05, although the change was not thought to be significant. The ratio of c/a was constant across all samples at approximately 0.3. A rigorous, full Rietveld refinement was performed (Y Li, University of Manchester, Brown et al. 2020) on compositions used in the publication Brown et al. 2020 but the interpretation did not change from the work carried out in this study. No evidence was seen of weak extra super-lattice reflections, identified by others by electron diffraction and assigned an orthorhombic unit cell (space group *Im2a,* Garcia-Gonzalez, 2007 and Torres-Pardo, 2011). The lack of distinct supercell reflections by powder X-ray diffraction was the reasoning for indexing on tetragonal axes on the basis of space group *P4bm* (Table 4.3.1). The true crystal symmetry of SNN will require future detailed study using electron and neutron diffraction.

The relative permittivity versus temperature response for all the compositions displayed two dielectric peaks (Figure 4.3.2 a-g) for tungsten bronze $Sr_{2-x-y}Y_yNaNb_{5-y}Z_yO_{15}$, as was the case for unmodified SNN. The higher temperature dielectric peak is denoted T_2 (at 306 ◦C for SNN, 1 kHz). This dielectric anomaly is reported by others to correspond to the formation, on cooling, of a supercell which induces ferroelectric behaviour: hence T_2 represents the Curie point (Torres-Pardo et al. 2011). Structural correlations are less well understood in the context of the lower

temperature dielectric peak T_1, which occurs at -15 ◦C in SNN (1 kHz) and shows frequency dispersion similar to a relaxor ferroelectric. An accompanying change in thermal expansion coefficient for related tungsten bronzes implies that the T_1 peak corresponds to a ferroelastic transition, but no associated structural deviations have been detected (Zhu et al. 2015).

The addition of dopants to unmodified SNN generally showed a reduction in relative permittivity variation from -55 to 300 ºC, from +/- 22 % to +/- 16 % (x = 0.025, y = 0.025) and +/- 9 % (x = 0.05, y = 0.05). The variation for unmodified SNN was regarded to be due to the disparity in ε_r values of the T_1 (1710) and T_2 (2150) peaks in the SNN sample (Figures 4.2.3 and 4.2.4). Results suggested that a lower relative permittivity variation could be achieved if the T_1 and T_2 peaks were of similar ε_r values (achieved through Ca^{2+} doping, see Figure 4.3.1). This could also be aided by T_2 being pushed to higher temperatures (~300 ºC).

The T_2 peak showed a clear suppression of ε_r with increased doping from SNN (2150) through to x = 0.025, y = 0.05 (1490), and x = 0.05, y = 0.05 (1310), brought about in part by increased broadening of T_2. The anomaly appeared to become significantly more diffuse as the level of substitution increased. The $\varepsilon_{r\,max}$ of T_2 in x = 0.05, y = 0.05 was approximately 60 % that of unmodified SNN and the full width at half maximum (FWHM) of the T_2 peak spanned approximately 44 ºC and 97 ºC for SNN and x = 0.05, y = 0.05 respectively.

Temperature of the T_2 peak with the addition of dopants was generally similar or higher to that of SNN (306 ºC), rising to 345 ºC in x = 0.025, y =0.025 (sintered 1350 ºC). This changed at the highest doping level of x = 0.05, y = 0.05 where T_2 was displaced to 255 ºC, around 90 ºC lower. This non-monotonic shift of T_2 with higher doping indicates a complex interplay between dopant level and temperature of the dielectric anomalies which may well relate to alterations in defect structures (possibly affecting NbO_6 tilts in the case of T_2).

T_1 showed no clear trends, reflective of the fact that this is a poorly understood phenomenon thought to be related to a ferroelastic transition in these materials. T_1 only undergoes any significant suppression at the maximum doping level of x = 0.05, y = 0.05. Here it underwent a qualitative increase in broadening, but less so than for T_2. For x = 0.025, y = 0.025 there was an increase in frequency

dispersion in comparison to SNN, with a difference in temperature of T_1 between frequencies 1 kHz and 1 MHz of 25 ^{o}C compared to 10 ^{o}C respectively.

The presence of zirconia secondary phase in the microstructure may at least in-part account for the drop in ε_r value at 25 $^{\circ}$C for x = 0.05, y = 0.05 (compared to x = 0.025, y = 0.025) but matrix strain effects consequent on transformation from tetragonal to monoclinic zirconia (on cooling from sintering temperatures) are thought unlikely, given the non-optimised sample density (92–93 % theoretical).

Dielectric loss tangents at 1 kHz all increased at higher temperatures (~ > 250 ^{o}C) (Figure 4.3.2). Initially this is due to the ferroelectric to paraelectric phase transition creating losses as ions realign themselves (polarisation rotation and domain wall motion). After this the losses drop slightly, followed by an increase through increased mobility of charge carriers at higher temperatures leading to increased polarisation. The effect is lessened at higher frequencies as some polarisation mechanisms begin to lag behind the field, and so decrease the dielectric loss. This effect generally showed improvement with increased Y^{3+}/Zr^{4+} doping, with values at 1 kHz of ≤ 0.06 for unmodified SNN (Table 4.2.2) and x = 0.025 and 0.05, y = 0 (-55 to 300 ^{o}C) (Table 4.3.2). These reduced to either ≤ 0.03 or ≤ 0.04 for all compositions with Y^{3+}/Zr^{4+} doping (Table 4.3.2).

The P-E hysteresis loops for all of the compositions studied were generally similar in appearance and showed clear evidence of ferroelectric character, as illustrated in Figure 4.3.5 a-b. This further supported the idea that the high temperature dielectric anomaly (T_2) represents the Curie point (T_C). The maximum polarisation (initially around 13 μC cm^{-2}) was reduced with increased doping, in line with a reduction of T_2 ε_r values. Values of remnant polarisation also generally decreased from that of SNN with increased doping (5.5 μC cm^{-2}). The coercive field values did not show a clear trend and were only slightly higher than SNN (12 kV cm^{-1}) with the addition of dopants, except for the highest levels at x = 0.05, y = 0.05 (11 kV cm^{-1}). Adding low quantities of dopants appeared to have a large effect on the maximum polarisation, whilst a small effect on the coercive field, indicating the mechanism of domain wall switching stayed the same. Additional polarisation analysis was reported in Brown et al. 2020 (undertaken by Hall, D. University of Manchester) and showed similar results to the above. Nonlinearity was observed in

the real and imaginary parts of the complex dielectric permittivity, departing from the classical Rayleigh Law. This nonlinearity was strongly suppressed in composition x = 0.05, y = 0.05, suggesting a reduced contribution to the electric field-induced polarisation from domain switching mechanisms, consistent with increasing atomic cation disorder.

Analysis of microstructures showed that all compositions contained similar phases to unmodified SNN (Figure 4.2.6 and 4.2.7) that were consistent with those found by XRD (Figure 4.3.2). This was also in agreement with the SNN metastable phase diagram (Chapter 2, Figure 2.8.4) which shows that stoichiometric formulations of SNN will contain second phase Sr modified $NaNbO_3$. The existence of secondary grains of sodium niobate and zirconia for the composition x = 0.05, y = 0.05 was identified in XRD patterns with grain sizes of ~ 5 µm and ~1 µm for each phase respectively (confirmed by the SEM-EDX analysis, Figure 4.3.9); there was also some evidence from EDX for the presence of Sr in the sodium niobate grains consistent with the phase diagram analysis of Tang et al. 1979 (Chapter 2, Figure 2.8.4). Cracking around ZrO_2 grains is possibly related to the increase in volume on cooling from a tetragonal to a monoclinic phase at about 1200 ^oC. No evidence was seen of elemental segregation, which would indicate a core-shell grain structure similar to that which gives a stable permittivity response in X7R $BaTiO_3$ based capacitor materials.

More detailed analysis by TEM-EDX (Aslam, Z. FIB section Harrington, J. University of Leeds) indicated an absence of core-shell grain structures and any form of elemental gradation within individual grains, plus confirmed the presence of Sr in sodium niobate grains and the possibility of Sr modified $NaNbO_3$ (Brown et al. 2020). Grain sizes were generally ≤ 12 µm for all compositions, including SNN, but the maximum grain sizes observed were larger, between 15 to 20 µm (Figure 4.3.8). Grains in unmodified SNN were generally 2 to 4 µm, with this increasing with the addition of Ca^{2+} to 3 to 9 µm (x = 0.025, y = 0) and 5 to 12 µm (x = 0.05, y = 0) (Figures 4.3.8 b and d). A reduction was then seen with the addition of Y^{3+} and Zr^{4+} with grains generally between 1 to 5 µm (x = 0.025, y = 0.025) and 2 to 9 µm (x = 0.05, y = 0.05) (Figures 4.3.8 c and e). The small grain size seen in composition x = 0.025, y = 0.025 was anomalous and would probably need to be remade before any conclusions are drawn from this.

In summary very low levels of chemical substitution of a tungsten bronze $Sr_{2-x-y}CaxY_yNaNb_{5-y}Zr_yO_{15}$ ferroelectric with Ca^{2+}, Y^{3+}, Zr^{4+} resulted in a significant change to low permittivity variation over a very large temperature range (+/- 9 % from -55 ^oC to 300 ^oC for x = 0.05, y = 0.05). Future fundamental studies of crystal structure and defect chemistry will be required to elucidate the exact reasons why such low levels of compositional modification by Ca^{2+}, Y^{3+} and Zr^{4+} bring about such a dramatic change in the permittivity response. However, even at this early stage it is possible to exclude core-shell microstructural mechanisms, of the type which convert perovskite $BaTiO_3$ into a X7R temperature stable dielectric. In addition to this, the reason is still to be resolved why compositions x = 0.025, y = 0.025 and x = 0.05, y = 0.05 are so flat. To begin to address this the individual effects of specific dopants will be examined in the next chapter.

Chapter 5. Further doping studies relating to $Sr_2NaNb_5O_{15}$ and characterisation of sodium deficient phase $Sr_{2.1}Na_{0.8}Nb_5O_{15}$

5.1 Introduction

Chapter 4 illustrated that low levels of chemical substitution of a tungsten bronze $Sr_2NaNb_5O_{15}$ ferroelectric with Ca^{2+}, Y^{3+}, Zr^{4+} (according to the formulation $Sr_{2-x-y}Ca_xY_yNaNb_{5-y}Zr_yO_{15}$) could produce a flat relative permittivity versus temperature response over a very wide temperature range (-55 to 300 ^oC), which is of potential relevance in the search for higher temperature capacitor materials. Despite this, the effects of each individual dopant was unknown and an issue persisted of second phase content in all compositions. Consequently, further investigations which form the basis of Chapter 5 are as follows

- The effect of A-site doping by partial substitution of Sr^{2+} by Y^{3+} in $Sr_{2-3x}Y_{2x}NaNb_5O_{15}$.
- The effect of B-site doping by partial substitution of Nb^{5+} by Zr^{4+} in $Sr_2NaNb_{5-4y}Zr_{5y}O_{15}$.
- $Sr_{2-x}Y_xNaNb_{5-y}Zr_yO_{15}$ was produced with equal amounts of Y^{3+} and Zr^{4+}; this composition is closely related to the flat permittivity sample $Sr_{2-x-y}Ca_xY_yNaNb_{5-y}Zr_yO_{15}$, described in Chapter 4 and Brown et al. 2020, but does not contain Ca^+ ions.
- The effect of A-site doping by partial substitution of Na^+ by Y^{3+} in $Sr_2Na_{1-3x}Y_xNb_5O_{15}$.
- Controlled deficiency in Na^+ content to eliminate a second phase and produce unfilled $Sr_{2.1}Na_{0.8}Nb_5O_{15}$ (SNN0.8) and associated doped compositions. Toward the end of this project the group became aware of the thermal instability of “filled” $Sr_2NaNb_5O_{15}$ (see Section 5.5, Figures 5.5.3 and 5.5.4 showing published phase diagrams). The range of solid solution $Sr_{2+x}Na_{1-2x}Nb_5O_{15}$ that are metastable at room temperature extends from approximately x = 0.05 to 0.2, meaning the stoichiometric composition lies outside the single phase region.

- Increasing A-site Na vacancies in SNN0.8 by partial substitution of Na^{+} by Y^{3+} in $Sr_{2.1}Y_xNa_{0.8-3x}Nb_5O_{15}$.

The primary goal was to identify the effect of each site dopant to investigate the likely effects of each on permittivity response in the initially studied multi-doped SNN: $Sr_{2-x-y}Ca_xY_yNaNb_{5-y}Zr_yO_{15}$ (see Chapter 4). A second purpose was to produce a single phase material. The assumption was made that these substitutions would take place due to similar sizes of ionic radii involved, and that the outcome of A-site substitution was expected to have a more substantial impact due to the larger size difference between Y^{3+} (1.075 Å, coordination 9) and Sr^{2+} (1.44 Å, coordination 12), being ~25 % smaller. Zr^{4+} (0.72 Å, coordination 9) on the other hand is closer in size to Nb^{5+} (0.68 Å, coordination 8), being only ~6 % larger (See Table 5.2.1 for cation radii and coordination numbers).

Table 5.1.1. Ionic radii of utilised cations with coordination numbers (Shannon, 1976).

Cation	Ionic radii (Coordination number)
Na^{+}	1.39 Å (12)
Sr^{2+}	1.44 Å (12)
Y^{3+}	1.075 Å (9)
Zr^{4+}	0.72 Å (6)
Nb^{5+}	0.64 Å (6)

5.2 Strontium sodium niobate (SNN) with single doping by yttrium (SNN-Y, Y^{3+} for Sr^{2+}) and single doping by zirconium (SNN-Z, Zr^{4+} for Nb^{5+})

Compositions of $Sr_{2-3x}Y_{2x}NaNb_5O_{15}$ (SNN-Y) were made with x = 0.0125 and 0.025 corresponding to Y^{3+} levels of 0.025 and 0.05 respectively, and $Sr_2NaNb_{5-4y}Zr_{5y}O_{15}$ (SNN-Z) were made with y = 0.01 and 0.02 corresponding to Zr^{4+} levels of 0.05 and 0.1 respectively. Note the as-formulated solid solution $Sr_2NaNb_{5-4y}Zr_{5y}O_{15}$ would require 20 % of the added Zr ions to occupy a non-B-site, for example an A1-site or possibly a C-site in the limiting $Sr_{2+x}Na_{1-2x}Nb_5O_{15}$ composition (x ~ 0.025).

Solid solution formulas and their associated shorthand notation are shown in Table 5.2.1.

Table 5.2.1. Table of compositions in Section 5.2 showing solid solution formulas, dopant levels, and shorthand notation.

Solid solution formula	Dopants	Shorthand notation
$Sr_{2-3x}Y_{2x}NaNb_5O_{15}$	x = 0.0125	SNN-Y
$Sr_{2-3x}Y_{2x}NaNb_5O_{15}$	x = 0.025	SNN-Y
$Sr_2NaNb_{5-4y}Zr_{5y}O_{15}$	y = 0.01	SNN-Z
$Sr_2NaNb_{5-4y}Zr_{5y}O_{15}$	y = 0.02	SNN-Z

Fabrication was carried out using the methodology outlined in Chapter 3, unless stated otherwise. The yttrium doped compositions were sintered for 4 hours at 1300 ^oC in air, whilst the zirconium doped compositions required a higher sintering temperature of 1350 ^oC to give comparable densities (> 90 % theoretical). The properties of the singly doped compositions are compared to unmodified SNN (Chapter 4, section 4.2) throughout this section.

5.2.1 Phase analysis

Figure 5.2.1 a-b shows the crushed sintered pellet X-ray powder diffraction patterns for $Sr_{2-3x}Y_{2x}NaNb_5O_{15}$ (x = 0.025) and $Sr_2NaNb_{5-4y}Zr_{5y}O_{15}$ (y = 0.02) respectively. All compositions showed similar phases to that of unmodified SNN, with the main phase indexed to the same tetragonal *P4bm* space group (ICDD 04-008-7203) and $NaNbO_3$ second phase (or Sr modified $NaNbO_3$) (ICDD 04-008-7203) (Figure 4.2.1).

No second phases relating to yttrium or zirconium were identified by XRD, in contrast to the SCNN-YZ composition from Chapter 4 where ZrO_2 was detected by XRD and SEM at 1.4 wt. % (Figure 4.3.2 b, doped at Ca^{2+}=0.05, Y^{3+}/Zr^{4+}=0.05). The SCNN-YZ composition from Chapter 4 displayed ZrO_2 peaks at 24.0 and 31.5 $^o2\theta$ and contained Zr^{4+} at 0.5 wt. % and 0.2 at. %. SNN-Z, y = 0.02 contained Zr^{4+} at 1 wt. % and 0.4 at. % but the XRD patterns did not display these peaks (log plot shown in Figure 5.2.2). A small peak at 31.5 $^o2\theta$ is present, but is much smaller than that in SCNN-YZ. Microstructure analysis (Section 5.2.4) suggested that ZrO_2 was not present in this composition.

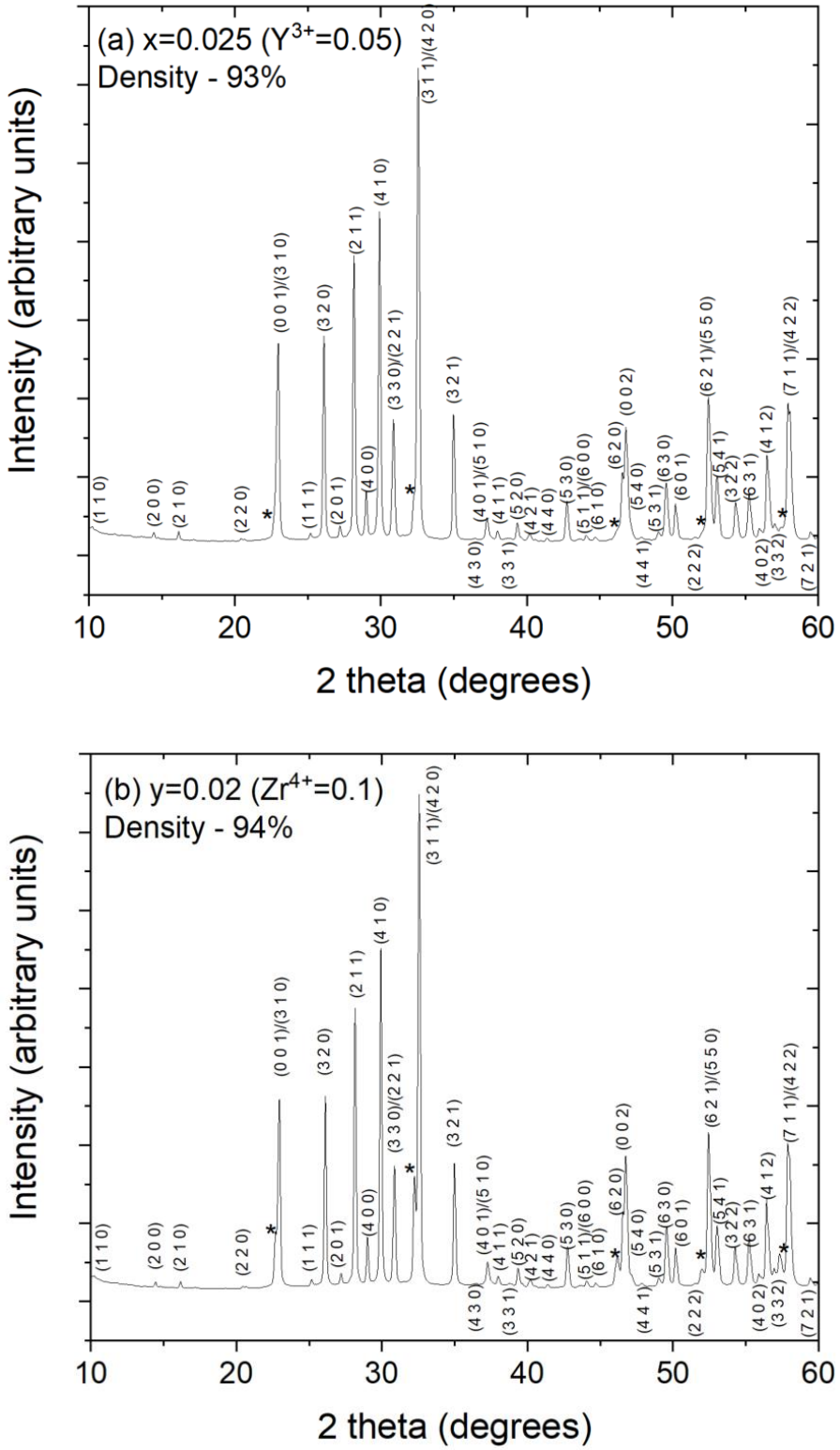

Figure 5.2.1 a-b. 12 hour powder XRD plots for a) $S_{2-3x}Y_{2x}NaNb_5O_{15}$ with x = 0.025, and b) $Sr_2Na_{1.0}Nb_{5-4y}Zr_{5y}O_{15}$ with y = 0.02. Indexed to ICDD 04-008-7203, tetragonal SNN, *P4bm*. Second phase Sr modified $NaNbO_3$ (*) was presnt in all samples (ICDD 04-009-3239).

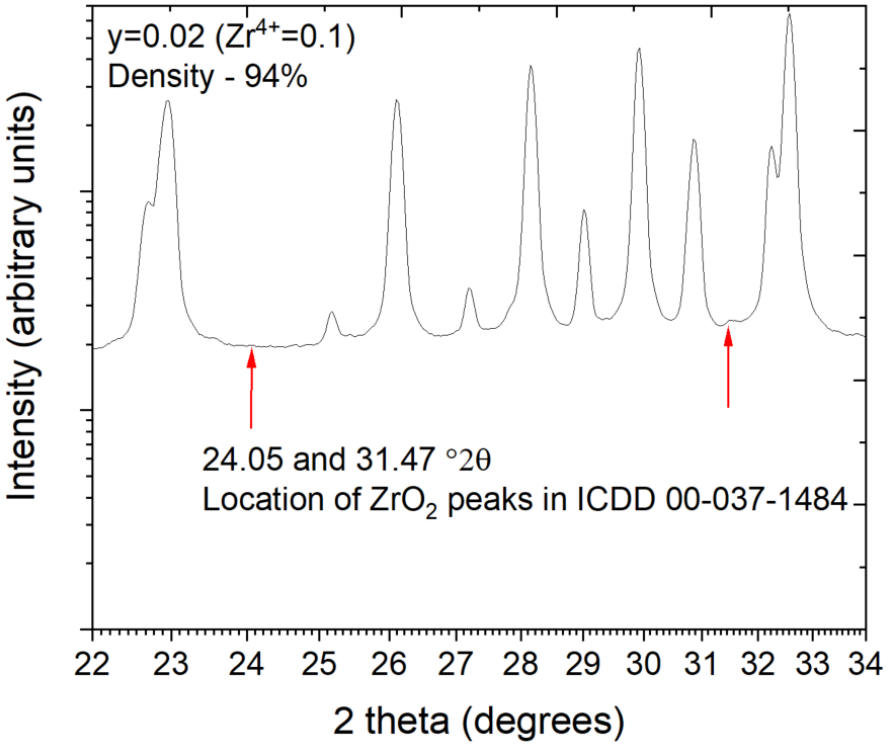

Figure 5.2.2. Log (intensity) plot of $Sr_2Na_{1.0}Nb_{5-4y}Zr_{5y}O_{15}$ with y = 0.02 for 22 – 34 °2θ. Second phase ZrO_2 peaks seen in SCNN-YZ (x = 0.05, y = 0.05, Chapter 4, Section 4.3) were not present in single doped compositions. A small peak at 31.47 °2θ was considered too small to be the 100 % (maximum intensity) ZrO_2 peak.

Unit cell refinements were performed for *P4bm* with crystallographic data summarised in Table 5.2.2 (fitting error 13 to 14 %). Relative geometric densities were between 91 and 94 % of calculated theoretical density, and second phase Sr modified $NaNbO_3$ decreased from SNN (6 wt. %) with Y^{3+} doping (down to 2 wt. %), whilst increasing with Zr^{4+} doping (up to 7 to 8 wt. %). Unit cell parameters obtained from routine XRD suggested a very slight decrease in *a* and *c* parameters for Y^{3+} doping, giving a contraction in estimated unit cell volume from 596.2 $Å^3$ (SNN) to 594.0 $Å^3$ (x = 0.025). The Zr^{4+} doped samples gave no indication of a change in lattice parameters compared to SNN.

Table 5.2.2. Crystallographic data for $S_{2-3x}Y_{2x}NaNb_5O_{15}$ with x = 0.0125, and 0.025, and $Sr_2NaNb_{5-4y}Zr_{5y}O_{15}$ with y = 0.01 and 0.02 from laboratory XRD measurements. Unmodified SNN data (Chapter 4.2) are also shown for comparison.

Composition	*a* = *b* Å	*c* Å	Volume Å^3	Geometric density g/cm^3	Percentage theoretical density	Tetragonality c/a	2nd phase wt. %	R_{WP} %
SNN	12.37	3.896	596.2	4.68	93%	0.31	5.8 $NaNb0_3$	11.5
x = 0.0125	12.36	3.893	594.7	4.60	91%	0.31	1.9 $NaNb0_3$	14
x = 0.025	12.36	3.888	594.0	4.71	93%	0.31	2.1 $NaNb0_3$	13
y = 0.01	12.37	3.897	596.3	4.76	94%	0.32	6.8 $NaNb0_3$	13.5
y = 0.2	12.37	3.895	596.0	4.80	94%	0.31	8.3 $NaNb0_3$	14

5.2.2 Dielectric analysis

Figure 5.2.3 a-e shows the temperature dependence of the relative permittivity and loss tangents for SNN, SNN-Y (x = 0.0125 and 0.025), and SNN-Z (y = 0.01 and 0.02) at 1 kHz, 10 kHz, 100 kHz, and 1 MHz. Dielectric data are summarised in Table 5.2.3 and a 1 kHz comparison plot is shown in Figure 5.2.4. All samples showed the expected two permittivity peaks characteristic of SNN, with a diffuse ferroelectric phase transition at high temperature (T_2) combined with relaxor behaviour at lower temperature (T_1).

With A-site doping with Y^{3+} for Sr^{2+} (assumed mechanism) the T_2 peak becomes more diffuse (suppressed) than for undoped SNN resulting in a decrease in $\varepsilon_{r\,max}$ (T_2), with 1 kHz ε_r values for SNN of 2150, dropping to 1290 at x = 0.025. The estimated width at half peak maximum (FWHM) of the T_2 peak increased from 44 °C in SNN to 83 °C in x = 0.025. B site doping with Zr^{4+} showed a less significant

reduction in the Curie point T_2 with ε_r values dropping to 1660 at y = 0.02, but with increased broadening, FWHM being 98 °C.

The temperature of the T_1 and T_2 peaks at 1 kHz showed a decrease with increased A and B-site doping. The temperature of peak T_2 (i.e. the Curie point) reduced from 306 °C for SNN, to 261 °C for SNN-Y (x = 0.025), and 257 °C for SNN-Z (y = 0.02). For the low temperature relaxor peak, T_1, the effect was greater for A-site doping, with T_m (1 kHz) dropping from -15 °C (SNN) to -53 °C (x = 0.025) and -28 °C (y = 0.02) (all 1 kHz values).

The T_1 peak showed no clear trends relating to $\varepsilon_{r\,max}$ (1 kHz), and values remained similar to SNN for x = 0.0125 (1710) and similar for y = 0.01 and 0.02 (1680 and 1750 respectively). However composition x = 0.025 showed substantial increase in size of T_1 peak with $\varepsilon_{r\,max}$ 1930. This was anomalous to the other results. Throughout this project there seemed to be no consistent relationship between the form of the T_1 relaxor peak and sample composition or relative density. Both A and B-site doping increased the frequency dependence of the T_1 peak, with a T_1 temperature difference between 1 kHz and 1 MHz of 9 °C for SNN, and 39 °C for SNN-Y (x = 0.025). For the y = 0.02 sample, T_1 (1 MHz) to T_1 (1 kHz) was 23 °C, and for y = 0.01 the corresponding value was 14 °C.

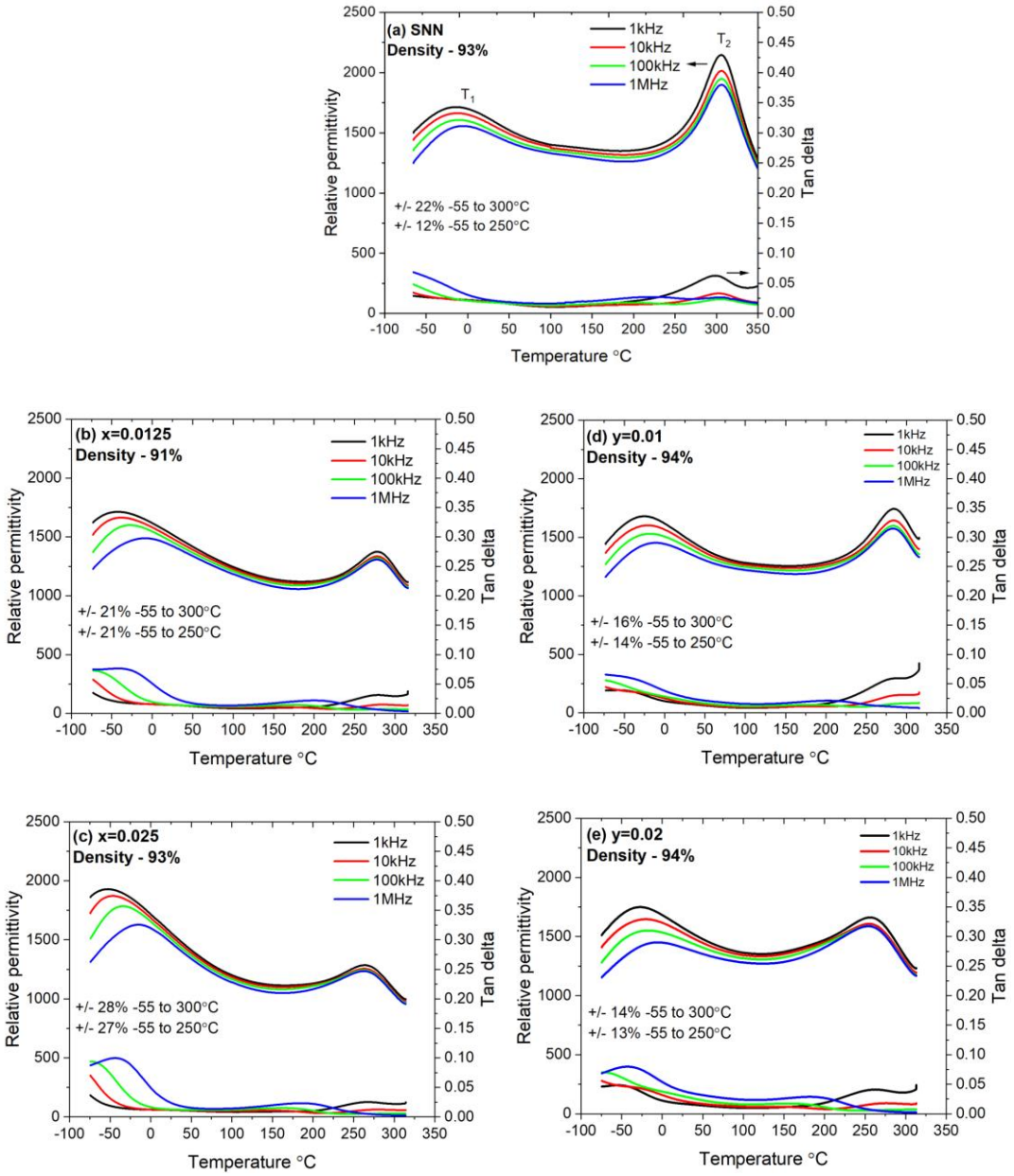

Figure 5.2.3 a-d. Multi-frequency permittivity and dielectric loss tangent versus temperature plots for a) SNN, $S_{2-3x}Y_{2x}NaNb_5O_{15}$ with b) x = 0.0125, c) x = 0.025, and $Sr_2NaNb_{5-4y}Zr_{5y}O_{15}$ with d) y = 0.01 and e) y = 0.02.

In terms of percent variation in permittivity from -55 to 300 °C (1 kHz) , the size of the low temperature T_1 peak (and a lack of understanding of the factors that regulate it) is often the controlling factor. The foregoing results show a similar % variation in response to A-site doping at -55 to 300 °C to SNN, from +/- 22 % for SNN, +/- 21 % (x = 0.0125), and +/- 28 % (x = 0.025). Similar values were recorded for -55 to 250 °C, +/- 21 % (x = 0.0125), and +/- 27 % (x = 0.025), much higher than

the +/- 12 % for SNN. The high level of T_2 suppression with Y^{3+} A-site doping caused a larger disparity in T_1 and T_2 peak sizes and resulted in a larger permittivity variation.

The B-site doping resulted in a smaller T_2 suppression and similar T_1 peak profile to undoped SNN, leading to an equalization in the T_1 and T_2 peak sizes. This led to a smaller variation across the temperature ranges for Zr^{4+} doping compared to A-site Y^{3+} doping (Figure 5.2.4). The permittivity variation from -55 to 300 °C dropped to +/- 16 % (y = 0.01), and +/- 14 % (y = 0.02). From -55 to 250 °C lower values were recorded of +/- 14 %, and +/- 13 % respectively, in line with SNN at +/- 12 % (-55 to 250 °C).

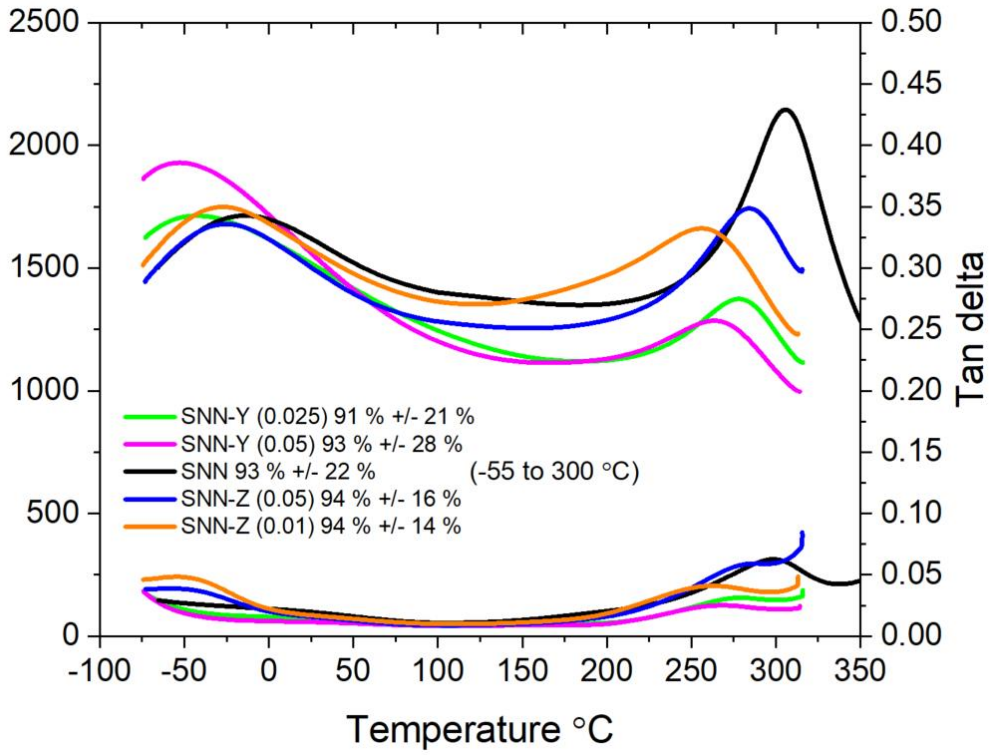

Figure 5.2.4. 1 kHz relative permittivity and dielectric loss tangent versus temperature plots for $S_{2-3x}Y_{2x}NaNb_5O_{15}$ with x = 0.0125, and 0.025, and $Sr_2NaNb_{5-4y}Zr_{5y}O_{15}$ with y = 0.01 and 0.02. Legend shows percentage theoretical density of the samples and relative permittivity variation (% above and below a median permittivity) from -55 to 300 °C. Unmodified SNN is also shown as a benchmark.

Dielectric loss tangents at 1 kHz losses improved with increasing Y^{3+} and deteriorated with increasing Zr^{4+} (Table 5.2.3). The lowest levels are found at x = 0.025 and were ≤ 0.025 for -62 to 263 °C and ≤ 0.035 for -73 to 314 °C, the latter encompassing the whole of the target temperature range. The narrowest temperature range of dielectric losses was y = 0.02, having ≤ 0.025 for -6 to 216 °C and ≤ 0.035 for -22 to 238 °C.

Table 5.2.3. Permittivity and loss tangents versus temperature data for $Sr_{2-3x}Y_{2x}NaNb_5O_{15}$ with x = 0.0125, and 0.025, and $Sr_2NaNb_{5-4y}Zr_{5y}O_{15}$ with y = 0.01 and 0.02. Values for unmodified SNN are also listed.

Composition	T_1 °C ($\varepsilon_{r\ max}$)	T_2 °C ($\varepsilon_{r\ max}$)	+/- % (-55 - 250°C)	+/- % (-55 - 300°C)	tan δ ≤0.025 °C	tan δ ≤0.030 °C	tan δ ≤0.035 °C
SNN density 93%	-15 (1714)	306 (2146)	12%	22%	-32 to 223	-65 to 238	-65 to 249
x = 0.0125, density 91%	-43 (1713)	277 (1374)	21%	21%	-58 to 253	-67 to 269	-73 to 316
x = 0.025, density 93%	-53 (1929)	261 (1285)	27%	28%	-62 to 263	-68 to 314	-73 to 314
y = 0.01, density 94%	-25 (1680)	285 (1743)	14%	16%	-14 to 227	-25 to 236	-35 to 244
y = 0.02, density 94%	-28 (1749)	257 (1661)	13%	14%	-6 to 216	-16 to 227	-22 to 238

5.2.3 Ferroelectric analysis

Typical ferroelectric P-E hysteresis loops at 40 kV cm^{-1} are shown for the doped ceramics in Figure 5.2.5 a-b, alongside unmodified SNN, with the data summarised in Table 5.2.4. Saturation was lower with A and B-site doping compared to SNN and P_{max} of 13 µC cm^{-2} for SNN dropped to 8.5 µC cm^{-2} with their addition (10 µC cm^{-2} in y = 0.01). This reduction could be associated with the reduction in T_2 ε_r

with increased doping (Table 5.2.2). P_r also fell from 5.5 µC cm^{-2} for SNN, to 3 µC cm^{-2} (Y^{3+} addition), and to 3.5 to 4.5 µC cm^{-2} (y = 0.02 and 0.01 respectively). A change in the E_c from 12 kV cm^{-1} for SNN was only seen with B-site doping, increasing to ~16 kV cm^{-1}.

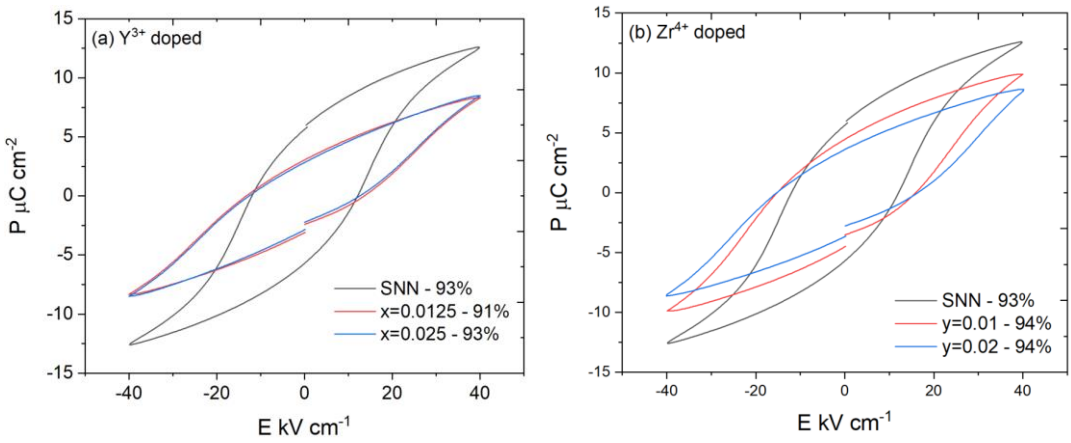

Figure 5.2.5. a-b. 40 kV cm^{-1} polarisation – electric field loop plots for a) $S_{2-3x}Na_{1.0}Y_{2x}Nb_5O_{15}$ with x = 0.0125, and 0.025 b) $Sr_2NaNb_{5-4y}Zr_{5y}O_{15}$ with y = 0.01 and 0.02. Unmodified SNN plot is also shown on each diagram for reference.

Table 5.2.4. Remnant polarisation (P_r) and coercive field (E_c) data at 40 kV cm^{-1} for $Sr_{2-3x}Na_{1.0}Y_{2x}Nb_5O_{15}$ with x = 0, 0.0125, and 0.025 and $Sr_2NaNb_{5-4y}Zr_{5y}O_{15}$ with y = 0.01 and 0.02.

Composition	P_r µC cm^{-2} (+/- 0.5)	E_c kV cm^{-1} (+/- 0.5)	P_{max} µC cm^{-2} (+/- 0.5)
SNN, density 93%	5.5	12	13
x = 0.0125, density 91%	3	13.5	8.5
x = 0.025, density 93%	3	12.6	8.5
y = 0.01, density 94%	4.5	16.0	10
y = 0.02, density 94%	3.5	16.5	8.5

5.2.4 Microstructural analysis

Back scattered scanning electron micrographs for unmodified SNN, x = 0.025, and y = 0.02 are shown in Figure 5.2.6 a-c. An SEM-EDX map for composition y = 0.02 is shown in Figure 5.2.7. Maximum grain size in SNN was 17 µm, with grains generally ≤ 10 µm, and most between 2 to 4 µm (Figure 5.2.6 a). With A-site Y^{3+} for Sr^{2+} substitution at x = 0.025 maximum grain size remained the same (16 µm), with most grains again ≤ 10 µm, but generally between 4 to 6 µm (Figure 5.2.6 b). A further increase in grain size was observed for B-site Zr^{4+} for Nb^{5+} substitution at y = 0.02, where a maximum grain size of 20 µm was seen, with most grains falling between 6 to 10 µm (Figure 5.2.6 c). Micro-cracks radiating from porosity in the structure were present in both x = 0.025 and y = 0.02, as in previous compositions (Chapter 4, Section 4.3.4). Darker Na^{+} rich grains, confirmed by SEM-EDX mapping (Figure 5.2.7) were less frequent in Y^{3+} for Sr^{2+} compoposition x = 0.025 (Figure 5.2.6 b), and consistent with the XRD data for this sample (Table 5.2.2). No other second phases relating to Y^{3+} or Zr^{4+} were detected in either composition. SEM-EDX maps of Zr^{4+} for Nb^{5+}, y = 0.02 (total Zr^{4+} = 0.1) showed no second phase ZrO_2, as might have been predicted due to its presence in $Sr_{2-x-y}Ca_xY_yNaNb_{5-y}Zr_yO_{15}$, x = 0.05, y = 0.05 from Chapter 4 (Figure 5.2.7).

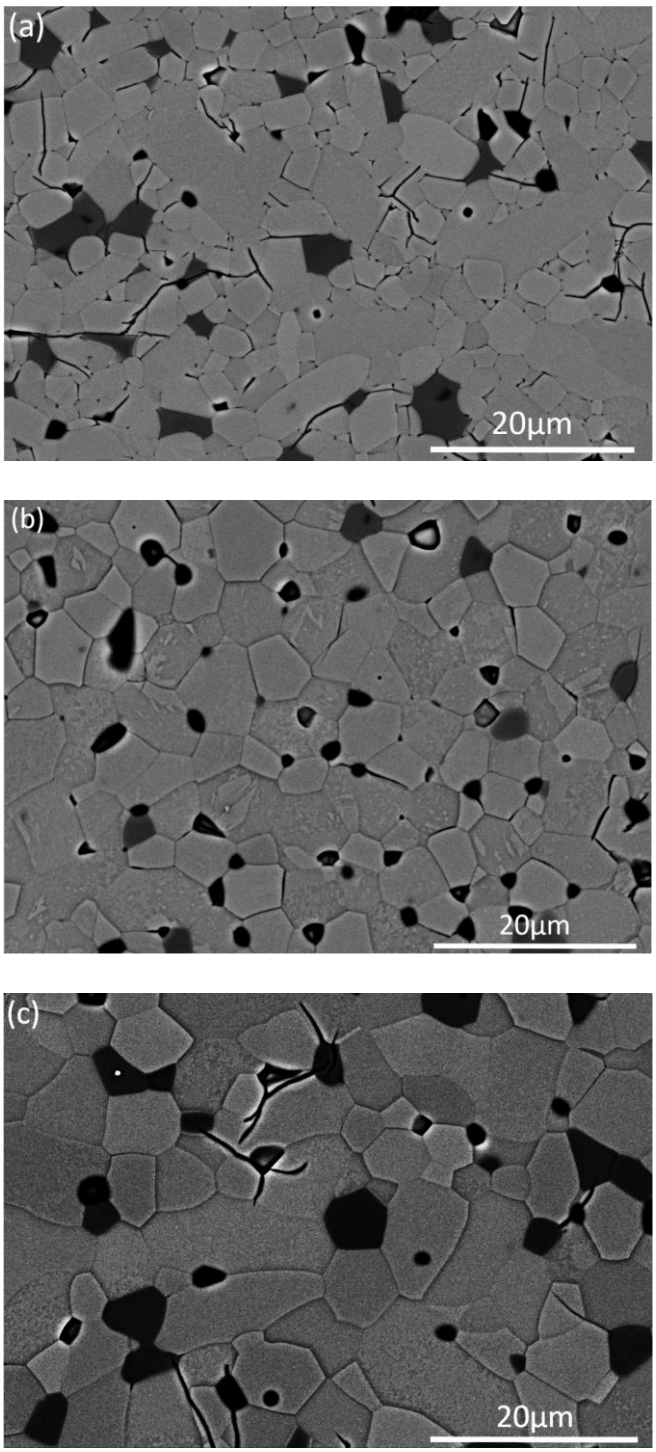

Figure 5.2.6 a-c. Back scattered scanning electron micrographs of a) unmodified SNN, b) $Sr_{2-3x}Na_{1.0}Y_{2x}Nb_5O_{15}$ with x = 0.025, and c) $Sr_2NaNb_{5-4y}Zr_{5y}O_{15}$ with y = 0.02.

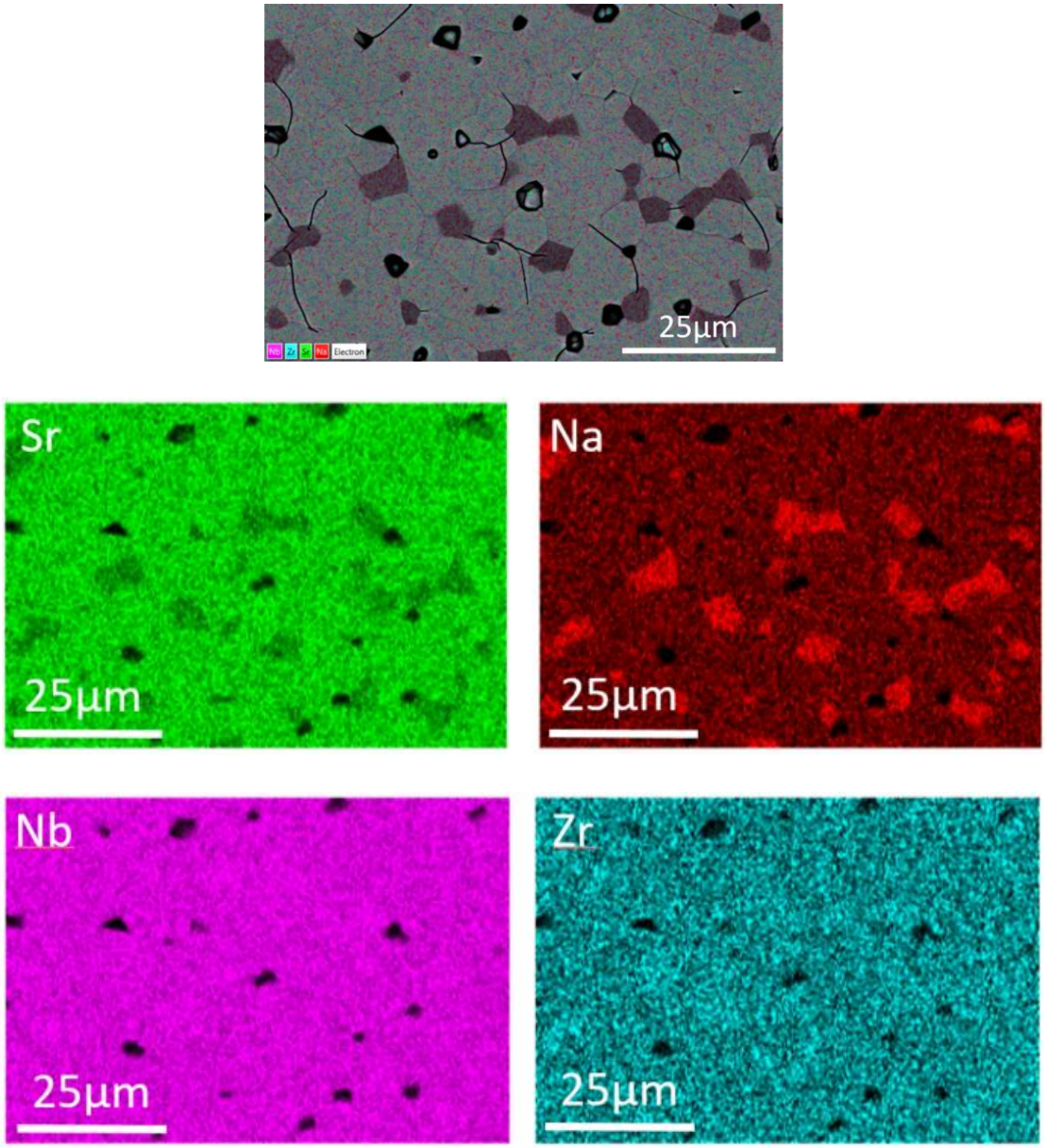

Figure 5.2.7. SEM-EDX maps of $Sr_2NaNb_{5-4y}Zr_{5y}O_{15}$ with y = 0.02. Darker grains are shown to be Na^+ rich and Sr^{2+} deficient, consistent with previous compositions. Preferential segregation of Zr onto $NaNbO_3$ grains was possible but more data is required to confirm this.

5.2.5 Summary Section 5.2: (Y^{3+} for Sr^{2+}; Zr^{4+} for Nb^{5+} single dopants)

Dense formulations (91 to 94 %) of $Sr_{2-3x}Y_{2x}NaNb_5O_{15}$ (x = 0.0125, and 0.025) and $Sr_xNaNb_{5-4y}Zr_{5y}O_{15}$ (y = 0.01, and 0.02) were made in order to ascertain the effect of individual doping on A and B-sites and each contribution to the flattened relative permittivity response over the large temperature range seen in Chapter 4 (composition x = 0.05, y = 0.05, +/- 9 % -55 to 300 ºC).

XRD revealed similar phases to SNN (Figure 4.2.1), with second phase $NaNbO_3$ (or Sr modified $NaNbO_3$) present in all samples, as reported by others for SNN (Garcia-Gonzalez, 2007 and Torres-Pardo, 2011). A-site doping with Y^{3+} showed a marked decrease in Sr modified $NaNbO_3$ content (2 wt. %) compared to SNN (6 wt. %). If this is Sr modified $NaNbO_3$, as suggested by Torres-Pardo and consistent with TEM results here (Brown et al. 2020), then one possibility is as Y^{3+} replaces Sr^{2+}, then Y^{3+} has a preference to substitute into SNN rather than Sr modified $NaNbO_3$ and so there is less Sr^{2+} to form the second phase. There are however, three Sr^{2+} vacancies for every two Y^{3+} ion additions in this formulation and the vacancies may be having a significant effect in stabilisation of the single phase. Jang et al. (2004), studying $K_3Li_2Nb_5O_{15}$ (KLN), reported that the Madelung energy of this “stuffed” TTB is unstable, and leads to second phase formation. This is the electrostatic, main contributing force to the binding energy of ionic crystals such as SNN (Kittel, 1953) and was found to decrease with A and C-site vacancies in the KLN TTB (most strongly with A_2 vacancies) (Figure 5.2.8). What is more, the vacancies in SNN-Y are likely to be on A_2 sites, given that the smaller Y^{3+} would probably preferentially sit on the A_1 sites. Triple-doped compositions from Chapter 4 would not see this vacancy driven effect as charge balance and stoichiometry is maintained by Y^{3+} and Zr^{4+} substitutions.

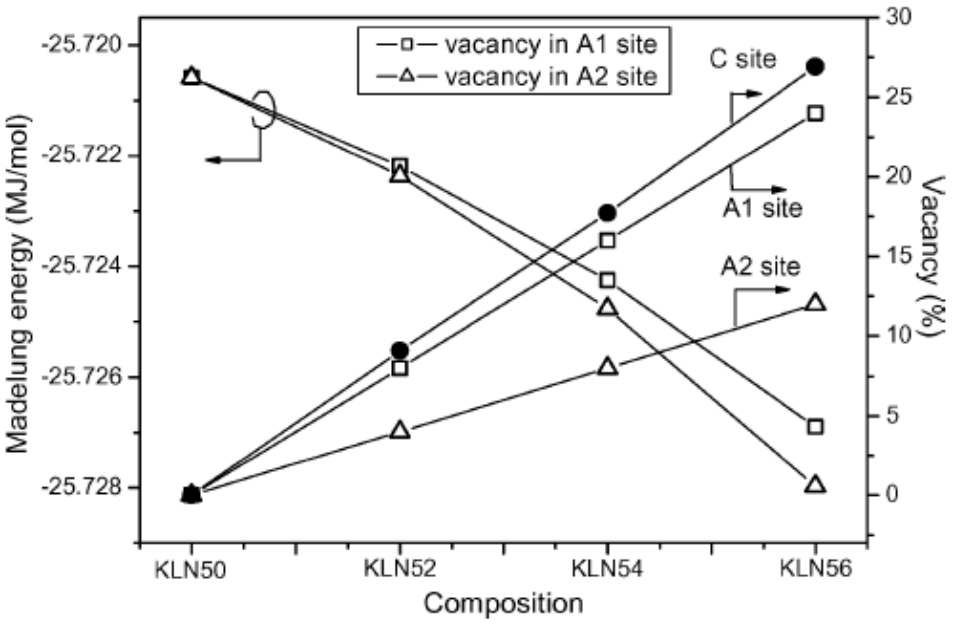

Figure 5.2.8. Vacancy of the alkali metal ion sites versus Madelung energy of $K_3Li_2Nb_5O_{15}$ (reproduced from Jang et al. 2004).

With B-site doping by Zr^{4+} where the Sr^{2+} remains constant, the second phase increased from 6 wt. % in SNN to 7-8 wt. %. This may not be a significant change and is consistent with SNN being a filled TTB with full A-site occupancy. No second phases relating to yttrium or zirconium were found by XRD in the single doped compositions, in contrast to SCNN-YZ (Chapter 4) where ZrO_2 was present at 1.4 wt. % in composition Ca^{2+} = 0.05, Y^{3+}/Zr^{4+} = 0.05 (Figure 4.3.2 b). The unit cell volume of SNN (596.2 $Å^3$) decreased with A-site doping to 594.0 $Å^3$ at Y^{3+} = 0.05, consistent with the substitution of a larger ion (Sr^{2+}, 1.44 Å) with a smaller one (Y^{3+}, 1.08 Å) causing shrinkage of the unit cell. The substitution on the B-site of more similar sized cations, Nb^{5+} (0.68 $Å^3$) by Zr^{4+} (0.72 $Å^3$), saw the unit cell volume remain constant (~596.0 $Å^3$).

All compositions displayed two dielectric peaks, with the higher temperature peak (T_2) interpreted to represent the Curie point, the onset of ferroelectric behaviour on cooling (Figure 5.2.3 b-e). Room temperature P-E hysteresis loops show ferroelectric characteristics (Figure 5.2.5 a-b). The 1 kHz T_2 peak showed a reduction in ε_r value and temperature with increased levels of both dopants, with the effect on ε_r value markedly greater for A-site doping, possibly due to the greater size difference of the substitution cation. The ferroelastic (T_1) peak lacked any clear ε_r trends, although a small reduction in peak temperature was observed with increased

doping (Table 5.2.2). A greater reduction in ε_r value for T_2 compared with T_1 with A-site doping could emphasise that the ferroelastic distortion is in the [1 1 0] or [1 0 0] direction, and so in the *a*-*b* plane, whereas the ferroelectric transition is related to changes in tilt and Jahn-Teller extensions of oxygen octahedral, in which B-site displacement in the *c* direction plays a role. The A-site doping appears to have a larger effect on the octahedral tilting (and therefore the ferroelectric transition, T_2) as the ferroelastic distortion already exists in the *a*-*b* plane, affecting T_1. A large increase in T_1 ε_r value of SNN-Y, x = 0.025 was unexpected and a higher doping level would be required to determine if this is a consistent trend.

Both A and B-site doping did however cause the SNN T_1 peak to become more relaxor like with increasing quantities. That is, the frequency dependence of T_1 increased with respect to temperature and ε_r value, as doping levels increased, presumably because of greater lattice inhomogeneity (structure and charge) pinning domains or polar nano regions (PNRs). The overall disparity in ε_r values of the T_1 and T_2 peaks from greater T_2 suppression with A-site doping caused a similar (but opposite) permittivity-temperature variation to SNN. Values of +/- 21 % for SNN-Y, x = 0.0125 were almost identical to unmodified SNN (+/- 22 %, -55 to 300 °C) and an increase in T_1 at x = 0.025 caused this variation to rise to +/- 28 % over the same temperature range. Doping with Zr^{4+} caused less suppression of T_2 and resulted in ε_r values being near equivilent to those at T_1. As a result the permittivity variation was reduced in comparison to SNN, to +/- 16 % for SNN-Z y = 0.01 and +/- 14 % for y = 0.02 (-55 to 300 °C). One possibility for the greater T_2 suppression with A-site doping is the larger difference in cation radii on this site is having a bigger influence on tilting of NbO_6 octahedra than substitution on the B-site. Both A and B-site doping caused T_2 suppression and broadening which could be related to domain wall pinning and/or formation of PNRs. These give a range of ferroelectric domains and thus Curie points, causing broadening of the peak.

Whilst permittivity variation deteriorated with increasing Y^{3+} and improved with increasing Zr^{4+}, the dielectric loss tangents at 1 kHz showed the opposite trend. Generally all compositions showed increases above ~200 °C, whilst the Zr^{4+} doped samples also displayed increases at lower temperatures (< 0 °C) (Figure 5.2.4). This could suggest ionic conductivity at high temperature from the lack of full inclusion of Zr^{4+} in the SNN lattice, whilst Y^{3+} appears to be completely substituted in, although

no evidence for this was seen from XRD or SEM (seen in SCNN-YZ x = y = 0.05 composition in Chapter 4). Maximum tan δ values from -55 to 300 °C for SNN were 0.06, these were reduced to 0.035 with the introduction of Y^{3+}. The high and low temperature rises were also not as steep in SNN-Y, resulting in the range of tan δ values which were ≤ 0.035 extending from approximately -73 to 315 °C, compared to -65 to 249 °C in SNN (Table 5.2.2). For SNN-Z the maximum tan δ values from -55 to 300 °C were similar to SNN at between 0.05 to 0.06 but the rises at low temperature were greater with increased Zr^{4+}. This gave a range of tan δ values which were ≤ 0.035 extending from approximately -35 °C (y = 0.01) and -22 °C (y = 0.02) to ~240 °C (Table 5.2.2).

P-E hysteresis loops were similar in appearance and showed reductions from SNN in maximum polarisation (13 μC cm^{-2}) and remnant polarisation (5.5 μC cm^{-2}) in all compositions (Table 5.2.4), which was consistent with the SCNN-YZ doping in Chapter 4 (Table 4.3.3). Coercive field values increased from SNN (12 kV cm^{-1}) for all compositions and were at their highest in Zr^{4+} = 0.1 (16.5 μC cm^{-2}), consistent with stonger domain wall pinning. This differed from highest doping in SCNN-YZ (x = 0.05, y = 0.05) where this composition showed the only reduction in coercive field from SNN, to 11 μC cm^{-2} (Table 4.3.3).

Microstructure analysis from SEM and SEM-EDX showed similar phase content to undoped SNN, in agreement with the phase diagram (Figure 5.5.3 , Tang et al. 1979). Lower levels of second phase $NaNbO_3$ were observed in A-site Y^{3+} for Sr^{2+} substituted samples than either unmodified SNN or B-site SNN-Z compositions, consistent with data from simple unit cell refinements of XRD patterns (Table 5.2.1) and discussed in this summary above. Average grain size increased from SNN where grains were generally ≤ 10 μm, and mostly 2 to 4 μm, to SNN-Y, x = 0.025 with grains mostly 4 to 6 μm, then SNN-Z. A further increase to 6 to 10 μm occurred with SNN-Z, y = 0.02 (Figure 5.2.6 a-c). Elemental segregation in the SNN-Z, y = 0.02 composition was a possibility due to the fact that 20 % of the substituted Zr^{4+} ions were expected to occupy a non B-site position, e.g. A-sites, grain boundaries, or Na vacancies. Although the EDX map for Zr suggests preferential occupancy on $NaNbO_3$ grains is a possibility, it is inconclusive and further work will be required to determine the true nature of this (Figure 5.2.7).

The data suggest that Zr^{4+} doping on the B-site alone would reduce the permittivity-temperature variation sufficiently and this is more effective than stand-alone A-site doping with Y^{3+}. However, Y^{3+} doping was needed to keep dielectric losses low. A study of co-doping with Y^{3+} and Zr^{4+} was therefore undertaken (Section 5.3). The compositions studied closely relate to the Chapter 4 composition, $Sr_{2-x-y}Ca_xY_yNaNb_{5-y}Zr_yO_{15}$ but without Ca^{2+} for Sr^{2+} substitution.

5.3 Strontium sodium niobate co-doped with Y^{3+} (for Sr^{2+}) and Zr^{4+} (for Nb^{5+}) (SNN-YZ)

Compositions of $Sr_{2-x}Y_xNaNb_{5-x}Zr_xO_{15}$ were produced using dopant levels of x = 0.025, and 0.05. The assumption was again made that Y^{3+} would substitute for Sr^{2+}, and Zr^{4+} for Nb^{5+} (as for all doped formulations, whether or not this assumption of site occupancy is valid awaits future crystallographic studies). The purpose was to determine the combined effect of the two dopants, previously studied in isolation in Section 5.2. The results also allow the contribution of additional substitution of Ca^{2+} for Sr^{2+}, reported in Chapter 4, to be examined. Fabrication was conducted as outlined in Chapter 3, and sintering at 1350 °C was required to achieve dense samples (> 90 % theoretical density).

5.3.1 Phase analysis

X-ray powder diffraction patterns showed similar phases to those previously ascertained, with indexing to the same tetragonal SNN *P4bm* (ICDD 04-008-7203), and the same $NaNbO_3$ (ICDD 04-009-3239) or Sr modified $NaNbO_3$ (ICDD 04-008-7203) second phase being present (Figure 5.3.1 showing x = 0.05). No second phases relating to yttrium or zirconium were detected by XRD. Crystallographic data from basic unit cell refinements (fitting error 13.5 %) are summarised in Table 5.3.1. The *a* and *c* parameters and unit cell volume remained constant until x = 0.05 where a slight decrease was observed, for example cell volume changed from 596.2 $Å^3$ (SNN) to 594.4 $Å^3$ (x = 0.05). Geometric densities were 95 % of calculated theoretical density for both compositions and the second phase remained similar with doping from ~6 wt. % in SNN and x = 0.025, to ~7 wt. % in x and y = 0.05.

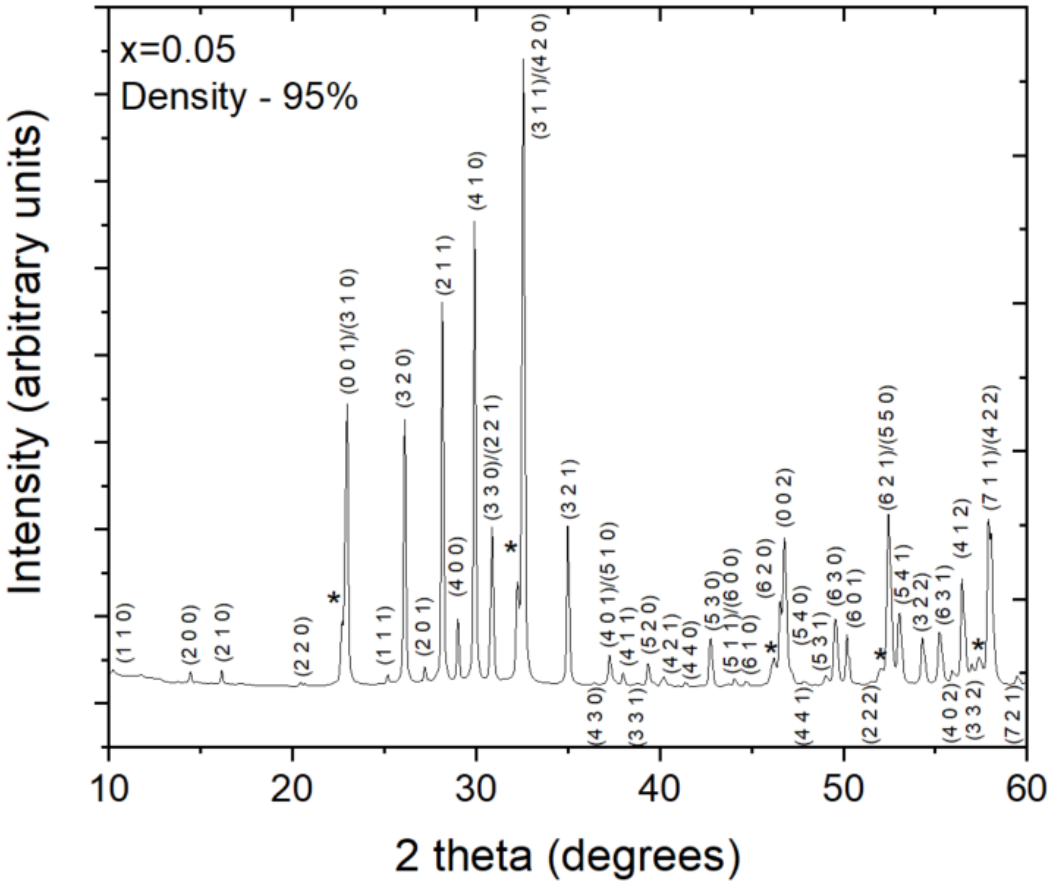

Figure 5.3.1. 12 hour powder XRD plots of $Sr_{2-x}Y_xNaNb_{5-x}Zr_xO_{15}$ with x = 0.05. Indexed to ICDD 04-008-7203, tetragonal SNN, *P4bm*. Second phase $NaNbO_3$ (*) was presnt in both samples (ICDD 04-009-3239).

Table 5.3.1. Crystallographic data of $Sr_{2-x}Y_xNaNb_{5-x}Zr_xO_{15}$ with x = 0.025, and 0.05, from X-ray powder diffraction unit cell refinements. Unmodified SNN (Chapter 4.2) is also shown for comparison.

Composition	*a* = *b* Å	*c* Å	Volume Å^3	Geometric density g/cm^3	Percentage theoretical density	Tetragonality c/a	2nd phase wt. %	R_{WP} %
SNN	12.37	3.896	596.2	4.68	93%	0.31	5.8 $NaNb0_3$	11.5
x = 0.025	12.37	3.895	596.0	4.82	95%	0.31	5.9 $NaNb0_3$	13.5
x = 0.05	12.36	3.891	594.4	4.84	95%	0.31	6.9 $NaNb0_3$	13.5

5.3.2 Dielectric analysis

The temperature dependence of relative permittivity and loss tangents at frequencies 1 kHz to 1 MHz are shown in Figure 5.3.2 a-c. A 1 kHz comparison plot is shown in Figure 5.3.3, and dielectric data are summarised in Table 5.3.2.

As in the single doped compositions (Section 5.2), increasing x showed a clear trend in reducing the T_2 ε_r value and temperature from SNN (2150 and 305 °C), dropping to 1867 and 282 °C for x = 0.025, and 1620 and 255 °C for x = 0.05. Composition x = 0.05 also showed what appeared to be a third dielectric anomaly at a slightly lower temperature to T_2 (approximately 178 °C) (Figure 5.3.2 c). It was accompanied by a notable peak in tanδ values. However this dielectric anomaly only occurred at 1 kHz and to a lesser extent 10 kHz (being absent at 100 kHz and 1 MHz). This frequency dependence suggests it may arise from a 'long-range' space-charge phenomonon. The drop in T_2 ε_r value was accompanied by a significant peak broadening at x = 0.05. The third dielectric anomaly made the FWHM difficult to estimate but an approximation of 44 °C (SNN) to 145 °C (x = 0.05) was made.

The effect on T_1 of co-doping with Y^{3+} and Zr^{4+} was to reduce peak temperature from -15 °C (SNN), to -39 °C (x = 0.025), and then to -66 °C (x = 0.05). The T_1 $\varepsilon_{r\,max}$ value remained constant at approximately 1710 (1 kHz). T_1 became more relaxor like with increasing x, with frequency dependence i.e. there was a more pronounced increasing in peak temperature T_m and decrease in $\varepsilon_{r\,max}$ with increasing frequency. The difference in T_m values between 1 kHz and 1 MHz data was 9 °C for SNN, 33 °C for SNN-YZ (x = 0.025), and 51 °C SNN-YZ (x = 0.05).

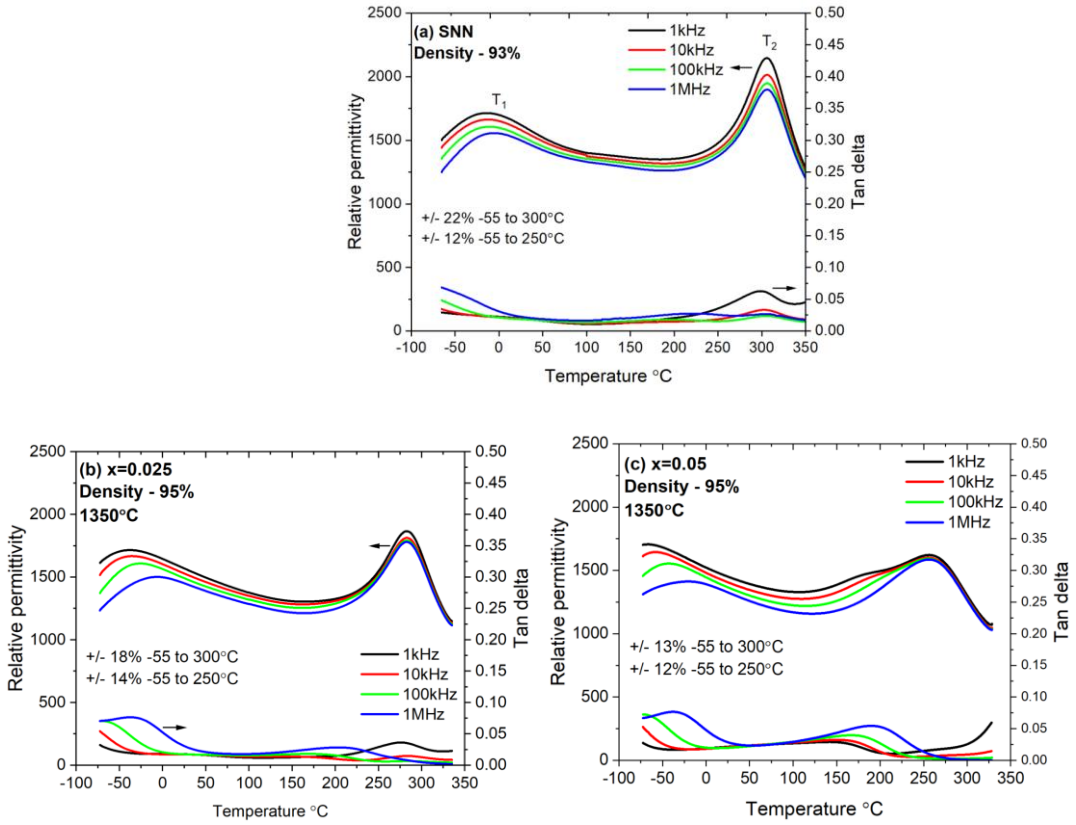

Figure 5.3.2 a-c. Multi-frequency permittivity and dielectric loss tangent versus temperature plots for a) unmodified SNN, and $Sr_{2-x}Y_xNaNb_{5-x}Zr_xO_{15}$ with b) x = 0.025, and c) x = 0.05.

Permittivity variation also improved with increasing x from -55 to 300 °C, with +/- 22 % for SNN being reduced to +/- 18 % in x = 0.025, and then +/- 13 % in x = 0.05. This was due to the reduction in T_2 ε_r with increasing doping and a broadening of the peak, with a full width half maximum of the peak spanning ~44 °C in SNN, ~50 °C in x = 0.025, and ~99 °C in x = 0.05.

Dielectric loss tangents at 1 kHz were much improved over SNN, with values of ≤0.035 widening in range with increasing x from -65 to 259 °C (SNN), to -73 to 266 °C (x = 0.025), and then -73 to 312 °C (x = 0.05) (Table 5.3.2). Values for ≤0.025 for composition x = 0.05 only fluctuate above this value intermittently between -69 and 300 °C, showing the dielectric losses for this composition almost meets capacitor standards outlined in Chapter 1.

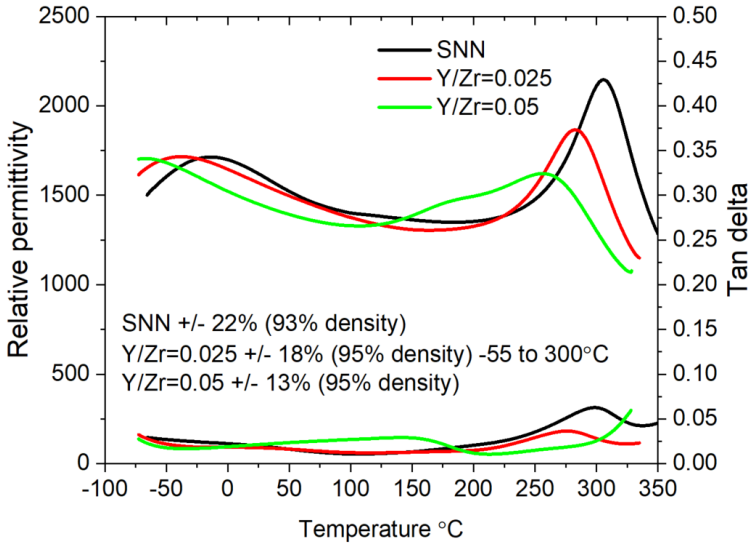

Figure 5.3.3. 1 kHz relative permittivity and dielectric loss tangent versus temperature plots for $Sr_{2-x}Y_xNaNb_{5-x}Zr_xO_{15}$ with x = 0.025, and 0.05. Legend shows percentage theoretical density and relative permittivity variation from -55 to 300 °C. Unmodified SNN is also shown.

Table 5.3.2. Permittivity and loss tangents versus temperature data for $Sr_{2-x}Y_xNaNb_{5-x}Zr_xO_{15}$ with x = 0.025, and 0.05. Unmodified SNN is also shown.

Composition	T_1 °C ($\varepsilon_{r\ max}$)	T_2 °C ($\varepsilon_{r\ max}$)	+/- % (-55 - 250°C)	+/- % (-55 - 300°C)	tan δ ≤0.025 °C	tan δ ≤0.030 °C	tan δ ≤0.035 °C
SNN density 93 %	-15 (1714)	306 (2146)	12%	22%	-32 to 223	-65 to 238	-65 to 249
x = 0.025 density 95 %	-39 (1716)	282 (1867)	14%	18%	-59 to 240	-69 to 253	-73 to 266
x = 0.05 density 95 %	-66 (1706)	256 (1622)	12%	13%	-69 to (fluctuates up to 300)	-73 to 306	-73 to 312

5.3.3 Ferroelectric analysis

The P-E hysteresis loops at 40 kV cm^{-1} are shown in Figure 5.3.4 alongside that of unmodified SNN. The loops show typical ferroelectric characteristics and measured values (Table 5.3.3) are similar to those of the zirconium only doped compositions in Section 5.2 (Table 5.2.3)

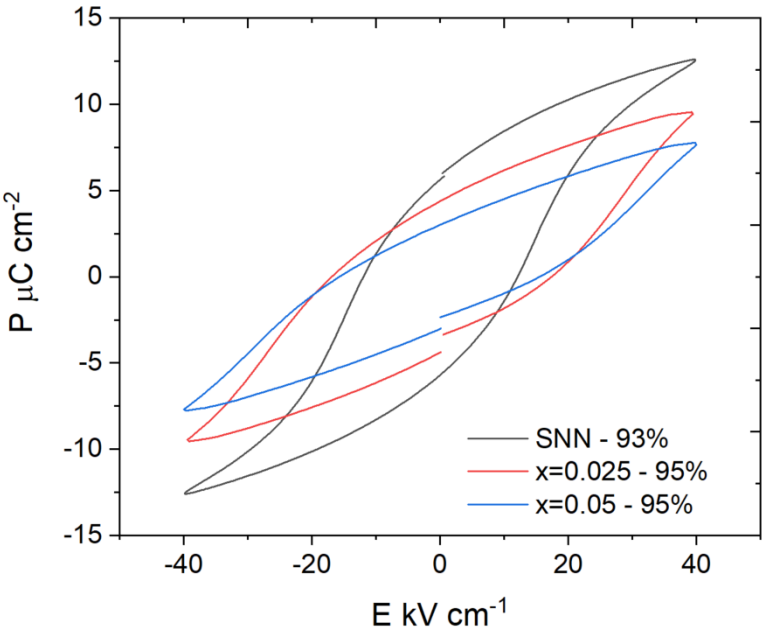

Figure 5.3.4. a-b. 40 kV cm^{-1} polarisation – electric field loop plots for $Sr_{2-x}Y_xNaNb_{5-x}Zr_xO_{15}$ with x = 0.025, and 0.05. Unmodified SNN is also shown for reference.

Table 5.3.3. Remnant polarisation (P_r) and coercive field (E_c) data at 40 kV cm^{-1} for $Sr_{2-x}Y_xNaNb_{5-x}Zr_xO_{15}$ with x = 0.025, and 0.05.

Composition	P_r μC cm^{-2} (+/- 0.5)	E_c kV cm^{-1} (+/- 0.5)	P_{max} μC cm^{-2} (+/- 0.5)
SNN, density 93%	5.5	12	13
x = 0.025	4.5	17.5	9.5
x = 0.05	3	15.5	8

5.3.4 Microstructural analysis

Back scattered scanning electron micrographs for SNN-YZ, x = 0.05 are shown in Figure 5.3.5, with SEM-EDX maps in Figure 5.3.6. Maximum grain size was 15 μm, with grains generally between 3 to 8 μm. Microcracks radiating from pores were again visible, consistent with all other compositions thus far. SEM-EDX confirmed the Na^+ enrichment of the darker grains, and their deficiency in Sr^{2+} and Y^{3+}. No other second phases were detected, specifically ZrO_2, which was observed $Sr_{2-x-y}Ca_xY_yNaNb_{5-y}Zr_yO_{15}$, x = 0.05, y = 0.05 from Chapter 4 (Figure 5.2.7). Zr^{4+} was homogenously distributed, with no suggestion of preferential distribution on $NaNbO_3$ grains. No other evidence of elemental segregation was observed.

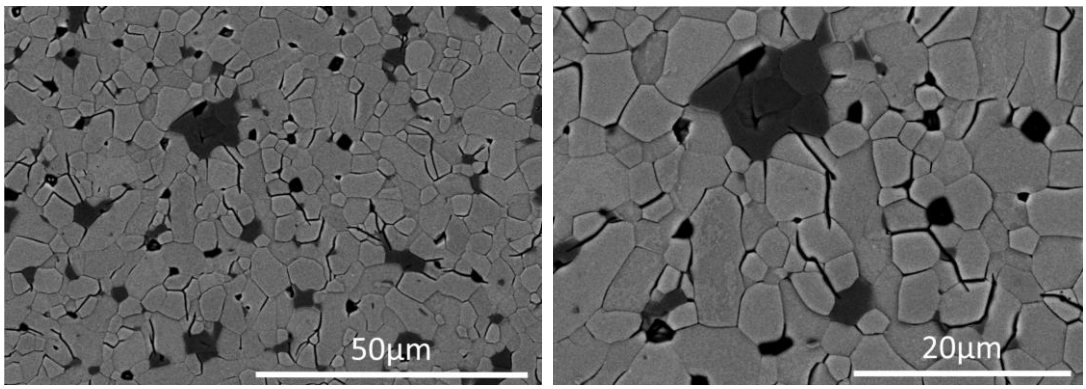

Figure 5.3.5. Back scattered scanning electron micrographs of $Sr_{2-x}Y_xNaNb_{5-x}Zr_xO_{15}$ with x = 0.05. Maximum grain size approximately 15 μm, with the majority 3 to 8 μm.

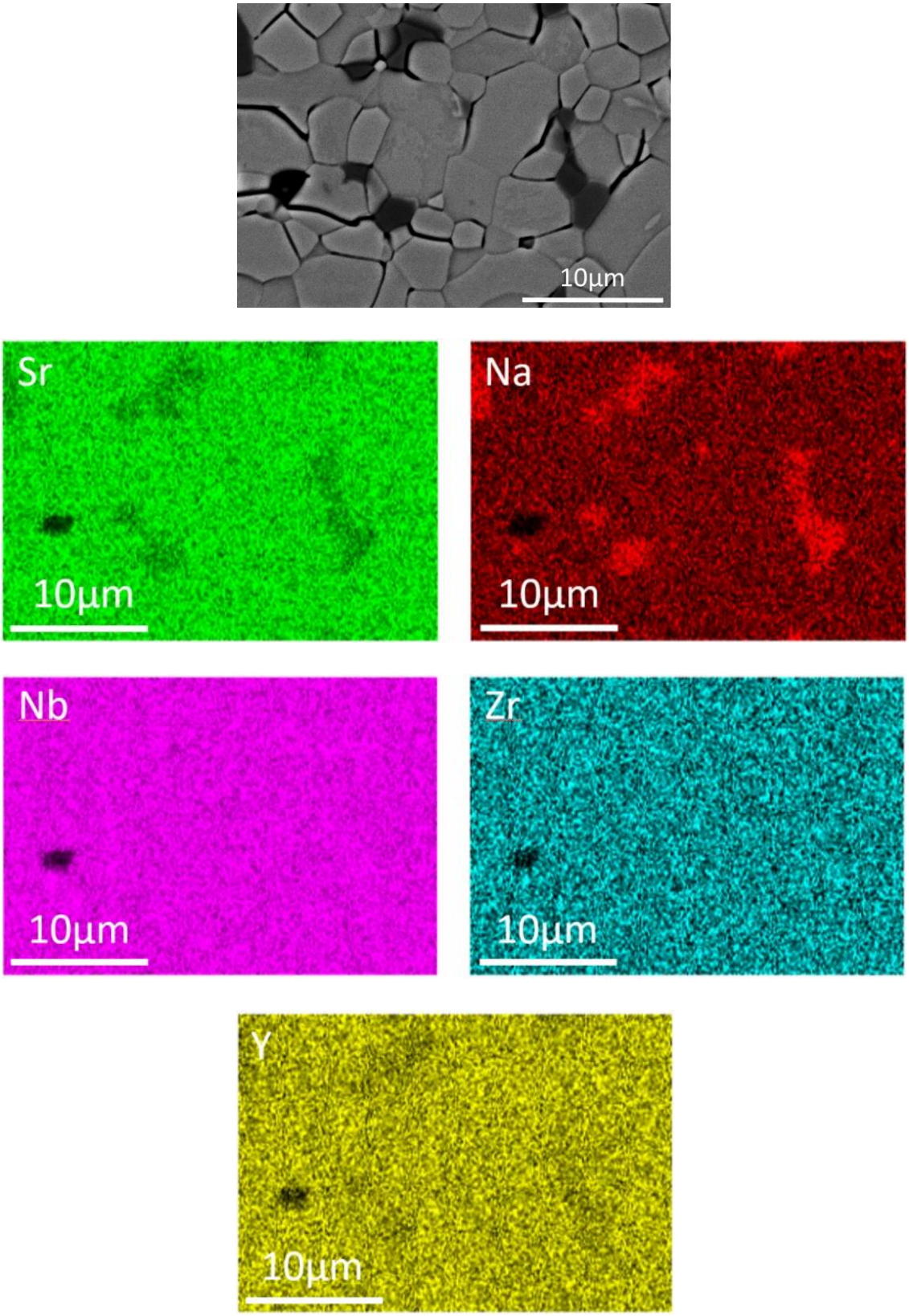

Figure 5.3.6. SEM-EDX maps of $Sr_{2-x}Y_xNaNb_{5-x}Zr_xO_{15}$ with x = 0.05. Darker grains are richer in Na^+ and deficient in Sr^{2+} and Y^{3+}. Nb^{5+} and Zr^{4+} were homogenous throughout the material.

5.3.5 Summary section 5.3: (co-doping SNN, Y^{3+} for Sr^{2+}; Zr^{4+} for Nb^{5+})

Dense ceramics (95 % of theoretical) of formulations $Sr_{2-x}Y_xNaNb_{5-x}Zr_xO_{15}$ (x = 0.025 and 0.05) were made to determine the effects of simultaneously co-doping Sr^{2+} A and Nb^{5+} B-sites in SNN with Y^{3+} and Zr^{4+} respectively. It was thought that the flattened relative permittivity response over a large temperature range seen in Chapter 4 for the Ca^{2+} modified samples $Sr_{2-x-y}Ca_xY_yNaNb_{5-y}Zr_yO_{15}$ (composition x = 0.05, y = 0.05, stability of permittivity +/- 9 % from -55 to 300 °C, composition x = 0.025, y = 0.025 +/- 16 % over the same temperature range) could be reliant on charge and some structural disorder at both sites (chemical inhomogenity).

The X-ray diffraction patterns were similar to SNN (Figure 4.2.1), with no secondary phase attributed to yttrium or zirconium present (Figure 5.3.1). Secondary phase $NaNbO_3$ (or a Sr modified $NaNbO_3$) was seen at similar levels to SNN (6 wt. %) in both compositions (6-7 wt. %). There was a slight reduction in unit cell volume at x = 0.05 (594 $Å^3$) compared to SNN and x = 0.025 (596 $Å^3$), consistent with similar levels of A-site single doping seen in Section 5.2 (Table 5.3.1).

The two dielectric peaks, T_1 and T_2, were present in both samples, but a third anomaly (T_3) was also seen in composition x = 0.05 at ~180 °C, slightly lower than T_2 (256 °C). A similar effect was seen by Cao et al. (2021) in Gd^{3+} doped SNN, and was attributed to vacancies causing space charge effects. The space charge explanation is consistent with the frequency dependence of this anomaly. Space charge can only follow an AC field up to 10^3 Hz (Moulson, 2003), and here we see the peak is absent at higher frequencies. A mechanism for the presence of vacancies is less clear though. SEM-EDX showed a homogenous distribution of Zr^{4+} but the composition SCNN-YZ, x = 0.05, y = 0.05 in Chapter 4 did show second phase ZrO_2 (Chapter 4, Figure 4.3.8). It is possible that this went undetected in this composition and resulted in B-site vacancies. This explanation could also go some way to explaining the flat permittivity response seen in SCNN-YZ, x = 0.05, y = 0.05 (Chapter 4, Figure 4.3.2 g).

Dielectric property trends were generally the same as for A and B-site only doping (Section 5.2), with T_2 reducing in ε_r value and peak temperature, and T_1 reducing in peak temperature whilst ε_r value remained constant (Table 5.3.2). The T_1 peak also became more frequency dependent with increasing dopants levels,

consistent with single doped A and B-site SNN compositions (Table 5.2.2). The reduction in T_2 was consistent with decreasing P_{max} and P_r values derived from P-E measurements, indicating a decrease in polarisation. Although E_c increased slightly with doping, consistent with a reduced domain mobility, this was not significant, suggesting the domain wall pinning mechanism remained the same (Figure 5.3.4). The addition of dopants primarily affected the polarisation. Permittivity variations as a function of temperature decreased with increased doping on both sites simultaneously, as T_2 reduced to a comparable size to T_1, from +/- 22 % for SNN to +/- 13 % for SNN-YZ (x = 0.05) at -55 to 300 ºC. Dielectric losses improved with increasing co-doping, being ≤ 0.035 over temperature range -73 to 312 ºC at x = 0.05, the same as SNN-Y x = 0.025 with A-site only doping (Section 5.2). This may suggest that the Y^{3+} doping dominates here and keeps losses low.

SEM-EDX maps (Figure 5.3.6) confirmed the phase content of SNN-YZ, x = 0.05 was similar to unmodified SNN, supporting crysallographic data obtaind by XRD (Table 5.3.1). As in all previous compositions, secondary phase grains were enriched in Na^+ and deficient in Sr^{2+}, but also observed was a deficiency in these areas of Y^{3+}. This supports the previously made assumption that Y^{3+} is substituting for Sr^{2+}. No elemental segregation was observed, Zr^{4+} being homogenously distributed throughout the material. This possibly indicates that the preferential distribution on $NaNbO_3$ grains potentially seen in single doped SNN-Z, y = 0.02 (Figure 5.2.7) may not have been a real effect, although the doping levels were higher in the single doped sample (Zr^{4+} = 0.1) compared to co-doped SNN-YZ (Zr^{4+} = 0.05). The most commonly encountered range of grain sizes increased from SNN (2 to 4 µm) to x = 0.05 (3 to 8 µm). This was larger than that of single doped SNN-Y, x = 0.025 (total Y^{3+} = 0.05, 4 to 6 µm), but smaller than that of single doped SNN-Z, y = 0.02 (total Zr^{4+} = 0.1, 6 to 10 µm)

Single A or B-site doping in Section 5.2 showed the individual dopants could induce changes to electrical properties, which could be beneficial or detrimental to the goals of this study. For instance, A-site doping with Y^{3+} improved the dielctric losses, but led to over suppression of the T_2 peak (in both x = 0.0125 and x = 0.025) giving an increase in the permittivity variation. An increase in the T_1 peak for an unknown reason in x = 0.025 further amplified this effect (Figure 5.2.3). The B-site doping with Zr^{4+} improved the permittivity variation but gave higher losses (i.e. a

narrower temperature range where the tan δ value lies below values 0.025, 0.03, and 0.035) (Table 5.2.2). Co-doping at increasingly higher levels appears to result in beneficial dielectric properties for achieving permittivity stability and supports the idea from Chapter 4 that multiple dopants are indeed needed to achieve this.

5.4 Strontium sodium niobate (SNN) with single doping by yttrium (SNN-Y, Y^{3+} for Na^{+})

Single doped $Sr_2Na_{1-3x}Y_xNb_5O_{15}$ was produced, with Y^{3+} substituting for Na^{+} (rather than Sr^{2+}, Section 5.2) (Fabrication, Gardener, J. Characterisation, Brown, T. University of Leeds) to determine the effect of substituting onto the alternative A-site cation. Doping levels were x = 0.05, giving the formulation $Sr_2Na_{0.85}Y_{0.05}Nb_5O_{15}$ and corresponding to composition x = 0.025 in Section 5.2 ($Sr_{1.925}Y_{0.05}NaNb_5O_{15}$). Comparison of Y^{3+} for Na^{+} and Y^{3+} for Sr^{2+} is made in this section. Fabrication of Y^{3+} for Na^{+} was carried out as in Section 5.2 but with a sintering temperature of 1350 ^{o}C (Y^{3+} for Sr^{2+}, x = 0.025 from Section 5.2 sintered 1300 ^{o}C).

X-ray diffraction patterns are shown for equivilantly doped compositions $Sr_{2-3x}Y_{2x}NaNb_5O_{15}$, x = 0.025 ($Y^{3+}$ for Sr^{2+} from Section 5.2) and $Sr_2Na_{1-3x}Y_xNb_5O_{15}$, x = 0.05 ($Y^{3+}$ for Na^{+}) (Figures 5.4.1 a and b respectively). The Y^{3+} for Sr^{2+} composition had shown reduced levels of second phase $NaNbO_3$, attributed to the formation of A-site vacancies (Section 5.2). The Y^{3+} for Na^{+} composition contained no second phase $NaNbO_3$, although some peaks that might be attributed to $SrNb_2O_6$ were present (ICDD 04-011-3157). This is unsurprising given that this substitution requires the removal of three Na^{+} ions for every addition of Y^{3+}, thus forming a greater number of A-site vacancies than Y^{3+} for Sr^{2+}.

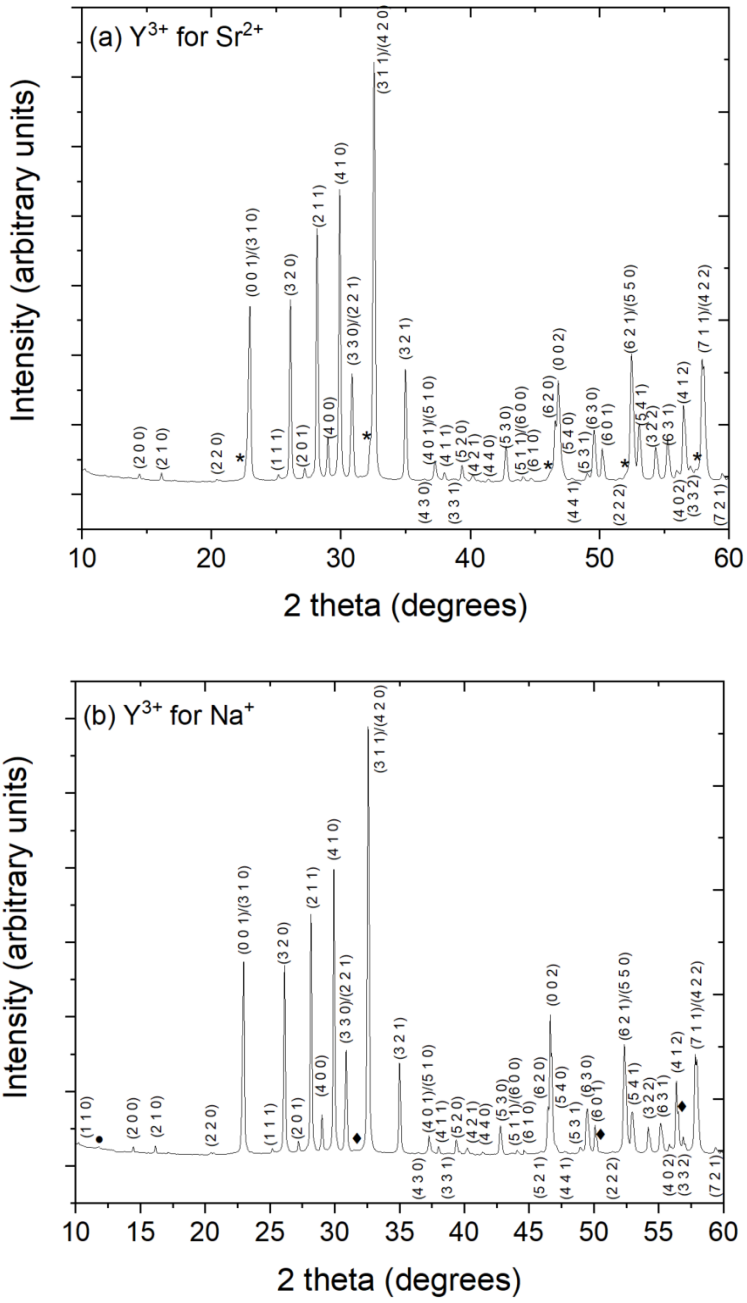

Figure 5.4.1 a-b. 12 hour powder XRD plots of a) $Sr_{2-3x}Y_{2x}NaNb_5O_{15}$ with x = 0.025 (section 5.2), and b) $Sr_2Na_{1-3x}Y_xNb_5O_{15}$ with x = 0.05. Indexed to ICDD 04-008-7203, tetragonal SNN, *P4bm*. Second phase $NaNbO_3$ (*) was present in $Sr_{2-3x}Y_{2x}NaNb_5O_{15}$ (ICDD 04-009-3239) but absent from $Sr_2Na_{1-3x}Y_xNb_5O_{15}$. Although $NaNbO_3$ was eliminated in $Sr_2Na_{1-3x}Y_xNb_5O_{15}$, possible second phase peaks of $SrNb_2O_6$ (♦) were seen (ICDD 04-011-3157) as well as an unidentified peak (●).

Figure 5.4.2 b shows the temperature dependence of the relative permittivity and loss tangents for the Y^{3+} for Na^{+} composition, with Y^{3+} for Sr^{2+} shown for comparison (Figure 5.4.3 a). Data at 1 kHz, 10 kHz, 100 kHz, and 1 MHz are summarised in Table 5.4.1. The T_2 temperature remained the same for both compositions, with T_1 decreasing from -53 °C in the Sr^{2+} substituted composition, to -72 °C in the Na^{+} substituted. For the Na^{+} substituted composition the $\varepsilon_{r\,max}$ value of T_1 decreased from 1930 to 1825, whilst T_2 $\varepsilon_{r\,max}$ value increased from 1290 to 1470. Dielectric loss tangents in the Na^{+} substituted composition increased sharply above 200 °C, possibly as a result of increased vacancies.

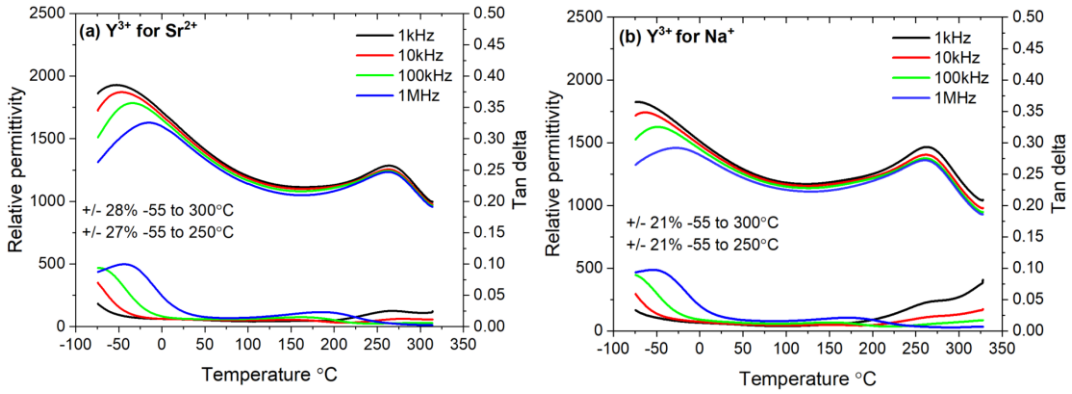

Figure 5.4.2 a-b. Multi-frequency permittivity and dielectric loss tangent versus temperature plots for a) $Sr_{2-3x}Y_{2x}NaNb_5O_{15}$ with x = 0.025 (Y^{3+} = 0.05) (section 5.2), and b) $Sr_2Na_{1-3x}Y_xNb_5O_{15}$ with x = 0.05.

Table 5.4.1. Permittivity and loss tangents versus temperature data for $Sr_{2-3x}Y_{2x}NaNb_5O_{15}$ with x = 0.025 (section 5.2), and $Sr_2Na_{1-3x}Y_xNb_5O_{15}$ with x = 0.05.

Composition	T_1 °C ($\varepsilon_{r\,max}$)	T_2 °C ($\varepsilon_{r\,max}$)	+/- % (-55 - 250°C)	+/- % (-55 - 300°C)	tan δ ≤0.025 °C	tan δ ≤0.030 °C	tan δ ≤0.035 °C
x = 0.025, Y^{3+} for Sr^{2+}	-53 (1929)	261 (1285)	27%	28%	-62 to 263	-68 to 314	-73 to 314
x= 0.05, Y^{3+} for Na^{+}	-72 (1825)	263 (1466)	21%	21%	-61 to 221	-70 to 231	-74 to 240

The net result of Y^{3+} for Na^{+} substitution is the formation of a more phase pure composition with an improved relative permittivity variation. However, it was also more lossy due to increased A-site vacancies. The role of A-site vacancies was thought to be worth exploring and is investigated in the next section.

5.5 Controlled Na^{+} deficiency $Sr_{2.1}Na_{0.8}Nb_5O_{15}$ (SNN0.8)

Chapter 4 and Chapter 5 (Sections 5.2-3) showed the potential of aliovalent doping of the $Sr_2NaNb_5O_{15}$ ceramic system with calcium, yttrium, and zirconium to obtain a flattened permittivity response over a large temperature range (Brown et al. 2020). However, all compositions have contained a second phase identified tentatively as $NaNbO_3$, but attributed by others as an SNN perovskite phase or Sr modified $NaNbO_3$ ($Sr_{0.25}Na_{0.5}NbO_3$) (Torres-Pardo et al. 2011, Morin et al. 1973). Analysis by TEM has shown that the second phase does indeed contain Sr (Brown et al. 2020), but $Sr_{0.25}Na_{0.5}Nb_2O_6$ produces a near identical XRD pattern to $NaNbO_3$ (ICDD 00-027-0788 and 04-009-3239 respectively). It would be advantageous to produce a single phase material, ideally with a consistent high density (≥ 95 %). Work by Yang et al. (2017 and 2019) suggested that single phase SNN and SCNN could be fabricated by using a deficit of Na^{+} in the stoichiometric quantities (i.e. using a Sr/Na ratio > 2). Yang et al. (2017) produced SCNN with varying levels of Na^{+}, using the formulation $(Sr_{0.925}Ca_{0.075})_{2.5-0.5x}Na_xNb_5O_{15}$, which corresponds to $Sr_{1.85}Ca_{0.15}NaNb_5O_{15}$ when using stoichiometric quantities of Na^{+}, as utilised in Chapter 4, Section 4.3.1. They reported single phase SCNN when $x \leq 0.8$, with densities ≥ 98 % (Figure 4.5.1).

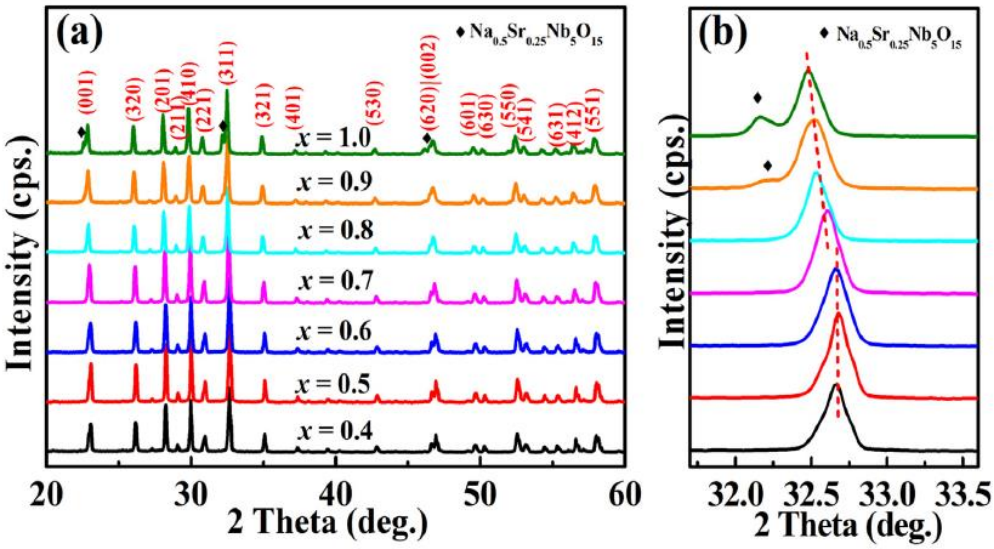

Figure 5.5.1. a) XRD patterns from the SCNN ceramics with different x; b) enlarged view of the XRD patterns in the range from 31.7 to 33.6 °2θ. Both show second phase material in composition x ≥ 0.9. (reproduced from Yang et al. 2017).

Similarly, Yang et al. (2019), produced SCNN with varying Ca^{2+} and sodium fixed at $Na_{0.8}$, with the formulation $(Sr_{1-x}Ca_x)_{2.1}Na_{0.8}Nb_5O_{15}$. They reported single phase material throughout from x = 0 to 0.15, with x = 0 representing unmodified SNN. No densities were reported (Figure 5.5.2). Both the 2017 and 2019 Yang et al. papers used fabrication conditions involving calcination at 1200 °C for 4 h and sintering at 1300 to 1360 °C for 4 h. The single phase nature of “unfilled” tetragonal tungsten bronze structures was supported by the work of Jang et al. (2004) (Chapter 2, Section 2.8.4) who state that the electrostatic instability that results in secondary phases is stabilised by the presence of A and C-site vacancies.

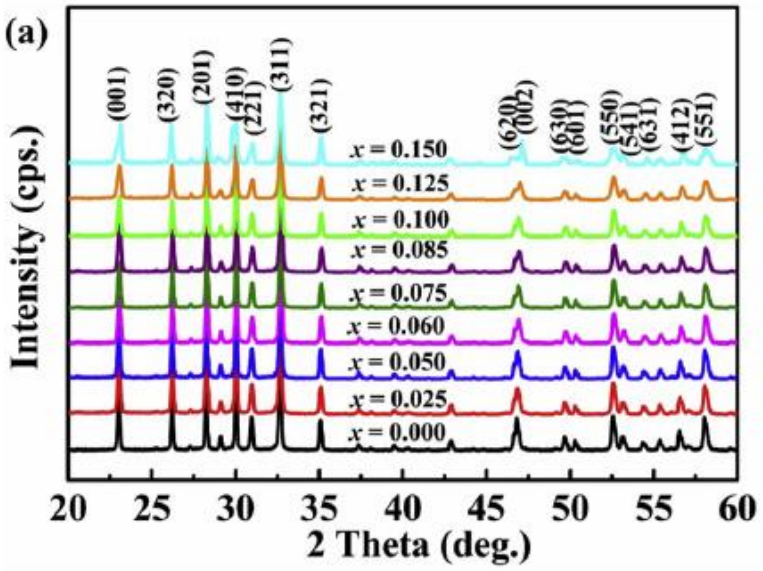

Figure 5.5.2**.** XRD patterns from the SCNN ceramics with different x, showing single phase material for all compositions (reproduced from Yang et al. 2019).

These results agree with the high temperature single phase field region for SNN in the $SrNb_2O_6$-$NaNbO_3$ phase diagram of Tang et al. 1979 (Figure 5.5.3) and Morin et al, 1973 (Figure 5.5.4), although these consider the $SrNb_2O_6$-$NaNbO_3$ phase equilibria at temperature only, with the additional effect of Ca unknown. They state that $Sr_2NaNb_5O_{15}$ (SNN1.0) lies just outside the metastable solid solution limit for $SrNb_2O_6$ in $NaNbO_6$ on cooling from sintering temperature to room temperature (Chapter 6 highlights thermodynamic stability issues), whilst $Sr_{2.1}Na_{0.8}Nb_5O_{15}$ (SNN0.8) is situated near the centre of the single phase field at the same temperature. Indeed, Li et al. (2019) identify the difficulty of producing single phase SNN1.0 using conventional mixed-oxide fabrication. This information had not been available at the beginning of this study but was subsequently used in later investigations.

The following refers to Ca-free $Sr_{2.1}Na_{0.8}Nb_5O_{15}$ (SNN0.8). SNN0.8 samples were produced as outlined in Chapter 3, up to and including the calcination process. Since the sintering process used in the cited papers did not state the precise temperature used, and one did not report densities (Yang et al. 2019), a literature search was conducted and a sintering study was undertaken to determine the best way to progress with SNN0.8. Four sintering regimes were found in the literature which had been used successfully by other groups (Lee et al. 1997, Li et al. 2019,

Zhang et al. 2019). An additional run was carried out under the standard conditions used for the majority of other samples in this study (1300 °C, 4 h).

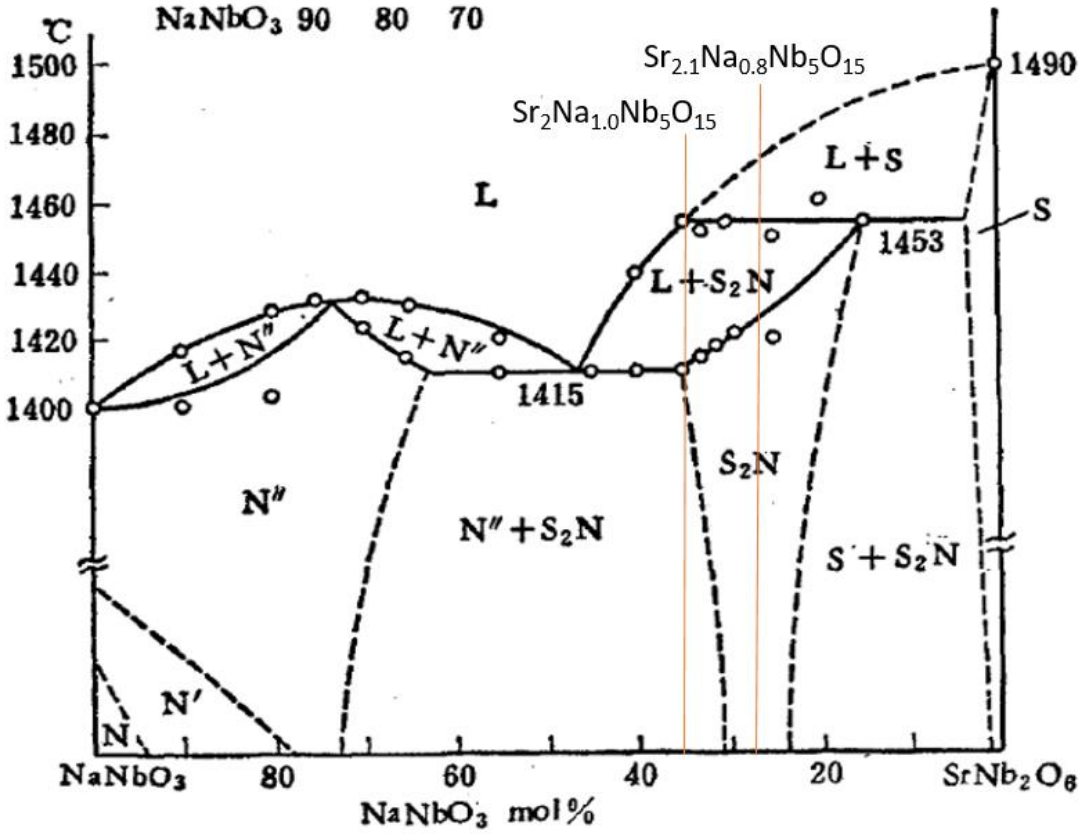

Figure 5.5.3. High temperature phase diagram of $NaNbO_3$ – $SrNb_2O_6$ system. SNN solid solution (labelled S_2N here) with formula $Sr_{2+x}Na_{1-2x}Nb_2O_6$ shows metastable projected room temperature composition limits from 24 mol.% $NaNbO_3$ to 76 mol. % $SrNb_2O_6$ through to the composition of 31 mol. % $NaNbO_3$ to 69 mol. % $SrNb_2O_6$. The stoichiometric formulation $Sr_2NaNb_5O_{15}$, prepared previously in Chapter 4 (33.3 mol. % $NaNbO_3$ and 66.6 mol.% $SrNb_2O_6$), is found to contain second phase Sr modified $NaNbO_3$ and the $Sr_2NaNb_5O_{15}$ lies just outside this stoichiometric solid solution limit at room temperature (which is $Sr_{2.05}Na_{0.9}Nb_5O_{15}$). The $Sr_{2.1}Na_{0.8}Nb_5O_{15}$ formulation, found by Yang et al. (2019) contains 27.6 mol.% $NaNbO_3$ and 72.4 mol. % $Sr_2Nb_2O_6$ and lies in the centre of the solid solution region. Also indicated is that melting occurs for this composition at 1425 ℃ (reproduced from Tang et al. 1979 with annotations by the author).

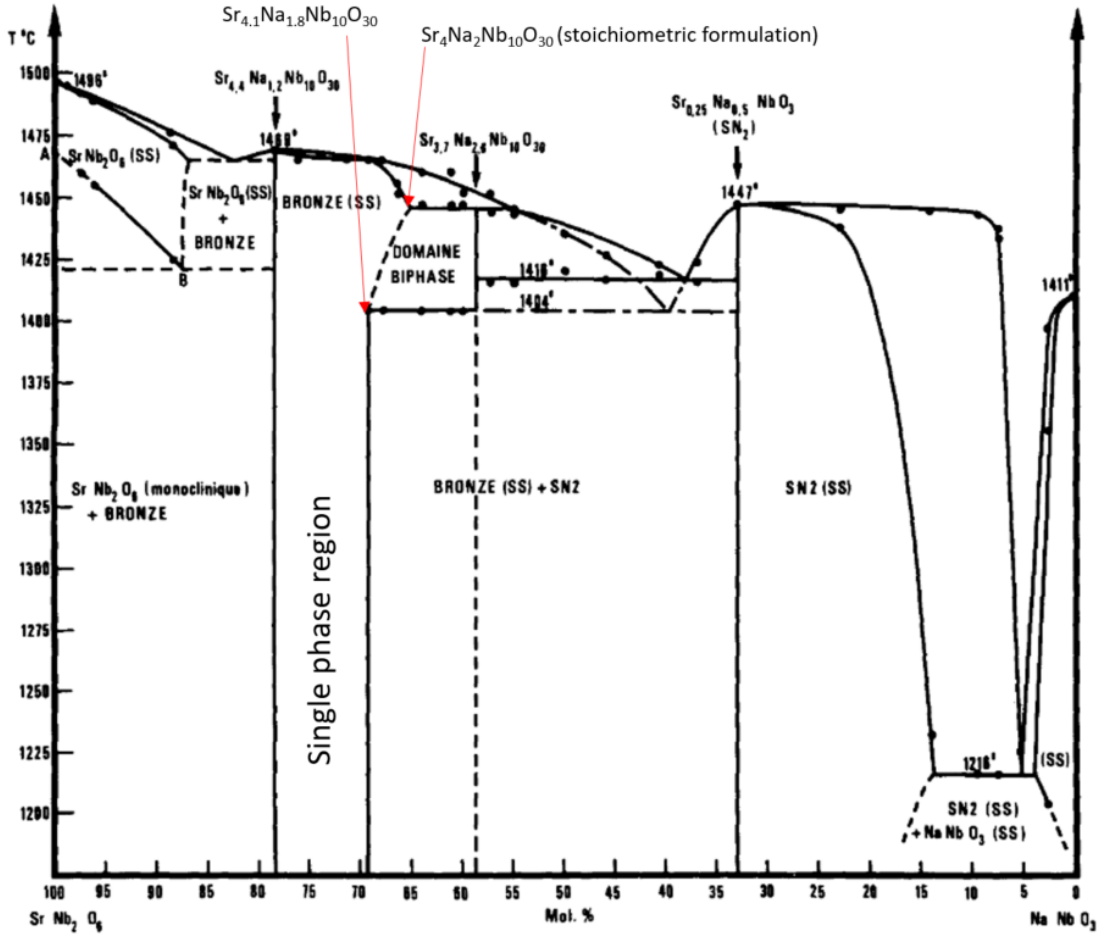

Figure 5.5.4. Phase diagram of $NaNbO_3$ – $SrNb_2O_6$ system. The metastable projected single phase region at room temperature lies between $Sr_{4.4}Na_{1.2}Nb_{10}O_{30}$ and $Sr_{4.1}Na_{1.8}Nb_{10}O_{30}$. The region widens at higher temperature (> 1400 °C) and includes the stoichiometric formulation $Sr_4Na_2Nb_{10}O_{30}$, however below this temperature it lies beyond it (reproduced from Morin et al. 1973 with annotations by the author).

All powders reported here were calcined at 1200 °C for 6 h unless otherwise stated. The results are summarised in Table 5.5.1. For this initial look at sintering routes the effect on densification was assessed by a rough estimate of percentage theoretical density calculated using that of SNN1.0 from Chapter 4 (5.03 g cm^{-3}). This was to avoid XRD measurements and unit cell refinements on potentially low density samples. All subsequent theoretical density calculations in this section are based on basic unit cell refinements of X-ray diffraction data from the relevant samples. Sintering temperatures from 1275 °C to 1450 °C were examined, with dwell times of 4 h.

A broad correlation was seen between the maximum temperature of the sintering conditions and the final density achieved (Table 5.5.1). The highest sintering temperature employed, 1450 °C, showed the highest density, 91 %.

Table 5.5.1. SNN0.8 sintering study data, showing maximum temperature, geometric and theoretical density.

Max T during sintering (°C)	Average geometric density (g/cm^3)	Percentage theoretical density compared to $Sr_2NaNb_5O_{15}$ (theoretical density 5.03g/cm3)
1275	3.49	69 %
1300	3.72	74 %
1350	4.18	83 %
1380	4.06	81 %
1450	4.58	91 %

The SNN1.0 samples reported in Chapter 4 had been sintered at 1300 °C and reached 93 % relative density. However, the SNN0.8 sample composition reached a relative density of only 74 % under the same conditions. This result suggests that SNN0.8 requires a higher sintering temperature to achieve comparable densities to SNN1.0, even though this is not consistent with Yang et al. (2017 and 2019). However, data from the SNN phase diagram (Tang et al. 1979, Figure 5.5.3) suggests that the sintering temperature of 1450 °C required to form dense SNN0.8 lies above the liquid phase limit for this composition (aproximately 1425 °C). An alternative synthesis route was found in a Nissan Motor Co. Ltd. patent (Akiume et al. 2003, US 2003/0151331 A1) which suggested dense SNN and SCNN ceramics could be produced by sintering at lower temperatures for longer periods. A two-stage extended sintering (ES) route of 1240 °C 6 h, followed by 1320 °C 25 h, as reported by Nissan, was therefore adopted and found to achieve pellets of 95 % of calculated theoretical density.

5.5.1 Phase analysis

The X-ray diffraction pattern for SNN0.8 (1450 °C, 91 %) is shown in Figure 5.5.5, alongside SNN1.0 (Figure 4.2.1, Chapter 4). Second phase $NaNbO_3$ (ICDD 04-009-3239) present in SNN1.0 was absent in SNN0.8. A full, indexed XRD of SNN0.8 made by the Nissan extended two-stage sintering route at 1240/1320 °C is shown in Figure 5.5.6 (SNN0.8 ES). It reveals the same phase as for the sample sintered at 1450 °C (Figure 5.5.5). This 1240/1320 °C extended sintering time sample will be compared against SNN1.0 and SNN0.8 (1450 °C) to probe the role of Na^+ deficiency and thermal history respectively.

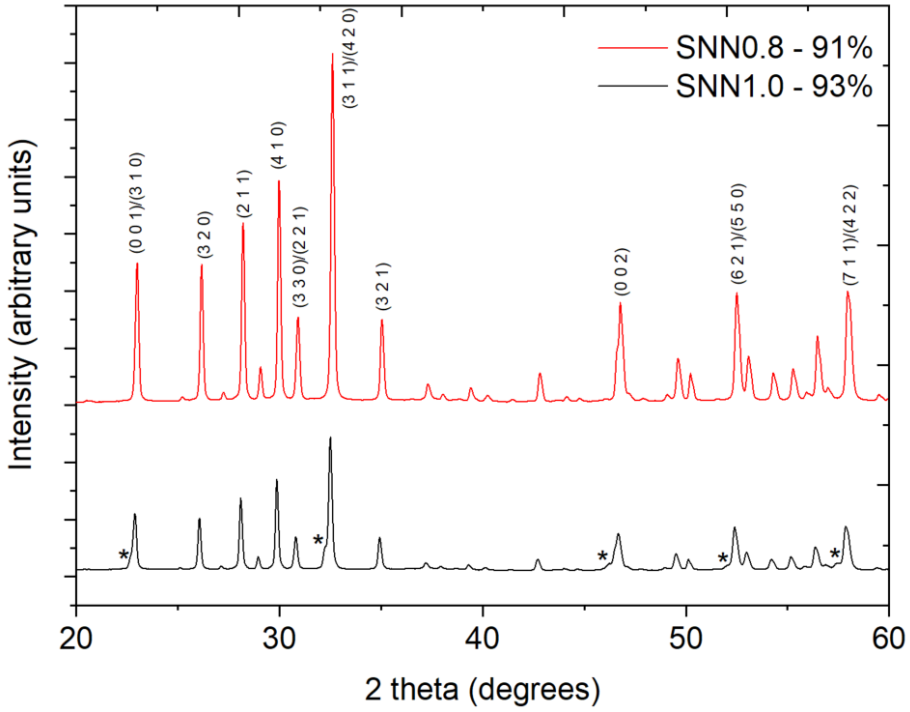

Figure 5.5.5. 12 h powder XRD plots of SNN0.8 (1450 °C, 91 %) and SNN1.0 (93 %) (Figure 4.2.1). Indexed to ICDD 04-008-7203, tetragonal SNN, *P4bm*. Second phase orthorhombic $NaNbO_3$ (*) (ICDD 04-009-3239) present in SNN1.0 is absent from SNN0.8 composition.

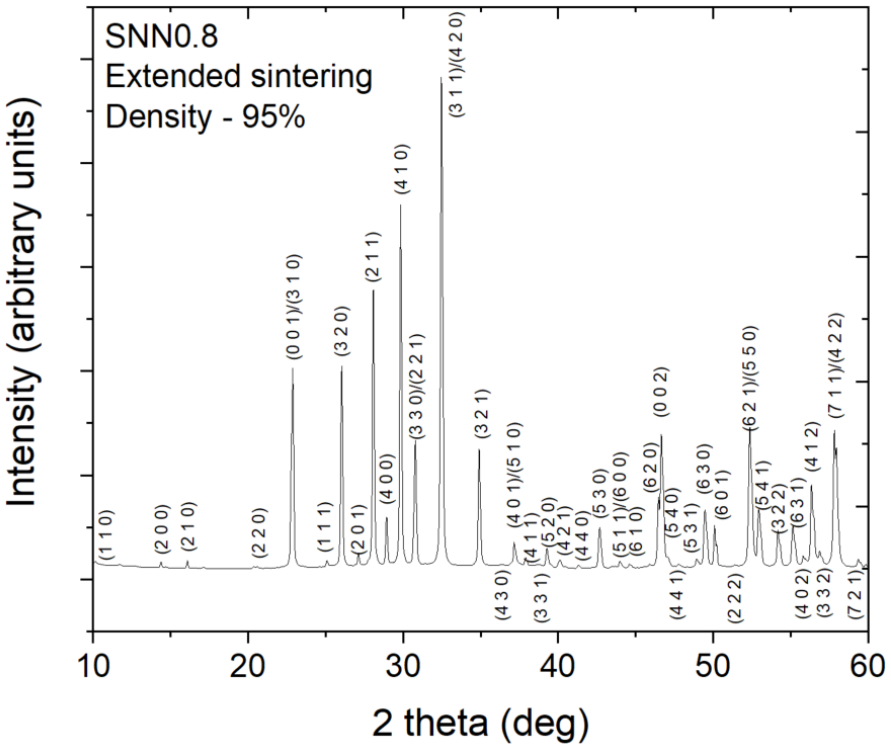

Figure 5.5.6. 12 h powder XRD plot of SNN0.8 (ES, 95 %). Indexed to ICDD 04-008-7203, tetragonal SNN, *P4bm*, indicating a single phase TTB structure has been formed. Basic unit cell refinement suggested that very low levels of $SrNb_2O_6$ may be present (Table 5.4.2).

Crystallographic data from basic unit cell refinements of SNN0.8 (1450 ^oC) and SNN0.8 (1240/1320 ^oC, ES) are summarised in Table 5.5.2. No second phase $NaNbO_3$ (or Sr modified $NaNbO_3$) was detected in the XRD patterns (Figures 5.5.5 and 5.5.6). Small quantities of $SrNb_2O_6$ (< 1 wt. %) were possibly detected by refinement but clear, unambiguous XRD peaks for the phase were not identified. Unit cell parameters and unit cell volume remained constant for SNN1.0 and SNN0.8 compositions.

Table 5.5.2. Crystallographic data for SNN1.0, and SNN0.8 (1450 °C and extended sintering), from X-ray powder diffraction unit cell refinements.

Composition	*a* = *b* Å	*c* Å	Volume Å^3	Geometric density g/cm^3	Percentage theoretical density	Tetragonality c/a	2nd phase wt. %	R_{WP} %
SNN1.0, density 93%	12.37	3.896	596.2	4.68	93 %	0.31	5.8 $NaNbO_3$	11.5
SNN0.8 (1450 °C), density 91%	12.37	3.896	596.2	4.58	91 %	0.31	-	13.2
SNN0.8 (1240/1320 °C, ES), density 95%	12.36	3.894	594.9	4.82	95 %	0.32	-	14.6

5.5.2 Dielectric analysis

Figure 5.5.7 a-c shows multi-frequency temperature dependence of the relative permittivity and dielectric loss tangents for both SNN0.8 compositions. A 1 kHz comparison plot (with SNN1.0) is also shown and dielectric data are summarised in Table 5.5.3. Permittivity peaks were present at T_1 and T_2 in SNN0.8, as in previous compositions. The T_2 peak ε_r value was suppressed from 2145 for SNN1.0 to 1665 for SNN0.8 (1450 °C) and 1975 for SNN0.8 (1240/1320 °C, ES). This suppression was accompanied with increased T_2 peak broadening for SNN0.8 (1240/1320 °C, ES), the temperature range at FWHM increasing from ~40 °C for SNN1.0 and SNN0.8 (1450 °C) to 80 °C for SNN0.8 (1240/1320 °C, ES). The T_2 peak temperature increased from 305 °C for SNN1.0, to 320 °C for SNN0.8 (1450 °C). A decrease to 280 °C was recorded for SNN0.8 (1240/1320 °C, ES). The large decrease in ε_r value when sintering at 1450 °C raises questions about the effect of thermal history on the electrical properties of SNN0.8, although density differences were another factor to consider. In fact the study of the effects of density and grain size (e.g. strain effects) on both T_1 and T_2 peak profiles and temperatures should form a key component of future work. The Na^+ deficiency in SNN0.8 also caused a decrease in T_1 temperature from -15 °C for SNN1.0 to ~45 °C for SNN0.8, and an

increase in ε_r value from 1715 for SNN1.0 to 1880 and 1990 for SNN0.8 1450 ^oC and 1240/1320 ^oC ES respectively.

Both SNN0.8 compositions were more relaxor like than SNN1.0, with greater frequency dependence for temperature and ε_r value between 1 kHz and 1MHz. Differences in temperature values between these frequencies increased from 9 ^oC for SNN1.0, to 24 ^oC for SNN0.8 (1450 ^oC), and 27 ^oC for SNN0.8 (1240/1320 ^oC, ES). In the absence of dopants to induce relaxor properties through compositional/structural disorder, this could be related to increased vacancies on A-sites caused by Na^+ deficiency.

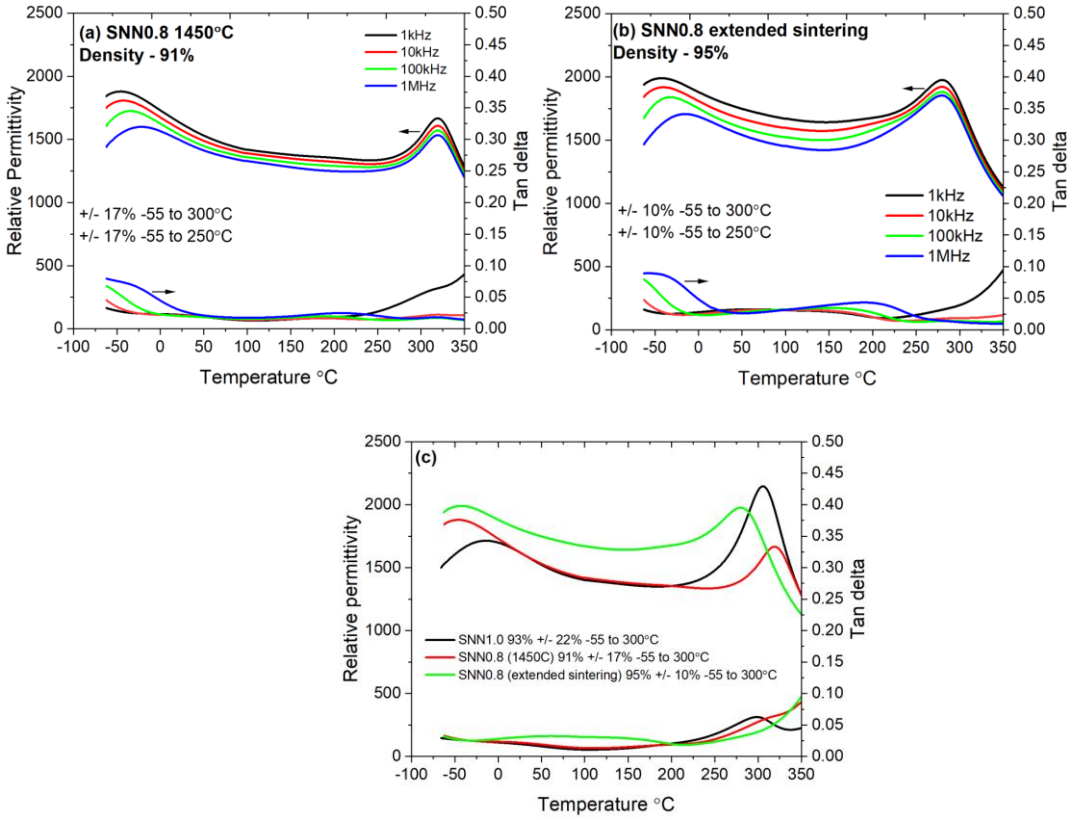

Figure 5.5.7 a-c. Multi-frequency relative permittivity and dielectric loss tangent versus temperature plots for a) SNN0.8 (1450 ^oC) and b) SNN0.8 (1240/1320 ^oC ES). c) 1kHz comparison plot including SNN1.0.

Table 5.5.3. 1 kHz relative permittivity and loss tangents versus temperature data for SNN0.8 (1450 °C), SNN0.8 (1240/1320 °C ES), and SNN1.0.

Composition	T_1 °C ($\varepsilon_{r\ max}$)	T_2 °C ($\varepsilon_{r\ max}$)	+/- % (-55 - 250°C)	+/- % (-55 - 300°C)	tan δ ≤0.025 °C	tan δ ≤0.030 °C	tan δ ≤0.035 °C
SNN1.0, density 93%	-15 (1714)	306 (2146)	12%	22%	-32 to 223	-65 to 238	-65 to 249
SNN0.8 (1450 °C), density 91%	-46 (1879)	319 (1667)	17%	17%	-32 to 243	-53 to 256	-62 to 267
SNN0.8 (1240/1320 °C, ES), density 95%	-42 (1990)	280 (1976)	10%	10%	176 to 256	-60 to 276 (but rises above 20 to 98)	-62 to 290

The permittivity-temperature variation improved for SNN0.8 (1450 °C) (+/- 17 %) and SNN0.8 (1240/1320 °C, ES) (+/- 10 %) compared to SNN1.0 (+/- 22 %) at -55 to 300 °C about a median permittivity. This was due partially to the decrease in T_2 $\varepsilon_{r\ max}$ value from SNN1.0 (2145) to SNN0.8 (1450 °C) (1670) and SNN0.8 (1975), and secondly, an increase in the base level permittivity from a space charge effect caused by increased vacancies. The ε_r values at 100 °C were 1400 for SNN1.0, 1420 for SNN0.8 (1450 °C), and 1670 for SNN0.8 (1240/1320 °C, ES).

Dielectric loss tangents at 1 kHz for the three compositions are summarised in Table 5.5.3. Losses for SNN1.0 and SNN0.8 (1450 °C) were similar, whilst those for SNN0.8 (1240/1320 °C, ES) were ≤ 0.035 over a larger temperature range (-62 to 290 °C). However, they were generally higher across the whole temperature range (e.g. ≤ 0.025 176 to 256 °C) due to a rise between approximately 20 to 100 °C, correlating with the increased base level permittivity at these temperatures.

It is noted that SNN0.8 will contain 'inherent' Na vacancies ($V_{Na'}$): $Sr_{2.1}Na_{0.8}Nb_5O_{15}$, $0.1V_{Na'}$. The results imply that the Na^+ deficiency/vacancies in SNN0.8 may be the reason for the changes in electrical properties (both relative

permittivity and dielectric losses) described above. The above results for SNN0.8 are consistent with it having more A-site vacancies than other SNN1.0 based compositions.

5.5.3 Ferroelectric analysis

The P-E hysteresis loops at 40 kV cm^{-1} are shown in Figure 5.5.8, with data summarised in Table 5.5.4. Typical ferroelectric loops are seen at room temperature and the loops were similar in appearance. Value of P_{max} fell from 13 µC cm^{-2} for SNN1.0, to 11 µC cm^{-2} for SNN0.8 (1240/1320 ^{o}C, ES), then 10 µC cm^{-2} for SNN0.8 (1450 ^{o}C), in line with falling T_2 ε_r value and increasing maximum sintering temperature (Table 5.4.3). Increasing coercive field, E_c, from 12 kV cm^{-1} for SNN1.0 to 15 kV cm^{-1} for SNN0.8 (1450 ^{o}C), and 17.5 kV cm^{-1} for SNN0.8 (1240/1320 ^{o}C, ES), suggests vacancies make the material harder, possibly with a domain pinning mechanism. This contrasts with doped compositions of SNN1.0 where dopants have a larger effect on the polarisation (Figures 5.2.5 and 5.3.4).

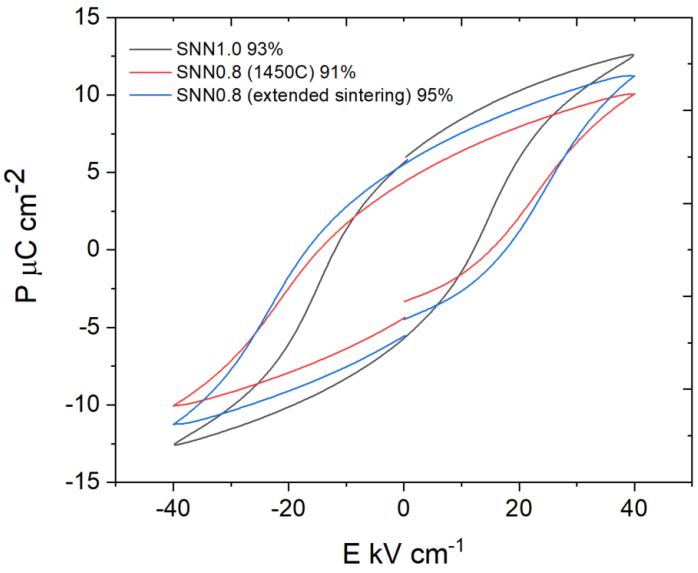

Figure 5.5.8. 40 kV cm^{-1} polarisation – electric field loop plots for SNN1.0, SNN0.8 (1450 ^{o}C) and SNN0.8 (1240/1320 ^{o}C, ES).

Table 5.5.4. Remnant polarisation (P_r) and coercive field (E_c) data at 40 kV cm^{-1} for SNN0.8 (1450 ^oC) and SNN0.8 (1240/1320 ^oC, ES).

Composition	P_r $\mu C\ cm^{-2}$ (+/- 0.5)	E_c $kV\ cm^{-1}$ (+/- 0.5)	P_{max} $\mu C\ cm^{-2}$ (+/- 0.5)
SNN1.0, density 93 %	5.5	12	13
SNN0.8 (1450 ^oC) density 91 %	4.5	15	10
SNN0.8 (1240/1320 ^oC, ES) density 95 %	5.5	17.5	11

5.5.4 Microstructural analysis

Back scattered scanning electron micrographs of SNN0.8 showed a single phase material with only pores present (consistent with 93 % density), unlike unmodified SNN1.0. The darker Na^+ rich grains seen in SNN1.0 (Figure 5.5.9 a) were absent from SNN0.8 (Figure 5.5.9 b-c), consistent with lack of $NaNbO_3$ diffraction peaks displayed in Figure 5.5.6. Maximum grain size in both SNN0.8 and SNN1.0 was approximately 17 µm, but the grain size generally increased in the SNN0.8 composition. Grains in SNN1.0 were generally between 2 and 4 µm, increasing in SNN0.8 to between 4 and 10 µm.

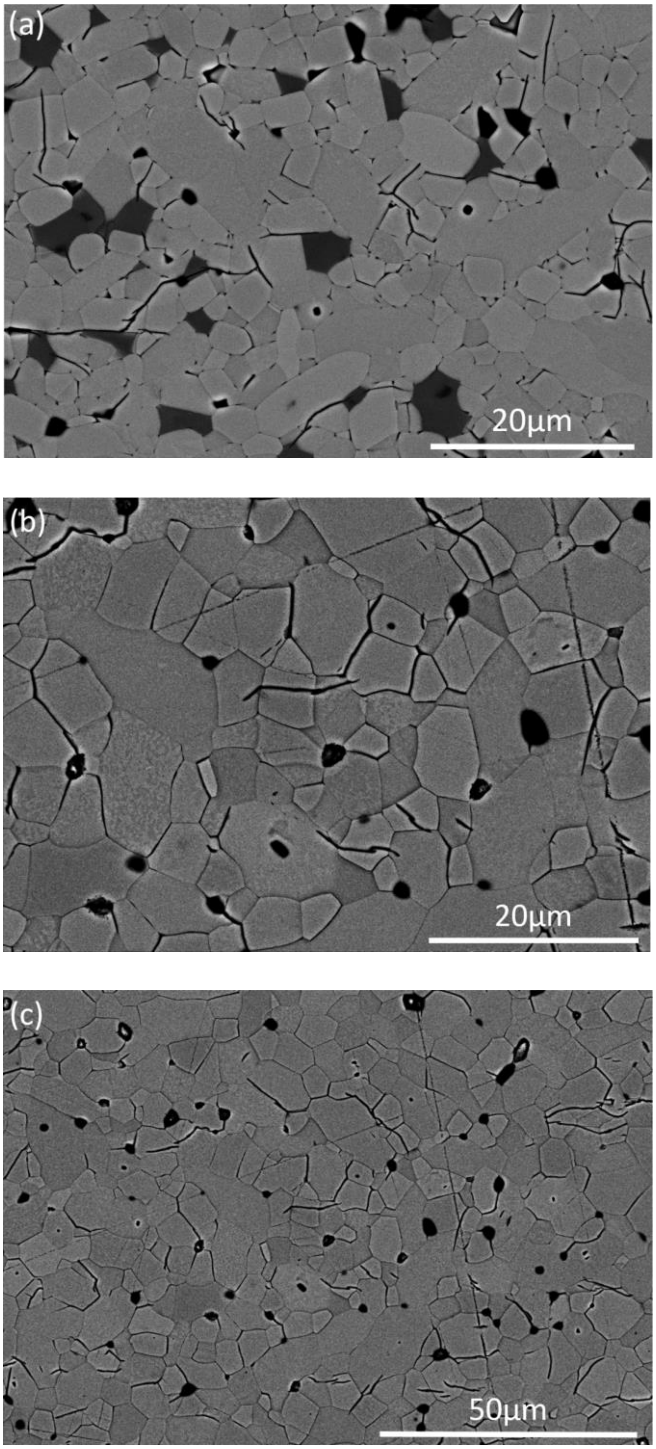

Figure 5.5.9. Back scatered scanning electron micrographs of a) SNN1.0, b) and c) SNN0.8 (1240/1320 ^{o}C, ES). Maximum grain size of SNN0.8 (1240/1320 ^{o}C, ES) was 17 µm, with grains generally from 4 to 10 µm. Grains in SNN1.0 were generally from 2 to 4 µm.

5.6 SNN0.8 co-doped with Ca, Y (for Sr), and Zr (for Nb)

The SNN0.8 composition was doped with equal levels of Ca^{2+}, Y^{3+}, and Zr^{4+}, to imitate the optimum sample from Chapter 4 (Section 4.31), $Sr_{2-2x}Ca_xY_xNaNb_{5-y}Zr_yO_{15}$, x = 0.05, y = 0.05 (SCNN-YZ 1.0). The formula was therefore $Sr_{2.1-x-y}Ca_xY_xNa_{0.8}Nb_{5-y}Zr_yO_{15}$, x = y = 0.05 (SCNN-YZ 0.8). The sample was sintered with an extended sintering run used for SNN0.8 (1240/1320 ^oC, ER) and produced pellets with an approximated density of 93 % of theoretical density. From the previous results the composition was expected to be show reductions in polarisation and $\varepsilon_{r\ max}$, and fewer losses compared to SNN0.8 due to the presence of dopants. It was also predicted to be phase pure and possibly show a space charge effect due to Na (A-site) vacancies.

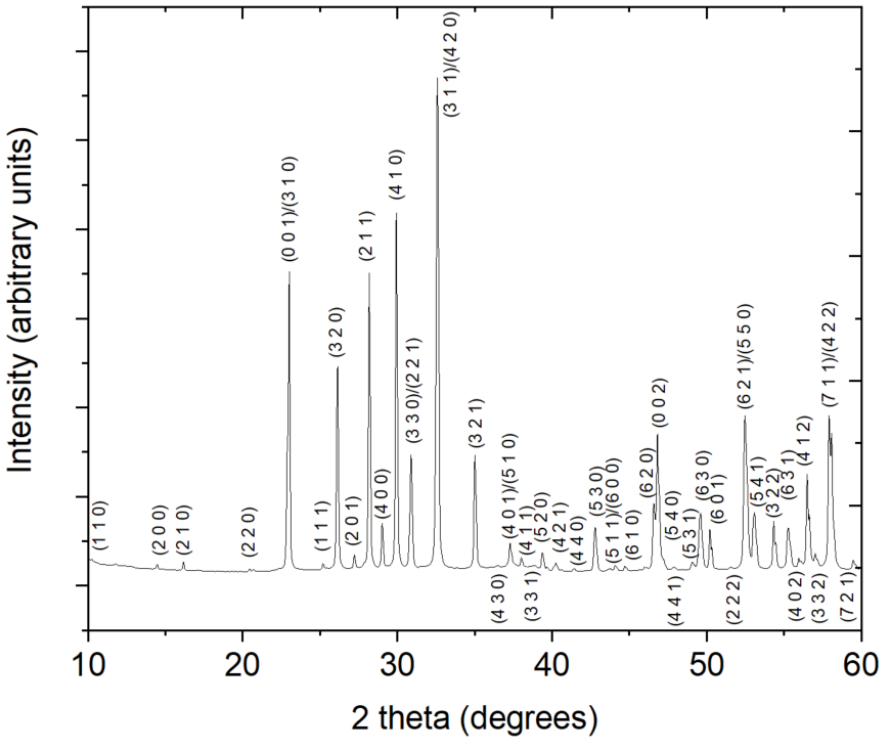

Figure 5.6.1. 12 hour powder XRD plots of $Sr_{2.1-2x}Ca_xY_xNa_{0.8}Nb_{5-y}Zr_yO_{15}$. Indexed to ICDD 04-008-7203, tetragonal SNN, *P4bm*. Second phase $NaNbO_3$ peaks were not observed.

XRD patterns (Figure 5.6.1) showed a single phase material like SNN0.8 (1240/1320 ^{o}C, ES) (Figure 5.5.6). Theoretical densities were less accurate than for preceding samples, for which HighScore refinement of lattice parameters was performed, the main purpose of co-doping SNN0.8 being a simple scope of the permittivity response. SEM and SEM-EDX was consistent with the XRD, showing a single phase material with no darker Na^{+} rich grains (Figures 5.6.2 and 5.6.3). No second phase ZrO_2 was detected in SCNN-YZ 0.8, which may have been expected, given its presence in SCNN-YZ 1.0 (Chapter 4, Figure 4.3.8). Grain size generally increased from 4 to 10 µm in unmodified SNN0.8 (Figure 5.5.9 b-c), to 5 to 15 µm in SCNN-YZ 0.8 with the addition of dopants. This increase was similar to that seen in SNN1.0 with the same level of doping, where the grain size increased from between 2 to 4 µm in SNN1.0, to between 3 to 9 µm in SCNN-YZ 1.0 (Chapter 4, Section 4.3.4).

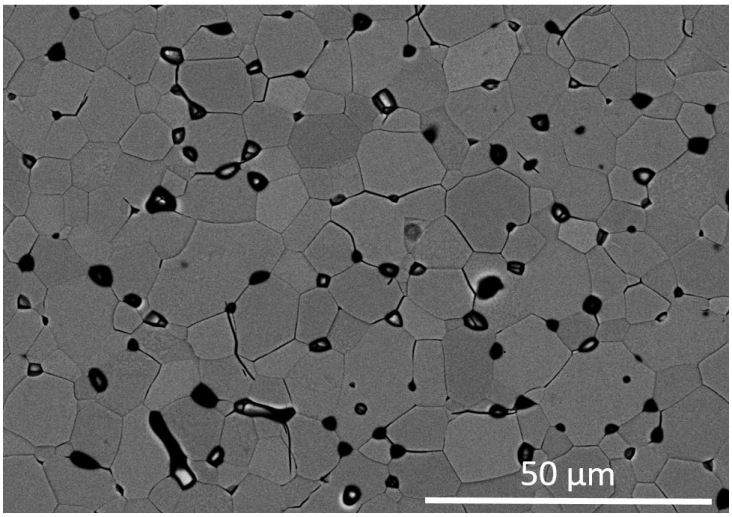

Figure 5.6.2. Back scattered scanning electron micrograph of $Sr_{2.1-2x}Ca_xY_xNa_{0.8}Nb_{5-y}Zr_yO_{15}$ (SCNN-YZ 0.8).

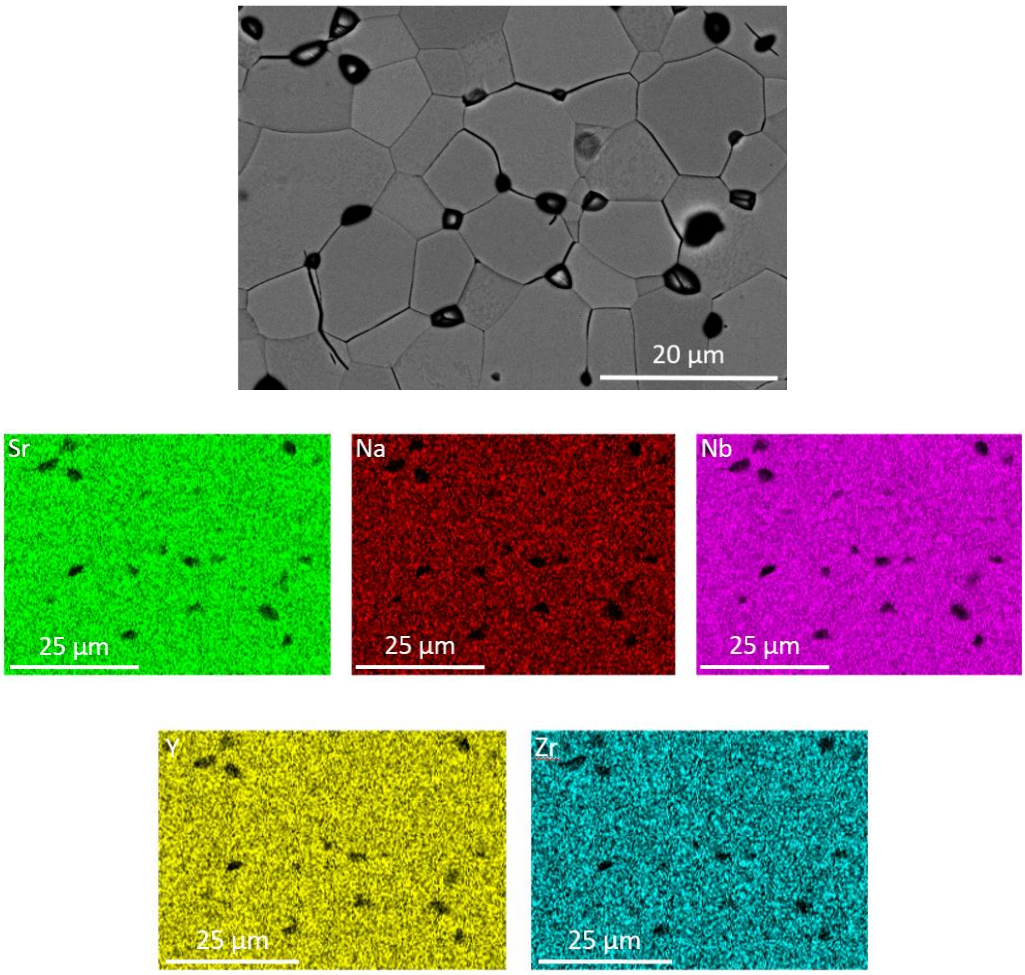

Figure 5.6.3. SEM-EDX maps of $Sr_{2.1-2x}Ca_xY_xNa_{0.8}Nb_{5-y}Zr_yO_{15}$ (SCNN-YZ 0.8) showing single phase material and homogenous distribution of elements.

Figures 5.6.4 a-b show the multi frequency relative permittivity and dielectric loss tangent versus temperature plots for SCNN-YZ 0.8, and a plot comparing the 1 kHz data to SCNN-YZ 1.0 respectively. SCNN-YZ 0.8 clearly shows a third permittivity peak (T_3), below T_2. The additional peak, T_3, is frequency dependent (peak temperature and $\varepsilon_{r\,max}$ value) and is not observed at 1 MHz (barely detectable at 100 kHz). A similar feature was also seen in SNN-YZ (x = 0.05, Figure 5.3.2 c). Other studies on doping SNN0.8 for SNN-Y (x = 0.05 for Na^+, Na^+ = 0.8) also display T_3 (Figure 5.6.5) (Gardener. J, University of Leeds). Cao et al. (2021) reported a similar effect in $Sr_{2-x}Gd_xNaNb_{5-x}Ti_xO_{15}$ (x = 0.05 and 0.08) and related its frequency dependent nature to the fact it only undergoes slow polarisation methods such as space charge polarisation. As was suggested in the summary of Section 5.3, this is thought to be related to vacancies in the material causing the space charge effect.

As both the compositions in Figures 5.6.4 a, and 5.6.5 contain $Na_{0.8}$, they will have intrinsic vacancies within the structure that may lead to this effect and correspondingly high losses.

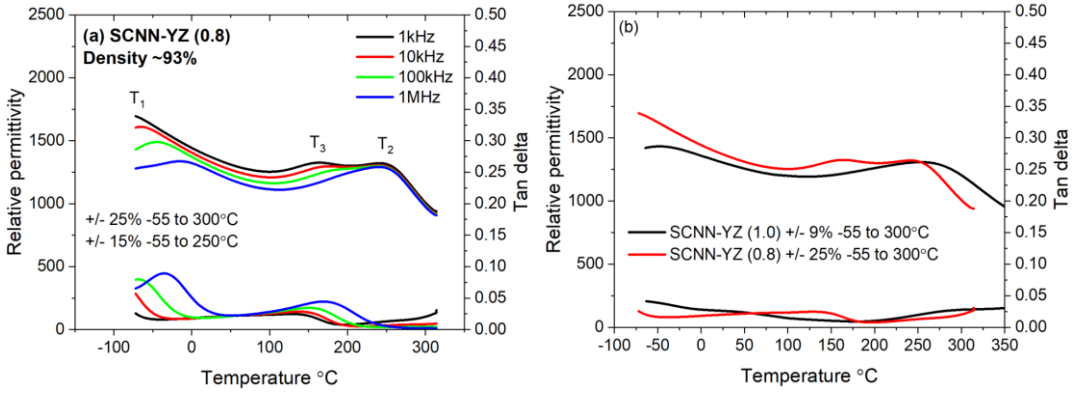

Figure 5.6.4. a) Multi-frequency relative permittivity and dielectric loss tangent versus temperature plots for $Sr_{2.1-2x}Ca_xY_xNa_{0.8}Nb_{5-y}Zr_yO_{15}$ x = 0.05, y = 0.05. b) 1 kHz comparison plot of $Sr_{2.1-2x}Ca_xY_xNa_{0.8}Nb_{5-y}Zr_yO_{15}$ against optimum composition from Chapter 4, $Sr_{2-2x}Ca_xY_xNaNb_{5-y}Zr_yO_{15}$, with permittivity-temperature variation of +/- 9 %, -55 to 300 °C. An extra permittivity peak (T_3) is present just below temperature of T_2 peak.

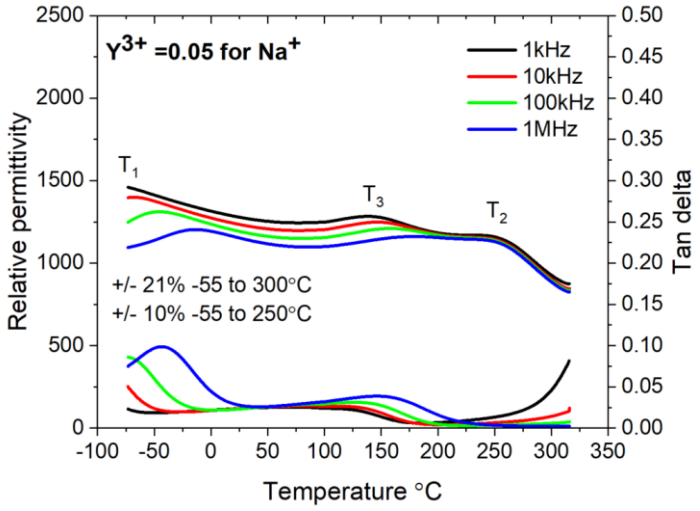

Figure 5.6.5. Multi-frequency relative permittivity and dielectric loss tangent versus temperature plots for $Sr_{2.1}Y_xNa_{0.8-3x}Nb_5O_{15}$, x = 0.05, with Y^{3+} substituting for Na^+. An extra permittivity peak (T_3) is present just below T_2 (Gardener. J, University of Leeds).

5.7 Summary section 5.5 controlled Na^+ deficiency $Sr_{2.1}Na_{0.8}Nb_5O_{15}$ (SNN0.8), and 5.6 co-doping SNN0.8 with Ca, Y, and Zr

Dense ceramics (95 % relative density) of formulation $Sr_{2.1}Na_{0.8}Nb_5O_{15}$ (SNN0.8) were made with a two-stage extended sintering run (> 25 h) at a maximum temperature of 1240/1320 ^oC. For shorter sintering runs (e.g. 4 h), it was found that for SNN0.8 a much higher temperature (1450 ^oC) was required to achieve comparably high densities. The higher sintering temperature (1450 ^oC) was found to be above the liquid phase limit reported for SNN (Figure 5.5.3 and 5.5.4). Second phase $NaNbO_3$ (or Sr modified $NaNbO_3$) which was persistent in SNN1.0 was eliminated for both sets of SNN0.8 sintering conditions (Figures 5.5.5 and 5.5.6). This is thought to be because of the inherent vacancies found in the “unfilled” SNN0.8 composition decrease and stabilise Madelung energy that otherwise can lead to second phase formation (Jang et al. 2004, see Section 5.2). This was also the case for the SCNN-YZ0.8 composition (Section 5.5) and the single doped SNN-Y0.8 (Y^{3+} for Na^+, Gardener. J, University of Leeds, Section 5.5). Both these compositions from Section 5.5 showed a third dielectric anomaly, also possibly related to vacancies and their creation of space charge polarisation at low frequencies. This could also be the reason for the raised baseline of permittivity seen in SNN0.8 (Figure 5.5.7 b).

The “unfilled” SNN compositions increased in grain size from 2 to 4 µm in SNN1.0, to 4 to 10 µm in SNN0.8. A further increase was seen with the addition of dopants from 5 to 15 µm in SCNN-YZ 0.8. The different sintering regimes between the SNN0.8 (1320 ^oC, 25 h) and SNN1.0 (1300 ^oC, 4 h) could relate to this as well as the compositional variations (vacancies) between the two.

The compositional change from SNN1.0 to SNN0.8 affected the electrical properties in a similar way to the addition of dopants (Section 5.2), making them more relaxor-like at T_1 and decreasing the T_2 $\varepsilon_{r\,max}$ value. Whilst adding dopants to SNN1.0 caused predominantly a drop in polarisation (P_{max}) in the P-E loops (Figures 5.2.5 and 5.3.4), in SNN0.8 the main effect observed was an increase in E_c.

However the vacancies in SNN0.8 did induce losses at high temperatures, and space charge effects at intermediate temperatures between T_1 and T_2. The drop in T_2 $\varepsilon_{r\,max}$ value for SNN0.8 1450 ^{o}C (1670, dropping from 2145 in SNN1.0, compared to 1975 in SNN0.8 1240/1320 ^{o}C, ES) was so pronounced that it raised the possibility that the thermal history of the sample was adversely altering the permittivity response. Thermal stability will be explored in more detail in Chapter 6.

Future studies should focus on a composition intermediate between the SNN1.0 and SNN0.8 compositions (SNN0.90 and 0.95) which would contain fewer vacancies but may still be single phase (Morin et al. 1973).

Chapter 6. Long term temperature stability of strontium sodium niobate (SNN) tetragonal tungsten bronzes

6.1 Introduction

Investigations into controlled Na^+ deficiency in Chapter 5 (Section 5.5) illustrated that a single phase SNN could be produced with the formula $Sr_{2.1}Na_{0.8}Nb_5O_{15}$ (SNN0.8). This was due to the fact that, unlike $Sr_2NaNb_5O_{15}$ (SNN1.0), SNN0.8 lies within the single phase field of the $NaNbO_3$ – $SrNb_2O_6$ system as shown in the metastable phase diagram reported in a Chinese language journal by Tang et al. (1979) (Figure 6.1.1). The metastable phase relations were determined from samples that underwent normal furnace cooling after high temperature processing (6 ^oC/min, 1300 ^oC, dwell 50 h). However the same authors reported an equilibrium phase diagram, constructed from XRD data of samples annealed for many hours at fixed temperatures (900, 1000, 1100 and 1300 ^oC for 200-300 h), (Figure 6.1.2). The latter diagram indicated that SNN is thermodynamically unstable below 1180 ^oC (Figure 6.1.2) (Figure 6.1.1 reproduced from Chapter 5, Section 5.5).

The purpose of this chapter was to study the temperature stability of SNN materials at the intended upper limits of operating temperatures of 300 ^oC, 400 ^oC and 600 ^oC maximum. The aim of this study being to discover if the material is practically metastable at or close to the intended capacitor operating temperature, and the rate of change associated with any decomposition at these temperatures. A structural study was first undertaken to determine thermal stability of the material (Section 6.2), followed by repeated permittivity-temperature measurements (Section 6.3).

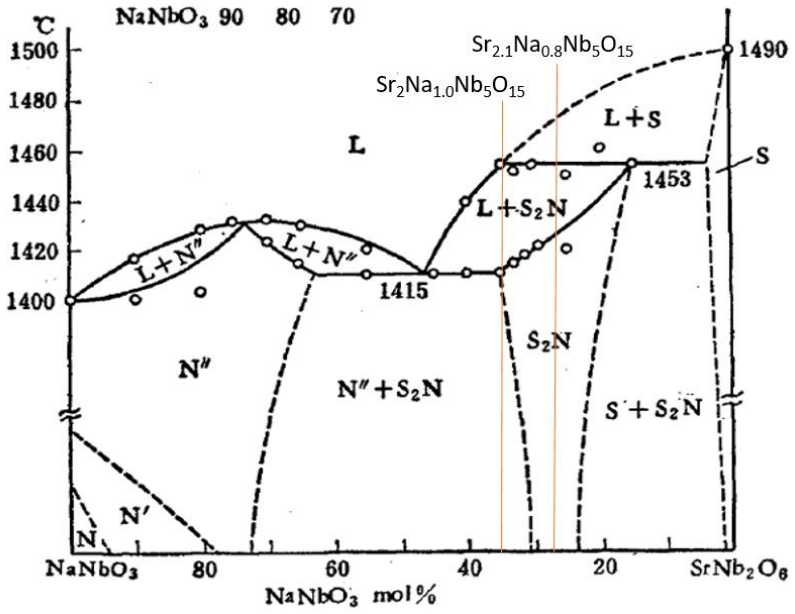

Figure 6.1.1. Metastable phase diagram of $NaNbO_3$ – $SrNb_2O_6$ system (reproduced from Tang et al. 1979).

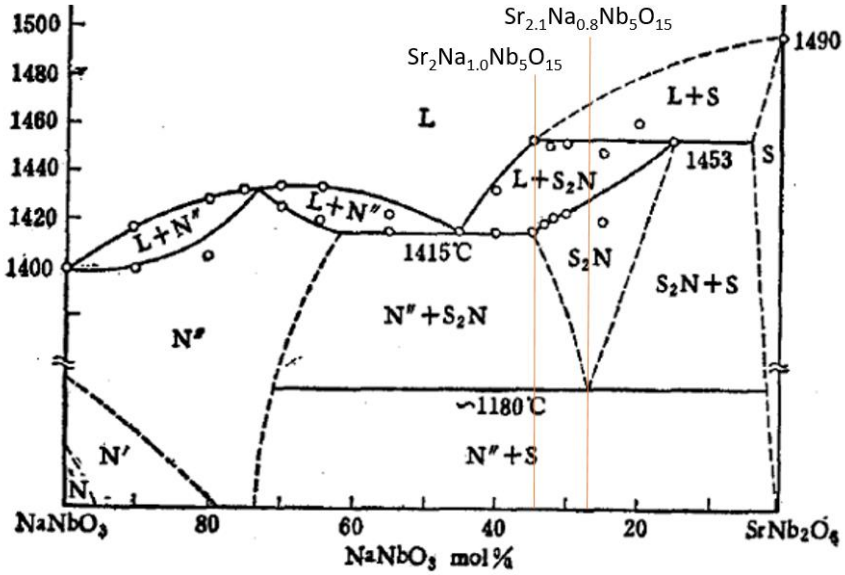

Figure 6.1.2. Equilibrium phase diagram of $NaNbO_3$ – $SrNb_2O_6$ system. SNN solid solution (labelled S_2N here) with formula $Sr_{2+x}Na_{1-2x}Nb_2O_6$ showing thermal instability of SNN below 1180 °C, where it becomes more stable as a two phase mixture of $NaNbO_3$ and $SrNb_2O_6$ (reproduced from Tang et al. 1979).

6.2 Phase analysis after annealing

Long term structural studies by XRD (at 24 to 45 weeks) of the thermal effect on calcined powder of $Sr_2NaNb_5O_{15}$ (SNN1.0), was conducted to identify any thermal decomposition i.e. compositional and structural changes. In-situ temperature variable X-ray diffraction measurements were taken at 600 ^oC and 400 ^oC (up to 50 h and 24 h respectively) (data acquisition by Dr F. Esat, University of Leeds; all data analysis/indexing is the work of the author). Samples of powder were also aged in furnaces held at 300 ^oC and separate samples held at 600 ^oC: room temperature XRD measurements were recorded periodically. These periodic room temperature measurements were also conducted at the same annealing temperatures with $Sr_{2-x-y}Ca_xY_xNaNb_{5-y}Zr_yO_{15}$, x = 0.05, y = 0.05 calcined powder (SCNN-YZ) (Chapter 4, Section 4.3). Crushed, fully sintered pellets of $Sr_{2.1}Na_{0.8}Nb_5O_{15}$ (SNN0.8) were also tested. The crushed, reaction sintered SNN0.8 produced using an extended sintering run (1240 ^oC 6 h, followed by 1320 ^oC 25 h, see Chapter 5, Section 5.5) were aged at 300 ^oC and 400 ^oC.

6.2.1 Methodology

In-situ X-ray diffraction was performed on a Malvern Panalytical, Empyrean with an Anton Parr HTK1200 stage, 45kV 40mA (data acquisition by Dr F. Esat, University of Leeds). An initial 30 min room temperature scan was performed before the annealing run, i.e. zero time. Heating then proceeded to 600 ^oC at 60 ^oC/min and after this temperature was reached, 10 min scans were performed from 10 to 60 $^o2\theta$ with step size 0.026 degrees every 10 min up to one hour. Following this a 30 min scan was performed every hour up to 50 h, and then again on cooling to room temperature, all with the same measurement parameters.

In a departure from Chapters 4 and 5 where a non-centrosymmetric tetragonal *P4bm* structure has been used to index all SNN structures at room temperature, here indexing to the orthorhombic *Im2a* structure identified by Torres-Pardo et al. (2011) was undertaken (ICDD 04-018-2808). This is because: a) the majority of workers now agree that an orthorhombic structure is likely for SNN at room temperature and b) 30 minute log (intensity) plots of the laboratory X-ray diffraction data carried out on

the Malvern Panalytical, Empyrean do reveal the small superlattice peaks of the orthorhombic phase. This is consistent with Garcia-Gonzalez et al. (2007) who reported room temperature (300 K) XRD data of $S_2NaNb_5O_{15}$ (some second phase Sr modified $NaNbO_3$ was present in the sample) indexed to the orthorhombic *Im2a* space group at room temperature. Their assignment to *Im2a* was identified with the aid of TEM- SAED at 300 K is reported in Torres-Pardo et al. (2011), and is also listed in ICDD file 04-018-2808. Garcia-Gonzalez et al. (2007) show the orthorhombic *Im2a* structure transforming to the centrosymmetric tetragonal *P4mbm* structure on heating from 300-720 K (27 to 447 ^oC) (Figure 6.2.1). Their XRD data are listed in ICDD 04-014-7370 for the *P4mbm* structure. They report the development of additional peaks to *Im2a* due to scattering from the (*hk*0) peaks being permitted by the tetragonal structure (Figure 6.2.1 below), plus the loss of minor orthorhombic superlattice reflections. That is, (*hk0*) reflections will be effected more in comparison to (*00l*) and (*hkl*) reflections becaust the *c*-axis halves but the *a* and *b* axis decrease by non-integer amounts. In addition, they assert that no other structural changes are evident on short, in-situ XRD scans up to 1500 K i.e. they report no change in the second phase content using relatively low signal to noise in-situ XRD scans.

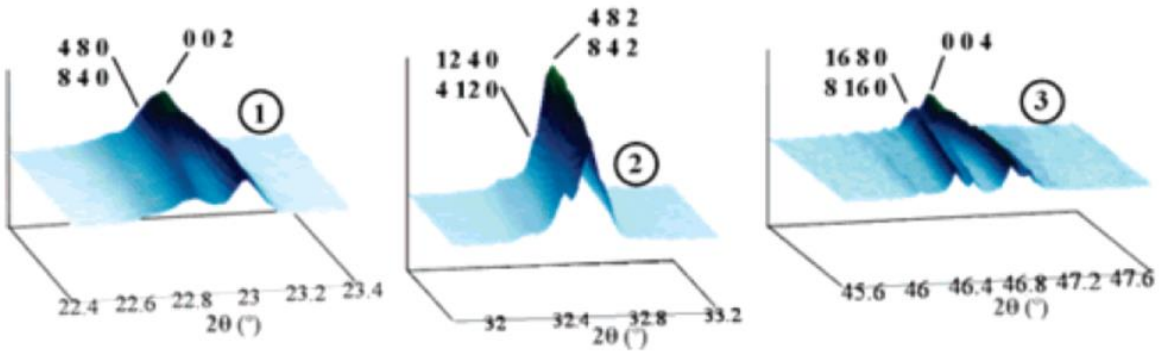

Figure 6.2.1. Temperature-dependent, in-situ powder X-ray diffraction data for $Sr_2NaNb_5O_{15}$ with some second phase $NaNbO_3$ (reported in and reproduced from Garcia-Gonzalez et al. 2007). Enlargement of three different 2-theta zones in three dimensions shows peak splitting due to additional reflections from (*h,k,*0) peaks on heating from 300 K (back, orthorhombic structure) to 700 K (front, tetragonal structure).

6.2.2 Overview of phase analysis reported in rest of Section 6.2

The work in the remainder of this Chapter investigates the thermal instability of the SNN phase and to help guide the reader an overview of the phases that form at each temperature with an indication of the quantities formed too is given in the Table below (Table 6.2.1). Heating was undertaken from 300 to 600 ^{o}C and SNN remained the main phase throughout all the time periods recorded, however, the structure is shown to convert from the room temperature orthorhombic *Im2a* phase to the tetragonal *P4mbm* phase on heating to temperatures above 400 ^{o}C. The tetragonal phase is seen to be retained on cooling to room temperature after heating to 600 ^{o}C. The composition of the SNN phase also must change on heating above 300 ^{o}C because new strontium niobate phases are shown to form in increasing concentration at higher temperatures and longer hold times. As will be shown in subsequent sections, phase identification has been undertaken by XRD and the key findings are summarised in the table below with the actual patterns and data analysis shown in more detail in the subsequent sections. A brief summary of Table 6.2.1 is given below.

When annealed at 600 ^{o}C the structure of compositions SNN1.0 and SCNN-YZ calcined powders changed from orthorhombic *Im2a* to tetragonal *P4mbm* on passing through T_c. Compositional change also occurred with strontium niobate phases developing in SNN1.0 after 2 to 3 h, then increasing with time up to 45 weeks. Sodium niobate was also seen to increase with time at 600 ^{o}C in SNN1.0. SCNN-YZ showed similar decomposition at 600 ^{o}C between 0 and 20 weeks. The development of extra phases in SNN1.0 up to 50 h prevented the structure from returning to an orthorhombic structure on cooling to room temperature, thus remaining tetragonal.

In situ X-ray diffraction on SNN1.0 annealed up to 24 h at 400 ^{o}C showed structural change to the tetragonal phase of SNN but no new phase formation and $NaNbO_3$ content remaining constant. Accordingly the SNN structure returns to orthorhombic on cooling to room temperature. SNN0.8 annealed up to 24 weeks at 400 ^{o}C with XRD measurements taken at room temperature displayed structural change to tetragonal and the formation of extra phases, but at a lower level than the comparable SNN1.0, 20 weeks, 600 ^{o}C.

At 300 °C, all compositions showed no development of extra phases up to 24/25 weeks. Although there was tentative evidence that some structural breakdown might begin to occur given enough time, higher resolution/lower signal to noise ratio data would be needed to confirm this, and the SNN phase appeared to remain orthorhombic throughout.

Table 6.2.1. Relative peak intensity in relation to the main SNN peak. N.B. complete absence of $Sr_2Nb_{10}O_{27}$ in some samples could be due to low scan quality making identification difficult. Comparable heat treatments and time lengths are highlighted for different compositions.

Composition	Heated to °C	Time	$SrNb_2O_6$ 29.1 °2θ (SN1)	$Sr_2Nb_{10}O_{27}$ 13.9 °2θ (SN2)	NaNbO3 (Sr modified) 32.2 °2θ (NN)	Indexed phase
SNN1.0 Calcined powder	RT	0 time	-	-	9.1 %	Orthorhombic
	300	2 weeks	5.2 %	-	15 %	Orthorhombic
	300	24 weeks	4.4 %	0.5 %	14.5 %	Orthorhombic
	400	24 hours	-	-	8.7 %	Tetragonal
	600	50 hours	2.7 %	0.5 %	32.2 %	Tetragonal
	600	2 weeks	3.9 %	2.7 %	41.6 %	Tetragonal
	600	20 weeks	14.7 %	1.9 %	39.1 %	Tetragonal
	600	45 weeks	25.9 %	1.3 %	43.8 %	Tetragonal
SNN0.8 crushed sintered pellet	RT	0 time	-	-	-	Orthorhombic
	300	25 weeks	-	-	-	Orthorhombic
	400	24 weeks	6.7 %	2.7 %	25.2	Tetragonal
SCNN-YZ x=y=0.05 calcined powder	RT	0 time	-	-	9.8 %	Orthorhombic
	300	24 weeks	-	-	10.1 %	Orthorhombic
	600	20 weeks	7.2 %	2.6 %	16.1 %	Tetragonal

6.2.3 SNN1.0 calcined powder – in-situ high temperature X-ray diffraction 600 °C

Figure 6.2.2 shows the log (intensity) XRD plot of SNN1.0 calcined powder produced in this study and recorded at room temperature from 10 to 50 °2θ. A full pattern comparison with orthorhombic *Im2a* ICDD 04-018-2808 is provided in Table 6.2.2. Note the clear presence of Sr modified $NaNbO_3$ second phase as previously reported in Chapter 4 (ICDD 04-009-3239). All peaks matched the orthorhombic *Im2a* reference file to within approximately 0.1 °2θ. Weak orthorhombic superlattice reflections found in other work (Garcia-Gonzalez et al. 2007) using high resolution techniques were thought to be present.

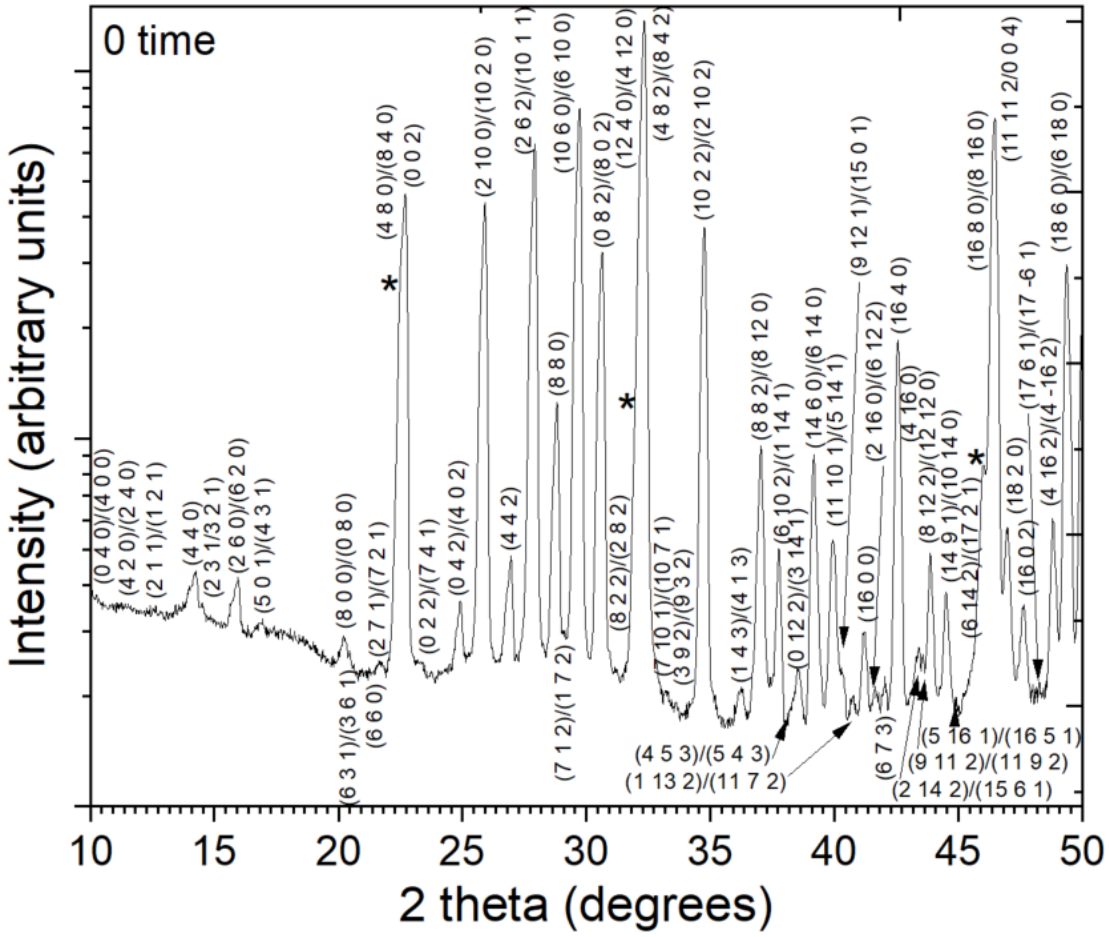

Figure 6.2.2. Log plot of 30 min powder X-ray diffraction pattern for $Sr_2NaNb_5O_{15}$ calcined powder at 0 weeks ageing and acquired at room temperature. Indexed to orthorhombic *Im2a* (ICDD 04-018-2808). Second phase Sr modified $NaNbO_3$ (*) was also present (ICDD 04-009-3239) (data acquired by Dr F. Esat, University of Leeds).

Table 6.2.2. Full pattern comparison of SNN1.0 calcined powder at room temperature with orthorhombic *Im2a* structure (ICDD 04-018-2808). Second phase $NaNbO_3$ indexed to ICDD 04-009-3239.

Peak	d-spacing	2 theta	Intensity	Relative intensity	hkl	Phase	ICDD 2 theta	Difference from ICDD
1	8.77	10.07	317	0.2	0 4 0/4 0 0	SNN	10.12	-0.05
2	7.82	11.3	205	0.2	4 2 0/2 4 0	SNN	11.3	0
3	6.99	12.64	276	0.2	2 1 1/1 2 1	SNN	12.69	-0.05
4	6.20	14.27	1176	0.9	4 4 0	SNN	14.32	-0.05
5	6.10	14.51	382	0.3	2 3 1/3 2 1	SNN	14.57	-0.06
6	5.55	15.95	1225	0.9	2 6 0/6 2 0	SNN	16.01	-0.06
7	5.22	16.95	432	0.3	5 0 1/4 3 1	SNN	17.02	-0.07
8	4.39	20.2	560	0.4	8 0 0/0 8 0	SNN	20.28	-0.08
9	4.34	20.46	357	0.3	6 3 1/3 6 1	SNN	20.49	-0.03
10	4.12	21.54	170	0.1	6 6 0	SNN	21.55	-0.01
11	4.10	21.64	222	0.2	2 7 1/7 2 1	SNN	21.71	-0.07
12	3.94	22.53	30656	22.6	0 2 0/0 0 2	NN	22.56	-0.03
13	3.92	22.65	39324	29.0	4 8 0/8 4 0	SNN	22.72	-0.07
14	3.91	22.7	44417	32.8	0 0 2	SNN	22.82	-0.12
15	3.81	23.33	280	0.2	0 2 2/7 4 1	SNN	23.45	-0.12
16	3.57	24.9	1233	0.9	0 4 2/4 0 2	SNN	25.02	-0.12
17	3.44	25.9	41613	30.7	2 10 0/10 2 0	SNN	25.99	-0.09
18	3.30	26.95	2344	1.7	4 4 2	SNN	27.04	-0.09
19	3.19	27.92	60066	44.3	2 6 2/10 1 1	SNN	28.01	-0.09
20	3.09	28.82	9926	7.3	8 8 0	SNN	28.87	-0.05
21	3.06	29.13	316	0.2	7 1 2/1 7 2	SNN	29.16	-0.03
22	3.00	29.72	76265	56.2	10 6 0/6 10 0	SNN	29.79	-0.07
23	2.91	30.64	29724	21.9	0 8 2/8 0 2	SNN	30.74	-0.1
24	2.87	31.15	148	0.1	8 2 2/2 8 2	SNN	31.17	-0.02
25	2.80	31.98	12348	9.1	2 2 0/2 0 2	NN	32.18	-0.2
26	2.77	32.24	94942	70.0	12 4 0/4 12 0	SNN	32.36	-0.12
27	2.77	32.33	135620	100.0	4 8 2/8 4 2	SNN	32.42	-0.09
28	2.69	33.29	236	0.2	7 10 1/10 7 1	SNN	33.31	-0.02
29	2.66	33.61	176	0.1	3 9 2/9 3 2	SNN	33.46	0.15
30	2.58	34.75	36022	26.6	10 2 2/2 10 2	SNN	34.82	-0.07
31	2.48	36.25	393	0.3	1 4 3/4 1 3	SNN	36.15	0.1
32	2.42	37.03	7871	5.8	8 8 2/8 12 0	SNN	37.12	-0.09
33	2.38	37.77	3352	2.5	6 10 2/1 14 1	SNN	37.85	-0.08
34	2.35	38.32	331	0.2	4 5 3/5 4 3	SNN	38.36	-0.04
35	2.33	38.51	724	0.5	0 12 2/3 14 1	SNN	38.58	-0.07
36	2.30	39.19	7382	5.4	14 6 0/6 14 0	SNN	39.19	0
37	2.25	39.95	3538	2.6	11 10 1/5 14 1	SNN	40.01	-0.06
38	2.24	40.29	652	0.5	9 12 1/15 0 1	SNN	40.32	-0.03
39	2.21	40.79	259	0.2	1 13 2/11 7 2	SNN	40.81	-0.02
40	2.19	41.24	1195	0.9	16 0 0	SNN	41.24	0
41	2.17	41.66	317	0.2	2 16 0/6 12 2	SNN	41.68	-0.02
42	2.15	42.05	448	0.3	6 7 3	SNN	42.07	-0.02
43	2.12	42.58	16664	12.3	16 4 0	SNN	42.58	0
44	2.12	42.68	7777	5.7	4 16 0	SNN	42.65	0.03
45	2.08	43.42	789	0.6	2 14 2/15 6 1	SNN	43.33	0.09
46	2.07	43.57	656	0.5	9 11 2/11 9 2	SNN	43.48	0.09
47	2.06	43.82	2924	2.2	8 12 2/12 12 0	SNN	43.91	-0.09
48	2.03	44.52	1964	1.4	14 9 1/10 14 0	SNN	44.56	-0.04
49	2.02	44.91	226	0.2	5 16 1/16 5 1	SNN	44.92	-0.01
50	1.98	45.78	2043	1.5	6 14 2/17 2 1	SNN	45.87	-0.09
51	1.97	46.02	6673	4.9	0 4 0/0 0 4	NN	46.07	-0.05
52	1.95	46.43	73003	53.8	16 8 0/8 16 0	SNN	46.39	0.04
53	1.95	46.48	73142	53.9	11 11 2/0 0 4	SNN	46.6	-0.12
54	1.93	46.98	3878	2.9	18 2 0	SNN	46.98	0
55	1.91	47.65	1656	1.2	16 0 2	SNN	47.64	0.01
56	1.88	48.27	244	0.2	17 6 1/17 -6 1	SNN	48.28	-0.01
57	1.86	48.8	4116	3.0	4 16 2/4 -16 2	SNN	48.9	-0.1
58	1.84	49.38	27669	20.4	18 6 0/6 18 0	SNN	49.4	-0.02

Figure 6.2.3 shows the in situ XRD of the same sample after being held at 600 °C for 50 h. The pattern has changed from Orthorhombic *Im2a* to Tetragonal *P4mbm*. This is consistent with previous reports of the changes in XRD pattern accompanying the ferroelectric to paraelectric transition of SNN1.0 (at ~ 300 °C) by Garcia-Gonzalez et al. (2007) (ICDD 04-014-7370). A full pattern comparison with tetragonal *P4mbm* ICDD 04-014-7370 is provided in Table 6.2.3. Indeed as would be expected, the XRD patterns recorded in-situ for much shorter times, for example 10 min immediately on reaching 600 °C, also showed the *P4mbm* pattern. Examples of the latter are shown in Figure 6.2.4.

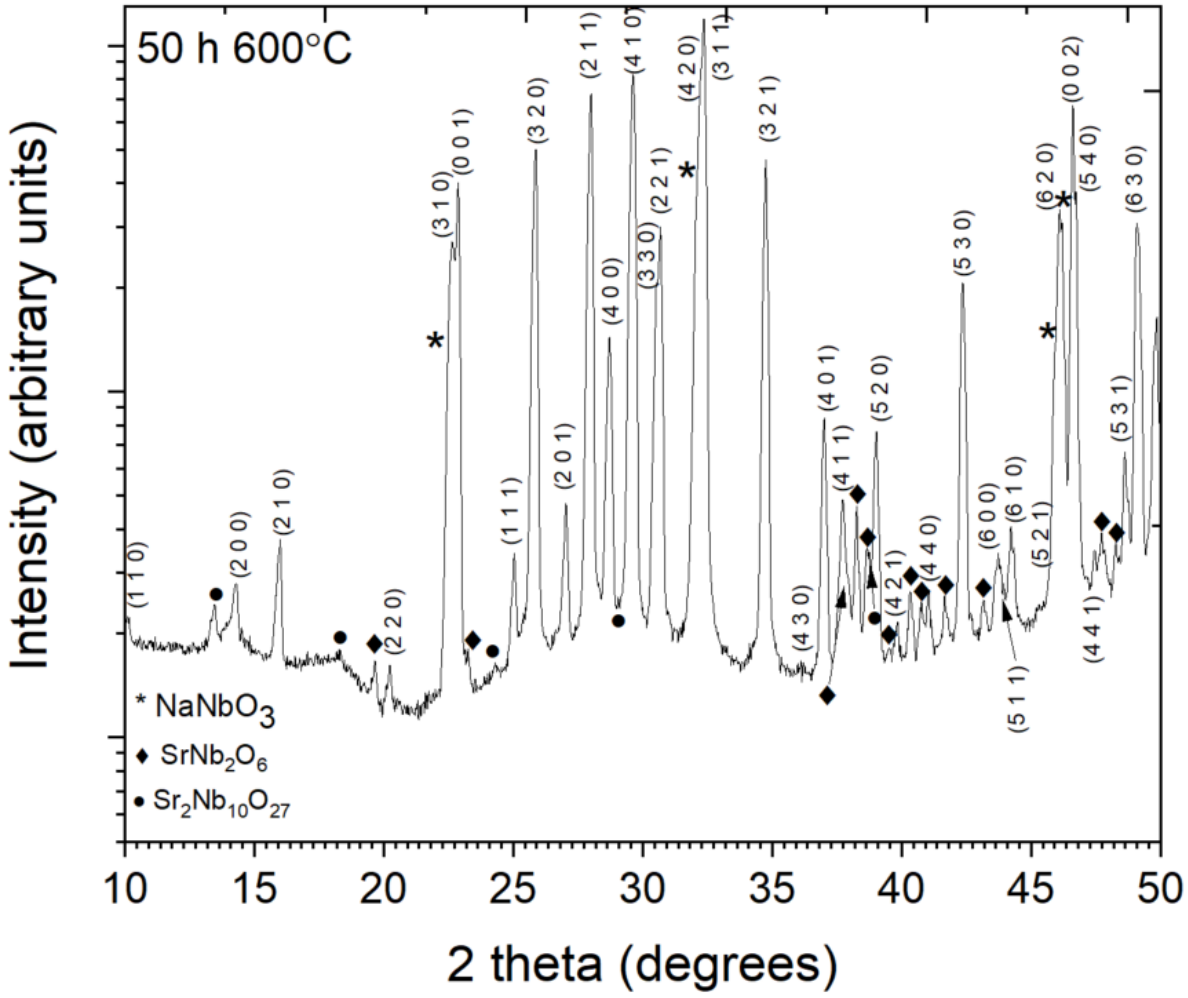

Figure 6.2.3. Log (intensity) plot of 30 min powder in situ X-ray diffraction pattern for $Sr_2NaNb_5O_{15}$ calcined powder at 50 h ageing at 600 °C. Indexed to tetragonal *P4mbm* (ICDD 04-014-7370). Second phase Sr modified $NaNbO_3$ (*) was present (ICDD 04-009-3239) along with the appearance of $SrNb_2O_6$ (♦) (ICDD 04-011-3157) and $Sr_2Nb_{10}O_{27}$ (●) (ICDD 01-088-4392) (Data acquired by Dr F. Esat, University of Leeds).

Table 6.2.3. Full pattern comparison of SNN1.0 calcined powder at 50 h ageing at 600 °C with tetragonal *P4mbm* structure (ICDD 04-014-7370). Second phase $NaNbO_3$ indexed to ICDD 04-009-3239. Third and fourth phase strontium niobates are indexed as: $SrNb_2O_6$ (ICDD04-011-3157) (red) and $Sr_2Nb_{10}O_{27}$ (ICDD 04-0880-4392) (blue). Blue text indicates unique tetragonal peaks, distinguishing from orthorhombic *Im2a.*

Peak	d-spacing	2 theta	Intensity	Relative intensity	hkl	Phase	ICDD 2 theta	Difference from ICDD
1	8.73	10.12	309	0.3	1 1 0	SNN	10.05	0.07
2	6.58	13.45	598	0.5	4 0 0	SN	13.93	-0.48
3	6.19	14.29	926	0.8	2 0 0	SNN	14.24	0.05
4	5.53	16	2111	1.8	2 1 0	SNN	15.93	0.07
5	4.84	18.31	208	0.2	1 7 0	SN	18.24	0.07
6	4.51	19.65	428	0.4	-1 0 2	SN	19.76	-0.11
7	4.38	20.23	465	0.4	2 2 0	SNN	20.19	0.04
8	3.95	22.49	13091	11.2	0 2 0/0 0 2	NN	22.56	-0.07
9	3.92	22.64	25739	22.0	3 1 0	SNN	22.7	-0.06
10	3.88	22.88	38931	33.3	0 0 1	SNN	23.03	-0.15
11	3.82	23.25	457	0.4	2 0 0	SN	23.02	0.23
12	3.66	24.3	163	0.1	1 2 1	SN	24.17	0.13
13	3.55	25.03	1817	1.6	1 1 1	SNN	24.97	0.06
14	3.44	25.88	48965	41.9	3 2 0	SNN	25.82	0.06
15	3.29	27.03	2868	2.5	2 0 1	SNN	26.98	0.05
16	3.18	28	70139	60.0	2 1 1	SNN	27.93	0.07
17	3.11	28.71	12062	10.3	4 0 0	SNN	28.7	0.01
18	3.07	29.05	154	0.1	0 1 3	SN	29.12	-0.07
19	3.01	29.63	80786	69.1	4 1 0	SNN	29.6	0.03
20	2.92	30.55	18634	15.9	3 3 0	SNN	30.48	0.07
21	2.91	30.68	28169	24.1	2 2 1	SNN	30.63	0.05
22	2.79	32.1	37891	32.4	2 2 0/2 0 2	NN	32.18	-0.08
23	2.77	32.28	87666	75.0	4 2 0	SNN	32.17	0.11
24	2.76	32.36	116868	100.0	3 1 1	SNN	32.31	0.05
25	2.58	34.75	45793	39.2	3 2 1	SNN	34.71	0.04
26	2.48	36.12	165	0.1	4 3 0	SNN	36.1	0.02
27	2.43	37.01	6792	5.8	4 0 1	SNN	36.96	0.05
28	2.38	37.72	3175	2.7	4 1 1	SNN	37.68	0.04
29	2.37	37.95	1119	1.0	-1 2 2/1 2 2	SN	37.94	0.01
30	2.35	38.27	2856	2.4	3 1 0/-3 0 2	SN	38.47	-0.2
31	2.33	38.66	1762	1.5	3 0 2	SN	38.69	-0.03
32	2.32	38.74	1661	1.4	0 16 0	SN	38.91	-0.17
33	2.31	39.03	5957	5.1	5 2 0	SNN	38.98	0.05
34	2.28	39.5	152	0.1	3 1 1	SN	39.42	0.08
35	2.26	39.83	492	0.4	4 2 1	SNN	39.79	0.04
36	2.23	40.31	978	0.8	-2 0 4	SN	40.13	0.18
37	2.21	40.76	775	0.7	-2 2 1/0 2 3	SN	40.56	0.2
38	2.20	41.05	960	0.8	4 4 0	SNN	41.04	0.01
39	2.17	41.66	759	0.6	-3 1 2	SN	41.87	-0.21
40	2.13	42.34	18634	15.9	5 3 0	SNN	42.36	-0.02
41	2.09	43.16	545	0.5	2 2 2	SN	43.23	-0.07
42	2.07	43.73	1308	1.1	6 0 0	SNN	43.65	0.08
43	2.06	43.81	1031	0.9	5 1 1	SNN	43.76	0.05
44	2.05	44.2	1895	1.6	6 1 0	SNN	44.28	-0.08
45	1.97	45.95	11862	10.1	0 4 0/0 0 4	NN	46.07	-0.12
46	1.97	46.09	31334	26.8	6 2 0	SNN	46.14	-0.05
47	1.96	46.2	28630	24.5	4 0 0	NN	46.18	0.02
48	1.96	46.29	10197	8.7	0 2 4	SN	46.29	0
49	1.95	46.62	64439	55.1	0 0 2	SNN	46.56	0.06
50	1.94	46.73	35633	30.5	5 4 0	SNN	46.75	-0.02
51	1.91	47.45	832	0.7	4 4 1	SNN	47.45	0
52	1.90	47.72	1258	1.1	1 2 4	SN	47.91	-0.19
53	1.88	48.27	985	0.8	-3 0 4	SN	48.26	0.01
54	1.87	48.61	3865	3.3	5 3 1	SNN	48.64	-0.03
55	1.85	49.09	27590	23.6	6 3 0	SNN	49.12	-0.03

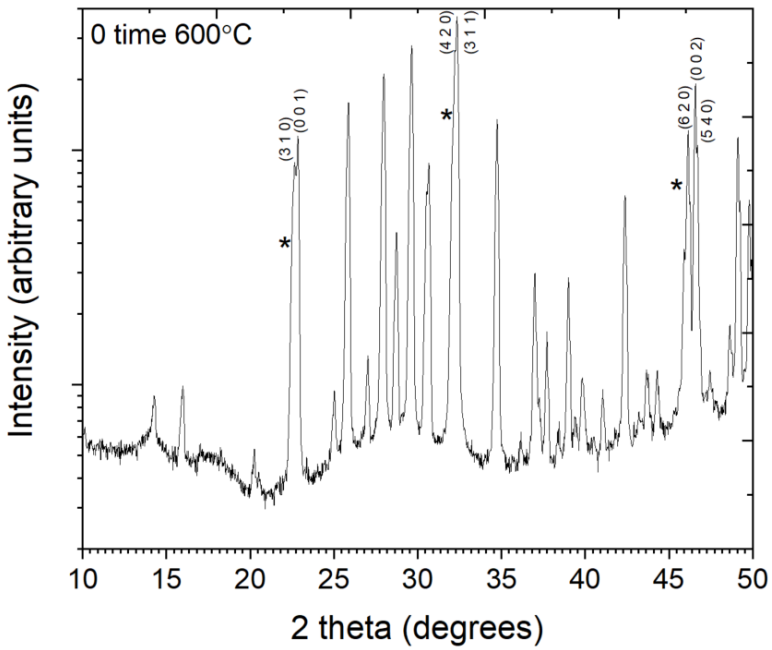

Figure 6.2.4. Log (intensity) plot of 10 min in situ powder X-ray diffraction pattern for $Sr_2NaNb_5O_{15}$ calcined powder at 0 time on first reaching 600 °C. The additional peaks at approximately 22.6, 32.4, and 46.4 °2θ indicate the transition from orthorhombic *Im2a* to tetragonal *P4mbm* (displayed *hkl* values). Second phase Sr modified $NaNbO_3$ (*) was present as shoulders of these peaks throughout heating (ICDD 04-009-3239) (Data acquired by Dr F. Esat, University of Leeds).

The emergence of weak reflections due to $SrNb_2O_6$ and $Sr_2Nb_{10}O_{27}$ was seen at 50 h (Figure 6.2.3). This was not reported by Garcia-Gonzalez et al. (2007) who perhaps did not hold at these temperatures for as long. $SrNb_2O_6$ indexed to ICDD 04-011-3157 was most clearly seen at 19.65 °2θ, whilst other peaks (most notably 13.48 °2θ) were attributed to $Sr_2Nb_{10}O_{27}$ (ICDD 01-088-4392). Strontium niobate "secondary" phase could form over a range of compositions depending on the sodium loss from the SNN structure. Here, in-situ X-ray diffraction measurements at 600 °C, taken every hour, reveal that for the initial SNN1.0 with second phase Sr modified $NaNbO_3$, a third and fourth phase $SrNb_2O_6$ and $Sr_2Nb_{10}O_{27}$ begins forming at between 2 and 3 hours, then remains relatively stable from 9 h up to the maximum time of the experiment (50 h, Figure 6.2.5 a-b).

The $NaNbO_3$ second phase peaks present in SNN1.0 at room temperature increased with heating from ~10 % (relative intensity in comparison to the main SNN peak), to ~30 % after 50 h heating (Table 6.2.1). This was inconsistent with the findings of

Garcia-Gonzalez et al. (2007), however the difficulty of measuring the intensity of a peak shoulder in the initial data must be acknowledged.

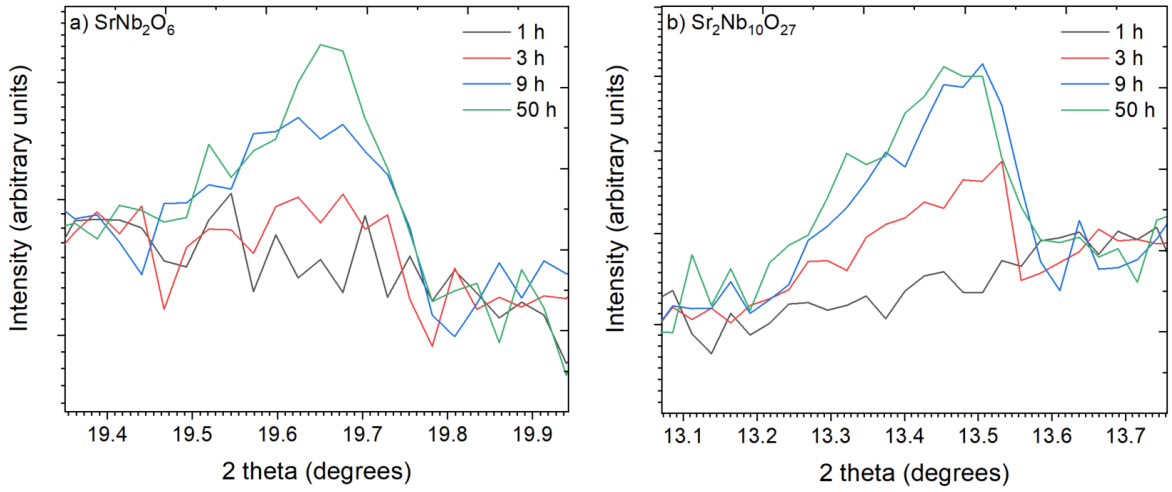

Figure 6.2.5 a-b. Log (intensity) plots of 30 min powder X-ray diffraction patterns for $Sr_2NaNb_5O_{15}$ calcined powder taken every hour at 600 °C: a) A third phase $SrNb_2O_6$, with peaks at approximately 19.65 °2θ, b) a fourth phase $Sr_2Nb_{10}O_{27}$ (as seen in Figure 6.2.3) indexed to ICDD 04-011-3157 and ICDD 04-088-4392 respectively have started to form at 3 h (red plot). The intensity of these reflections then remain constant from 9 h up to 50 h (Data acquired by Dr F. Esat, University of Leeds).

On cooling to room temperature following ageing for 50 h at 600 °C, it would be expected the high temperature tetragonal phase return to orthorhombic as the temperature dropped through T_c, as reported by Gonzalez et al. 2007 (the *Im2a* to *P4mbm* transition is associated with the ferroelectric to paraelectric change at T_c). Comparison of the orthorhombic 0 time plot, the tetragonal 50 h 600 °C plot, and the measurements taken on returning to room temperature, show that this is not the case for the sample annealed for 50 h. This suggests that the partial decomposition of SNN1.0 indicated by the presence of secondary, strontium niobate, also changes the thermal stability of the main SNN phase. The 'high temperature' *P4mbm* phase (non-ferroelectric) is retained to room temperature rather than transforming back to *Im2a*.

Figure 6.2.6 a, illustrates the additional tetragonal peaks at 46.1, 46.6, and 46.7 °2θ seen to develop at 50 h 600 °C (red plot) remain after the sample cools to room temperature (the 0 time peak at 46.4 and 46.5 °2θ splitting into the tetragonal 620,

002 and 540 peaks at 600 °C). The enlarged 10 to 22 °2θ region, showing the weak orthorhombic peaks present pre-heating at 0 time (black plot) at approximately 16.9, 20.5, and 21.7 °2θ, remain missing when cooled to room temperature (blue plot), whilst strontium niobate peaks that formed on heating remain (Figure 6.2.6 b).

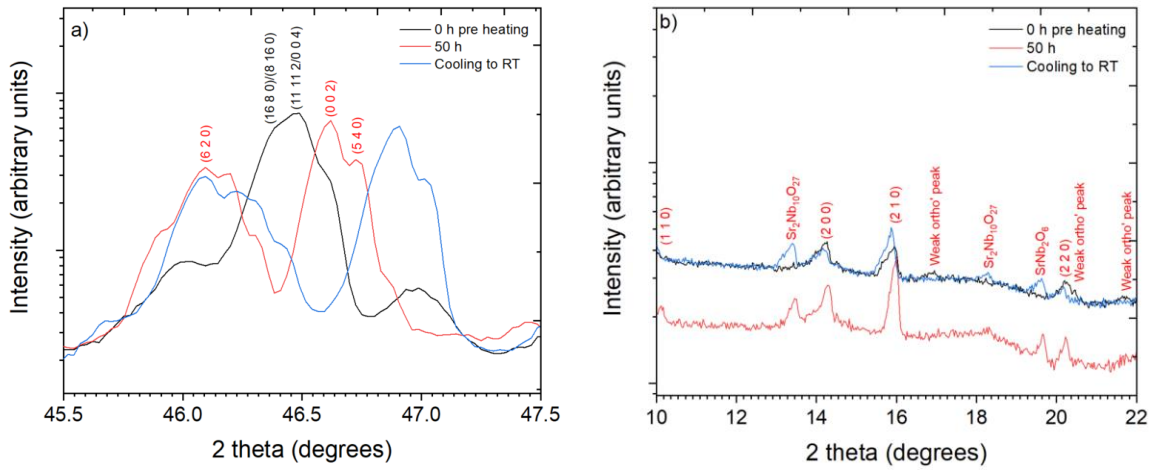

Figure 6.2.6 a-b. Log (intensity) plot powder X-ray diffraction patterns of $Sr_2NaNb_5O_{15}$ calcined powder before heating (black), 600 °C for 50 h (red), and on returning to room temperature (blue): a) Enlarged 45.5 to 47.5 °2θ region showing additional tetragonal peaks developed during heating (red) remains on cooling to room temperature (blue) (indexed to tetragonal *P4mbm* ICDD 04-014-7370: red *hkl* values and orthorhombic *Im2a* ICDD 04-018-2808: black *hkl* values). b) Weak orthorhombic peaks present before heating (black) do not reappear after cooling (blue). Third and fourth strontium niobate phases formed on heating to 600 °C (red) remain after cooling (blue) (indexed to tetragonal *P4mbm* ICDD 04-014-7370). (Data acquired by Dr F. Esat, University of Leeds).

6.2.4 SNN1.0 calcined powder – in-situ high temperature X-ray diffraction 400 °C

The same in-situ XRD experiment was repeated on the SNN1.0 calcined powder but to a temperature of 400 °C (60 °C/min) for 24 h to determine if the same structural and compositional changes would occur at lower temperature.

The sample showed the same additional tetragonal peaks on heating to 400 °C as the 600 °C (Section 6.2.3) at approximately 22, 32, and 46 °2θ, which was consistent with a change from a room temperature orthorhombic *Im2a* to a tetragonal *P4mbm* structure on passing through T_c (T_2). The tetragonal structure remained throughout the 24 h, and then, unlike the 600 °C sample, the process is reversible on cooling to room temperature (Figure 6.2.7). No significant third or fourth phase was observed forming at this temperature and time and so the original two phase composition remained constant. As the phase distribution was unaltered by heating to 400 C, the SNN phase was 'free' to reversibly change structure back to orthorhombic on passing below T_c.

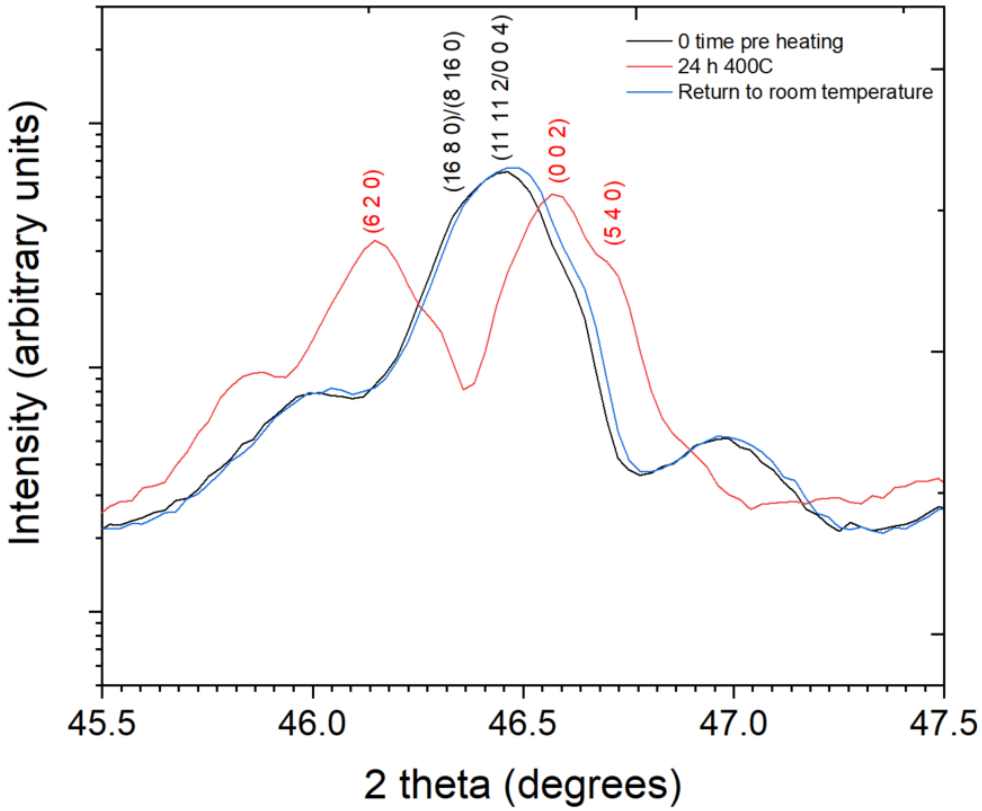

Figure 6.2.7. Log (intensity) plot of 30 min powder X-ray diffraction patterns for $Sr_2NaNb_5O_{15}$ calcined powder at 0 time pre heating (black plot), 24 h at 400 °C (red plot), and after returning to room temperature (blue plot). The additional peaks on heating indicate the transition from an orthorhombic *Im2a* structure (black hkl values) to a tetragonal *P4mbm* structure (red *hkl* values). On cooling to room temperature the structure reverts back to orthorhombic, probably on passing through the T_c of the material (Data acquired by Dr F. Esat, University of Leeds).

6.2.5 Long term annealing at 600 °C and 300 °C

Effects on the structure and composition were seen at 600 °C within 50 h. To determine the long-term thermal effects on SNN1.0, calcined powder was stored in a furnace at 300 °C and 600, with 24 min X-ray diffraction measurements taken periodically on cooling to room temperature. A 12 h scan was performed on the 600 °C sample at 45 weeks. Measurements were taken on a Bruker D8 X-ray diffractometer as described in Chapter 3. Figure 6.2.8 shows a 12 h X-ray diffraction scan of SNN1.0, calcined powder stored for 45 weeks at 600 °C. The pattern was indexed to the same tetragonal *P4mbm* structure as the 50 h sample (Figure 6.2.3), although the fit was not as good after the extended heat treatment. Peak positions were generally shifted to higher 2θ values, probably because the second phase content had developed to an extent as to create a compositionally different material to the original (leading to a smaller unit cell). The cooling of the sample before measurements were taken raised the possibility of a mixed orthorhombic and tetragonal phase. Higher quality data (both resolution and signal to noise ratio) would be needed to address this in the current work. Further confirmation that the SNN had broken down to at least a three phase material was found from SEM-EDX maps of the calcined powder taken after 46 weeks (Figure 6.2.9).

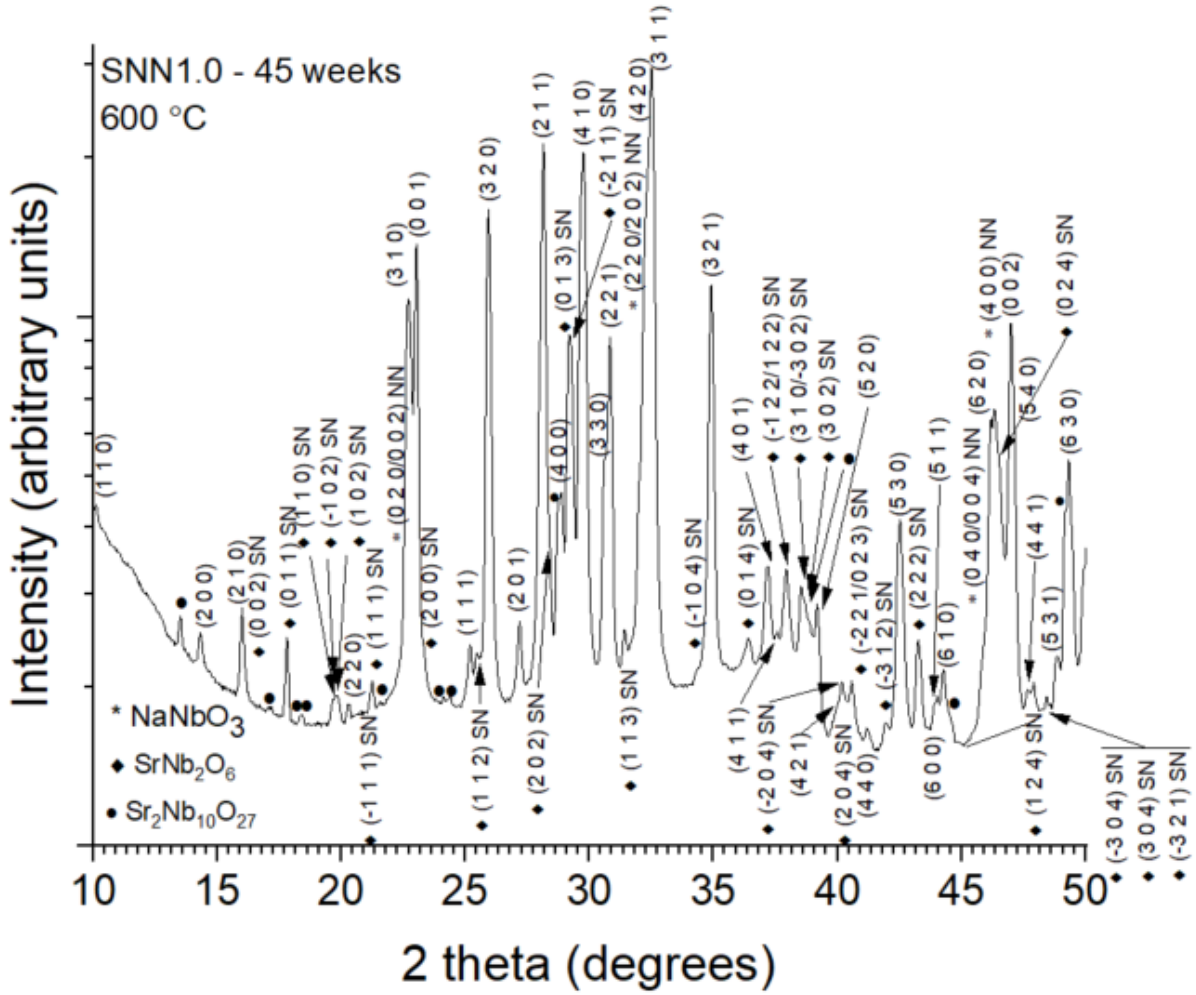

Figure 6.2.8. Log (intensity) plot of 12 h powder X-ray diffraction pattern for $Sr_2NaNb_5O_{15}$ calcined powder at 45 weeks and 600 °C. Indexed to tetragonal *P4mbm* (ICDD 04-014-7370). Second phase Sr modified $NaNbO_3$ (*) was present (ICDD 04-009-3239) along with third and fourth phases of strontium niobate. $SrNb_2O_6$ (♦) (ICDD 04-011-3157) and $Sr_2Nb_{10}O_{27}$ (●) (ICDD 01-088-4392).

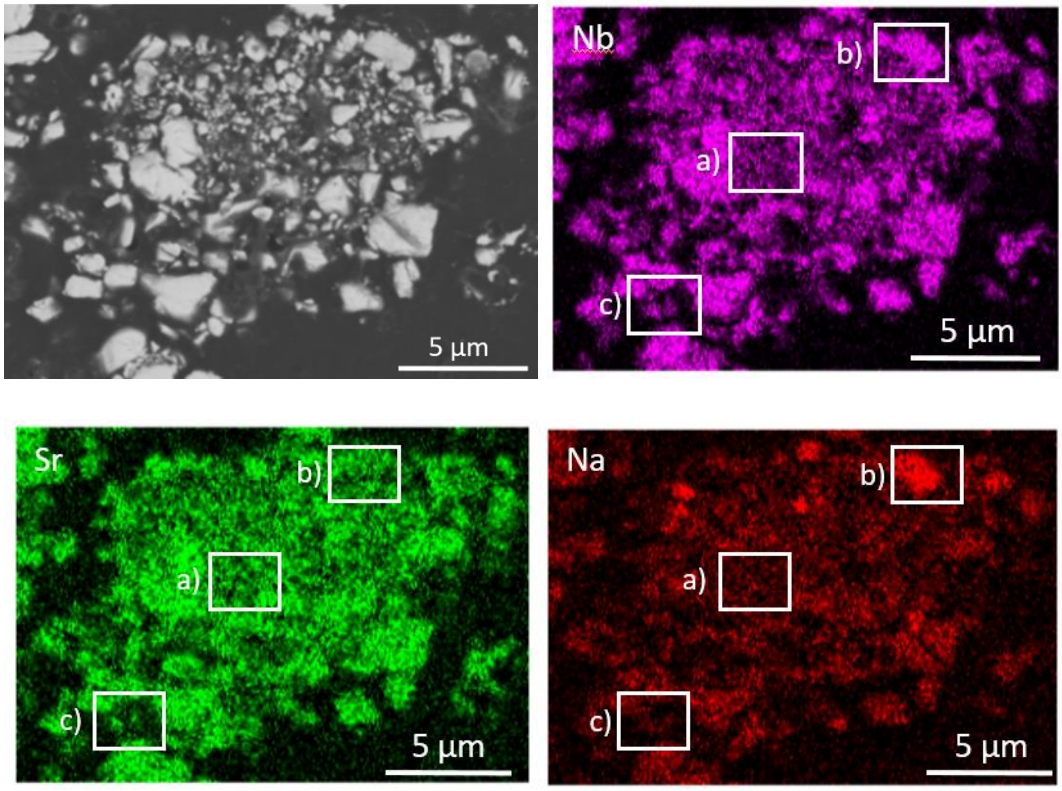

Figure 6.2.9. Back scattered SEM image and SEM-EDX maps of SNN1.0 calcined powder held for 46 weeks at 600 ^{o}C. Highlighted areas show probable a) SNN phase, b) Sr modified $NaNbO_3$ phase, and c) Sr phase, based on the expected compositional variation for these phases.

Figure 6.2.10 shows the X-ray diffraction pattern at the maximum time of 24 weeks at 300 ^{o}C. Lower resolution 24 min scans performed on the Bruker D8 (as opposed to the 30 min, 0 time, room temperature scan on the Malvern Panalytical, Empyrean, see Figure 6.2.2) made the distinguishing of weak orthorhombic peaks difficult to identify with confidence. Additional tetragonal peaks were not present (unlike Figure 6.2.3), indicating that at 300 ^{o}C and 24 weeks the structure remained orthorhombic. This was consistent with the T_c of the material being approximately 300 ^{o}C (see Chapter 4, Section 4.2.2) and so it will not have transformed to the centrosymmetric tetragonal phase. A small amount of thermal decomposition may have occurred because a cautious approach might say there are signs of $Sr_2Nb_{10}O_{27}$ around 13 and 24 $^{o}2\theta$. However, this assignment is ambiguous (due to the low resolution scan) and there is no significant evidence for the presence of a third or fourth phase. Clearly

the breakdown to these additional phases occurs at a much slower rate at 300 °C than at 600 °C, if it occurs at all.

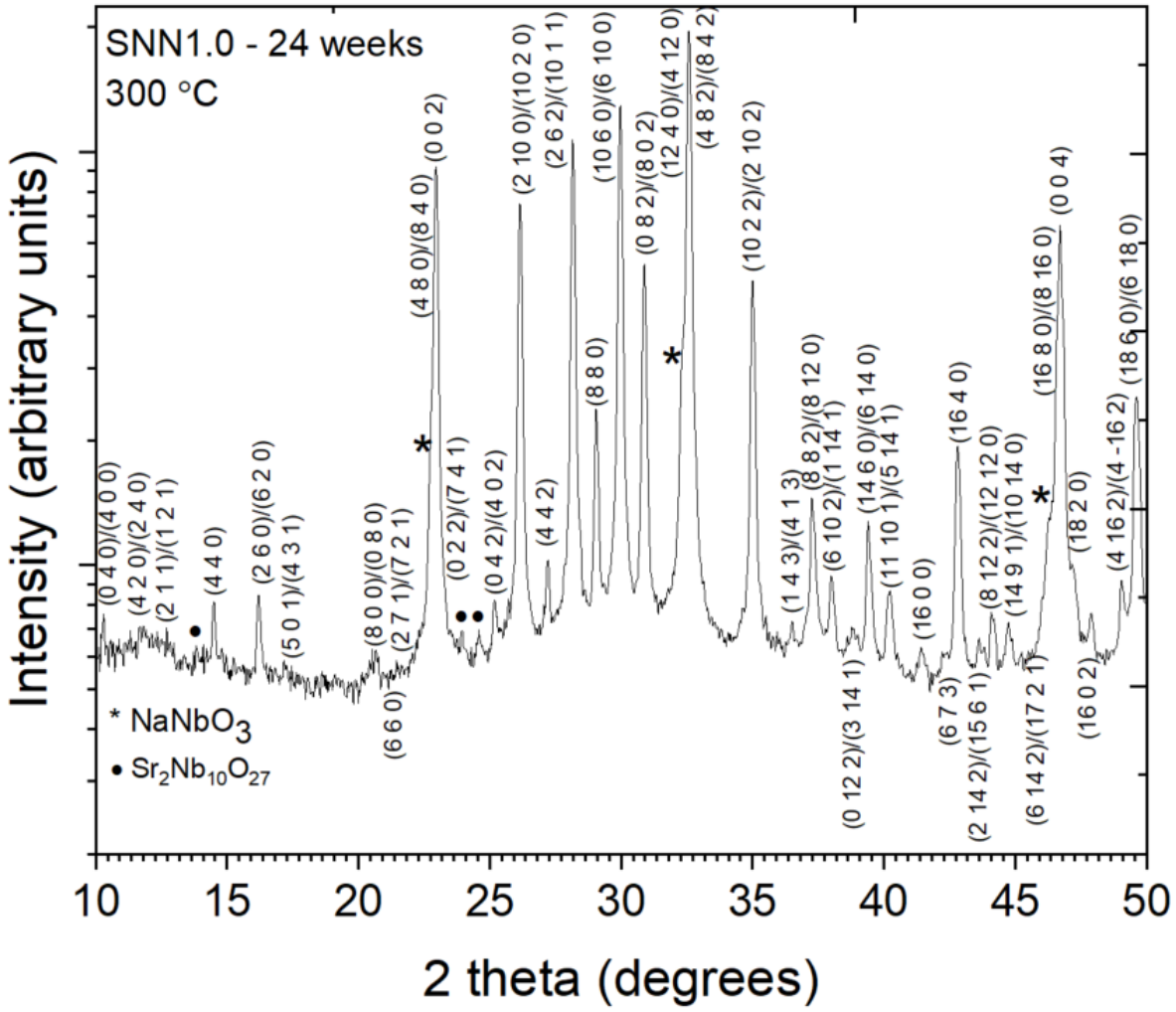

Figure 6.2.10. Log (intensity) plot of 24 min powder X-ray diffraction pattern for $Sr_2NaNb_5O_{15}$ calcined powder at 24 weeks and 300 °C. Indexed to orthorhombic *Im2a* (ICDD 04-018-2808). Second phase Sr modified $NaNbO_3$ (*) (ICDD 04-009-3239) was present, with the possibility of $Sr_2Nb_{10}O_{27}$ (●) (ICDD 01-088-4392) also forming over the extended time period.

Further annealing experiments were carried out on $Sr_{2-x-y}Ca_xY_xNaNb_{5-y}Zr_yO_{15}$ x = 0.05, y = 0.05 calcined powder (SCNN-YZ) (Chapter 4, Section 4.3) and $Sr_{2.1}Na_{0.8}Nb_5O_{15}$ (SNN0.8) crushed sintered pellets produced using an extended sintering run (1240 °C 6 h, followed by 1320 °C 25 h, see Chapter 5, Section 5.5). Both compositions showed no structural change or development of extra phases when held at 300 °C for 25 weeks (SNN0.8) and 24 weeks (SCNN-YZ). Annealing at higher temperatures of 400 °C (SNN0.8, 24 weeks) and 600 °C (SCNN-YZ, 20 weeks) resulted in the expected phases and additional tetragonal peaks developing

as in SNN1.0 calcined powder and these peaks are shown in Figures 6.2.11 and 6.2.12 respectively.

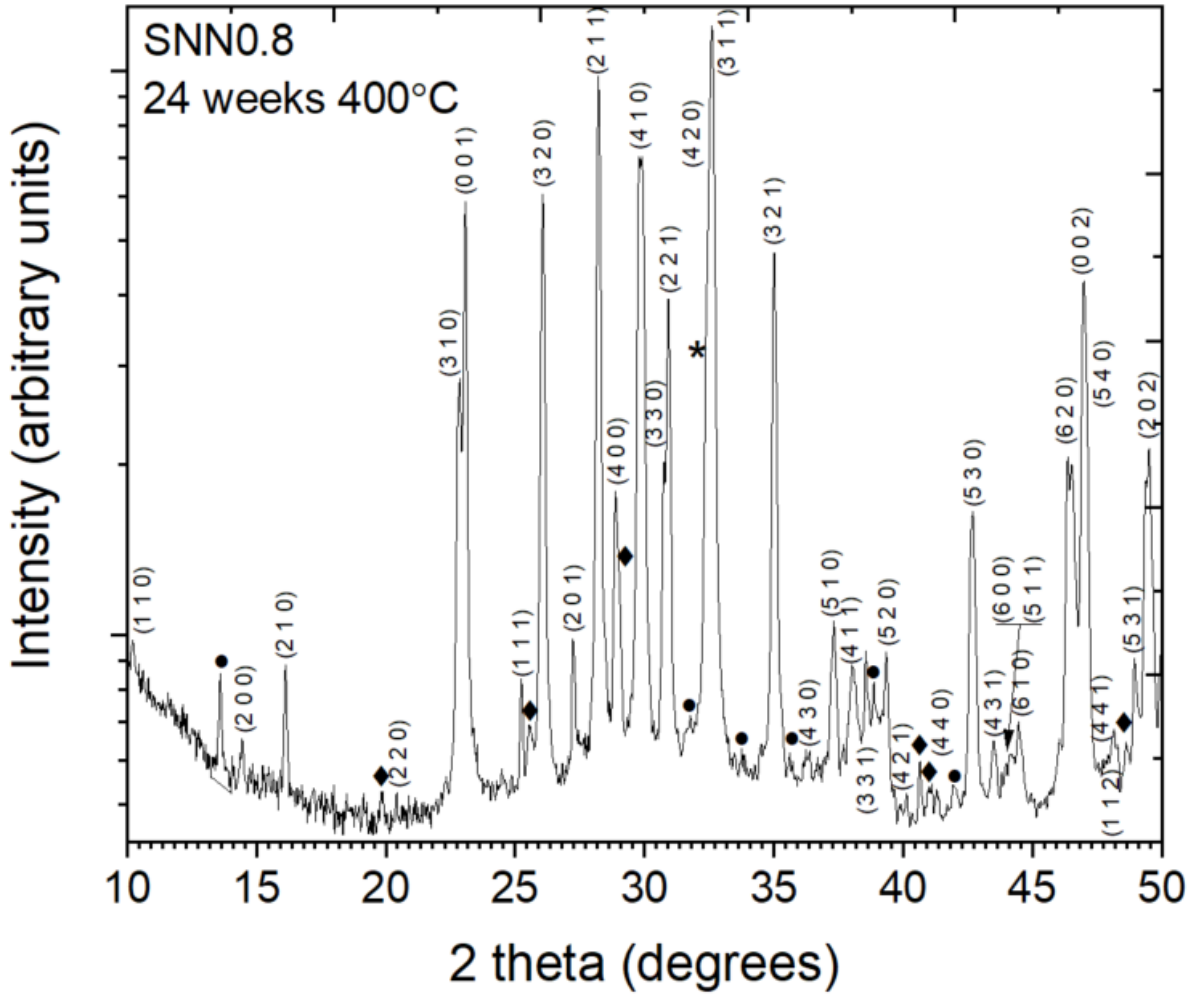

Figure 6.2.11. Log (intensity) plot of 24 min powder X-ray diffraction pattern for $Sr_{2.1}Na_{0.8}Nb_5O_{15}$ calcined powder, 24 weeks at 400 °C. Indexed to tetragonal *P4mbm* (ICDD 04-014-7370). At this time and temperature compositional breakdown has started with phases of $SrNb_2O_6$ (♦) (ICDD 04-011-3157) and $Sr_2Nb_{10}O_{27}$ (●) (ICDD 01-088-4392) present.

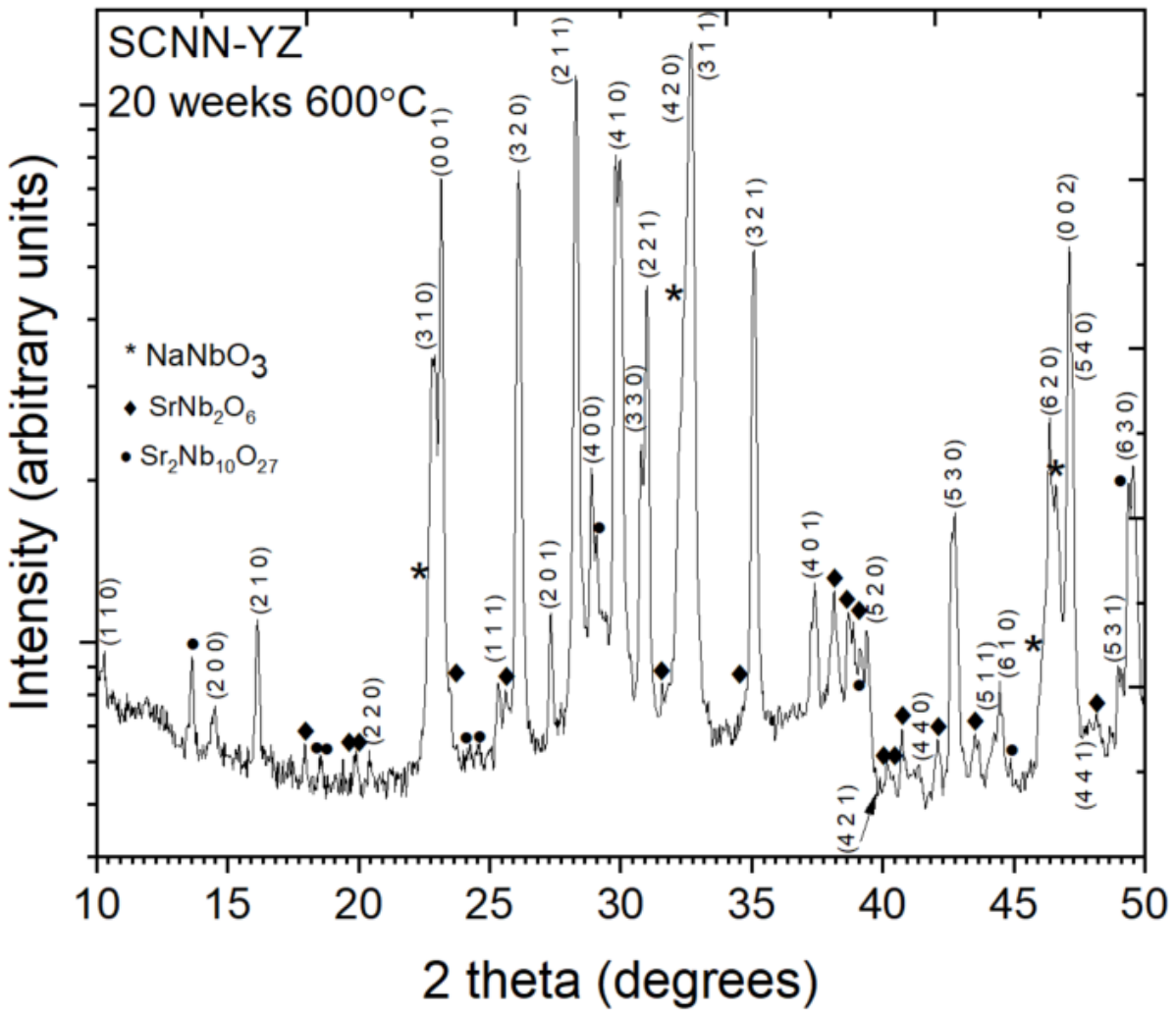

Figure 6.2.12. Log (intensity) plot of 24 min powder X-ray diffraction pattern for $Sr_{2-x-y}Ca_xY_xNaNb_{5-y}Zr_yO_{15}$ x = 0.05, y = 0.05 calcined powder calcined, 20 weeks at 600 °C. Indexed to tetragonal *P4mbm* (ICDD 04-014-7370), also present is Sr modified $NaNbO_3$ (*) (ICDD 04-009-3239). At this time and temperature compositional breakdown has started with phases of $SrNb_2O_6$ (♦) (ICDD 04-011-3157) and $Sr_2Nb_{10}O_{27}$ (●) (ICDD 01-088-4392) present.

6.2.6 Summary: SNN1.0 calcined powder and SNN0.8 sintered pellet annealing experiments

Detailed study of X-ray diffraction log (intensity) plots of SNN1.0 calcined powder (consisting of SNN1.0 and some second phase $NaNbO_3$), determined the SNN phase could be indexed to an orthorhombic *Im2a* structure at room temperature, in line with a proportion of the literature but often requiring high resolution analysis techniques to identify. This was on the basis of weak orthorhombic peaks which would disappear on heating through T_c and on the change to a tetragonal structure on heating, evident by additional tetragonal peak formation. Garcia-Gonzalez (2007) reported this structural change, initially identifying the room temperature phase with TEM-SAED analysis and then confirming by XRD, which the data in this chapter agreed with. In-situ XRD experiments at 600 ^oC and 400 ^oC showed that SNN1.0 calcined powder changes from an orthorhombic to a centrosymmetric tetragonal structure during heating to either temperature. The T_c of SNN1.0 is approximately 300 ^oC, therefore this change probably occurs on passing through this temperature. Extra phase formation was significant at 600 ^oC (both $Sr_2Nb_{10}O_{27}$ and $SrNb_2O_6$), altering the composition from SNN1.0 and possibly explaining why the structural change becomes irreversible when cooled from this temperature. At 400 ^oC, 24 h the extra phase formation was not seen and the SNN1.0 structure reverts back to an orthorhombic structure on cooling to room temperature. An extended annealing experiment at 600 ^oC (45 weeks) showed compositional breakdown to an even greater extent, the presence of the extra phases also being confirmed by SEM-EDX. A similar extended experiment on SNN1.0 calcined powder for 24 weeks at 300 ^oC (the intended maximum operating temperature for a capacitor material) showed promising phase stability over this time. The structure remained orthorhombic and although some very minor extra phase, and therefore compositional breakdown may have been detected, it was ambiguous given the resolution of the scan used. Future experiments at this temperature with higher resolution methods are required to determine the true stability. Similar levels of decomposition and structural change were identified in SCNN-YZ at comparable times and temperatures.

Preliminary annealing experiments were also conducted on single phase SNN0.8, this time in the form of crushed sintered pellets. Compositional breakdown might be

expected to be reduced or non-existent due to the formulation being single phase and positioned in the centre of the single phase field of the binary phase diagram. Breakdown to second and third phase $Sr_2Nb_{10}O_{27}$ and $SrNb_2O_6$ was however seen at 400 ^oC, 24 weeks, but the composition was again stable at 300 ^oC. Both of these results came with the caveat that only low resolution XRD scans were used on these samples. The reason for this could be that the lines in the metastable phase diagram (Figure 6.1.1) are projected, and in fact, there is no equilibrium single phase field at room temperature (Figure 6.1.2). In fact decomposition could be more rapid in SNN0.8 than SNN1.0 due to the increased ease of moving atoms around a vacancy rich structure, although a lack of comparable annealing times and temperatures in this study mean this cannot be confirmed. Further experiments into the long term stability of SNN0.8 will need to be conducted including in-situ, high temperature XRD and higher resolution analysis techniques, as well as investigation into the threshold time of the irreversible structural change from an orthorhombic to tetragonal SNN phase for all compositions. The initial results here show that an accelerated breakdown at 600 ^oC can probably be expected for all SNN compositions.

6.3 Permittivity changes resulting from annealing at 300 to 600 °C

Potential thermal instability in the permittivity temperature response was identified in Chapter 5 where compositions of SNN0.8 sintered at higher temperatures showed a sharp decrease in ε_r values, especially at the T_2 permittivity peak, compared to that sintered at lower temperatures (Figure 5.5.7 a-b). Studies by Tang et al. (1979) indicated that SNN is thermodynamically unstable below 1180 °C (Figure 6.1.1) and the above XRD analysis indicate thermal breakdown does indeed occur above 300 °C.

A sintered pellet of SNN0.8 (ES) ($Sr_{2.1}Na_{0.8}Nb_5O_{15}$, extended sintering, Chapter 5, Section 5.4) underwent six consecutive permittivity versus temperature measurements each of which reached a maximum temperature of ~600 °C (approximately 12 h run, 2 °C/min, dwell 15 min). All measurements were taken within a two month period and the sample was stored in a vacuum desiccator between runs. The silver electrode was removed and reapplied after the third run to ensure its integrity. Relative permittivity versus temperature plots are shown in Figure 6.3.1, plots showing changes in T_2 $\varepsilon_{r\,max}$ value are shown in Figure 6.3.2, and data are summarised in Table 6.3.1. Dates for each measurement are also displayed here. Values for T_2 ε_r dropped with each subsequent run from 1775 (Run 1) to 960 (Run 6), a decrease of 815 (or to 54 % of the original value). Values of T_2 peak temperature dropped approximately 10 °C from run 1 to run 6 (Figure 6.3.2). The T_2 peak was significantly flattened by run 5, so accurate determination of ε_r and peak temperature thereafter was difficult. Approximations are given in Table 6.3.1, and this may have resulted in the anomalous increase in peak temperature for run 6 (Figure 6.3.2).

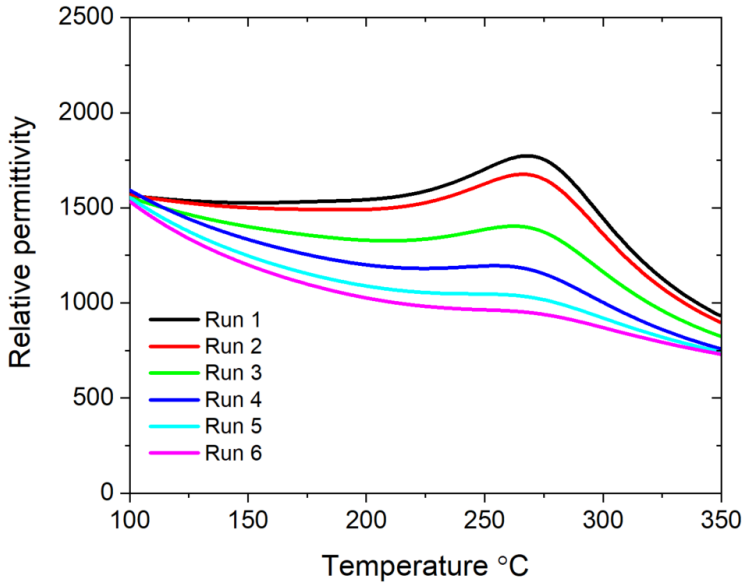

Figure 6.3.1. 1 kHz high temperature relative permittivity versus temperature plots for SNN0.8 (ES) showing six consecutive measurements of the same sample up to ~600 °C. The high temperature permittivity peak (T_2) decreased with each successive run.

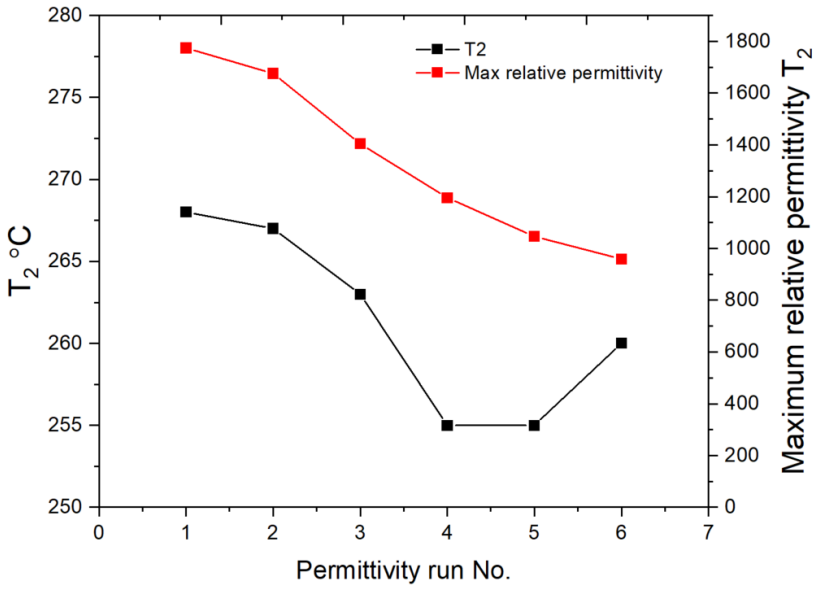

Figure 6.3.2. T_2 peak temperature and ε_r value for SNN0.8 (ES) at 1 kHz for six consecutive permittivity versus temperature measurements up to ~600 °C. An increase in T_2 temperature in run 6 is likely due to the difficulty of identifying the peak due to the flattened permittivity response. Given the temperature reading errors of T_2 are approximately 25 to 30 °C for runs 5 and 6 this increase is not thought to be significant.

This experiment was recognised as being flawed due to the use of a silver electrode at high temperatures and the possibility of diffusion of Ag ions into the material. However the results are reported due to the clear decrease of the permittivity response with increased exposure to temperature (Figures 6.3.1 and 6.3.2). In addition to this, compositional breakdown was observed by X-ray diffraction taken after the completion of the six permittivity measurements compared to those taken before (Figure 6.3.3). The appearance of peaks assigned to $Sr_2Nb_{10}O_{27}$ (ICDD 01-088-4392) at 13.5 $^o2\theta$ and $SrNb_2O_6$ (ICDD 04-011-3157) at 19.8 $^o2\theta$ illustrates this. A structural change from orthorhombic to tetragonal was also observed, most clearly seen with the additional peak formation at approximately 22.5 $^o2\theta$ and 46 $^o2\theta$. In fact the plots in Figure 6.3.3 are similar to those in Section 6.2 showing SNN0.8 before and after long term annealing at 400 ^{o}C (Figures 6.2.12 and 6.2.13).

Table 6.3.1. T_2 peak temperature and ε_r value for SNN0.8 (ES) at 1 kHz for six consecutive permittivity versus temperature measurements up to ~600 °C. The date of each measurement is also shown.

SNN0.8 ESR ISO 2nd pellet	T_2 °C (reading error °C)	T_2 ε_r (reading error)
Run 1 01/10/21	268 (+/- 10)	1774 (+/- 10)
Run 2 28/10/21	267 (+/- 10)	1676 (+/- 10)
Run 3 15/11/21	263 (+/- 15)	1404 (+/- 10)
Run 4 (new electrode) 23/11/21	255 (+/- 20)	1196 (+/- 10)
Run 5 (new electrode) 24/11/21	255 (+/- 25)	1046 (+/- 10)
Run 6 (new electrode) 25/11/21	260 (+/- 30)	959 (+/- 10)

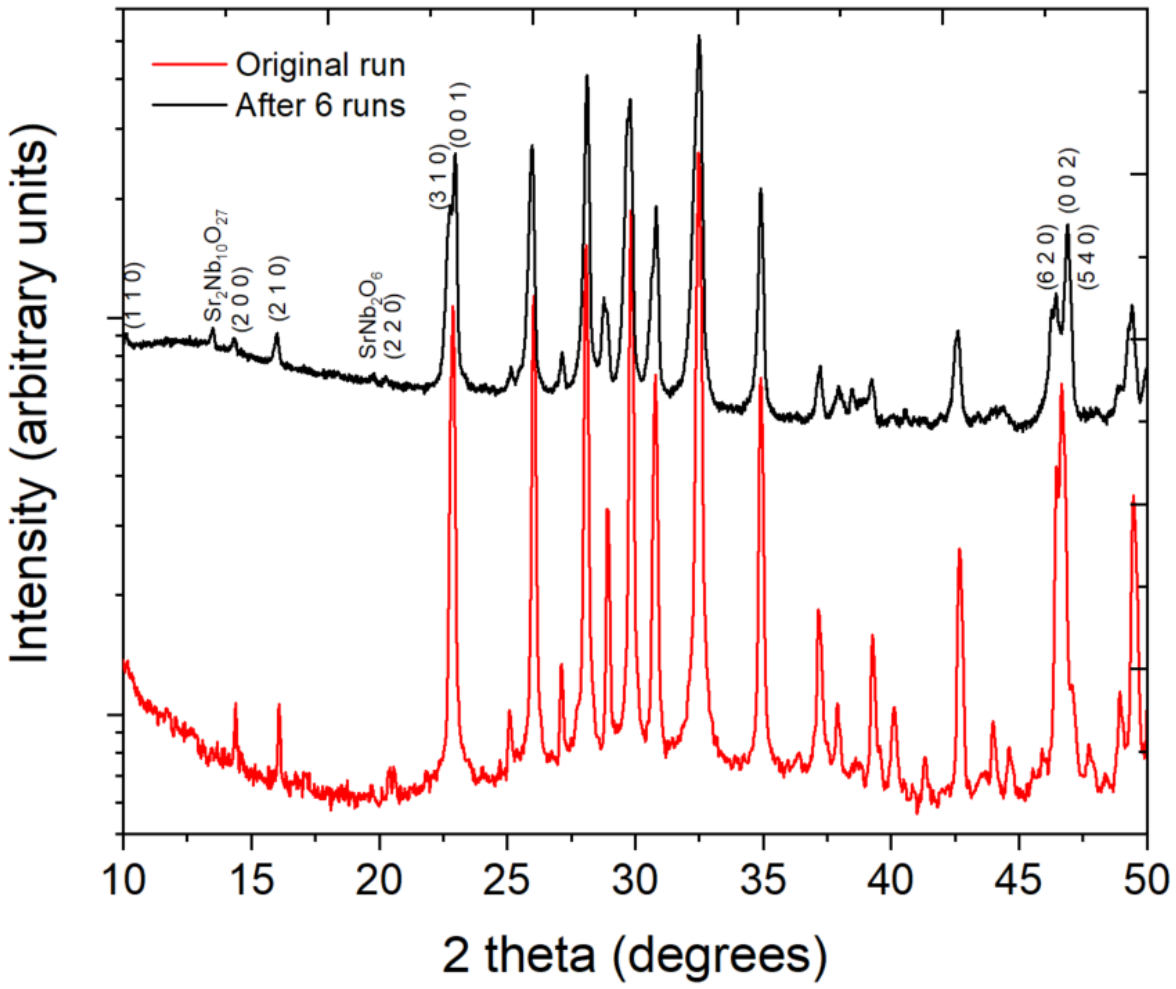

Figure 6.3.3. Log (intensity) plot XRD patterns of SNN0.8 (ER) whole sintered pellet before (red) and after six permittivity versus temperature measurements up to ~600 °C (black). The higher resolution of the black plot is due to it being a 5 h scan, as opposed to 24 min. After six permittivity-temperature measurements, a structural change from the orthorhombic to tetragonal main phase is evident because of peak splitting occurring at approximately 22.5 and 46 °2θ. Additional structural (and likely compositional) changes are evident in the 10 to 20 °2θ region where second and third phase $SrNb_2O_6$ (ICDD 04-011-3157) and $Sr_2Nb_{10}O_{27}$ (ICDD 01-088-4392) begin to form. SNN hkl values indexed to tetragonal *P4mbm* only for simplicity (ICDD 04-014-7370).

These results indicate that SNN0.8 could indeed undergo a degradation of electrical properties when heated to ~600 °C because of structural change and compositional breakdown. Further measurements were performed on a different pellet with the temperature taken to only ~300 °C to test any effect at the maximum capacitor operating temperature. The initial six measurements were taken within a week, the following four were made six weeks later and within approximately a week of each other. The sample was stored in a vacuum desiccator between runs. Figure 6.3.4 a shows the relative permittivity versus temperature plots when taken to 300 °C and initially seem to indicate that the ε_r value remains stable. However, some variation was seen with consecutive runs, as shown from the enlarged image (Figure 6.3.4 b), and a plot of T_2 $\varepsilon_{r\,max}$ values does show a decrease with consecutive runs (Figure 6.3.5). The increase at run 7 could be related to the six week gap between run 6 and 7, a downward trend was subsequently resumed. The drop in ε_r value was significantly less than that at 600 °C, with the decrease from run 1 (1580) to run 6 (1550) at 300 °C being only 30 (or a drop to only 98 % of the original value), compared to 815 when the temperature was taken to 600 °C (or a drop to 54 % of the original value) (Figures 6.3.1 and 6.3.2).

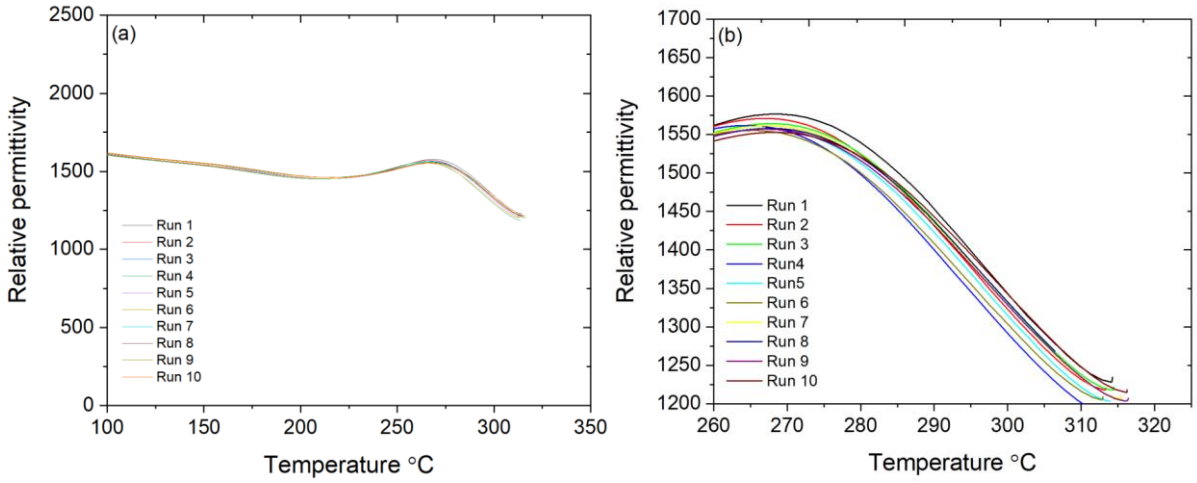

Figure 6.3.4 a-b. a) 1 kHz high temperature relative permittivity versus temperature plots for SNN0.8 (ES) showing ten consecutive measurements of the same sample up to ~300 °C, b) enlarged image illustrating some variation between consecutive runs.

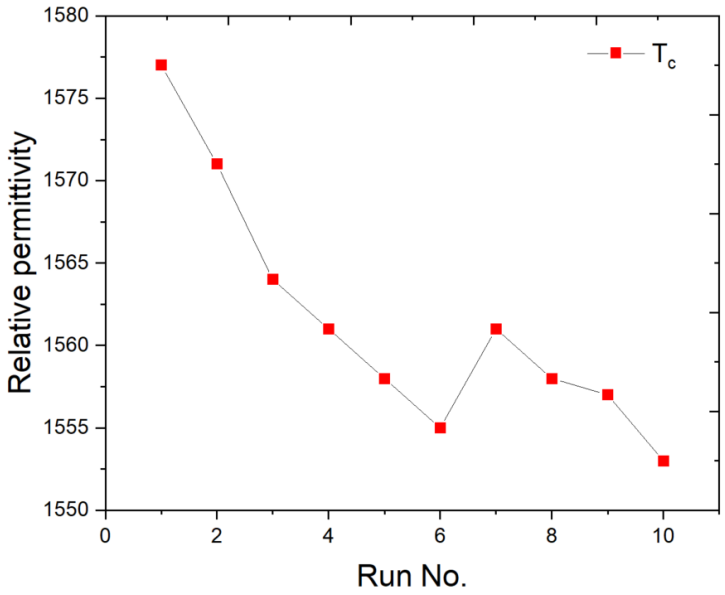

Figure 6.3.5. Plot of T_2 peak temperature (T_c) with consecutive permittivity versus temperature measurements to ~300 °C. A gap of six weeks between runs 6 and 7 is shown by a break in the downward trend. The ε_r intensity reading errors of T_2 are approximately 10 and so the step-break at run 6 is not thought to be significantly different to run 8.

6.4 Summary: Thermal related permittivity changes

A significant and cumulative drop in the permittivity-temperature response of SNN0.8 was observed with repeated measurements up to 600 °C. Although this was possibly due to the use of silver electrodes at high temperatures, XRD of the samples revealed that thermal decomposition of the SNN phase was occurring. Repeated permittivity-temperature measurements to 300 °C displayed greater stability, although a downward trend was still observed.

The drop in permittivity of SNN0.8 may be the result of thermal decomposition into strontium niobate, sodium niobate and a modified SNN phase as observed in Section 6.2. However, the presence of Na vacancies in the SNN0.8 could also enable A-site cation ordering with a corresponding change in T_c and $\varepsilon_{r\,max}$ as is established for $Ba_2NaNb_5O_{15}$ and $Sr_xBa_{1-x}Nb_2O_6$ (Aamlid et al. 2020). Further work on the structure and composition of the SNN phase retained after heating and partial decomposition will be required to address this (See Future Work Section 7.3).

Chapter 7. Conclusions and future work

7.1 Final Overview

A novel high temperature dielectric ceramic has been demonstrated through the doping of the tungsten bronze strontium sodium niobate, $Sr_2NaNb_5O_{15}$ (SNN1.0) with low levels of, Ca^{2+}, Y^{3+} and Zr^{4+} to introduce chemical inhomogeneity. The resulting materials, $Sr_{2-x-y}Ca_xY_xNaNb_{5-y}Zr_yO_{15}$ (SCNN-YZ) displayed diffuse dielectric peaks with high and stable relative permittivity from -55 to 300 ^oC and included the presence of a few weight percentage of a second phase Sr modified $NaNbO_3$ phase. The choice of Ca^{2+} as a dopant of SNN was based on literature reports that the $\varepsilon_{r\,max}$ values of the two dielectric peaks became more evenly matched, which was considered a good starting point for further doping with the aim of restricting the variation in permittivity to within the Electronics Industries Alliance R-type ±15 % value.

At sample composition x = y = 0.025, the ε_r values were 1565 ± 15 % from -65 °C to 325 °C (at 1 kHz). At a slightly higher level of doping, x = y = 0.05, ε_r values were 1310 ± 10 % from -65 °C to 300 °C (at 1 kHz). Values of the dielectric loss tangent, tanδ are ≤ 0.025 from -60 °C to 280 °C, for x = y = 0.025, with tanδ increasing to 0.035 at 325 ºC, and for x = y = 0.05, tanδ, ≤ 0.035 from -34 to 378 °C (Chapter 4, Section 4.3.2). Microstructural analyses excluded core-shell mechanisms being responsible for the flattening of the ε_r –T response. Composition SCNN-YZ for x = y = 0.05 uniquely showed extra phase ZrO_2 grains, identified by SEM-EDX (Chapter 4, Section 4.3.4).

Having demonstrated very favourable dielectric properties in the Ca^{2+}, Y^{3+}, and Zr^{4+} tri-doped SNN1.0 samples, an investigation into single doped SNN1.0 with Y^{3+} or Zr^{4+} was carried out to examine the individual effects of each dopant in the peak suppression and attainment of R-type stability in relative permittivity (Chapter 5, Section 5.2). A-site Y^{3+} for Sr^{2+} $Sr_{2-3x}Y_{2x}NaNb_5O_{15}$ (x = 0.0125, and 0.025, SNN-Y) and B-site Zr^{4+} for Nb^{5+} $Sr_2NaNb_{5-4y}Zr_{5y}O_{15}$ (y = 0.01, and 0.02, SNN-Z) were prepared assuming these substitution on the tungsten bronze lattice sites for Sr and Nb respectivelys. Y^{3+} for Sr^{2+} substitution showed a marked decrease in Sr modified $NaNbO_3$ second phase content and this was linked to an increase in A-site

vacancies in this composition leading to a stabilisation of the single phase (Chapter 5, Section 5.2.1). A single doped composition of SNN-Y, x = 0.05 but with Y^{3+} for Na^{+} substitution, $Sr_2Na_{1-3x}Y_xNb_5O_{15}$ (fabrication, Gardener, J. characterisation, Brown, T. University of Leeds) was free from Sr modified $NaNbO_3$ second phase, which would support that the presence of A-site vacancies reduced second phase content as this substitution requires the removal of three Na^{+} ions for every addition of Y^{3+}, thus forming a greater number of A-site vacancies than in the Y^{3+} for Sr^{2+} ceramic (Chapter 5, Section 5.4).

The high temperature T_2 dielectric peak in SNN-Y and SNN-Z showed a reduction in ε_r value and temperature with increased levels of dopant at 1kHz, with the effect markedly greater for A-site doping. Neither single dopants gave anything like the flat response seen in SCNN-YZ (x = y = 0.05). No clear trends were observed in relation to the low temperature T_1 dielectric peak, although some broadening and a greater frequency dependence was observed with increased doping (Chapter 5, Section 5.2.2). Similar trends in relative permittivity were seen in co-doped compositions of $Sr_{2-x}Y_xNaNb_{5-x}Zr_xO_{15}$ (x = 0.025 and 0.05) and the temperature response was flattened closer to that of the tri-doped material, however, a third dielectric anomaly was observed in composition x = 0.05 at ~180 °C. This was frequency dependent indicating it to be a space charge effect, possibly caused by the presence of vacancies (Cao et al. 2021). Undetected ZrO_2 second phase like that seen in SCNN-YZ, x = y = 0.05 (Chapter 4), would create B-site vacancies.

On discovering that SNN was a solid solution $Sr_{2+x}Na_{1-2x}Nb_5O_{15}$ (SNN), and that on cooling from sintering temperatures the SNN1.0 composition, x = 0, lies outside the single phase solid solution region at room temperature, investigations were undertaken on a composition in the centre of this region at x = 0.1, $Sr_{2.1}Na_{0.8}Nb_5O_{15}$ (SNN0.8, Chapter 5, Section 5.5). This A-site vacancy rich formulation could allow a stable single phase due to a reduction in the Madelung energy of the SNN phase caused by the presence of vacancies (Jang et al. 2004). This vacancy induced mechanism would also explain the reduced extra phase content of SNN-Y (Chapter 5, Section 5.2.5). It was found that an extended sintering run (1320 °C, 25 h) would achieve a sufficiently dense and single phase sample of SNN0.8. Standard sintering conditions (~4 h), at a higher temperature of 1450 °C did also achieve densities of > 90 % but was accompanied by large decreases in relative

permittivity. This raised questions about the thermal history of the samples adversely affecting the permittviity response and led to the thermal stability investigation of Chapter 6. Finally, doped composition of SNN0.8, $Sr_{2.1-x-y}Ca_xY_xNa_{0.8}Nb_{5-y}Zr_yO_{15}$ (SCNN-YZ 0.8, x = y = 0.05) and A-site vacancy rich Y^{3+} for Na^+ $Sr_{2.1}Y_xNa_{0.8-3x}Nb_5O_{15}$, (SNN-Y0.8, x = 0.05, Gardener. J, University of Leeds) both displayed a third dielectric peak at ~180 ^oC that was a space charge effect previously attributed to the presence of A-site vacancies (Chapter 5, Section 5.6).

Although the dielectric properties of the SCNN-YZ ceramics appear favourable in terms of developing new high temperature capacitor materials, the presence of Na (A-site) vacancies in the SNN solid compositions is a drawback. This was particularly acute in SNN0.8 compositions that showed an apparent dependence of permittivity on the materials thermal history. Literature reports that SNN is metastable below ~1180 ^oC confirmed this concern (Tang et al. 1979). The significance of this from a capacitor application perspective would depend on the kinetics of any decomposition. Therefore temperature instability studies relating to phase stability were conducted in Chapter 6.

Annealing of SNN1.0 (600 ^oC and in situ X-ray diffraction 400 ^oC, 24 h), SCNN-YZ (x = y = 0.05) (600 ^oC) calcined powder and SNN0.8 crushed sintered pellets (400 ^oC) all showed a structural change of the SNN phase from orthorhombic *Im2a* to tetragonal *P4mbm* on passing through T_c (Chapter 6, Sections 6.2.3. 6.2.4 and 6.2.5). Compositional decomposition was observed at 600 ^oC, with extra phases of strontium niobate forming after about 2 h and increasing with time up to 45 weeks (Chapter 6, Sections 6.2.3 and 6.2.5). In situ X-ray diffraction showed the change in composition of SNN1.0 at 600 ^oC resulted in the SNN phase remaining tetragonal on cooling to room temperature, whilst SNN1.0 at 400 ^oC (in situ X-ray diffraction, 24 h) saw no extra phase formation and the SNN structure returned to orthorhombic on cooling. Breakdown was oberved in SNN0.8 at 400 ^oC after annealing for 24 weeks (Chapter 6, Figure 6.2.11).

At 300 ^oC (around T_c (T_2)), all compositions retained the orthorhombic structure for the SNN phase up to ~24 weeks, and no significant additional phases were identified although some tentative evidence of structural decomposition was present in the XRD patterns (Chapter 6, Table 6.2.1). This will be pusued in future

work because higher resolution/lower signal to noise ratio X-ray diffraction data are needed to confirm if the structure and the composition changes or remains intact at this temperature.

7.2 Conclusions

The main conclusions of this study are as follows.

Tungsten bronze, strontium sodium niobate, $Sr_2NaNb_5O_{15}$ with low levels of, Ca^{2+}, Y^{3+} and Zr^{4+} doping displayed diffuse dielectric peaks with high and stable relative permittivity of 1310 ± 10 % from -65 °C to 300 °C (at 1 kHz; $Sr_{2-x-y}Ca_xY_xNaNb_{5-y}Zr_yO_{15}$ x= y = 0.05). Therefore, the permittivity variation target of +/- 15 % from -55 °C to 300 °C set in the objectives section (Chapter 1) was achieved and exceeded. Single dopants of Y^{3+} or Zr^{4+} in $Sr_2NaNb_5O_{15}$ do not reproduce the flat permittivity response of the above material however co-doped materials nearly do. The novel approach of doping with three similarly sized cations was shown to allow the controlled suppression of the high temperature permittivity peak (T_2) to a similar size to the low temperature peak (T_1), thus reducing the relative permittivity variation across the temperature range.

X-ray diffraction data revealed that $Sr_2NaNb_5O_{15}$ always contained some second phase Sr modified $NaNbO_3$ while the introduction of Na (A-site) vacancies in SNN up to at least $Sr_{2.1}Na_{0.8}Nb_5O_{15}$ results in single phase formation (but increases the dielectric losses of the material at high temperature above ~ 250 °C). The presence or absence of extra phase material was confirmed with SEM and SEM-EDX imaging.

The structural and ferroelectric thermal instability of SNN compositions was identified through high temperature annealing and repeated high temperature permittivity measurement experiments. $Sr_2NaNb_5O_{15}$ and $Sr_{2.1}Na_{0.8}Nb_5O_{15}$ plus doped variations are metastable and will breakdown to strontium niobate and sodium niobate phases at temperatures above 300 ^oC, with the rate increasing as temperature increases. The metastable nature of SNN was previously identified in foreign language papers but the changing rates of structural decomposition with

increasing temperature and the ferroelectric instability have not been previously recognised.

Thus the main overall output of this thesis is that co or triple doped SNN compositions with minimal Na (A-site) vacancies are likely the best formulations to obtain R-type Class II capacitor performance despite the presence of small amounts of second phase (Sr modified $NaNbO_3$) in these materials. The thermal instability above 300 ^oC however remains a concern.

7.3 Future work

- Confirmation of relative permittivity stability in triple doped SCNN YZ vs vacancy rich SNN 0.8 below 300 ^oC with impedance spectroscopy to determine loss mechanism (begun by Dr J. Gardener, see Appendix A).
- Production of a series of $Sr_{2+x}Na_{1-2x}Nb_5O_{15}$ (SNN) (x = 0.05 to 0.15) to determine a threshold for producing a single phase SNN (ideally with a standard sintering regime) like SNN0.8, but without Na^+ vacancies. Comparison of data such as relative permittivity versus temperature and SEM to determine the effects of vacancies on the material properties.
- Novel doping of this single phase SNN composition with Y^{3+} and Zr^{4+} to attain stable relative permittivity, suitable for use in a R-type Class II capacitor. The ideal outcome is to produce a temperature stable single phase material with < +/- 15 % relative permittivity variation.
- SNN1.0 in situ XRD at 1000 ^oC to determine increased/complete breakdown of the SNN phase at this elevated temperature. Also a threshold time for the commencement of additional phase formation at 300 ^oC should be determined using the same technique. This will determine whether the material could be practically stable for the desired application.

- High-resolution (synchrotron) X-ray diffraction data on annealed samples of SNN to determine rates and activation energies for breakdown i.e. kinetics.
- Raman Spectroscopy of B-site-O stretching vibrations at 845 cm^{-1}, B-site-O bending vibrations at 630 cm^{-1} and the O-B-site-O bending vibrations at 250 cm^{-1} to determine local co-ordination changes/distortions in Nb octahedra on doping with elements and vacancies (ensuring that radiation damage does not occur in the process).
- Investigation into thermal instability of other TTB compositions to determine whether the addition of dopants or the presence of A-site vacancies will alter the rate of thermal decomposition. This was briefly looked at but a more detailed study is required to draw any conclusions.

Chapter 8 – References

Aamlid, S.S., Selbach, S.M. and Grande, T. (2020). Structural Evolution of Ferroelectric and Ferroelastic Barium Sodium Niobate Tungsten Bronze [online]. *Inorganic Chemistry*, 59(12), pp.8514–8521. [Accessed 15/11/21] Available at: https://doi.org/10.1021/acs.inorgchem.0c00958

Akimune, Y et al. 2003. *Piezoelectric material and method for manufacture thereof*. US 2003/0151331 A1

Arnold, D. and Morrison, F. (2009). B-cation effects in relaxor and ferroelectric tetragonal tungsten bronzes. [online] *Journal of Materials Chemistry*, 19(36), p.6485. [Accessed 22/01/19] Available at: http://doi.org/10.1039/b912535c

Bell, A. (2008). Ferroelectrics: The role of ceramic science and engineering. [online] *Journal of the European Ceramic Society*, 28(7), pp.1307-1317. [Accessed 26/07/19] Available at: http://doi.org/10.1016/j.jeurceramsoc.2007.12.014

Bokov, A. (1992). Recent advances in diffuse ferroelectric phase transitions. *Ferroelectrics*. 131(1),pp.49-55. [Accessed 22/07/19] Available at: https://doi.org/10.1080/00150199208223391

Bokov, A. and Ye, Z. (2006). Recent progress in relaxor ferroelectrics with perovskite structure. *Journal of Materials Science*, 41(1), pp.31-52. [Accessed 15/08/22] Available at: http://doi.org/DOI:10.1007/s10853-005-5915-7 .

Brown, T., Brown, A., Hall, D., Hooper, T., Li, Y., Micklethwaite, S., Aslam, Z. and Milne, S. (2020). New high temperature dielectrics: Bi-free tungsten bronze ceramics with stable permittivity over a very wide temperature range. [online] *Journal of the European Ceramic Society*, 41 (6), pp. 3416-3424. Available at: https://doi.org/10.1016/j.jeurceramsoc.2020.10.034

Cao, L., Yuan, Y., Zhang, X., Li, E. and Zhang, S., 2020. Relaxor Nature and Energy Storage Properties of Sr2–xMxNaNb5–xTixO15 (M = La3+ and Ho3+) Tungsten Bronze Ceramics.[online] *ACS Sustainable Chemistry & Engineering*, 8(47), pp.17527-17539. Available at: https://dx.doi.org/10.1021/acssuschemeng.0c06861

Callister, W. and Rethwisch, D. (2015). *Fundamentals of materials science and engineering*. 5th ed. Hoboken: Wiley.

Choi, D., Baker, A., Lanagan, M., Trolier-McKinstry, S. and Randall, C. (2013). Structural and Dielectric Properties in (1−x)BaTiO3-xBi(Mg1/2Ti1/2)O3Ceramics (0.1 ≤ x ≤ 0.5) and Potential for High-Voltage Multilayer Capacitors.[online] *Journal of the American Ceramic Society*, 96(7), pp.2197-2202. [Accessed 07/08/19] Available at: http://doi.org/DOI:10.1111/jace.12312

Cross, L. (1994). Relaxorferroelectrics: An overview. [online] *Ferroelectrics*, 151(1), pp.305-320. [Accessed 05/05/19] Available at: http://doi.org/DOI:10.1080/00150199408244755

Cullity, B. and Stock, S. (2014). *Elements of x-ray diffraction*. 3rd ed. Pearson Education Limited.

Demic, S., Ozcivan, A., Can, M., Ozbek, C. and Karakaya, M. (2017). Recent Progresses in Perovskite Solar Cells. Intech [online] [Accessed 10 July 2019] Available at: http://doi.org/10.5772/65019

Dept. of Chemistry & Biochemistry, University of Oklahoma, (2019), *Symmetry in Crystallography.* University of Oklahoma. [Accessed 02/09/22] Available at: http://xrayweb.chem.ou.edu/notes/symmetry.html

Doitpoms.ac.uk. (2018). DoITPoMS - TLP Library Ferroelectric Materials. [online] Available at: https://www.doitpoms.ac.uk/tlplib/ferroelectrics/printall.php [Accessed 25 Mar. 2019].

Fan, X., Wang, Y. and Jiang, Y. (2011). Structure and electrical properties of MnO2-doped Sr2−xCaxNaNb5O15 lead-free piezoelectric ceramics. [online] *Journal of Alloys and Compounds*, 509(23), pp.6652-6658. [Accessed 23/01/19] Available at: https://doi.org/10.1016/j.jallcom.2011.03.130

Fan, J., Yang, B., Wei, L. and Wang, Z. (2015). B-cation effect on relaxor behavior and electric properties in Sr2NaNb5−Sb O15 tungsten bronze ceramics. [online] *Ceramics International*. 42(3),pp.4054-4062. [Accessed 10 March 2022] Available at: https://doi.org/10.1016/j.ceramint.2015.11.077

Felder, J.B., Wong-Ng, W., Qabbani, R.A., Roth, R.S., Toby, B.H. and Chan, J.Y. (2019). Structural investigation of the 'tripled-tetragonal-tungsten-bronze' phases Sr2M10−O27− (M = Nb, Ta). [online] *Polyhedron*, 170, pp.359–363. [Accessed 22/09/22] Available at: https://doi.org/10.1016/j.poly.2019.06.003

Feng, W., Zhu, X. and Chen, X., (2021). Crystal structure, dielectric, and ferroelectric characteristics of zirconate tantalate ceramics with tungsten bronze structure. [online] *Journal of Materials Science: Materials in Electronics*, 32(6), pp.7481-7490. [Accessed 14/09/21] Available at: https://doi.org/10.1007/s10854-021-05461-0

Gao, L., Yadgarov, L., Sharma, R., Korobko, R., McCall, K., Fabini, D., Stoumpos, C., Kanatzidis, M., Rappe, A. and Yaffe, O. (2021). Metal cation s lone-pairs increase octahedral tilting instabilities in halide perovskites. [online] *Materials Advances*. 2(14),pp.4610-4616. [Accessed 16/08/22] Available at: https://doi.org/10.1039/d1ma00288k

García-González, E., Torres-Pardo, A., Jiménez, R. and González-Calbet, J. (2007). Structural Singularities in Ferroelectric Sr2NaNb5O15. *Chemistry of Materials*, 19(14), pp.3575-3580. [Accessed 17/07/19] Available at: http://doi.org/10.1021/cm071303w

Gardner, J. and Morrison, F. (2014). A-site size effect in a family of unfilled ferroelectric tetragonal tungsten bronzes: Ba4R0.67Nb10O30 (R = La, Nd, Sm, Gd, Dy and Y).[online] *Dalton Trans.*, 43(30), pp.11687-11695. [Accessed 24/01/19] Available at: https://doi.org/10.1039/c4dt00126e

Gardner (2016) Thesis

Gardner, J., Yu, F., Tang, C., Kockelmann, W., Zhou, W. and Morrison, F. (2016). Relaxor-to-Ferroelectric Crossover and Disruption of Polar Order in “Empty” Tetragonal Tungsten Bronzes. [online] *Chemistry of Materials*, 28(13), pp.4616-4627. [Accessed 21/01/19], Available at: http://doi.org/10.1021/acs.chemmater.6b01306

Gardner, J. and Morrison, F. (2016). Manipulation of polar order in the “empty” tetragonal tungsten bronzes: $Ba_{4-x}Sr_xD_{y0.67}\square_{1.33}Nb_{10}O_{30}$, x = 0, 0.25, 0.5, 1, 2, 3. [online] *Applied Physics Letters*. 109(7),p.072901. [Accessed 21/01/19], Available at: https://doi.org/10.1063/1.4960712

Geusic, J., Levinstein, H., Rubin, J., Singh, S. and Van Uitert, L. (1967). The nonlinear optical properties of Ba2NaNb5O15. [online] *Applied Physics Letters*. 11(9),pp.269-271. [Accessed 02/09/22], Available at: https://doi.org/10.1063/1.1755129

Guyonnet, J. 2014. *Ferroelectric Domain Walls*. Cham: Springer International Publishing.

Hammond, C. 2015. *The basics of crystallography and diffraction*. Oxford University Press.

Hao, S., Li, J., Yang, P., Wei, L. and Yang, Z. (2017). Enhanced electrical properties and strong red light-emitting in Eu^{3+}-doped $Sr_{1.90}Ca_{0.15}Na_{0.9}Nb_5O_{15}$ ceramics. [online] *Journal of the American Ceramic Society*. 100(12),pp.5620-5628. [Accessed 10 March 2022], Available at: https://doi.org/10.1111/jace.15085

Hao, S., Li, J., Sung, Q., Wei, L. and Yang, Z. (2019). Improved electrical properties and good thermal luminescent stability of Sm^{3+}-doped $Sr_{1.90}Ca_{0.15}Na_{0.90}Nb_5O_{15}$ multifunctional ceramics. [online] *Journal of Materials Science: Materials in Electronics*. 30(14),pp.13372-13380. [Accessed 10 March 2022], Available at: https://doi.org/10.1007/s10854-019-01704-3.

Hass, D. and Wadley, H. (2011). A Dielectric Sensing Approach for Controlling Matrix Composition During Oxide-Oxide Ceramic Composite Processing. *Journal of Nondestructive Evaluation*. 30(2), pp.81-90. [Accessed 13 August 2022], Available at: https://doi.org/10.1007/s10921-011-0093-9

Hennings, D. (1987). Barium titanate based ceramic materials for dielectric use. [online] *International Journal of High Technology Ceramics*, 3(2), pp.91-111. [Accessed 05/07/19] Available at:

https://www.sciencedirect.com/journal/international-journal-of-high-technology-ceramics/vol/3/issue/2

Huang, W., Chen, Y., Li, X., Wang, G., Liu, N., Li, S., Zhou, M. and Dong, X. (2018). Ultrahigh recoverable energy storage density and efficiency in barium strontium titanate-based lead-free relaxor ferroelectric ceramics. [online] *Applied Physics Letters*, 113(20), p.203902. [Accessed 20/02/20] Available at: http://doi.org/10.1063/1.5054000

IEEE standard definitions of terms associated with ferroelectric and related materials. (2003). [online] *IEEE Transactions on Ultrasonics, Ferroelectrics and Frequency Control*, 50(12), pp.1613-1646. [Accessed 25/07/19] Available at: http://doi.org/10.1109/TUFFC.2003.1256301

Ishihara, T. 2009. *Perovskite Oxide for Solid Oxide Fuel Cells*. Boston, MA: Springer-Verlag US.

Jaffe, B., Cook, W. and Jaffe, H. 1971. *Piezoelectric ceramics by Bernard Jaffe and William R. Cook Jr and Hans Jaffe*. London: Academic Press.

Jang, C., Lee, J., Kim, J., Cho, S. and Lee, H. (2004). Phase Stability of Tungsten-Bronze-Structured KLN Ceramics: Effect of Excess Nb2O5. [online] *Journal of Electroceramics*. 13(1-3),pp.847-850. [Accessed 06 September 2022] Available at: https://link.springer.com/article/10.1007/s10832-004-5202-z

Kingery, W., Bowen, H. and Uhlmann, D. 1976. *Introduction to ceramics*. New York: Wiley.

Kittel, C. 1953. *Introduction to solid state physics*. New York: Wiley.

Lanfredi, S., Gênova, D., Brito, I., Lima, A. and Nobre, M. (2011). Structural characterization and Curie temperature determination of a sodium strontium niobate ferroelectric nanostructured powder. [online] *Journal of Solid State Chemistry*. 184(5),pp.990-1000. [Accessed 08 March 2022] Available at: http://doi.org/10.1016/j.jssc.2011.03.001

Lee, H. and Freer, R., (1997). The mechanism of abnormal grain growth in Sr0.6Ba0.4Nb2O6ceramics. *Journal of Applied Physics*, 81(1), pp.376-382. [Accessed 08 March 2022] Available at: https://doi.org/10.1063/1.364122

Lee, W., Huang, C., Tsao, L. and Wu, Y. 2009. Chemical composition and tolerance factor at the morphotropic phase boundary in (Bi0.5Na0.5)TiO3-based piezoelectric ceramics. *Journal of the European Ceramic Society*. 29(8),pp.1443-1448. [Accessed 15 August 2022] Available at: http://doi.org/10.1016/j.jeurceramsoc.2008.08.028

Levin, I., Stennett, M., Miles, G., Woodward, D., West, A. and Reaney, I. (2006). Coupling between octahedral tilting and ferroelectric order in tetragonal tungsten bronze-structured dielectrics. [online] *Applied Physics Letters*, 89(12), p.122908. [Accessed 14/01/19] Available at: http://doi.org/10.1063/1.2355434

Li, L., Yang, B., Chao, X., Wu, D., Wei, L. and Yang, Z., (2019). Effects of preparation method on the microstructure and electrical properties of tungsten bronze structure Sr2NaNb5O15 ceramics. *Ceramics International*, 45(1), pp.558-565. [Accessed 19/05/2020] Available at: https://doi.org/10.1016/j.ceramint.2018.09.208

Malič, B., Koruza, J., Hreščak, J., Bernard, J., Wang, K., Fisher, J. and Benčan, A. (2015). Sintering of Lead-Free Piezoelectric Sodium Potassium Niobate Ceramics.

[online] *Materials*, 8(12), pp.8117-8146. [Accessed 23/01/20] Available at: http://doi.org/10.3390/ma8125449

Matsuo K., Kie R., Akimune Y., and Sugiyama T. (2002). Preparation of Lead-Free $Sr_{2-x}Ca_xNaNb_5O_{15}$ (x=0.1)-Based Piezoceramics with Tungsten Bronze Structure. [online]. *Journal of Ceramics Society of Japan* 110 (5), 491-494. [Accessed 26/05/2021] Available at: http://doi.org//10.2109/jcersj.110.491

McNulty, J., Pesquera, D., Gardner, J., Rotaru, A., Playford, H., Tucker, M., Carpenter, M. and Morrison, F. (2020). Local Structure and Order–Disorder Transitions in “Empty” Ferroelectric Tetragonal Tungsten Bronzes. [online] *Chemistry of Materials*. 32(19),pp.8492-8501. [Accessed 23/01/20] Available at: https://dx.doi.org/10.1021/acs.chemmater.0c02639

Mikhail Smirnov (PD), Pierre Saint-Grégoire (MIPA) (2013). An innovative approach of structural instabilities in tetragonal tungsten bronze crystals through the concept of rigid unit modes. [online] [Accessed 14/01/19] Available at: **arXiv:1302.3692v2**

Miller, A., Rotaru, A., Arnold, D. and Morrison, F. (2015). Effect of local A-site strain on dipole stability in A6GaNb9O30 (A = Ba, Sr, Ca) tetragonal tungsten bronze relaxor dielectrics. [online] *Dalton Transactions*, 44(23), pp.10738-10745. [Accessed 21/01/19] Available at: http://doi.org/10.1039/c4dt03936j

Morin, D., Colin, J. and Le Roux, G. (1973). Equilibre de phases et caracterisation dielectrique des niobates mixtes de strontium et de sodium. *Materials Research Bulletin*. 8(9),pp.1089-1101. [Accessed 25/07/22] Available at: https://doi.org/10.1016/0025-5408(73)90116-5

Moulson, A. (2003). *Electroceramics*. Chichester: John Wiley & Sons.

Olsen, G., Sørby, M., Selbach, S. and Grande, T. 2017. Role of Lone Pair Cations in Ferroelectric Tungsten Bronzes. [online] *Chemistry of Materials*. 29(15),pp.6414-6424. [Accessed 16/08/22] Available at: https://doi.org/10.1021/acs.chemmater.7b01817

Pecharsky, V. and Zavalij, P. (2009). *Fundamentals of powder diffraction and structural characterization of materials*. Boston, MA: Springer US.

Pandu, R. (2014). CrFe 2O4 - BiFeO3 Perovskite Multiferroic Nanocomposites – A Review. Materials Science Research India [online] Vol. 11(2), pp128-145 [Accessed 29 April 2018] Available at: http://dx.doi.org/10.13005/msri/110206

Raju, G.G. Dielectrics in Electric Fields. New York: Taylor & Francis, 2003.

Ravez, J., Budin, J. and Hagenmuller, P. (1972). Etude comparative des propriétés cristallographiques, diélectriques et d'optique non linéaire des phases ABCNb5O15 (A = Ca, Sr, Ba, B = Ca, Sr, Ba, C = Na, K) de type “bronzes oxygénés de tungstène quadratiques. [online] *Journal of Solid State Chemistry*. 5(2), pp. 239-246. [Accessed 08 March 2022] Available at: https://doi.org/10.1016/0022-4596(72)90034-5

Ravez, J. and Simon, A. (2001). Some Solid State Chemistry Aspects of Lead-Free Relaxor Ferroelectrics. *Journal of Solid State Chemistry*. 162(2),pp.260-265. . [Accessed 15 August 2022] Available at: https://doi.org/10.1006/jssc.2001.928

Roncal-Herrero, T., Harrington, J., Zeb, A., Milne, S. and Brown, A. (2018). Nanoscale compositional segregation and suppression of polar coupling in a relaxor ferroelectric. [online] *Acta Materialia*, 158, pp.422-429. [Accessed 04/01/19] Available at: http://doi.org/10.1016/j.actamat.2018.07.053

Rotaru, A., Miller, A., Arnold, D. and Morrison, F. (2014). Towards novel multiferroic and magnetoelectric materials: dipole stability in tetragonal tungsten bronzes. [online] *Philosophical Transactions of the Royal Society A: Mathematical, Physical and Engineering Sciences*. 372(2009),p.20120451. . [Accessed 16/08/22] Available at: http://doi.org/10.1098/rsta.2012.0451

Said, M., Velayutham, T., Gan, W. and Abd Majid, W. (2015). The structural and electrical properties of SrxBa(1−x)Nb2O6 (SBN) ceramic with varied composition. [online] *Ceramics International*, 41(5), pp.7119-7124. [Accessed 03/05/19] Available at http://dx.doi.org/10.1016/j.ceramint.2015.02.023

Sebastian, M. 2010. *Dielectric Materials for Wireless Communication*. Burlington: Elsevier Science.

Shannon, R.D. Central Research and Development Department, Experimental Station, E. I. Du Pont de Nemours and Company, Wilmington, Delaware 19898, U.S.A. Published in Acta Crystallographica. (1976). A32, Pages 751-767

Shvartsman, V. and Lupascu, D. (2011). Lead-Free Relaxor Ferroelectrics. [online] *Journal of the American Ceramic Society*. 95(1),pp.1-26. [Accessed 15/08/22] Available at http://dx.doi.org/10.1111/j.1551-2916.2011.04952.x

Simon, A. and Ravez, J. 2006. Solid-state chemistry and non-linear properties of tetragonal tungsten bronzes materials. [online] *Comptes Rendus Chimie*. 9(10),pp.1268-1276. [Accessed 16/08/22] Available at http://dx.doi.org/10.1016/j.crci.2006.04.001

Stewart, M. Cain, M.G. Hall, D.A. Ferroelectric hysteresis measurement & analysis, Natl. Phys. Lab. Rep. CMMT(A) 152 (1) (1999).

Takeda, T. 2009. *Dielectric ceramic composition and monolithic ceramic capacitor*. US 2009/0290285 A1

Takenaka, H., Grinberg, I., Liu, S. and Rappe, A. (2017). Slush-like polar structures in single-crystal relaxors.[online] *Nature*, 546(7658), pp.391-395.[Accessed 22/07/19] Available at: http://doi.org/doi:10.1038/nature22068

Tang Di-Sheng, Liang Jing-Kui, Shi Ting-Jun, Zhang Yu-Ling, Tian Jing-Hua, Li Wen-Xiu. (1979) Investigation of the pseudo-ternary system $SrNb_2O_6$-$NaNbO_3$-$LiNbO_3$. [online] *Acta Physica Sinica*, 28(1): 62-77. [Accessed 25/07/21] Available at: 10.7498/aps.28.62

Torres-Pardo, A., Jiménez, R., González-Calbet, J. and García-González, E. (2011). Structural Effects Behind the Low Temperature Nonconventional Relaxor Behavior of the Sr2NaNb5O15 Bronze. [online] *Inorganic Chemistry*, 50(23), pp.12091-12098. [Accessed 02/08/19] Available at: http://doi.org/dx.doi.org/10.1021/ic2016098

Van Uitert, L., Levinstein, H., Rubin, J., Capio, C., Dearborn, E. and Bonner, W. (1968). Some characteristics of niobates having “filled” tetragonal tungsten bronze-like structures. [online] *Materials Research Bulletin*. 3(1),pp.47-57. [Accessed 02/08/19] Available at: http://doi.org/10.1016/0025-5408(68)90024-X

Wang, H., Liu, Y., Yang, T. and Zhang, S. (2019). Ultrahigh Energy-Storage Density in Antiferroelectric Ceramics with Field-Induced Multiphase Transitions. [online] *Advanced Functional Materials*, 29(7), p.1807321. [Accessed 20/02/20] Available at: http://doi.org/10.1002/adfm.201807321

Wei, L., Yang, Z., Han, X. and Li, Z. (2012). Structures, dielectric and ferroelectric properties of Sr2-xCaxNaNb5O15 lead-free ceramics. [online] *Journal of Materials*

Research, 27(07), pp.979-984. [Accessed 05/01/19] Available at: http://doi.org/10.1557/jmr.2012.32

Wei, L., Yang, Z., Gu, R. and Ren, H., (2010). The Phase Formation, Microstructure, and Electric Properties of Tungsten Bronze Ferroelectric Sr2NaNb5O15Ceramics. [online] *Journal of the American Ceramic Society*,.93. [Accessed 29/06/20] Available at: http://doi.org/10.1111/j.1551-2916.2010.03683.x

Wei, L., Yang, Z., Ren, H. and Chen, X. (2010). Phase Transitional Behaviour and Electrical Properties of Sr2K0.1Na0.9Nb5−xTaxO15 Ceramics. [online] *Journal of the American Ceramic Society*. 93(12),pp.3986-3989. [Accessed 29/06/20] Available at: http://doi.org/10.1111/j.1551-2916.2010.04177.x

West, A. (2014). *Solid State Chemistry and its Applications*. Somerset: Wiley.

Whittle, T., Howard, C. and Schmid, S. (2021). Structures and phase transitions in barium sodium niobate tungsten bronze (BNN). [online] *Acta Crystallographica Section B Structural Science, Crystal Engineering and Materials*. 77(6),pp.981-985. [Accessed 03/09/22] Available at: https://doi.org/10.1107/S2052520621010301

Williams, D. and Carter, C. (2009). *Transmission Electron Microscopy*. Boston, MA: Springer US.

Xie, R., Akimune, Y., Matsuo, K., Sugiyama, T., Hirosaki, N. and Sekiya, T. (2002) [1]. Dielectric and ferroelectric properties of tetragonal tungsten bronze Sr2−xCaxNaNb5O15 (x=0.05–0.35) ceramics. [online] *Applied Physics Letters*, 80(5), pp.835-837. [Accessed 20/12/18] Available at: http://doi.org/10.1063/1.1446997

Xie, R. and Akimune, Y., (2002) [2]. Lead-free piezoelectric ceramics in the (1 − x)Sr2NaNb5O15–xCa2NaNb5O15(0.05 ≤ x ≤ 0.35) system. [online] *J. Mater. Chem.*, 12(10), pp.3156-3161. [Accessed 29/06/20] Available at: http://doi.org/10.1039/b202923p

Yang, L., Li, X., Allahyarov, E., Taylor, P., Zhang, Q. and Zhu, L. (2013). Novel polymer ferroelectric behaviour via crystal isomorphism and the nano-confinement effect. [online] *Polymer*, 54(7), pp.1709-1728. [Accessed 09/03/20] Available at: http://dx.doi.org/10.1016/j.polymer.2013.01.035

Yang, P., Li, L., Hao, S., Chao, X., Wei, L. and Yang, Z. (2017). Electrical and transparent properties induced by structural modulation in (Sr0.925Ca0.075)2.5–0.5Na Nb5O15 ceramics. [online] *Journal of the European Ceramic Society, 37, 2605-2613.* [Accessed 16/05/20] Available at: http://dx.doi.org/10.1016/j.jeurceramsoc.2017.02.035

Yang, B., Li, J., Yang, P., Wei, L. and Yang, Z. (2019). Effects of A-site cations on the electrical behaviours in (Sr1-xCax)2.1Na0.8Nb5O15 tungsten bronze ferroelectrics. [online] *Materials Chemistry and Physics*, 243, p.122006. [Accessed 05/11/20] Available at: https://doi.org/10.1016/j.matchemphys.2019.122006

Zeb, A. and Milne, S.J. (2015). High temperature dielectric ceramics: a review of temperature-stable high-permittivity perovskites. *Journal of Materials Science: Materials in Electronics*, [online] 26(12), pp.9243–9255. [Accessed 13/10/22] Available at: https://doi.org/10.1007/s10854-015-3707-7

Zeb, A., ullah Jan, S., Bamiduro, F., Hall, D.A. and Milne, S.J. (2018). Temperature-stable dielectric ceramics based on Na0.5Bi0.5TiO3. *Journal of the European*

Ceramic Society, 38(4), pp.1548–1555. [Accessed 14/10/22] Available at: https://doi.org/10.1016/j.jeurceramsoc.2017.12.032

Zhang, X., Ye, W., Bu, X., Zheng, P., Li, L., Wen, F., Bai, W., Zheng, L. and Zhang, Y., (2021). Remarkable capacitive performance in novel tungsten bronze ceramics. *Dalton Transactions*, 50(1), pp.124-130. [Accessed 13/10/22] Available at: http://doi.org/10.1039/d0dt03511d

Zhu, X., Fu, M., Stennett, M., Vilarinho, P., Levin, I., Randall, C., Gardner, J., Morrison, F. and Reaney, I. (2015). A Crystal-Chemical Framework for Relaxor versus Normal Ferroelectric Behavior in Tetragonal Tungsten Bronzes. [online] *Chemistry of Materials*, 27(9), pp.3250-3261. [Accessed 15/01/19] Available at: https://doi.org/10.1021/acs.chemmater.5b00072

Li Zhu, X., Bai, Y., Liu, X. and Ming Chen, X. (2011). Ferroelectric phase transition and low-temperature dielectric relaxations in Sr4(La1−xSmx)2Ti4Nb6O30 ceramics. *Journal of Applied Physics*, 110(11), p.114101.[Accessed 05/12/19] Available at: https://doi.org/10.1063/1.3664857

Appendix A

Ferroelectric Ageing

Other work on the long duration ferroelectric ageing of permittivity of SNN0.8 (data acquired by Dr J. Gardener, University of Leeds) was consistent with a reduction in permittivity over temperature and time at temperature. Here the sample was de-aged by heating to 25 °C above T_c for 15 min and then cooled to the measurement temperature of 250 °C and held there in a DC-field (Modulab XM MTS software, Solartron Analytical, UK). Permittivity measurements were taken for up to nearly 1000 hours and show a steady decrease with time, indicating an increased dependence on thermal history (Figure 6.4.1 a). This is in contrast to tri-doped SNN ($Sr_{2-x-y}Ca_xY_yNaNb_{5-y}Zr_yO_{15}$, x = y = 0.05, Chapter 4, Section 4.3) which remained relatively stable over a similar time period. This raises the possibility that the ferroelectric stability is indeed connected to the Na^+ vacancies (or lack of them) within the material and its thermal history.

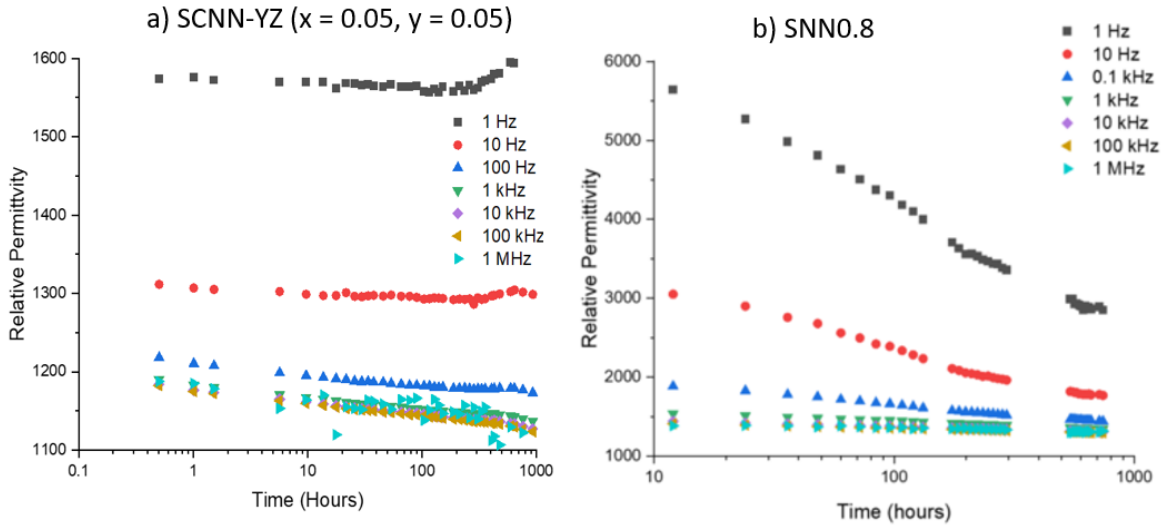

Figure 1 (Appendix A) a-b. Long duration permittivity measurements at 250 °C for a) $Sr_{2-x-y}Ca_xY_yNaNb_{5-y}Zr_yO_{15}$, x = 0.05, y = 0.05 b) $Sr_{2.1}Na_{0.8}Nb_5O_{15}$ (ES) indicating an increased

dependence on thermal history leading to a decrease in ε_r value for compositions with Na^+ deficiency (data acquired and plots by Dr J. Gardener, University of Leeds).

Long duration permittivity measurements on deaged samples of SNN0.8 and SCNN-YZ (heated to 25 ^oC above T_c for 15 min and then cooled to the measurement temperature of 250 ^oC) under a DC-field showed that SNN0.8 was more susceptible to ferroelectric ageing than a composition based on SNN1.0. As the measurement temperature was below T_c, structural (changing to a higher symmetry) and compositional changes (not observed below 300 ^oC in Chapter 6) could be ruled out as a mechanism for the reduction in capacitance. It is likely related to the formation of a more A-site vacancy rich SNN phase in SNN0.8 becoming a major factor. Movement of vacancies at high temperatures and under the influence of a DC electric field may disrupt the polar nanoregions of the ferroelectric phase that could cause a drop in permittivity. Although migration of vacancies towards grain boundaries could also cause a space charge effect which will contribute towards polarisation (as seen in some SNN0.8 compositions, see Chapter 5, Section 5.6), this is likely to be less than the contribution from polar nanoregions. The presence of Na vacancies in the SNN0.8 could also enable A-site cation ordering with a corresponding change in Tc and $\varepsilon_{r\,max}$ as is established for BNN and SBN (Aamlid et al. 2020.

Appendix B

(see below)

Journal of the European Ceramic Society xxx (xxxx) xxx

Contents lists available at ScienceDirect

Journal of the European Ceramic Society

journal homepage: www.elsevier.com/locate/jeurceramsoc

New high temperature dielectrics: Bi-free tungsten bronze ceramics with stable permittivity over a very wide temperature range

Thomas Brown [a], Andy P. Brown [a], David A. Hall [b], Thomas E. Hooper [a,*], Yizhe Li [b], Stuart Micklethwaite [a], Zabeada Aslam [a], Steven J. Milne [a,*]

[a] School of Chemical and Process Engineering, University of Leeds, Leeds, LS2 9JT, UK
[b] School of Materials, University of Manchester, Manchester, M13 9PL, UK

ARTICLE INFO

Keywords:
High temperature dielectrics
Bi-free
Pb-free
Tungsten bronze
Microstructure

ABSTRACT

High relative permittivity, ε_r, over a very wide temperature range, −65 °C to 325 °C, is presented for ceramics designed to be compatible with base metal electrode multilayer capacitor manufacturing processes. We report a ≥ 300 °C potential Class II capacitor material, free from Bi or Pb ions, developed by doping $Sr_2NaNb_5O_{15}$ with Ca^{2+}, Y^{3+} and Zr^{4+} ions, according to the formulation $Sr_{2-2z}Ca_zY_zNaNb_{5-z}Zr_zO_{15}$. For sample composition z = 0.025, ε_r values are 1565 ± 15 % (1 kHz) from −65 °C to 325 °C. At a slightly higher level of doping, z = 0.05, ε_r values are 1310 ± 10 % from −65 °C to 300 °C. Values of the dielectric loss tangent, tanδ are ≤ 0.025 from −60 °C to 290 °C, for z = 0.025, with tanδ increasing to 0.035 at 325 °C. Microstructural analyses exclude core-shell mechanisms being responsible for the flattening of the ε_r –T response.

1. Introduction

Commercially available Class II high volumetric efficiency ceramic capacitors based on ferroelectric $BaTiO_3$ ceramics are specified from −55 °C to 125 °C–175 °C for materials referred to by the Electronics Industries Alliance codes as X7R-X9R (where R signifies stability in capacitance within ± 15 % of the room temperature value). For emerging power electronics applications relevant to the energy transition, an upper operating temperature ceiling of < 200 °C is insufficient [1]. High voltage power electronics for renewable energy generation and distribution require passive components that can operate alongside wide band gap semiconductors at junction temperatures of 250 °C–300 °C [2]. There are also a number of other applications where new Class II capacitors must maintain stable performance to ≥ 300 °C, for example distributed engine control systems for aerospace applications to reduce fuel consumption and improve reliability; and for drill-bit feedback systems in deep-well geothermal energy exploration [3]. Potential applications also arise in electric and hybrid vehicles.

In a bid to address these strategically important technological requirements, compositionally complex relaxor ferroelectrics with the perovskite ABO_3 crystal structure have been researched by many academic groups, recently with a focus on energy storage density measurements of multilayer samples [1–12]. Unfortunately, all of these materials contain bismuth oxide (or lead oxide). This prevents their application in base metal (Ni) electrode multilayer ceramic capacitors – the main market. Bismuth or lead containing oxide ceramics are thermodynamically incompatible with metallic nickel electrode materials under the high temperature, chemically-reducing conditions used to co-fire base metal electrodes and the ceramic layers [13]. Hence most reports of MLCCs made with Bi or Pb containing ceramic dielectrics use expensive precious metal electrodes, at best Ag/Pd. The mainstream multilayer capacitor industry replaced precious metal electrodes with nickel, and to a lesser extent copper, many years ago on cost and security of supply consideration. For Bi-containing ceramic dielectrics co-fired with Cu there is a restricted processing window. Thermodynamic calculations indicate MLCCs would have to be co-fired at temperatures <940 °C, and oxygen partial pressures, $Po_2 < 10^{-7}$ atm. [14]. By adding a series of liquid forming sintering fluxes to a $Na_{0.5}Bi_{0.5}TiO_3$ – based piezoceramic formulation, it proved possible to reduce the sintering temperature from 1150 °C to 900 °C, thereby enabling Cu electrodes to be demonstrated, but dielectric losses were higher than for samples fired in air [14]. A further issue or Bi- ceramic dielectrics relates to loss of volatile bismuth oxide during ceramic processing. Our interest in researching Pb, Bi-free high temperature dielectrics stems from industrial translation challenges of existing materials for applications in mass market Ni-electrode MLCCS.

* Corresponding authors.
E-mail addresses: T.E.Hooper@leeds.ac.uk (T.E. Hooper), s.j.milne@leeds.ac.uk (S.J. Milne).

https://doi.org/10.1016/j.jeurceramsoc.2020.10.034
Received 21 May 2020; Received in revised form 12 October 2020; Accepted 19 October 2020
Available online 21 October 2020

The best of the bismuth containing relaxor high temperature dielectrics are based on $Na_{0.5}Bi_{0.5}TiO_3$. For example, formulations in the $Na_{0.5}Bi_{0.5}TiO_3$-$Ba_{0.8}Ca_{0.2}Ti_{1-y}Zr_yO_3$-$NaNbO_3$ system developed in our laboratory have ε_r values of 1300 ± 15 % from −55 °C to 300 °C [8]. In other temperature-stable relaxors, such as (Ba,Ca)TiO_3-$BiMg_{0.5}Ti_{0.5}O_3$ or $BaTiO_3$-$BiZn_{0.5}Ti_{0.5}O_3$ solid solutions [7], the range of stable dielectric permittivity extends to upper temperatures exceeding 300 °C (~500 °C in some materials) but the lower limit is well above the Electronic Industries Appliance 'X' specified lower working temperature of −55 °C. Moreover, in many cases dielectric loss tangent values are relatively high, at least over part of the temperature span.

The need to discover alternative materials that avoid the use of heavy metal oxides so enabling integration with (Ni) base metal electrode MLCCs motivated us to shift the focus of research away from perovskite ferroelectrics. The criteria was to find a parent ferroelectric with dielectric anomalies at higher temperatures than for $BaTiO_3$ - the starting point for X7R capacitor materials. $BaTiO_3$ materials are limited to modest upper operating temperatures due to a Curie peak temperature of ~130 °C. Our criteria for designing new Bi-free next generation Class II dielectrics that could operate at significantly higher temperatures was to first select a parent ferroelectric with a higher Curie point, T_c, than $BaTiO_3$ *and* with a high $\varepsilon_{r\ max}$ value at T_c, such that even after compositionally engineering a suppression of the permittivity peak, high Class II levels of permittivity were retained over an extended temperature range. This led us to the tungsten bronze ferroelectric and nonlinear optics literature. The material we selected, $Sr_4Na_2Nb_{10}O_{30}$, not only satisfied this selection criteria in terms of Curie point (305 °C) and $\varepsilon_{r\ max}$ value (~1400), it also displayed a second, lower temperature permittivity peak at −15 °C [15,16]. We considered that this would be of value in helping achieve stable permittivity to −55 °C, the EIA 'X' standard lower working temperature for a Class II capacitor. Relative permittivity varies by more than ± 20 % across the temperature range -55 °C to 300 °C for $Sr_4Na_2Nb_{10}O_{30}$.

The tungsten bronze crystal structure involves corner sharing of BO_6 octahedra in two crystallographic orientations (here B = Nb^{5+}) leaving three types of distinct crystallographic sites available for lower valence cations, labelled A2, A1 and C, in the generic formula $(A2)_4(A1)_2(C)(B1)_2(B2)_8O_{30}$ [15–22], with co-ordination numbers 15, 12 and 9 for A2, A1 and C sites respectively. The primary cell is tetragonal, but due to the existence of superstructures, either commensurate or incommensurate that involves modulation of the oxygen sublattice, the true symmetry may be orthorhombic with a much larger unit cell. A schematic of the tetragonal primary cell and its relationship to the larger orthorhombic unit cell is shown in Fig. 1. When viewed along the [001] direction, the A2 sites are visible as pentagonal channels, and the A2 square and C triangular channels. Our selection, $Sr_4Na_2Nb_{10}O_{30}$ is an example of a 'filled' tungsten bronze, so called because all A sites are occupied (although the C sites are empty). An early crystallographic study of a closely related tungsten bronze, $Ba_4Na_2Nb_{10}O_{30}$ was reported by researchers at Bell Telephone Laboratories [17]. However, $Sr_4Na_2Nb_{10}O_{30}$ is less widely reported, although some crystallographic information is available from a combination of X-ray and electron diffraction [15,16].

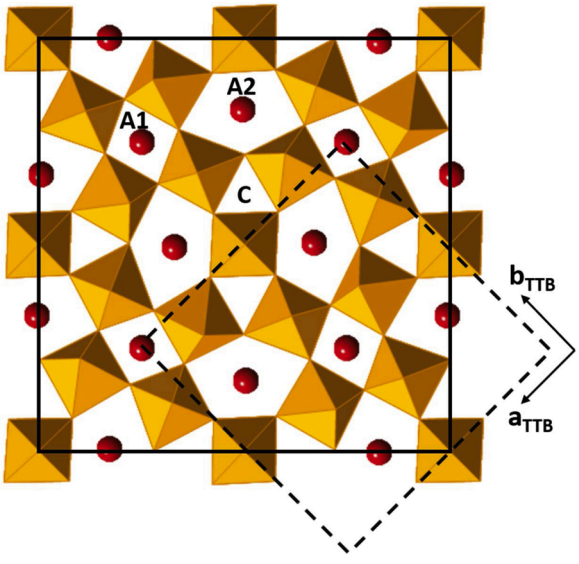

Fig. 1. Pseudocubic tetragonal primary cell of tungsten bronze structure (dashed lines) viewed along the [001] direction and its spatial relationship to a larger orthorhombic unit cell arising from by a superstructure (solid lines; after Ref [20]. In $Sr_4Na_2Nb_{10}O_{30}$ Sr^{2+} and Na^+ ions are distributed over the A1 and A2 sites (red) formed by corner sharing NbO_6 octahedra (orange) (For interpretation of the references to colour in this figure legend, the reader is referred to the web version of this article).

In $Sr_4Na_2Nb_{10}O_{30}$ tungsten bronze ferroelectrics a change from paraelectric to ferroelectric occurs with no change in crystal system: electrical properties may be strongly influenced by subtle changes to octahedral tilt systems, defect structures and crystal superstructures [15–22]. Structure-property correlations have been less widely studied than for perovskite ferroelectrics and there is still much to learn. The results reported below will provide added stimulus for future wide-ranging studies to understand the fundamental structure-property relationships for this exciting new type of high temperature dielectric.

2. Experimental

For convenience, the chemical formula of the parent niobate phase ($Sr_4Na_2Nb_{10}O_{30}$) is expressed as $Sr_2NaNb_5O_{15}$ (SNN) in the remainder of the text. The substituted compositions are expressed assuming a solid solution formula $Sr_{2-2z}Ca_zY_zNaNb_{5-z}Zr_zO_{15}$. The assumption is that Ca^{2+} and Y^{3+} substituents will occupy A1/A2 sites and Zr^{4+} the Nb^{5+} (B) sites; C sites will remain empty. Sample formulations with z = 0, 0.025 and 0.05 were prepared using the mixed oxide route. The compositions correspond to a very low level of substitution. Only 1.25 at.% of the Sr^{2+} (A) sites are substituted by Y^{3+} in composition z = 0.025, and 2.5 at.% in z = 0.05. For B sites, the Zr^{4+} for Nb^{5+} levels are 0.05 at.% and 1 at.% for compositions z = 0.025 and 0.05 respectively.

Starting reagents of: strontium carbonate (Aldrich, 99.9 %); calcium carbonate (Aldrich, >99 %); sodium carbonate (Sigma-Aldrich, 99.95 %); niobium oxide (Alfa Aesar, 99.9 %); yttrium oxide (Alfa Aesar, 99.9 %) and zirconium oxide (Alfa Aesar, 99.7 %). Powders were mixed in appropriate ratios before ball-milling for up to 24 h using stabilised zirconia grinding media, in isopropanol. Dried powders were calcined at 1200 °C for 6 h (heating rate 5 °C/min) in high purity alumina crucibles. The calcined powders with the addition of 2 wt.% of binder (Optapix AC112, Zschimmer & Schwarz) were ball milled in water for 24 h, dried and passed through a 300 μm mesh nylon sieve, before pressing uniaxially at 100 MPa (for 90 s) in a 1 cm diameter steel die. After uniaxial pressing, the green pellets were isopressed (200 MPa for 5 min) in an isostatic press (Stanstead fluid power, Essex, UK). Binder burn-out was performed at a heating rate of 1 °C/min to a dwell temperature of 550 °C and held for 5 h. Sintering was carried out after embedding the pellets in a powder of the same composition. Maximum densities were obtained at a sintering temperature of 1300 °C or 1350 °C; dwell times were 4−5 h. Sintered ceramic densities were measured from measured pellet dimensions and mass; the theoretical density was estimated from the nominal unit cell contents and measured lattice parameters.

Phase analysis by powder X-ray diffraction (XRD) was carried out using a Bruker D8 X-ray powder diffractometer. Unit cell lattice parameters of an adopted pseudo-tetragonal structure were obtained by full pattern Rietveld refinement using TOPAS 5.0 software (Bruker AXS, Karlsruhe, Germany). In the refinement analysis, the peak shape function was determined by the fundamental parameters of the X-ray diffractometer geometry. The refined parameters are background

function coefficient, lattice constant, scale factor, and atomic coordination.

In order to prepare specimens for microstructural characterisation by scanning electron microscopy, ceramic pellets were mounted in epoxy resin (Epothin, Buehler) and ground with P240, P600 and P2500 silicon carbide paper. Subsequent sequential polishing was carried out using Texmet P microcloths with MetaDi 2 diamond suspensions of decreasing particle size: 9 μm, 3 μm and 1 μm. A final polish was carried out with ChemoMet and MasterMet 0.06 μm colloidal silica on a Buehler EcoMet 300 grinder/polisher. Chemical etching was carried out with a 2:1 ratio of hydrofluoric acid and concentrated nitric acid for 90 s at room temperature.

Scanning electron microscopy (SEM) was performed using a Hitachi SU8230 high performance cold field emission instrument fitted with an Oxford Instruments Aztec energy dispersive X-ray analysis (EDX) system with 80 mm^2 X-Max SD detector and analysis software. For transmission electron microscopy (TEM), thin sample lamellae were prepared via the in-situ lift-out method using a FEI Helios G4 CX Dual Beam - High resolution monochromated, field emission gun, scanning electron microscope (FEG-SEM) with precise Focused Ion Beam (FIB). In the Dual Beam microscope, 500 nm of platinum (Pt) was electron beam deposited (at 5 kV, 6.4 nA for the electron source) onto the surface of the target area. This was followed by a second Pt layer (1 μm) using the FIB (at 30 kV, 80 pA for the liquid Ga ion source). An initial lamella was cut (by the FIB at 30 kV, 47 nA), before a final cut-out was performed (at 30 kV, 79 nA). Final thinning and polishing of the lamellae to electron transparency was performed with a low energy ion beam (5 kV, 41 pA). The lamellae were attached, using ion beam deposited Pt onto a copper FIB lift-out grid (Omniprobe, USA) mounted within the SEM chamber (in-situ) ready for transfer to the TEM. The lamellae were imaged using a FEI Titan Themis^3 300 kV TEM fitted with a SuperX EDX system and Velox processing software.

For electrical measurements, silver electrodes were applied to opposite pellet faces (Sun Chemical, Gwent Electronic Materials). Relative permittivity, ε_r, and loss tangent, tanδ, were measured at low-field as a function of temperature at fixed frequencies using a Hewlett Packard, HP4284 LCR analyser. An environmental chamber was used for lower temperatures down to -65 °C (TJR; Tenney Environmental-SPX, White Deer, CA). Ferroelectric hysteresis measurements were carried out using a HP33120A function generator in combination with a HVA1B

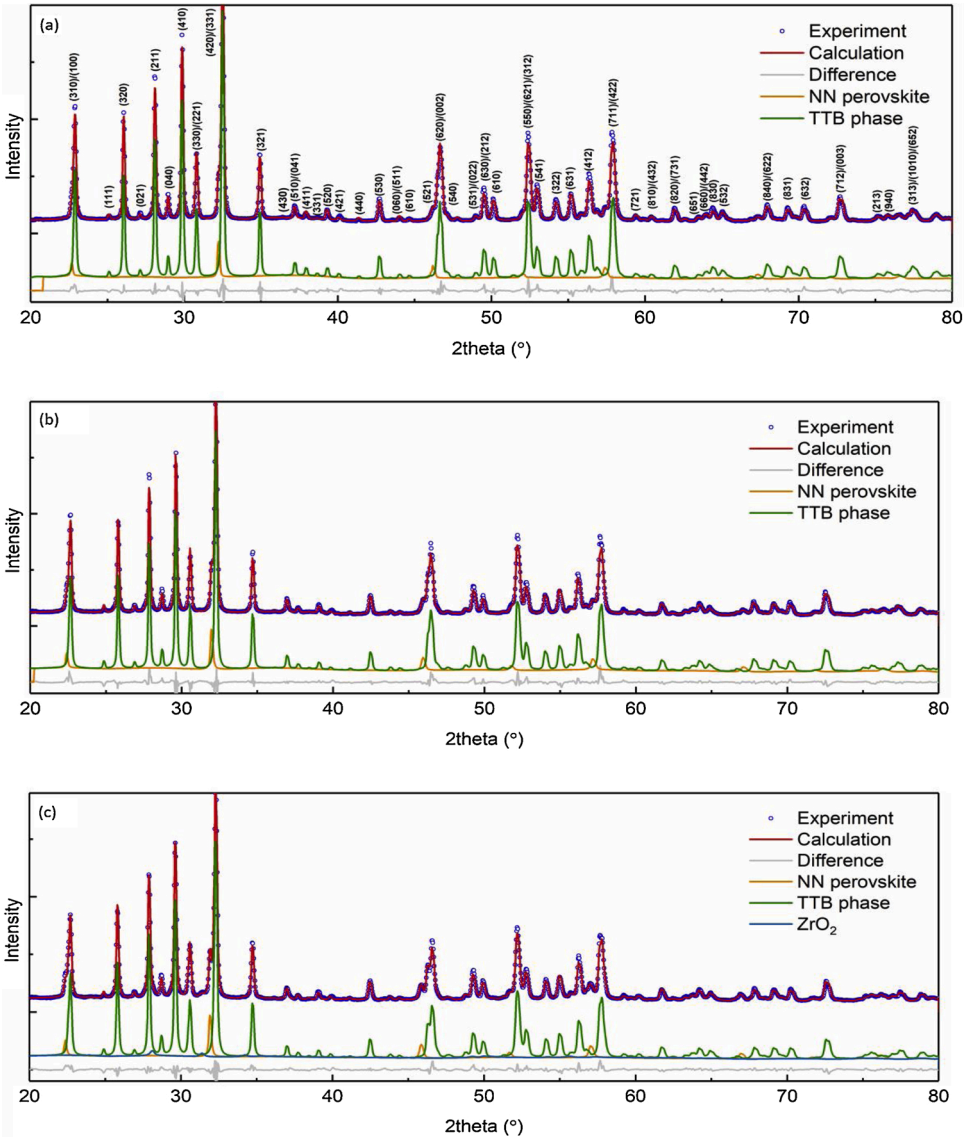

Fig. 2. Full pattern Rietveld refinements for $Sr_{2-2z}Ca_zY_zNaNb_{5-z}Zr_zO_{15}$: a) z = 0; b) z = 0.025; c) z = 0.05. The terms NN and TTB in the legends refer to a sodium niobate type perovskite second phase and the pseudo tetragonal tungsten bronze main phase respectively.

high voltage amplifier (Chevin Research, Otley, UK), using a sinusoidal electric field waveform with a frequency of 2 Hz. The measured electric field-time and current-time waveforms were processed to yield polarisation-electric field (*P-E*) loops and effective complex permittivity values using the method described previously.[23]

3. Results and discussion

Full-pattern refinements of X-ray powder diffraction data for crushed sintered pellets are shown in Fig. 2. Secondary phase $NaNbO_3$ was present in all three samples as has been reported by others for SNN [20, 21]. In the present work, increasing the calcination and sintering times failed to eliminate the extra phase. Therefore, even for unmodified SNN the notional formula $Sr_2NaNb_5O_{15}$ may be inaccurate: for example, the Na rich secondary phase may be due to Sr^{2+} occupancy of a fraction of the perceived Na^+ sites, giving a formula $Sr_{2+x}Na_{1-2x}Nb_5O_{10}$ [24]. Monoclinic ZrO_2 secondary phase was identified only in the z = 0.05 sample. All phases were included in the Rietveld refinements.

We found no convincing evidence from XRD of weak extra superlattice reflections reported at around 20°2θ or 37°2θ which others have observed with the aid of electron diffraction, and attributed to an orthorhombic unit cell (Space Group *Im2a*). These reports relate to SNN samples which had been fabricated by sintering for 2 days at 1250 °C, followed by rapid quenching to room temperature [20]. Some workers have assigned SNN to a different orthorhombic space group, *Cmm*2 [25]. However the lack of any distinct supercell reflections in our XRD patterns prompted us to index on tetragonal axes, and to refine the data on the basis of space group *P4bm*. This tetragonal space group has been used in the past to index SNN samples obtained by calcining mixed oxide powders at 1150 °C for 12 h in an oxygen atmosphere [26]. The ambiguity in the literature as to space groups for SNN may in part relate to structural variations associated with different synthesis conditions. In a further example of the uncertainties in indexing diffraction patterns, a recent study of Ca^{2+} modified SNN reports a tetragonal phase for SNN with no Ca^{2+} substitution, changing to orthorhombic with increasing levels of Ca^{2+} substitution [24,27]. Verification of the true crystal system of SNN produced in our laboratory must await a detailed future study using electron and neutron diffraction. The emphasis of the present communication is to report microstructures and electrical properties of a new potential high temperature capacitor material.

Crystallographic data refined on *P4bm* are summarised in Table 1. The modifications by Ca^{2+}, Y^{3+}, Zr^{4+} produced a slight contraction in cell volume, Table 1, consistent with solid solution formation.

Scanning electron micrographs of polished and etched sections of z = 0 and z = 0.05 are shown in Fig. 3. Observed grain sizes were similar (< 10 μm) for both compositions. Densities were 92–93 % of estimated theoretical values. The possibility of elemental segregation within the grains was investigated by SEM-EDX and TEM-EDX. For X7R $BaTiO_3$ based capacitor materials, a core-shell grain structure brought about by a variety of additive oxides is responsible for inducing a temperature stable permittivity response (from −55 °C to 125 °C). Thus it was important to establish if a comparable microstructure-strain mechanism was responsible for flattening the ε_r-T response of SNN. The SEM-EDX analysis for z = 0.05 showed no elemental gradation within grains, Fig. 4. The existence of secondary grains of sodium niobate and zirconia identified in XRD patterns (Fig. 1) with grain sizes of ~ 5 μm and ~1 μm respectively was confirmed by the SEM-EDX analysis; there was also some evidence from EDX for the presence of Sr in the sodium niobate grains. More detailed analysis using TEM-EDX confirmed an absence of core-shell grain structures, or indeed any form of elemental gradation within individual grains, Fig. 5.

The relative permittivity-temperature, ε_r-*T* response of the parent tungsten bronze $Sr_2NaNb_5O_{15}$ ceramic (SNN) is presented in Fig. 6a. The higher temperature dielectric peak, at 305 °C, is denoted T_2. For other tungsten bronzes, this dielectric anomaly is reported to correspond to the formation, on cooling, of a supercell which induces ferroelectric behaviour: hence T_2 represents the Curie point [16]. Structural correlations are less well understood in the context of the lower temperature dielectric peak T_1, which occurs at -14 °C in SNN (1 kHz) and shows frequency dispersion similar to a relaxor ferroelectric. An accompanying change in thermal expansion coefficient for related tungsten bronzes implies that the T_1 peak corresponds to a ferroelastic transition, but no associated structural deviations have been detected [18]. For z = 0 (SNN), the 'standard' dielectric peaks created a variation in ε_r of ±22 % across the important temperature range, −55 °C to 300 °C, Fig. 6a. This is well outside the R-type ± 15 % stability level required of a Class II capacitor material. Consequently partial substitution of Sr^{2+} by Ca^{2+} was investigated for $Sr_{2-x}Ca_xNaNb_5O_{15}$ x < 0.1. The ε_r-*T* responses of SNN and Ca-SNN ceramics of comparable densities were generally similar. This finding is consistent with other reports [27]. Further chemical modifications, involving co-substitution of Ca^{2+}, Y^{3+} for Sr^{2+} and Zr^{4+} for Nb^{5+} were investigated in an attempt to supress the temperature variability in permittivity and attain R-type performance.

For the Ca^{2+}, Y^{3+}, Zr^{4+} modified SNN sample composition z = 0.025, which had a very similar phase content to undoped SNN, the T_2 peak temperature increased to 345 °C, from a value of 305 °C in unmodified SNN (at 1 kHz); there was also a decline in the $\varepsilon_{r\ max}$ value due to increased broadening, Fig. 6b. For the lower temperature peak, there was very little change in peak temperature T_1 with substituent doping (−18 °C compared to −14 °C for SNN z = 0), but there was an increase in frequency dispersion. For sample composition z = 0.025 the difference

Table 1
Summary of (pseudo) tetragonal lattice parameters, goodness of fit, R_{wp} and phase fractions from Rietveld analysis for $Sr_{2-2z}Ca_zY_zNaNb_{5-z}Zr_zO_{15}$.

Composition	a (Å)	c (Å)	V (Å^3)	R_{wp}%	%$NaNbO_3$
z = 0	12.365 (90)	3.8958 (2)	595.73 (3)	4.58	5.0
z = 0.025	12.362(9)	3.8920 (1)	594.84 (9)	4.99	7.4
z = 0.05	12.363(0)	3.8861 (1)	593.97 (3)	4.27	7.3 (+2.5 ZrO_2)

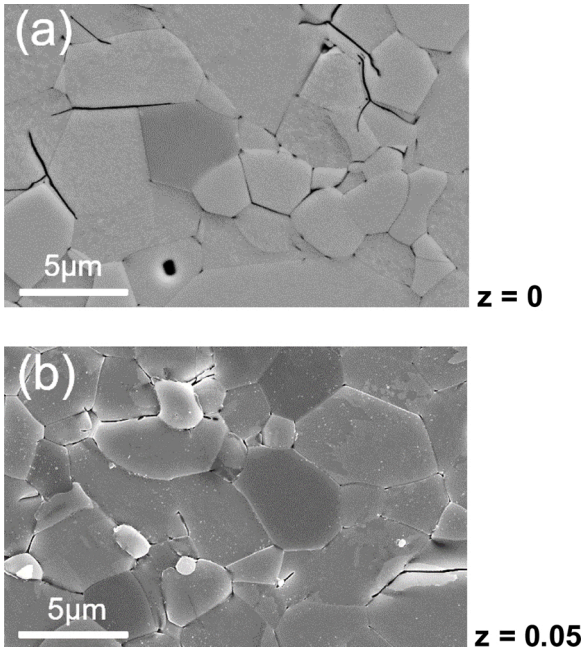

Fig. 3. SEM micrographs of $Sr_{2-2z}Ca_zY_zNaNb_{5-z}Zr_zO_{15}$: (a) z = 0 and (b) z = 0.05 (sintered for 4 h at 1300 °C).

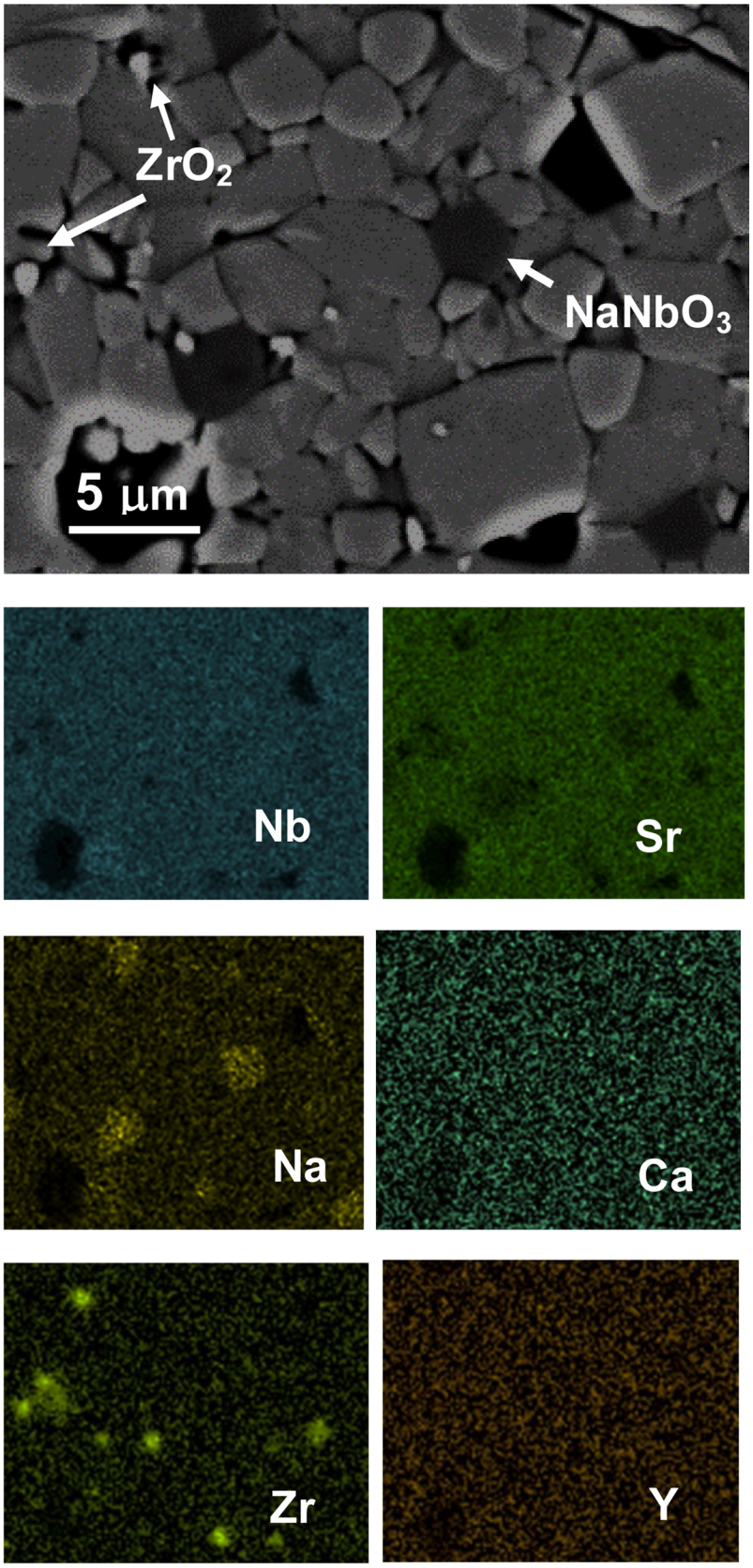

Fig. 4. SEM-EDX images of sample composition z = 0.05 showing a secondary Na-rich phase, consistent with the $NaNbO_3$ phase identified by XRD, and ZrO_2 grains (sintered at 1300 °C for 4 h).

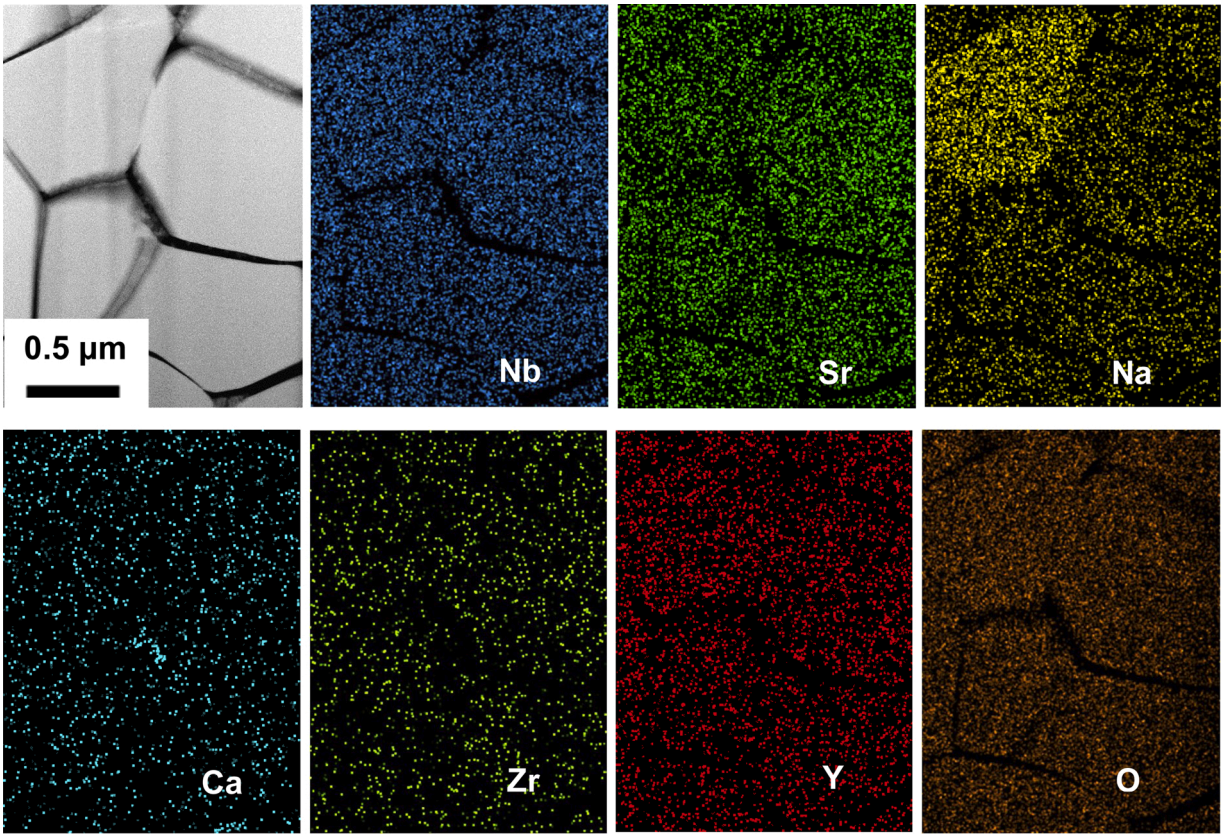

Fig. 5. Scanning TEM-EDX images confirming a lack of any detectable elemental gradation across grains - in contrast to conventional perovskite $BaTiO_3$ X7R temperature-stable dielectrics. Striations in HAADF* image (top left) are a 'curtaining' artefact of the FIB-SEM thinning method used to prepare the TEM specimen. * HAADF = high angle annular dark-field.

in temperature, ΔT, of $\varepsilon_{r\ max}$ temperatures (Tm) between frequencies 1 kHz and 1 MHz was 25 °C, compared to 10 °C for unmodified SNN, z = 0.

For a higher level of chemical substitution, z = 0.05, the T_2 anomaly was now displaced to 255 °C, some 90 °C below the T_2 peak for z = 0.025, Fig. 6c. This non-monotonic shift of T_2 with z indicates a complex interplay between dopant level and temperature of the dielectric anomalies which may well relate to alterations in defect structures (possibly affecting NbO_6 tilts in the case of T_2). The T_2 anomaly also became significantly more diffuse as the level of substitution increased. As a result, the $\varepsilon_{r\ max}$ value at T_2 was approximately 60 % of that observed for unmodified SNN, z = 0. There was also an increase in broadening of the T1 peak, Fig. 6c, but less so than for T2. The presence of zirconia secondary phase in the microstructure may at least in-part account for the drop in $\varepsilon_{r\ 25\ °C}$ value compared to z = 0.025, but matrix strain effects consequent on transformation from tetragonal to monoclinic zirconia (on cooling from sintering temperatures) are thought unlikely, given the non-optimised sample density (92–93 % theoretical).

The net effect of these chemical modifications on peak temperatures and peak profiles was to achieve the requisite $\varepsilon_r \pm 15$ %, R-type consistency in ε_r over very wide ranges of temperature. For z = 0.025 the measured variation in the ε_r data was within ± 13 % of a median value of 1565 for temperatures extending from –65 °C to 325 °C (the median ε_r value occurred at ~105 °C). A further improvement in temperature-stability was achieved for higher levels of Ca^{2+}, Y^{3+} and Zr^{4+} substitution. The z = 0.05, sample composition gave a median value of $\varepsilon_r = 1310$ with a ± 10 % variation from temperatures of -65 °C to 300 °C. Very relevant to consideration as a capacitor material, the median value of ε_r in z = 0.05 ceramics occurred at 25 °C. Comparisons of the 1 kHz ε_r-T plots for z = 0, z = 0.025 and 0.05 are shown in Fig. 7 to highlight the development of temperature stable permittivity.

The low-field dielectric loss tangent values at 1 kHz were ≤ 0.035 from −65 °C to 320 °C (tanδ ≤ 0.025 from −60 °C to 290 °C) for z = 0.025. Losses were slightly higher in the z = 0.05 sample, with tanδ < 0.04. Dielectric data for these 92–93 % dense samples are summarised in Table 2.

Phase stability and electrical properties of SNN have been reported for only a limited number of other cation substitutions, and no specific discussion of temperature stability of permittivity has been presented. Substitution of Sb^{5+} for Nb^{5+} produced a change from orthorhombic *Ccm*2 to tetragonal *P4bm* Space Group, and shifted T_c to lower temperatures [28]. An evolution from orthorhombic to tetragonal crystal system was also induced by Eu^{3+}, and there was some indication from ε_r-T The same research group also examined Sm^{3+} substitution in relation to thermal luminescent properties [29,30].

The P-E hysteresis loops for all of the compositions studied were generally similar in appearance and showed clear evidence of ferroelectric character, as illustrated in Fig. 8a. The maximum polarisation (initially around 13 µC. cm^{-2}) was reduced and the switching range around the coercive field became wider as z increased from 0 to 0.05. Significant dielectric nonlinearity and loss were evident in the sub-

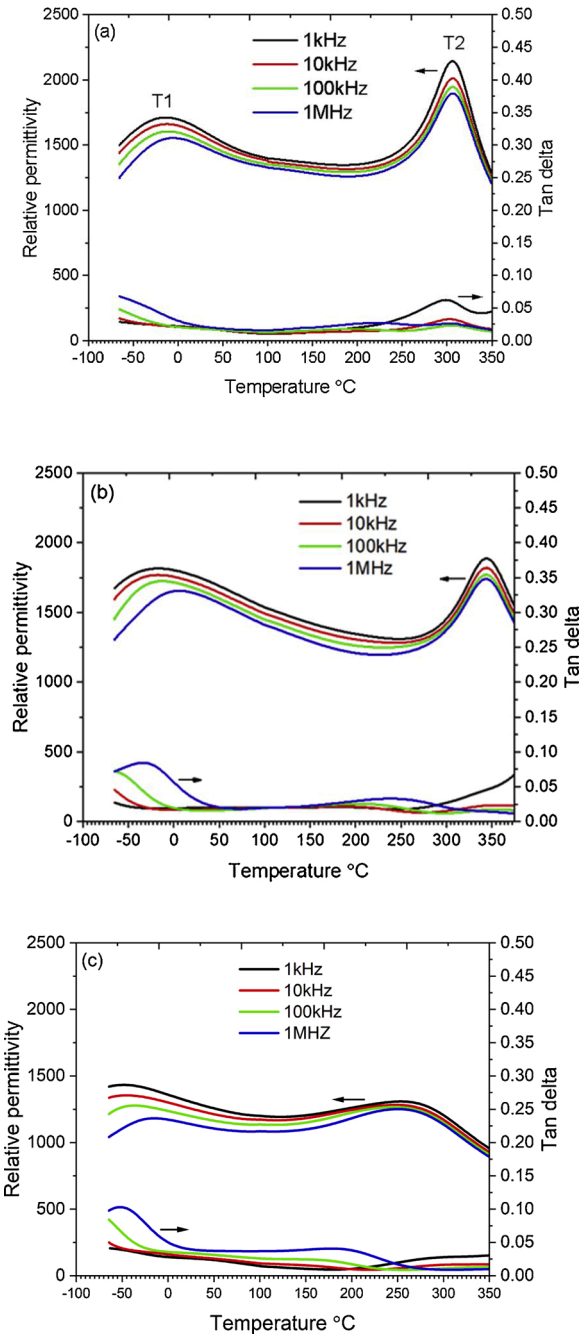

Fig. 6. Relative permittivity-temperature and loss tangent–temperature responses for $Sr_{2-2z}Ca_zY_zNaNb_{5-z}Zr_zO_{15}$: a) SNN z = 0; b) z = 0.025; c) z = 0.05.

coercive field range, as illustrated in Fig. 8b. For example, the effective tanδ value at an electric field amplitude of 4 kV cm^{-1} was determined as 0.154 for the undoped SNN, reducing to 0.081 and 0.060 for z = 0.025 and 0.05, respectively.

Nonlinearity was also apparent in the real and imaginary parts of the complex dielectric permittivity, as shown in Fig. 9. The observed behaviour generally departs from the classical Rayleigh Law (linear ε_r-E_{max} relation) [23], tending towards a quadratic response in the field range up to 15 kV cm^{-1}. The degree of nonlinearity was strongly suppressed for z = 0.05, indicating reduced contributions to the electric field-induced polarisation from domain switching mechanisms, consistent with increasing disorder.

In summary, the primary dielectric parameters of Bi-free and Pb-free dielectric ceramics produced by very low levels of chemical substitution of a tungsten bronze $Sr_2NaNb_5O_{15}$ ferroelectric with Ca^{2+}, Y^{3+}, Zr^{4+} are class leading and very significant in the quest to develop base metal electrode Class II capacitor materials capable of operating over very wide temperature ranges. Future fundamental studies of crystal structure and defect chemistry will be required to elucidate the reasons why such low levels of compositional modification by Ca^{2+}, Y^{3+} and Zr^{4+} bring about such a dramatic change in the permittivity response. However, even at this early stage it is possible to exclude core-shell microstructural mechanisms, of the type which convert perovskite $BaTiO_3$ into a X7R temperature stable dielectric. Moreover, the concentrations of Ca^{2+}, Y^{3+}, Zr^{4+} required to flatten the permittivity response of SNN are far below those required to produce significant broadening of Curie peaks in perovskites due to compositional heterogeneity effects. It is anticipated that this first report of a novel high temperature dielectric with intriguing composition-property relationships will generate a range of follow-on research encompassing microstructural, compositional, phase stability and fundamental mechanistic studies.

4. Conclusions

A high permittivity, Class II, ceramic dielectric that offers stable permittivity to > 300 °C and which does not contain problematic bismuth or lead oxides is demonstrated. Chemical substitution of $Sr_2NaNb_5O_{15}$ by Ca^{2+}, Y^{3+} and Zr^{4+} ions results in a material which more than satisfies the technologically important −55 °C to 300 °C temperature range of stable capacitance required for next generation power capacitor materials. For the formulation $Sr_{2-2z}Ca_zY_zNaNb_{5-z}Zr_zO_{15}$, z = 0.025, values of ε_r lie in the range 1565 ± 13 % for temperatures from −65 °C to 325 °C. At a higher dopant content, z = 0.05, the twin dielectric peaks become even more diffuse, giving ε_r values of 1310 ± 10 % from temperatures of −65 °C to 300 °C. Dielectric loss tangent values are ≤ 0.035 (1 kHz) across the full temperature range of stable permittivity for sample composition, z = 0.025, and tanδ ≤ 0.025 from −60 °C to 290 °C. Limiting dielectric losses were slightly higher, tanδ ≤ 0.04, for z = 0.05 samples. These primary dielectric properties are of high impact given the growing demands for next generation Class

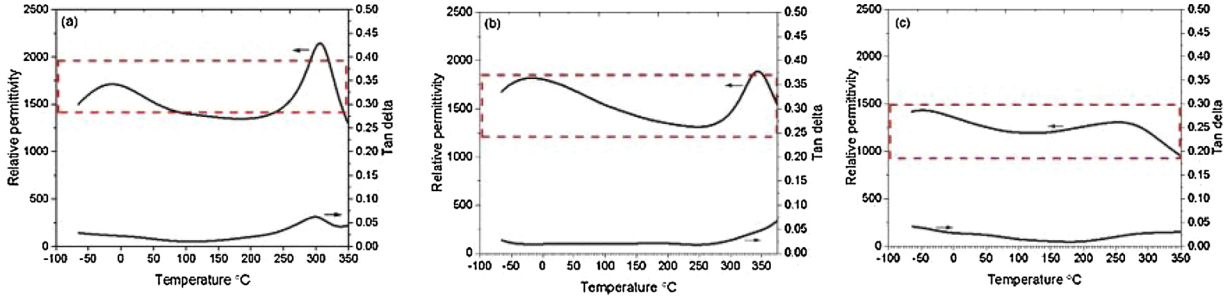

Fig. 7. Comparisons of the 1 kHz relative permittivity, highlighting the stability in ε_r values from -65 °C to ≥ 300 °C in $Sr_{2-2z}Ca_zY_zNaNb_{5-z}Zr_zO_{15}$: (a) z = 0; (b) z = 0.025; (c) z = 0.05. The dashed outline indicates the ± 15 % limits required by the EIA. Dielectric loss tangent plots^#% are also shown.

Table 2
Summary of dielectric data of 92-93 % dense $Sr_{2-2z}Ca_zY_zNaNb_{5-z}Zr_zO_{15}$: ceramics (1 kHz data).

Sample Code	Intended Product Composition	ε_r median (T)	± % ε_r T range	*T* range Tanδ ≤ 0.035	Tanδ ≤ 0.03	Tanδ ≤0.025
z = 0	$Sr_{2.0}Na_{1.0}Nb_{5.0}O_{15}$	1733 *(277 °C)*	22 % −65 °C to 300 °C	−65 °C to 249 °C	−65 °C to 238 °C	−32 °C to 223 °C
z = 0.025	$Sr_{1.95}Ca_{0.025}Na_{1.0}Y_{0.025}Zr_{0.025}Nb_{4.975}O_{15}$	1565 *(110 °C)*	13 % −65 °C to 325 °C	−65 °C to 320 °C	−65 °C to 310 °C	−60 °C to 290 °C
z = 0.05	$Sr_{1.90}Ca_{0.05}Na_{1.0}Y_{0.05}Zr_{0.05}Nb_{4.95}O_{15}$	1310 *(25 °C)*	10 % −65 °C to 300 °C	−40 °C to 370 °C*	−20 °C to 320 °C	+20 °C to 270 °C

* For z = 0.05, tanδ increased to 0.04 between -40 °C and– 65 °C.

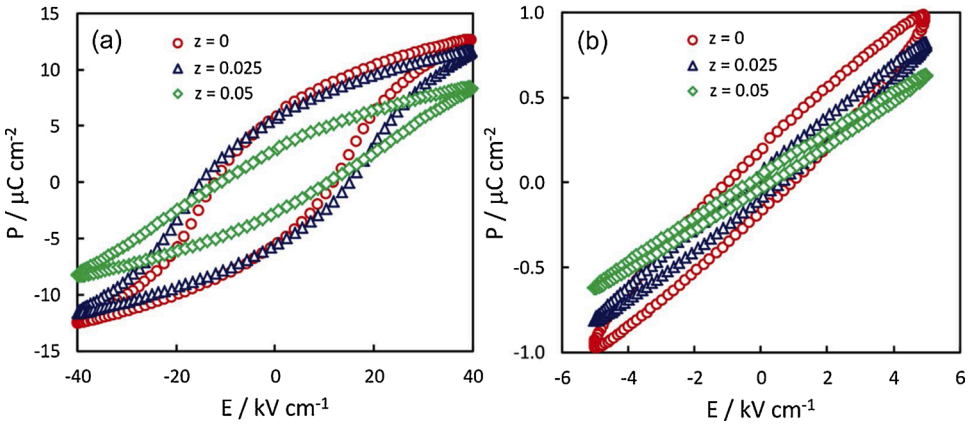

Fig. 8. Comparison of P-E loops for (a) E_{max} =40 kV cm^{-1} and (b) E_{max} =5 kV cm^{-1}.

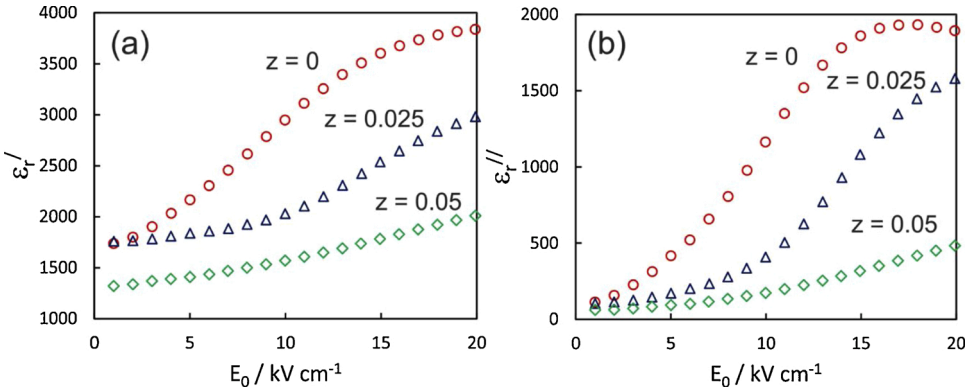

Fig. 9. Variations in (a) real and (b) imaginary parts of relative permittivity as a function of increasing electric field amplitude.

II capacitors that can operate at temperatures well beyond the limit of existing market-leading $BaTiO_3$ based capacitors (under 200 °C). The absence of any volatile bismuth oxide component is highly advantageous in the search for industrially-relevant dielectrics for future base metal electrode high temperature multilayer ceramic capacitors.

Declaration of Competing Interest

The authors declare that they have no known competing financial interests or personal relationships that could have appeared to influence the work reported in this paper.

Acknowledgements

S.J. Milne wishes to thank J. Bultitude, KEMET Electronics Corp. for invaluable background discussions on capacitor materials. A PhD scholarship for T. Brown was provided by School of Chemical and Process Engineering, University of Leeds.

Appendix A. Supplementary data

Supplementary material related to this article can be found, in the online version, at doi:https://doi.org/10.1016/j.jeurceramsoc.2020.10.034.

References

[1] J. Watson, G. Castro, A review of high-temperature electronics technology and applications, J. Mater. Sci. Mater. Electron. 26 (2015) 9226–9235, https://doi.org/10.1007/s10854-015-3459-4.
[2] Q. Li, F.-Z. Yao, Y. Liu, G. Zhang, H. Wang, Q. Wang, High-temperature dielectric materials for electrical energy storage, Annu. Rev. Mater. Res. 48 (3) (2018) 1–3, https://doi.org/10.1146/annurev-matsci-070317-124435.
[3] R. Phillips, J. Bultitude, A. Gurav, K. Park, S. Murillo, P. Flores, M. Laps, High temperature ceramic capacitors for deep well applications, CARTS International 2013 Proceedings, March 25–28, Houston, Texas, USA.
[4] R. Dittmer, W. Jo, D. Damjanovic, J. Rödel, Lead-free high-temperature dielectrics with wide operational range, J. Appl. Phys. 109 (2011), 034107, https://doi.org/10.1063/1.3544481.
[5] H. Ogihara, C.A. Randall, S. Trolier-McKinstry, High-energy density capacitors utilizing 0.7$BaTiO_3$–0.3$BiScO_3$ Ceramics, J. Am. Ceram. Soc. 92 (8) (2009) 1719–1724, https://doi.org/10.1111/j.1551-2916.2009.03104.x.
[6] H. Qi, R. Zuo, A. Xie, A. Tian, J. Fu, Y. Zhang, S. Zhang, Ultrahigh energy-storage density in $NaNbO_3$-based lead-free relaxor antiferroelectric ceramics with

nanoscale domains, Adv. Funct. Mater. 19 (2019) 1903877, https://doi.org/10.1002/adfm.201903877.
[7] A. Zeb, S.J. Milne, Stability of high-temperature dielectric properties for (1−x) Ba0.8$Ca_{0.2}TiO_3$–xBi ($Mg_{0.5}Ti_{0.5}$)O_3 ceramics, J. Am. Ceram. Soc. 96 (9) (2013) 2887–2892, https://doi.org/10.1111/jace.12412.
[8] A. Zeb, S. Ullah Jan, F. Bamiduro, D.A. Hall, S.J. Milne, Temperature-stable dielectric ceramics based on Na0.5Bi0.5TiO_3, J. Eur. Ceram. Soc. 38 (4) (2018) 1548–1555, https://doi.org/10.1016/j.jeurceramsoc.2017.12.032.
[9] T. Roncal-Herrero, J. Harrington, A. Zeb, S.J. Milne, A.P. Brown, Nanoscale compositional segregation and suppression of polar coupling in a relaxor ferroelectric, Acta Mater. 158 (2018) 422–429, https://doi.org/10.1016/j.actamat.2018.07.053.
[10] G. Wang, J. Li, X. Zhang, Z. Fan, F. Yang, A. Feteira, D. Zhou, D.C. Sinclair, et al., Ultrahigh energy storage density lead-free multilayers by controlled electrical homogeneity, Energy Environ. Sci. 12 (2019) 582–588.
[11] Q. Xu, M.T. Lanagan, W. Luo, L. Zhang, J. Xie, H. Hao, M. Cao, Z. Yao, H. Liu, Electrical properties and relaxation behaviour of Bi0.5Na0.5TiO_3-$BaTiO_3$ ceramics modified with $NaNbO_3$, J. Eur. Ceram. Soc. 36 (10) (2016) 2469–2477, https://doi.org/10.1016/j.jeurceramsoc.2016.03.011.
[12] Q. Xu, Z. Song, W. Tang, H. Hao, L. Zhang, M. Appiah, M. Cao, Z. Yao, Z. He, H. Liu, Ultra-wide temperature stable dielectrics based on Bi0.5Na0.5TiO_3–$NaNbO_3$ system, J. Am. Ceram. Soc. 98 (10) (2015) 3119–3126, https://doi.org/10.1111/jace.13693.
[13] Y. Fang, M.T. Lanagan, D.K. Agrawal, G.Y. Yang, C.A. Randall, T.R. Shrout, A. Henderson, M. Randall, A. Tajuddin, An investigation demonstrating the feasibility of microwave sintering of base-metal-electrode multilayer capacitors, J. Electroceramics 15 (2005) 13–19, https://doi.org/10.1007/s10832-005-0374-8.
[14] G. Yesner, A. Safari, Development of a lead-free copper co-fired BNT-based piezoceramic sintered at low temperature, J. Am. Ceram. Soc. 101 (2018) 5315–5322, https://doi.org/10.1111/jace.15777.
[15] E. García-González, A. Torres-Pardo, R. Jiménez, J.M. González-Calbet, Structural singularities in ferroelectric $Sr_2NaNb_5O_{15}$, Chem. Mater. 19 (14) (2007) 3575–3580, https://doi.org/10.1021/cm071303w.
[16] A. Torres-Pardo, R. Jiménez, J.M. González-Calbet, E. García-González, Structural effects behind the low temperature nonconventional relaxor behavior of the $Sr_2NaNb_5O_{15}$ bronze, Inorg. Chem. 50 (23) (2011) 12091–12098, https://doi.org/10.1021/ic2016098.
[17] P.B. Jamieson, S.C. Abrahams, J.L. Bernstein, Ferroelectric tungsten bronze-type crystal structures. I. Barium strontium niobate $Ba_{0.27}Sr_{0.75}Nb_2O_{5.78}$, J. Chem. Phys. 48 (1968) 5048, https://doi.org/10.1063/1.1668176.
[18] X. Zhu, M. Fu, M.C. Stennett, P.M. Vilarinho, I. Levin, C.A. Randall, J. Gardner, F. D. Morrison, I.M. Reaney, A crystal-chemical framework for relaxor versus normal ferroelectric behavior in tetragonal tungsten bronzes, Chem. Mater. 27 (9) (2015) 3250–3261, https://doi.org/10.1021/acs.chemmater.5b00072.
[19] I. Levin, M.C. Stennett, G.C. Miles, D.I. Woodward, A.R. West, I.M. Reaney, Coupling between octahedral tilting and ferroelectric order in tetragonal tungsten bronze-structured dielectrics, Appl. Phys. Lett. 89 (2006) 122908, https://doi.org/10.1063/1.2355434.
[20] J. Gardner, F.D. Morrison, A-site size effect in a family of unfilled ferroelectric tetragonal tungsten bronzes: $Ba_4R_{0.67}Nb_{10}O_{30}$ (R = La, Nd, Sm, Gd, Dy and Y), J. Chem. Soc. Dalton Trans. 43 (2014), https://doi.org/10.1039/C4DT00126E, 16887–11695.
[21] J.C. Toledano, L. Pateau, Differential thermal analysis of ferroelectric and ferroelastic transitions in barium sodium niobite, J. Appl. Phys. 45 (4) (1974) 1611, https://doi.org/10.1063/1.1663464.
[22] L. López-Conesa, J.M. Rebled, A. Ruiz-Caridad, A. Torres-Pardo, M.L. Ruiz-Gonzalez, J.M. González-Calbet, G. Dezanneau, S. Estradé, F. Peiró, Cation disorder in $Sr_{0.67}Ba_{0.33}Nb_2O_6$ assessed by aberration corrected stem, Results Mater. 3 (2019) 100038.
[23] M. Stewart, M.G. Cain, D.A. Hall, Ferroelectric hysteresis measurement & analysis, Natl. Phys. Lab. Rep. CMMT(A) 152 (1) (1999).
[24] B. Yang, J. Li, P. Yang, L. Wei, Z. Yang, Effects of A-site cations on the electrical behaviors in $(Sr_{1-x}Ca_x)_{2.1}Na_{0.8}Nb_5O_{15}$ tungsten bronze ferroelectrics, Mater. Chem. Phys. 243 (2020) 122006, https://doi.org/10.1016/j.matchemphys.2019.122006.
[25] J. Ravez, J.-P. Budin, P. Hagenmuller, Etude comparative des propriétés cristallographiques, diélectriques et d'optique non linéaire des phases ABCNb5O_{15} (A = Ca, Sr, Ba, B = Ca, Sr, Ba, C = Na, K) de type "bronzes oxygénés de tungstène quadratiques, J. Solid State Chem. 5 (1972) 239, https://doi.org/10.1016/0022-4596(72)90034-5.
[26] S. Lanfredi, D.H.M. Gênova, I.A.O. Brito, A.R.F. Lima, M.A.L. Nobre, Structural characterization and Curie temperature determination of a sodium strontium niobate ferroelectric nanostructured powder, J. Solid State Chem. 184 (2011) 990–1000, https://doi.org/10.1016/j.jssc.2011.03.001.
[27] L. Wei, Z. Yang, X. Han, Z. Hu, Structures, dielectric and ferroelectric properties of $Sr_{2-x}Ca_xNaNb_5O15$ lead-free ceramics, J. Mater. Res. 27 (2012) 979–984, https://doi.org/10.1557/jmr.2012.32.
[28] J. Fan, B. Yang, L. Wie, Z. Wang, B-cation effect on relaxor behavior and electric properties in $Sr_2NaNb_{5-x}Sb_xO_{15}$ tungsten bronze ceramics, Ceram. Int. 42 (3) (2016) 4054–4062, https://doi.org/10.1016/j.ceramint.2015.11.077.
[29] S. Hao, J. Li, P. Yang, L. Wei, Z. Yang, Enhanced electrical properties and strong red light-emitting in Eu^{3+}-doped Sr1.90$Ca_{0.15}Na_{0.9}Nb_5O_{15}$ ceramics, J. Am. Ceram. Soc. 100 (12) (2017) 5620–5628, https://doi.org/10.1111/jace.15085.
[30] S. Hao, J. Li, Q. Sung, L. Wei, Z. Yang, Improved electrical properties and good thermal luminescent stability of Sm^{3+}-doped $Sr_{1.90}Ca_{0.15}Na_{0.90}Nb_5O_{15}$ multifunctional ceramics, J. Mater. Sci. Mater. Electron. 30 (14) (2019) 13372–13380, https://doi.org/10.1007/s10854-019-01704-3.